

1991

A numerical model for a bubble in nucleate pool boiling

Rajendra K. Patil
Iowa State University

Follow this and additional works at: <https://lib.dr.iastate.edu/rtd>

 Part of the [Mechanical Engineering Commons](#)

Recommended Citation

Patil, Rajendra K., "A numerical model for a bubble in nucleate pool boiling " (1991). *Retrospective Theses and Dissertations*. 9674.
<https://lib.dr.iastate.edu/rtd/9674>

This Dissertation is brought to you for free and open access by the Iowa State University Capstones, Theses and Dissertations at Iowa State University Digital Repository. It has been accepted for inclusion in Retrospective Theses and Dissertations by an authorized administrator of Iowa State University Digital Repository. For more information, please contact digirep@iastate.edu.

8

92

1

2

1

7

7

U·M·I

MICROFILMED 1992

INFORMATION TO USERS

This manuscript has been reproduced from the microfilm master. UMI films the text directly from the original or copy submitted. Thus, some thesis and dissertation copies are in typewriter face, while others may be from any type of computer printer.

The quality of this reproduction is dependent upon the quality of the copy submitted. Broken or indistinct print, colored or poor quality illustrations and photographs, print bleedthrough, substandard margins, and improper alignment can adversely affect reproduction.

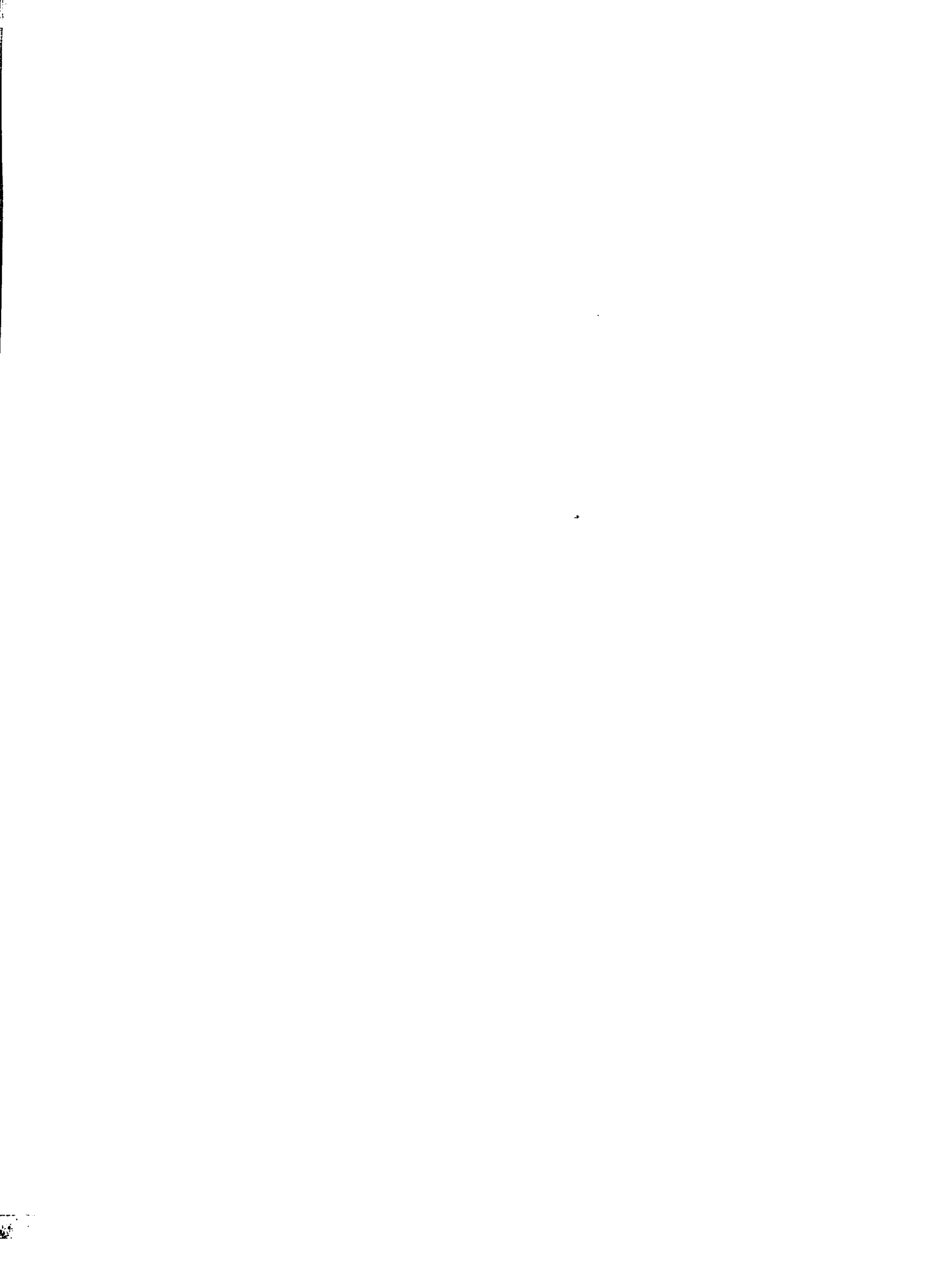
In the unlikely event that the author did not send UMI a complete manuscript and there are missing pages, these will be noted. Also, if unauthorized copyright material had to be removed, a note will indicate the deletion.

Oversize materials (e.g., maps, drawings, charts) are reproduced by sectioning the original, beginning at the upper left-hand corner and continuing from left to right in equal sections with small overlaps. Each original is also photographed in one exposure and is included in reduced form at the back of the book.

Photographs included in the original manuscript have been reproduced xerographically in this copy. Higher quality 6" x 9" black and white photographic prints are available for any photographs or illustrations appearing in this copy for an additional charge. Contact UMI directly to order.

U·M·I

University Microfilms International
A Bell & Howell Information Company
300 North Zeeb Road, Ann Arbor, MI 48106-1346 USA
313/761-4700 800/521-0600



Order Number 9212177

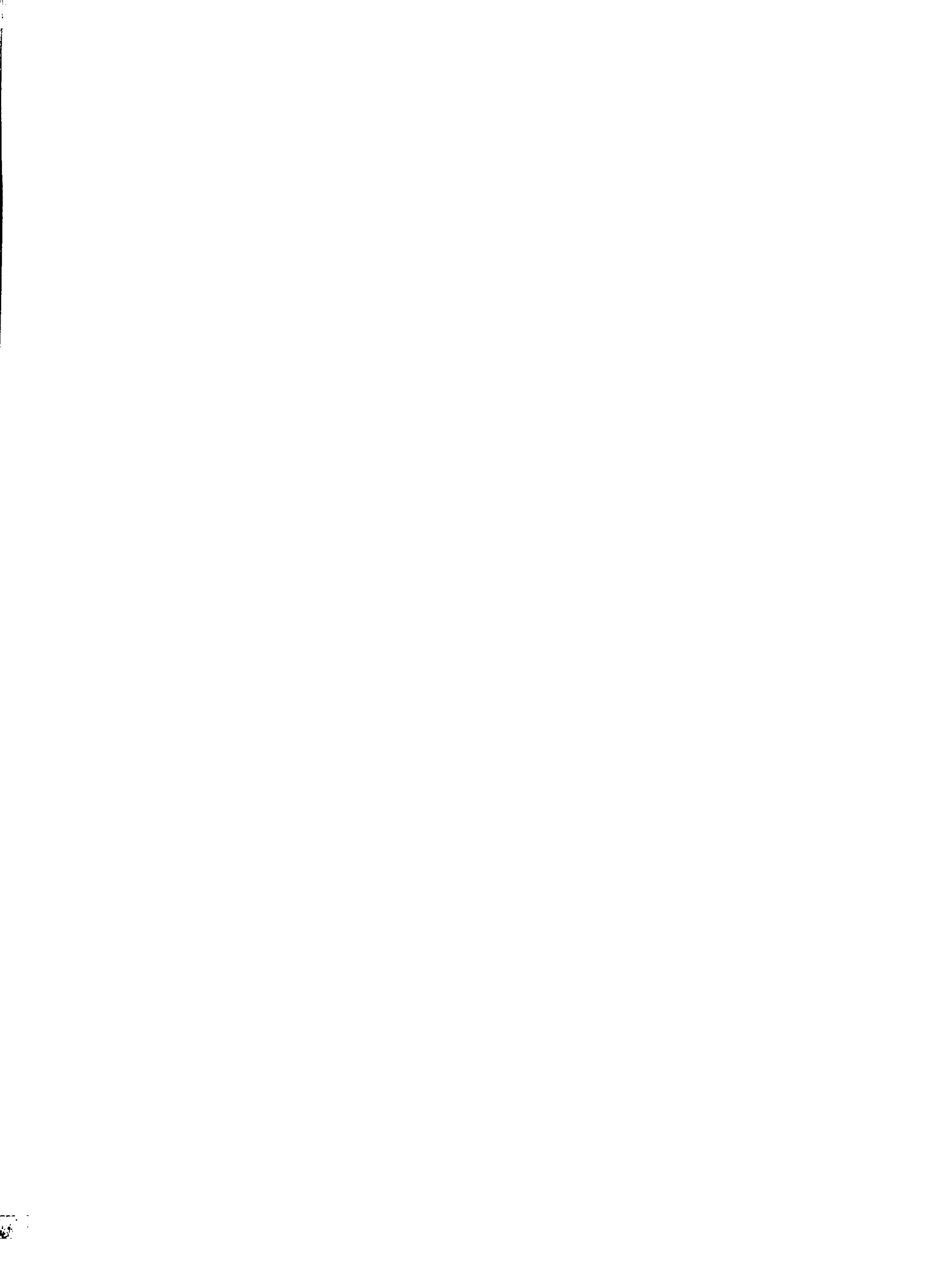
A numerical model for a bubble in nucleate pool boiling

Patil, Rajendra K., Ph.D.

Iowa State University, 1991

U·M·I

300 N. Zeeb Rd.
Ann Arbor, MI 48106



A numerical model for a bubble in nucleate pool boiling

by

Rajendra K. Patil

**A dissertation Submitted to the
Graduate Faculty in Partial Fulfillment of the
Requirements for the Degree of
DOCTOR OF PHILOSOPHY**

Major: Mechanical Engineering

Approved:

Signature was redacted for privacy.

In Charge of Major Work

Signature was redacted for privacy.

For the Major Department

Signature was redacted for privacy.

For the Graduate College

Members of the Committee:

Signature was redacted for privacy.

Iowa State University

Ames, Iowa

1991

TABLE OF CONTENTS

NOMENCLATURE	xii
ACKNOWLEDGMENTS	xv
1. INTRODUCTION	1
1.1 General	1
1.2 Literature Survey	3
1.2.1 Microlayer	6
1.2.2 Growth of Bubbles	9
1.2.3 Shape of the Bubble	14
1.2.4 Bubble Surface	16
1.2.5 Departure	20
1.2.6 Temperature Distribution in the Bulk Fluid	23
1.2.7 The Vapor Inside the Bubble	24
1.2.8 Statistical Characteristics	25
1.2.9 Computational Models	26
1.3 Scope of the Present Study	29
2. THE SECOND GENERATION MODEL OF BUBBLE GROWTH	33
2.1 Assumptions	33
2.2 Formulation	34

2.2.1	Vapor in the Bubble	36
2.2.2	Liquid in the Vicinity of the Bubble	41
2.2.3	Vorticity/Streamfunction Formulation	42
2.3	Non-dimensionalization	44
2.3.1	Non-dimensional Equations	46
2.3.2	Initial and Boundary Conditions	48
2.4	Asymptotic Equations Appropriate for $t \rightarrow \infty$ Limit	49
2.5	Numerical Method	50
2.5.1	Finite Differencing	51
2.5.2	Dynamic Relaxation	54
2.5.3	Computational Resources	58
2.6	Verification of Method	62
2.6.1	Steady State Problem of Heat Diffusion Through a Spherical Shell	62
2.6.2	Homogeneous Boiling	63
2.6.3	Flow-Field Due to Specified Growth Rate	64
2.7	Results	64
2.7.1	Thermophysical Properties and Dimensionless Parameters	64
2.7.2	Heterogeneous Boiling in an Inviscid Medium	66
2.7.3	Heterogeneous Boiling in a Viscous Medium	72
2.8	Comparison with Available Experimental Data	84
2.9	Conclusions	84
3.	THE THIRD GENERATION MODEL OF BUBBLE GROWTH	88
3.1	Microlayer	89

3.2	Heated Surface	92
3.3	Vapor and the Non-condensing Gas in the Bubble	92
3.3.1	Initial State	92
3.3.2	Governing Equations	95
3.4	Boundary Conditions	96
3.5	Non-dimensionalization	99
3.6	The Dimensionless Governing Equations	100
3.7	Dimensionless Boundary Conditions	103
3.8	Dimensionless Initial Conditions	104
3.9	Numerical Method	105
3.10	Computational Method	106
3.11	Results and Discussion	109
3.11.1	The Non-dimensional Parameters and Description of the Com- putational Runs	109
3.11.2	The Vapor Variables	110
3.11.3	Various Bubble Growth Theories	112
3.11.4	The Microlayer Profile	117
3.11.5	The Similarity Solution	122
3.11.6	Comparison of Heat Flow Through the Cap and Through the Microlayer	123
3.11.7	Mass Flow Through the Bubble	125
3.11.8	Height of Formation of Microlayer	129
3.11.9	The Relationship of R and t	130
3.11.10	The Constant C_z of Microlayer Formation	140

3.12 Conclusions	140
4. GENERAL CONCLUSIONS	145
5. LIMITATIONS OF THE PRESENT STUDY AND SCOPE OF THE FUTURE WORK	147
BIBLIOGRAPHY	150
APPENDIX A. NATURAL CONVECTION INSIDE THE BUBBLE	166
A.1 Formulation	166
A.2 Boundary Conditions	168
A.3 Results	169
APPENDIX B. GOVERNING EQUATIONS FOR RELATING QUANTITIES ON EITHER SIDE OF THE VAPOR-FLUID INTERFACE	177
B.1 Vapor Velocity	177
B.2 Mass Balance Across the Interface	179
B.3 Momentum Balance	180
B.4 Energy Balance	180
APPENDIX C. THE FLOW FIELD INSIDE THE BUBBLE WITH MICROLAYER	184
C.1 Boundary Conditions	186
C.2 Finite Differencing	187
C.3 Results	188

LIST OF TABLES

Table 2.1:	Bubble growth in homogeneous boiling	63
Table 2.2:	Thermo-physical properties of water	65
Table 2.3:	Non-dimensional parameters used in the second generation model	65
Table 2.4:	Bubble growth in heterogeneous saturated boiling	67
Table 2.5:	The percent difference between the value of η from the viscous case and that from the inviscid case	83
Table 3.1:	Non-dimensional parameters used in the third generation model	110
Table 3.2:	Ratio \mathcal{R}_1 in saturated boiling	128
Table 3.3:	Ratio \mathcal{R}_1 in subcooled boiling ($Pr = 0.7777$)	128
Table 3.4:	Ratio \mathcal{R}_2 in saturated boiling	129
Table 3.5:	Ratio \mathcal{R}_2 in subcooled boiling ($Pr = 0.7777$)	129
Table 3.6:	Description of bubble growth data from the literature	135
Table 3.7:	Regression analysis with the data in figures 3.17 and 3.18	136

LIST OF FIGURES

Figure 1.1:	Typical boiling curve for water at 1 atm	2
Figure 1.2:	The interrelationship of many parameters in nucleate boiling	4
Figure 1.3:	Illustration of the “locking” of a bubble surface in a symmetric flow	18
Figure 2.1:	The second generation model in physical coordinates	35
Figure 2.2:	An expanding hemispherical control volume of a fixed quantity of mass	37
Figure 2.3:	An infinitesimally thin control volume containing a portion of the bubble surface	38
Figure 2.4:	Typical computational grid	55
Figure 2.5:	An algorithm for the method of dynamic relaxation	56
Figure 2.6:	Variation of relaxation parameter against iteration number, $Ja=50$, $Sb=0$, Grid size: 17×17 , Viscous case	59
Figure 2.7:	Cumulative number of iterations with and without dynamic relaxation, $Ja=50$, $Sb=0$, Grid size: 17×17 , Viscous case . . .	60
Figure 2.8:	Exponent m versus subcooling number (inviscid medium) . .	68
Figure 2.9:	Temperature contours around a bubble during diffusion con- trolled period of growth (Inviscid case)	69

Figure 2.10: “Surface plot” of temperature against the computational domain, $Ja = 10$ $Sb = 0.25$, Inviscid case	71
Figure 2.11: Asymptotic nature of temperature at various points in the computational domain against time, $Ja = 20$, $Sb = 0$, Grid size: 17×17 , Viscous case	73
Figure 2.12: Asymptotic nature of vorticity at various points in the computational domain against time, $Ja = 20$, $Sb = 0$, Grid size 17×17 , Viscous case	74
Figure 2.13: Comparison of bubble growth in viscous, inviscid, and homogeneous boiling	75
Figure 2.14: Exponent m in $R = 2c Ja^m \sqrt{t}$	76
Figure 2.15: Exponent m versus subcooling number (viscous medium)	77
Figure 2.16: Temperature distribution in diffusion controlled phase, $Ja = 10$, $Sb = 0.25$, Viscous case	79
Figure 2.17: Streamfunction distribution in diffusion controlled phase, $Ja = 10$, $Sb = 0.25$, Viscous case	80
Figure 2.18: Vorticity distribution in diffusion controlled phase, $Ja = 10$, $Sb = 0.25$	81
Figure 2.19: Comparison of the growth constants for viscous and inviscid cases	82
Figure 2.20: Comparison between experimental data from the literature and the predictions from the second generation model	85
Figure 3.1: The third generation model in physical coordinates	90
Figure 3.2: Schematic of a microlayer	91

Figure 3.3:	Illustration for the necessity of non-condensable gas in a bubble at the initial state	94
Figure 3.4:	The flowchart for the third generation model	108
Figure 3.5:	Vapor variables versus time (Third generation model)	111
Figure 3.6:	Comparison of predictions of bubble growth from the homogeneous boiling, second, and third generation models	113
Figure 3.7:	Temperature contours in the liquid and in the solid during the diffusion controlled growth period (Saturated boiling)	115
Figure 3.8:	Temperature contours in the liquid and in the solid during the diffusion controlled growth period (Subcooled boiling)	116
Figure 3.9:	“Surface plot” of temperature. Third generation model (Saturated boiling)	118
Figure 3.10:	“Surface plot” of temperature. Third generation model (Subcooled boiling)	119
Figure 3.11:	Microlayer profile (Saturated boiling)	120
Figure 3.12:	Microlayer profile (Subcooled boiling)	121
Figure 3.13:	Local rate of evaporation at the cap portion of the bubble, Saturated boiling	124
Figure 3.14:	Local rate of evaporation at the cap portion of the bubble, Subcooled boiling	126
Figure 3.15:	The ratio of heat added to the bubble from the microlayer to that from its cap portion	127
Figure 3.16:	Graph illustrating the relationship between $\frac{\delta Q}{R}$, Ja , and Pr	131

Figure 3.17: Relationship of $\eta_1 = \eta Pr^{\frac{1}{2}}$ with Ja (experimental and computational) where $\eta = \bar{R}/\sqrt{\alpha_l \bar{t}}$ 133

Figure 3.18: Relationship of $\eta_2 = \eta Pr^{\frac{1}{4}}$ with Ja (experimental and computational) where $\eta = \bar{R}/\sqrt{\alpha_l \bar{t}}$ 136

Figure 3.19: Relationship of $\eta_2 = \eta Pr^{\frac{1}{4}}$ with Ja in subcooled boiling where $\eta = \bar{R}/\sqrt{\alpha_l \bar{t}}$ 138

Figure 3.20: The exponent m versus Ja 139

Figure 3.21: Relationship of $\eta_2 = \eta Pr^{\frac{1}{4}}$ with Ja with various values of C_z where $\eta = \bar{R}/\sqrt{\alpha_l \bar{t}}$ 141

Figure A.1: Steady state solution of the problem of natural convection inside a bubble (temperature) 170

Figure A.2: Steady state solution of the problem of natural convection inside a bubble (streamfunction) 171

Figure A.3: Steady state solution of the problem of natural convection inside a bubble (vorticity) 172

Figure A.4: The transient solution of the problem of natural convection inside the bubble at $\bar{t} = 3 \times 10^{-3}$ sec (Temperature) 174

Figure A.5: The transient solution of the problem of natural convection inside the bubble at $\bar{t} = 3 \times 10^{-3}$ sec (Streamfunction) 175

Figure A.6: The transient solution of the problem of natural convection inside the bubble at $\bar{t} = 3 \times 10^{-3}$ sec (Vorticity) 176

Figure B.1: An expanding control volume with no efflux of mass through the cap portion 178

Figure B.2: An infinitesimally thin control volume containing the liquid- vapor interface	181
Figure C.1: The flow-field inside a bubble with microlayer	189
Figure C.2: The velocity field inside a bubble with microlayer	191

NOMENCLATURE

C	Specific heat of liquid
D	Diameter
f, F	Streamfunction
g	Standard gravity
h_{fg}	Latent heat of evaporation
Ja	Jakob number, $C_l(T_s - T_{sat})/(\epsilon_0 h_{fg})$
k	Thermal conductivity. Iteration number
K	$\frac{k_l}{k_b}$
N	Number of moles
P	Pressure
Pr	Prandtl number, (ν/α)
q	Rate of heat flow
q''	Heat flux
R	Bubble radius
R^*	Gas constant
r	Radius
Sb	Subcooling number, $(T_{sat} - T_\infty)/(T_s - T_{sat})$
Su	Superheating number, $(T_\infty - T_{sat})/(T_s - T_{sat})$

T	Temperature
t	Time
u	Radial component of velocity
v	Angular component of velocity
\dot{V}	Volume flow rate of liquid across a liquid vapor interface
We	Weber number, $(\rho v_0 \alpha^2)/(\sigma R_0)$
y	Vertical distance from the heated surface
z	Microlayer thickness

Greek symbols:

α	Thermal diffusivity of liquid
ϵ	Ratio of density of vapor to that of liquid
δ	Boundary layer thickness
ϕ	Dependent variable, T , F , or Ω
η	Similarity coordinate, Growth constant $\frac{R}{\sqrt{t}}$
λ	$\frac{\alpha_l}{\alpha_b}$
ω, Ω	Vorticity
ν	Kinematic viscosity
ρ	Liquid density
σ	Surface tension
ψ	Angular coordinate
∇	Diffusion operator

Subscripts:

<i>b</i>	Heated surface
<i>bs</i>	Bottom of the microlayer
<i>c</i>	Cap portion of the bubble
<i>d</i>	Departure, dry
<i>h</i>	Heated surface
<i>l</i>	Liquid
<i>lo</i>	Liquid immediately next to bubble surface
<i>m</i>	Microlayer
<i>o</i>	Initial value
<i>s</i>	Heated surface
<i>t</i>	Total (including cap portion and microlayer)
<i>sat</i>	Saturation value
<i>v</i>	Vapor

ACKNOWLEDGMENTS

It is difficult to express one's true feelings of gratitude and appreciation to my advisor Professor Joseph Prusa who guided me in the last four years with extreme care, patience, and diligence. He has always been accessible, helpful and willing to advice so much so that my motivation doubled time and again. His long sessions of teaching me numerous details are greatly appreciated. I believe that this training will lead me through a long period of time in my professional career. I also thank Carol Prusa, his wife, whose kind cooperation with Dr. Prusa made possible his devotion of late hours to this research.

I am indebted to Prof. Kenneth Heimes who provided the necessary help in mathematics at many instances. His guidance for the formulation of the microlayer is particularly appreciated. I am thankful to the other members of my program of study committee, Prof. Richard Pletcher, Prof. Michael Pate, and Prof. Ambar Mitra for their many suggestions during this research and for reviewing the thesis.

Finally, thanks are due to many of my friends who provided me with the moral support I needed for a commitment of a long duration for this research.

Financial support provided by the National Science Foundation (Grant No. CBT 8451145) and by the Department of Mechanical Engineering, Iowa State University is kindly acknowledged.

1. INTRODUCTION

1.1 General

The process of boiling has the capacity to achieve a high rate of heat flux at a low level of temperature difference. In recent technological advances such as nuclear reactors, jet propulsion, electric power, electronics, air-conditioning and refrigeration, the boiling process is a very attractive means of heat transfer. It can be used to cool devices effectively, improve efficiency and reduce cost. The two basic types of boiling are pool boiling and flow boiling. Pool boiling is boiling on a heated surface submerged in a pool of initially quiescent liquid. Flow boiling is boiling in a flowing stream of fluid.

The basic modes of pool boiling, first observed by Nukiyama (1935), can be explained with help of the boiling curve (Figure 1.1). At low wall superheat $T_s - T_{sat}$ (ΔT_e , which is excess temperature of the wall over that of the saturation temperature), there exists only natural convection. With higher ΔT_e , bubbles appear on the surface and with a further increase of ΔT_e , they coalesce and form jets and columns. The transition boiling mode is characterized by an unstable vapor film on the surface. The entire surface is covered by vapor blanket during the film boiling mode when the heat transfer takes place by conduction through the vapor and by radiation.

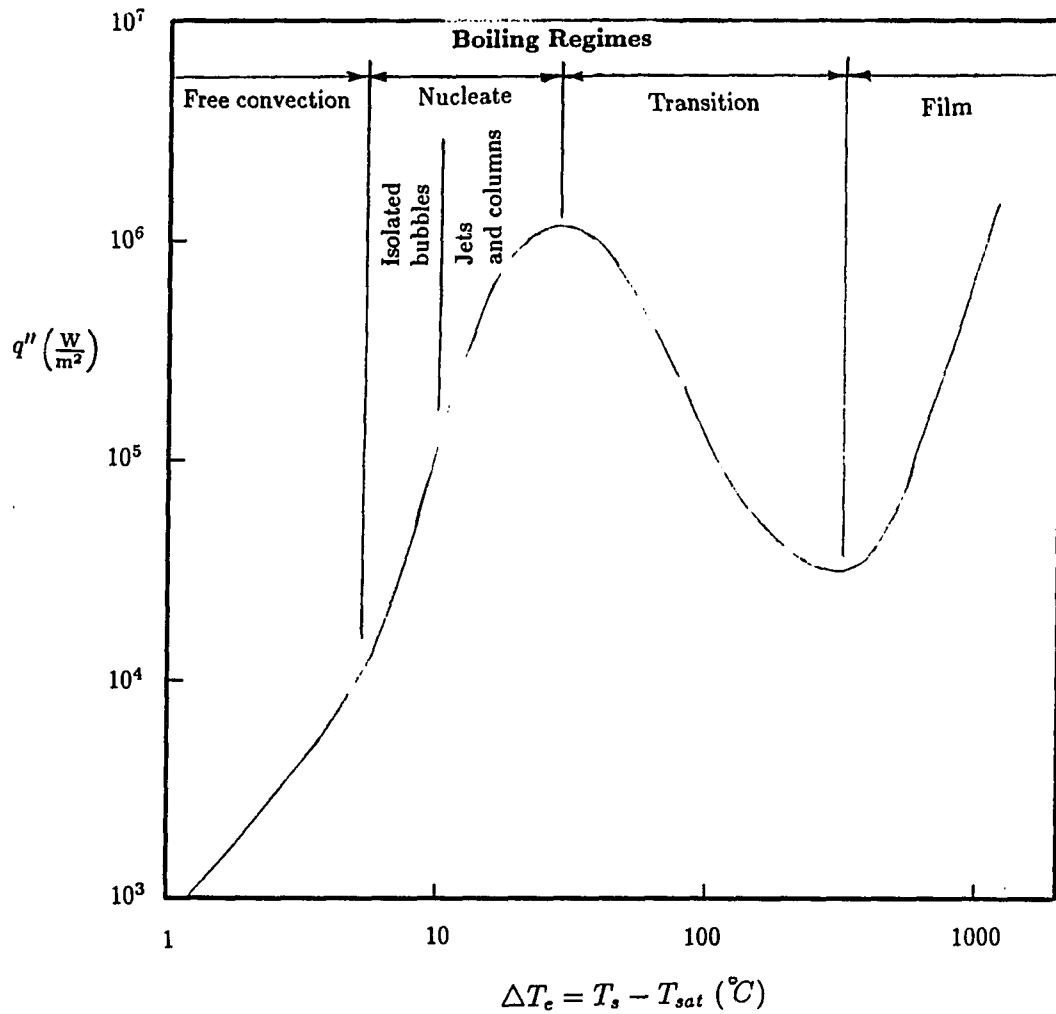


Figure 1.1: Typical boiling curve for water at 1 atm

The term nucleate boiling is derived from the fact that bubbles are formed at nucleation sites. Nucleate boiling is the most commonly observed, most efficient, and the most studied mode in boiling heat transfer. It is also at the focus of the present research. Bubbles form at preferred sites in nucleate boiling. The sites are the places where the vapor phase develops with less free energy required than the surrounding fluid, which could be either in bulk fluid or more probably, formed on a foreign object at microscopic cavities. Initial growth of a bubble is controlled by inertia and surface tension effects. The growth rate is small at first but soon increases as surface tension effects become less significant. As the bubble size increases, the inertia effect loses significance and growth is controlled by the rate of diffusion of heat to the bubble. Under certain circumstances, a "microlayer" may form below the bubble. The microlayer is a thin film of liquid on the order of a few microns thick that remains on the heated surface over which the bubble grows.

Many microscopic, macroscopic, and statistical phenomena form a part of the process of nucleate boiling. The interrelation of these is depicted in Figure 1.2 [1]. Only the bubble growth rate is within the scope of the present research and has been investigated using computational means. However, literature on all aspects related to nucleate boiling is surveyed.

1.2 Literature Survey

Man's acquaintance with boiling is as old as discovery of fire. However, in-depth scientific study of the boiling process has begun only relatively recently. Early works by Leidenfrost (1756, Leidenfrost phenomenon), Lord Rayleigh (1917, inertial pressure), Jakob (1931, influence of surface properties) and Nukiyama (1935, boiling

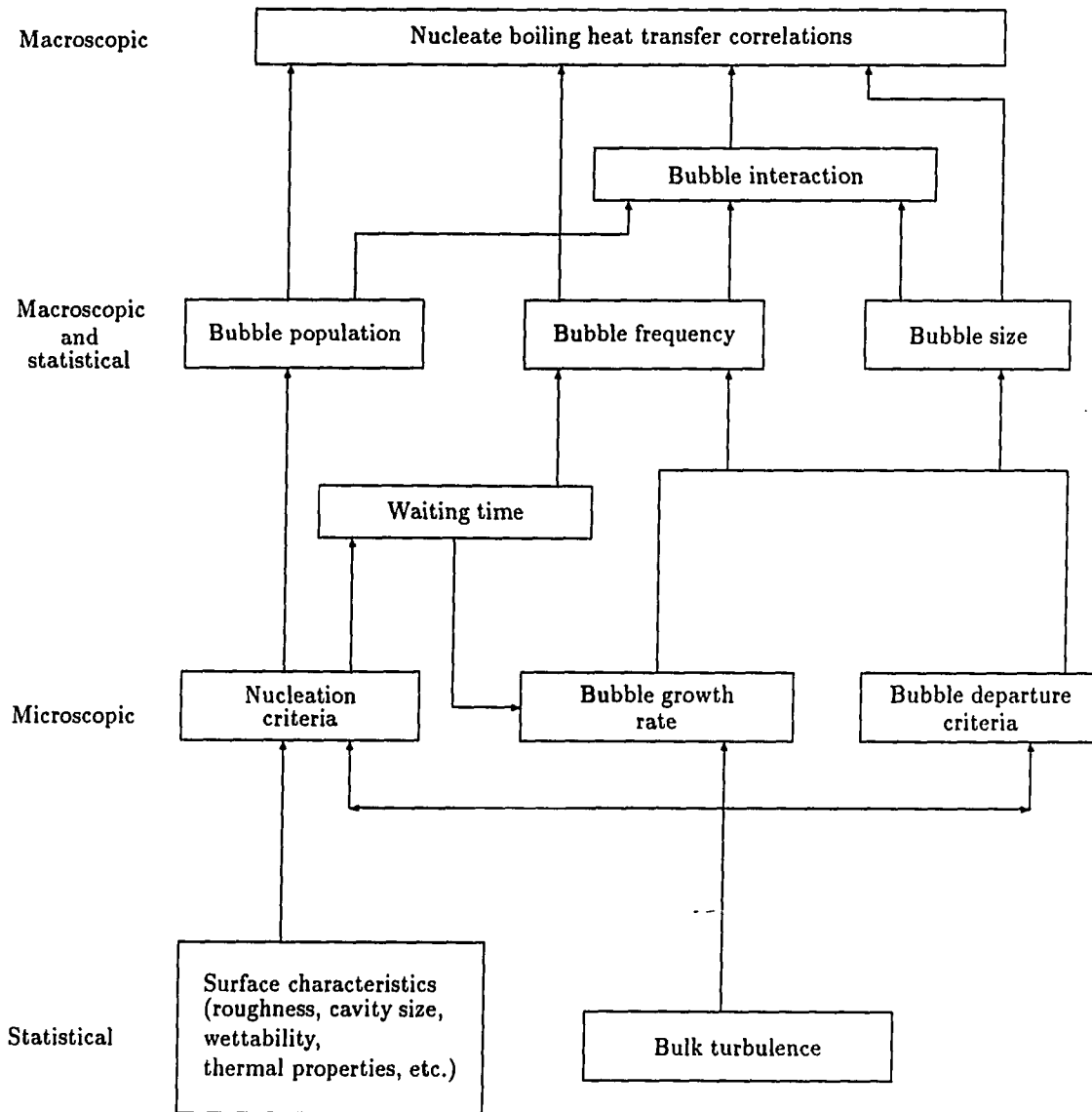


Figure 1.2: The interrelationship of many parameters in nucleate boiling

curve) are well known.

Lord Rayleigh [2] addressed the problem of pressure distribution in infinite homogeneous incompressible fluid from where a spherical portion has been suddenly removed. His result of dynamic pressure during implosion is also valid during expansion of bubbles:

$$P = \rho \left(\frac{3}{2} \dot{R}^2 + R \ddot{R} \right)$$

and is widely used in context of nucleate boiling.

Forster and Greif [3] in 1959 discuss four mechanisms of nucleate boiling that were then known.

- Mechanism 1: Some form of random microconvection close to the heated wall is excited by the bubble activity. However, they claim that according to this mechanism, the heat flux should strongly depend on the temperature difference $T_s - T_\infty$ (ΔT_s) which is the driving potential for the heat flow. Experimental data suggests that for the same superheat $T_s - T_{sat}$, the heat flux is unaffected while subcooling of fluid (ΔT_s) may increase. So this mechanism must be abandoned.
- Mechanism 2: In boiling heat transfer with forced convection, the bubbles on the surface increase the turbulent exchange of liquid between the heated surface and the bulk liquid. In this case the heat flux should depend strongly on the ratio of mean bubble diameter and the pipe diameter. However, the experiments show that doubling the pipe diameter leaves the heat flux unchanged. This mechanism must also be abandoned.
- Mechanism 3: A bubble absorbs latent heat of vaporization while it grows,

which is returned to the bulk liquid when the bubble collapses or rises. In addition heat flux is carried by latent heat *through the bubble* by mass transfer.

- Mechanism 4: In addition to latent heat transport, bubbles also transfer heat by pushing a quantity of hot liquid from the heating surface into the bulk liquid.

As more research revealed that nucleate boiling involved many aspects, researchers began to study each separately to gain a further understanding of this complex process. Details of this research are grouped under the following eight headings:

1. Microlayer
2. Growth of bubbles
3. Shape of the bubble
4. Bubble surface
5. Departure
6. Temperature distribution in the bulk fluid
7. Vapor inside the bubble
8. Statistical characteristics

Each of these aspects is discussed in the following sections.

1.2.1 Microlayer

In experiments of subcooled nucleate boiling, Gunther and Kreith [4] observed the latent heat content of the vapor volume in bubble could account for only 1 to

2 percent ($Ja = 8.86, Sb = 1.96$) while Snyder and Robin [5] found it to be 1 to 10 percent of the total heat transfer from the wall.

Moore and Mesler [6] observed rapid fluctuations in temperature of the surface on which nucleate boiling was occurring and inferred that evaporation of a thin liquid layer underlying the bubble must be the cause. Cooper and Lloyd [7] formed precisely located micro-thermometers such that the bubble grew over four thermometers. From the measured surface temperatures they deduced a definite existence of a thin microlayer. They explain that unless the fluid is strongly non-wetting, the fluid close to the heated surface gets "overtaken" by the growing bubble thus forming a microlayer. Existence of a microlayer underneath a bubble in nucleate boiling have been reported by Rogers and Mesler [8], Mesler [9], Yu and Mesler [10], Hospeti and Mesler [11] from their surface temperature measurements; Katto and Shoji [12] by optical measurements; and by Kotake [13] with the help of hydrodynamical analysis. Sernas and Hooper [14] and Yesin and Jeffers [15] explain their observed high rate of bubble growth with microlayer evaporation.

Cooper and Lloyd [7] use the Navier-Stokes equations for an analysis of hydrodynamics of bubble formation and deduce that the thickness of the microlayer at the point of its formation ($\bar{\delta}_o$) is equal to the displacement thickness of the boundary layer on the wall formed due to growing bubble. They further show that $\bar{\delta}_o$ must be equal to approximately $0.8\sqrt{\nu t_g}$, where t_g is the time taken for the bubble to grow to the point in question. This result agrees well with their experimental observations (toluene, isopropyl alcohol, 6.9 and 13.8 kPa, $\frac{\dot{q}}{A} = 22 \times 10^4$ and $47 \times 10^4 \frac{W}{m^2}$, $T_s - T_\infty = 0$ to $7.8^\circ C$). Van Ouwkerk [16] found the same initial microlayer thickness even with a different experimental technique (n-Heptane, Benzene, Carbon-

tetrachloride). Cooper and Lloyd explain that the factors tending to make bubbles grow rapidly will tend to encourage formation of a microlayer, and these include high wall temperature, high heat flux, high bulk temperature, low system pressure¹. After being formed, the microlayer is subject to evaporation. Thus the surface may have a dry portion close to the center of the nucleation site. There is a possibility that the microlayer might subsequently "roll up" from the dry inner region under the action of surface forces, thus increasing the dry area even without evaporation. However, observations of surface temperatures (and their comparison with those found from calculated latent heat absorption by microlayer) by Cooper and Lloyd indicate that this is not happening. Cooper [17] shows analytically that the dry radius must be a constant fraction of the bubble radius.

Koffman and Plesset [18] used laser interferometry to observe microlayer thickness and its time history. Their plots of microlayer profiles for water and ethanol appear to be wedge-like. The initial microlayer thickness ($\bar{\delta}_0$) was of the order 2 microns (water, 1 atm, $q'' = 104 \text{ kW/m}^2$, $\Delta T_s = 21.7 \text{ }^\circ\text{C}$). Based on their observations the value of c in $\bar{\delta}_0 = c\sqrt{\nu t}$ was found to be 0.33 to 0.5 – little lower than given by Cooper and Lloyd (0.8). They also conclude that if radial flow in the microlayer is neglected, then evaporation rates of the microlayer require heat fluxes of the order 1000 kW/m^2 for both water and ethanol.

Dwyer and Hsu [19] have solved hydrodynamic equations for microlayer formation assuming the bubble grows according to the relation $\bar{R} = \eta \bar{t}^n$. They conclude that $\bar{\delta}_0$ is given by $\bar{\delta}_0 = \frac{\pi^2}{\pi^2 + 2n} K_n \sqrt{\nu t}$, where K_n is expressed as an integral in terms of the exponent of t (n), where t is time. Voutsinos and Judd [20] also used laser

¹Low system pressure reduces ρ_v and thus increases growth rate.

interferometry to study growth and evaporation of microlayer with di-chloromethane boiling at half atmosphere. At $T_s - T_{sat} = 20.5$ °C, $T_{sat} - T_\infty = 5.6$ °C, and $q'' = 61$ kW/m² a microlayer approximately 5 micrometer thick was recorded. The dry spot radius was approximately 30% of the radius of the bubble. The initial microlayer thickness was approximately half that given by Cooper and Lloyd and that by Olander and Watts [21] ($\bar{\delta}_o = \frac{\pi}{4\sqrt{3}} \frac{\sqrt{Pr}}{Ja} R$). Various experiments [7] [16] [20] have yielded the value of $\frac{\bar{\delta}_o}{\sqrt{\nu t_g}}$ ranging from 0.3 to 1.0. Cooper, Judd, and Pike [22] used dimensional analysis to find reasons for above discrepancy. They found that if $\bar{\delta}_o$ is expressed as $\bar{\delta}_o = \bar{\delta}_o(\eta, \rho, \mu, \sigma)$ then, in the absence of gravity, $\frac{\bar{\delta}_o}{\sqrt{\nu t_g}}$ (called δ_o^+) is a function of only two non-dimensional parameters: $\frac{Ja}{\sqrt{Pr}}$ and $\frac{t_g}{Ja^6 \alpha^3 \rho^2 / \sigma^2}$ (called t_g^+). Ja , the Jakob number is the ratio of the sensible heat of the liquid to the latent heat (- it may be thought of as a dimensionless heat transfer rate). They argue that if σ is not an important parameter, then δ_o^+ must be a function of $\frac{Ja}{\sqrt{Pr}}$ only, and hence constant against time, however, it is not, and therefore t_g^+ must be important. When the values of δ_o^+ from Cooper and Lloyd [7], Voutsinos and Judd [20], and their results were plotted against t_g^+ by Cooper, Judd, and Pike, all merged into a single curve explaining that δ_o^+ is a unique function of t_g^+ .

1.2.2 Growth of Bubbles

The rate of bubble growth in a homogeneous infinite superheated medium during the diffusion controlled asymptotic phase has been found by Scriven [23]. Mikic, Rohsenow and Griffith [24] have found the relation of growth of a bubble in a homogeneous medium, which is valid throughout the bubble's lifetime. They also give a

growth relation for a bubble in a heterogeneous medium (such as on a heated surface) in a non-uniform temperature field.

Han and Griffith [25] and Han and Griffith [26] explain the bubble's heterogeneous growth in the following way. Following the departure of a bubble from a surface, its place is taken by fluid at bulk temperature. A thermal boundary layer grows in absence of convection due to the conduction at the wall. If the boundary layer thickness $\bar{\delta}_s$ is defined as $\Delta T_s / \left(- \frac{\partial T}{\partial y} \Big|_{y=0} \right)$, then until the initiation of the next bubble, $\bar{\delta}_s$ would grow to a value $\pi \alpha \sqrt{t_w}$, where t_w is the "waiting time" between departure and the initiation of bubbles at a nucleation site. They observed that in the initial period, the bubble grows rapidly and laterally. They propose that a piece of the thermal layer is picked up by the growing bubble and is carried away when the bubble departs. By this kind of repeated transportation of thermal layer, heat is transferred to the fluid from the heated wall. This mechanism is termed "bulk convection". In the area away from the bubble, heat is transferred by usual natural convection in a continuous manner. Their experimental results match well with their theory. Mikic and Rohsenow [27] agree with the above mechanism. They have shown an agreement between growth of a bubble from their bulk convection theory and some experimental observations of other reporters. By keeping a thermocouple in bulk fluid, van Stralen and Sluyter [28] did find occasional evidence of a peak in temperature as the bubble passed over it, suggesting the presence of superheated thermal layer around bubble (water, $q'' = 7.5 \times 10^5 \text{ W/m}^2$, $\Delta T_s = 21 \text{ }^\circ\text{C}$, height of probe above surface = 10^{-4} m , $D_d = 1.5 \times 10^{-3} \text{ m}$). However, from their plots temperature against time, it appears that this peak in temperature was not observed during the growth of every bubble. Bulk convection as a principal mechanism is also proposed by Yu and Mesler [10],

Judd and Hwang [29] and van Stralen [30] [31]. The terms "liquid-vapor exchange" theory or "relaxation microlayer" theory are sometimes used to denote the "bulk convection" theory.

Notably, the above mechanism has neglected the contribution to bubble growth from the microlayer. In fact, Mikic and Rohsenow [27] mention that if evaporation of the microlayer is one of the governing mechanisms in nucleate boiling, then one would expect that the bubble growth on a heated surface should have exhibited different characteristics than the bubble in uniformly heated liquid. However, the theories that neglect microlayer mechanism and are based on model used in the derivation of a bubble growth in a uniformly superheated liquid gave a very good agreement with experimental results.

As discussed before, the existence of the microlayer seems an indisputable fact, as also its major role towards bubble growth in many cases. Cooper and Lloyd [7] found that the volume due to evaporation of the microlayer calculated from their relation $\bar{\delta}_o = 0.8\sqrt{\nu t}$ was approximately 10 % larger than the bubble volume at a 1.7 °C subcooling (except in the initial short period of growth, for toluene on glass with $q'' = 13.8 \text{ kw/m}^2$). At higher subcooling ($T_{sat} - T_{\infty} 7.8 \text{ °C}$) the microlayer evaporation was 2 to 3 times larger than the bubble volume implying that a large amount of evaporation from the microlayer and condensation at the cap portion of the bubble must be taking place, especially during subcooled boiling. Their analysis considering microlayer evaporation and evaporation/condensation at cap portion and experimental results match well for the above two cases. Hospeti and Mesler also found that the microlayer volume evaporated was 12 % more than the bubble volume (water, 1 atm, $\Delta T_s = 14.44 \text{ °C}$).

Lee and Nydahl [32] have found from their computational results that the contribution of the microlayer to the bubble growth till departure is 87 % (water, 1 atm, $\Delta T_s = 8.5$ °C). Fath and Judd [33] report 40 % contribution from microlayer (methelene chloride, $\frac{1}{2}$ atm), while Voutsinos and Judd [20] report 25 % contribution for the same conditions.

To analyze the bubble growth, Cooper [17] has considered the case when bubbles grow much in excess of the thermal boundary layer ($k\Delta T_s/q_{\text{mean}}''$) on the wall – meaning the growth must occur due to the evaporation of the microlayer. He argues that for many non-metallic fluids boiling at pressures below 1 atmosphere, the assumption will be valid during most of the growth period. This assumption has been found to be true by Yesin and Jeffers, at least for their experimental conditions (water, 1 atm $T_s = 117$ °C, $T_\infty = 90$ °C), who report that the initial radius growth rate was 300 cm/sec and the boundary layer velocity $\sqrt{\alpha t}$ was 0.6 cm/sec. The bubble rapidly grew through the thin superheated layer (27 micrometer) on the wall and spent most of its life protruding into the subcooled bulk fluid. The main difficulty in finding the microlayer contribution analytically, however, seems to be that although the vapor-side temperature of the microlayer can be assumed to be the saturation temperature at the bubble pressure, the wall side temperature of the microlayer is unknown since the wall may cool down due to microlayer evaporation. Thus Cooper considers the two extreme cases, namely, poorly conducting liquid on a highly conducting wall and vice versa. With an additional assumption that the bubble remain hemispherical, he derives that for the former case,

$$R \doteq 2.5 \frac{Ja}{\sqrt{Pr}} \sqrt{\alpha t}.$$

For the later case,

$$R \doteq 1.12 \sqrt{\frac{k_s \rho_s C_s}{k_l \rho_l C_l}} Ja \sqrt{\alpha_l t}.$$

Comparison of these relations is made [17] with growth data of several bubbles of Cole and Shulman [34], and Cooper and Lloyd [7] after checking for the validity of the foregoing assumptions, and the agreement is found satisfactory. Cooper also considers the case when the bubble does *not* grow far in excess of the thermal boundary layer on the wall. After taking into account the contribution to growth from the bubble cap he concludes that the microlayer contribution to the growth still predominates over that from from the cap portion. However, he argues that the microlayer does not play an important role at higher pressures, when it would occur but will not, on its own, cause the bubble to grow beyond the thermal boundary layer on the heated surface. For metallic fluids, the flow of vapor across the curved surface of the bubble will be of the same order of magnitude as that through the microlayer.

Cooper [17] has noted the similarity between his expression for bubble growth (with microlayer) on a heated surface and Scriven's [23] expression for growth of a bubble in infinite superheated medium (homogeneous boiling). Both these expressions yield similar answers if T_s in the former expression were equal to T_∞ in the later, even though the mechanisms involved in the respective cases are quite different. There does not seem to be any explanation available for this similarity.

In heterogeneous boiling, a growth rate $R = 2Ja\sqrt{\alpha_l t}$ for near spherical bubbles and a growth rate $R = 3Ja\sqrt{\alpha_l t}$ for hemispherical bubbles is reported by Cooper [17]. Sernas and Hooper [14] report growth rate given by $R = 4.59\sqrt{t}$ (R in cm and t in sec, water, $T_s - T_{sat} = 12.77$ °C). Their analysis shows that only a microlayer can explain such a high rate of growth. Yesin and Jeffers [15] observe the value of the

growth constant in the above expression to be $2.5 \text{ cm}/\sqrt{\text{sec}}$.

Cooper and Chandratilleke [35] made 250 tests on bubbles in nucleate pool boiling in six categories: positive, negative, and zero gravity, with saturated and subcooled boiling. From dimensional analysis, they have established specific non-dimensional groups that could be used as parameters to find any quality in bubble growth. Among these are $L^+ = \frac{L}{Ja^4 \alpha^2 \rho / \sigma}$, $t^+ = \frac{t}{Ja^6 \alpha^3 \rho^2 / \sigma^2}$, $g^+ = g Ja^8 \alpha^4 (\rho / \sigma)^3$, Ja / \sqrt{Pr} , where L is any length of interest (say δ_s , dry radius, height or width of a bubble), and α and ρ are the thermal diffusivity and density of the liquid respectively.

Saini, Gupta and Lal [36] have mentioned that the non-dimensional parameter $\frac{k_l \rho_l c_{p_l}}{k_s \rho_s c_{p_s}}$ is significant when material properties of the heated surface are considered.

Cooper, Judd, and Pike [22] have found from their experiments that

$$\frac{\text{rate of growth of volume of bubble}}{\text{surface area of bubble}} = b \sqrt{t}$$

where b ($\sim Ja \sqrt{\alpha}$) is a more or less a constant and this applies regardless of hemispherical or spherical shape provided the growth is diffusion controlled. The surface area of the bubble includes the area of the microlayer as well.

1.2.3 Shape of the Bubble

Bubbles are classified as spherical, hemispherical, oblate. Shape is decided by relative magnitude of surface tension force (due to the curvature of the bubble surface) and the inertial force exerted on the bubble by the bulk fluid [19] [35] [7] [37]. If the former predominates (as in a rapidly growing bubble), the bubble growing on a flat surface will be hemispherical. If the latter predominates, the bubble will tend towards a spherical shape. Hence the factors tending to make bubbles grow rapidly will make hemispherical bubbles [7] [19]. The factors that would promote high rate of growth

are high wall temperature (it encourages flow of heat into the bubble from the wall), high heat flux and a smooth surface (it serves to raise wall temperature) [17], good wetting [19].

Cooper and Lloyd [7] have found the relative magnitude of inertial and surface tension forces from the observed bubble growth data for toluene on glass. For their four tests, inertia force predominated and the bubbles were observed to be hemispherical. During their test when the surface tension force predominated over the inertial force by a factor of about five (except in the initial fraction of millisecond) a spherical shape would be expected. However, the bubbles still grew with intermediate shape.

Hospeti and Mesler [11] observed that initial surface temperature (during nucleation) is more important factor in determining the growth rate and thus its shape; higher temperature would lead to a hemispherical bubble and lower temperature to a spherical. They also observe that ratio of vapor volume formed at the base (from the microlayer) to the total volume of the bubble shows a dependency on the bubble shape. The ratio is smallest for spherical bubbles, largest for hemispherical, and intermediate for oblate size bubbles.

Joosten et al. [38] explain that distortions in bubble shape do not take place because of different amounts of evaporation rates at the cap portion since ρ_v/ρ is small, and the volume of liquid evaporated is much smaller than the vapor. They claim that the distortions take place due to gravity.

Bubbles were observed to be near hemispherical shape (except immediately before their departure when the bottom showed a pinching effect) by van Stralen [39] (water, 4 to 26 kPa, $Ja = 108$ to 2689, $q'' \sim 50 \text{ kW/m}^2$), Zijl et al. [40] ($p=104 \text{ kPa}$, $Ja = 579$), and by Joosten et al. [38] (water, 16.2 kPa, $Ja = 125$ to 328). However,

Cooper [37] mentions that at high pressure, inertial force is not much bigger than the surface tension force and bubble will round off early.

Cooper, Judd, and Pike [22] show that $\frac{D}{H}$ (D =width, H =height of the bubble) could be uniquely determined by t^+ in uniformly superheated fluid and zero gravity. For the case of bubble growth on a wall, $t^+ / (\delta_s^+)^{\frac{3}{4}}$ could uniquely determine $\frac{D}{H}$ in various tests of Cooper and Chandratilleke at zero gravity. If gravity is present, then g^+ can be used as a one parameter variation of above cases. In all cases, small t^+ give $\frac{D}{H} = 2$ (hemispherical bubble) and large t^+ give $\frac{D}{H} = 1$ (spherical bubble).

Note that t^+ depends on Ja^6 and Ja can vary widely. Observations have been reported with Ja ranging from 1 to 3000. Hence, depending on the range t^+ may assume, a bubble may remain either spherical or hemispherical throughout its lifetime. In the later case during the departure, the bubble still remains close to hemispherical in shape except for the "pinching action" at the bottom.

Interestingly, Zysin et al. [41] raised a solid sphere from a heated surface in a non-boiling environment. The distorted image due to the "mirage" effect that was observed appeared just like a bubble being "pinched off" the surface. They applied the corrections of the above effect to real bubbles in boiling (water, 1 atm, subcooling 5 to 30 °C) and concluded that the bubbles remain spherical throughout their life.

1.2.4 Bubble Surface

The Italian physicist Carlo Marangoni (1840-1925) was the first to note that the temperature and composition gradients give rise to surface tension gradients which in turn give rise to interfacial motion. The effect is known as the Marangoni effect. Sternling and Scriven [42] observed motion in interface joining two phases, one of

which was richer in solute concentration than the other. The surface motion gave rise to cells in bulk fluid similar to the "Rayleigh-Benard" cells in buoyancy driven flow, indicating the presence of surface tension gradients.

Groenveld [43] measured the thickness of a meniscus entrained on the surface of a tube which is being withdrawn from a liquid and found it less than predicted for theories for *pure* liquid. They argue that presence of impurities caused to lower surface tension which enabled the surface to sustain tangential stresses. In his experiment on an air bubble on a heated surface in a pool of pure water, Kenning [44] observed interfacial motion of several cm/sec with modest temperature gradients. However, addition of trace of surfactant immediately caused stagnation. Huplik and Raithby [45] carried out the same experiment with air bubbles and also with vapor bubbles at low heat flux with a downward facing surface. They observed maximum velocities of 5 cm/sec (bubble size approximately 10 mm). Again a small quantity of surfactant made the fluid stagnant. Kenning [46] suggests that in a system with strongly adsorbed molecules, it is helpful to regard the interface as a third phase of negligible thickness separating the two bulk phases – applicable to insoluble as well as soluble surfactants – with due allowance of interchange of substrate between surface and bulk. Insoluble films always oppose interfacial motion, soluble films can do so only in the event the rate of adsorption/desorption is slow compared with the time scale of the motion.

It is well known that buoyant motion of small bubbles is closer to a rigid sphere than to that expected for fluid spheres capable of interfacial and internal circulation [47]. Kenning and Cooper [47] propose the following explanation to this phenomenon. Surface active material is either steadily adsorbed at the front of the bubble or is al-

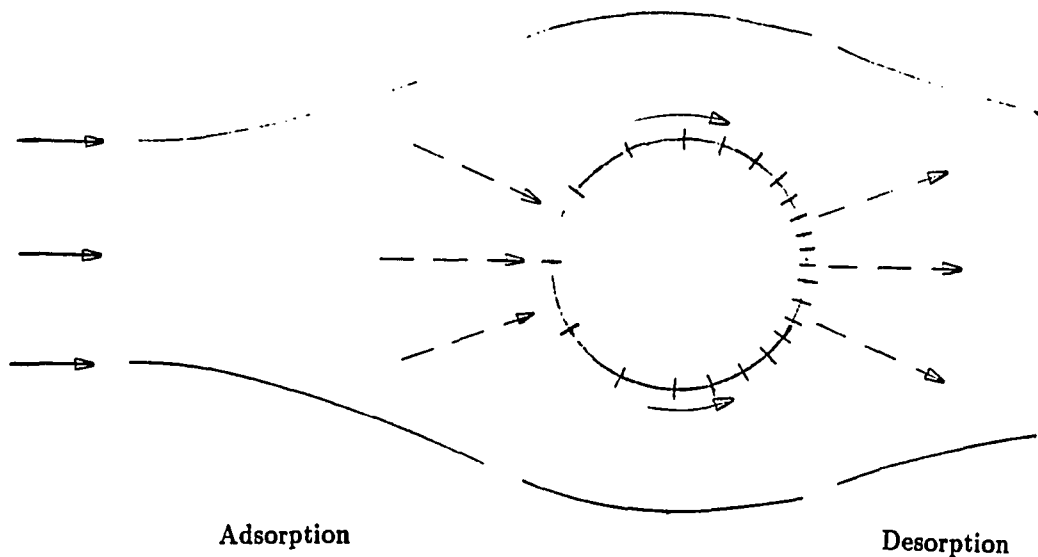


Figure 1.3: Illustration of the “locking” of a bubble surface in a symmetric flow

ready present on the surface which forms a film of monomolecular thickness. Relative movement of the external bulk phase tends to sweep the surface film toward the rear of the bubble. There its escape is either prevented by its insolubility or impeded by the kinetics of the desorption process and/or diffusion in the bulk phase. Consequently the movement of the surface film is slower than that of the main stream and so velocity gradients normal to the boundary are produced. The resulting shear stress tends to compress the film causing the gradient of decreasing surface tension from front to rear of the surface. Because of the axial symmetry of the flow, the surface film “locks” the surface, isolating the internal fluid from interfacial shear stresses (Figure 1.3). This is the mechanism which can explain Kenning’s and Huplik and Raithby’s experiments.

Kenning and Cooper [48] have made photographic observations of flow past a

hemispherical bubble in *crossward* direction. They again deduced that the surface active agents formed a unimolecular, incompressible, insoluble film which has negligible resistance to shear, i.e., zero surface viscosity, (meaning shear from the bulk is balanced by surface tension gradients). Due to the asymmetry, however, the film is swept to the rear of the bubble by flowing liquid with a relatively large viscous traction near the tip of the bubble. At the rear, the escape of the film is impeded by kinetics of desorption process and/or slow rates of diffusion in the liquid phase, so it starts to recirculate. The surface has negligible film thickness and exhibits a two-dimensional continuity.

According to Kenning [46], a surface behaves like a two-dimensional gas with two degrees of freedom per molecule obeying an equation of state $\frac{\pi}{\lambda} = kT$, where π is surface pressure, λ is surfactant concentration, and T is the temperature. Surface films resist deformation, and coefficients of shear viscosity and dilational viscosity can be defined having dimensions of force/time. The interaction between bulk fluid and the surface is through viscous drag, diffusion and/or adsorption of surfactant.

Does significant surface activity occur in practical boiling systems (- which may employ highly purified liquids)? Kenning and Cooper [48] have listed in this context many sources by which impurities will enter into boiling systems. Their measurements of water from a boiler indicated that some surfactant will generally be present in boiling systems unless stringent precautions are taken to exclude it. According to Groenveld [43] even exhaling on the surface will change surface tension noticeably. It must be pointed out however that the reduction in surface tension by surfactants will be negligible at high temperatures that occur in pressurized boiling.

A mathematical modeling of surface can be found in Sternling and Scriven [42],

Scriven and Sternling [49], Kenning [44], Yih [50] and Kenning [46]. A completely general formulation of the dynamics of a Newtonian fluid interface – a two-dimensional analogue of Navier-Stokes equations – is found in Scriven [51].

1.2.5 Departure

Four forces are involved in the departure mechanism - inertia force of the liquid acting on the bubble, buoyancy force of the bubble, surface tension force and viscous drag of the surrounding fluid [1]. A well known formula by Fritz [52] is a balance between buoyancy force and the surface tension force:

$$D_d = 0.0208\theta \left(\frac{\sigma}{g(\rho_l - \rho_v)} \right)^{1/2}$$

where θ is the contact angle in degrees. However, bubbles have been observed to depart from downward oriented surface also [7] [35], i.e. in negative gravity, and hence this formula may have a limited applicability. A formula by Cole and Shulman [53] has an additional factor accounting for inertial forces. Cole and Shulman also provide a formula for departure diameter when system pressure is known. Han and Griffith [25] have verified Fritz's relation with their three bubbles (water, 1 atm, $T_{sat} - T_{\infty} = 3.88$ °C). More involved formulae are available in Hsu [1] and Cooper [17]. Data for departure diameter by Nishikawa et al. [54] (water, ethanol) match well with the relation given by Cole and Shulman for pressures ranging from 0.588 to 19.6 Pa. Through their computational results, Lee and Nydahl [32] found that departure took place when the drag force and the buoyancy force balanced; surface tension force being an order of magnitude smaller (water, 1 atm, $\Delta T_s = 8.5$ °C, saturated boiling). van Stralen [39] (water, $2 < p < 26$ kPa) and Judd and Hwang [29] (methelene

chloride, $51 < p < 100$ kPa) have found that the departure radius decreases as system pressure increases. With the increase of heat flux, Fath and Judd [33], and Judd and Hwang [29] found departure radius to decrease.

By way of dimensional analysis, Cooper, Judd, and Pike [22] conclude that the departure time can be written as $t_d = \frac{\text{constant}}{g^{+3/2}}$, if g^+ is much greater than unity. They argue that relation of this type is the only one to be expected if stresses from inertia and gravity are greatly exceeding those from surface tension and viscosity (i.e. large g^+). Their experiments confirm the above relationship and predict the value of the constant to be 4. At smaller g^+ their experiments yielded t_d^+ somewhat less than $4/g^{+3/2}$. They explain from their functional relation $X^+ = f(Ja/\sqrt{Pr}, t^+, g^+)$ that the effect of Ja/\sqrt{Pr} has been generally found to be small and hence the viscosity may not be playing any roll. This means that the effect of surface tension is to assist the departure of the bubble. When dimensional analysis is applied to departure size, Cooper, Judd, and Pike give the non-dimensional departure diameter $D_d^+ = \frac{12}{g^{+3/2}}$. When effect of δ_s is considered Cooper and Chandratilleke [35] found $\frac{D_d}{\delta_s^+} (1 + 0.02\sqrt{g^+}) \simeq 7$. They explain that higher subcooling would lead to earlier departure and departure "against gravity" is favored by subcooling. Correlation of Fritz matches their data in the range $10^{-6} < g^+ < 10^{-3}$ but not outside this range.

Jensen and Memmel [55] have compared twelve bubble departure diameter correlations from the literature with a wide range of experimentally observed bubble departure diameters in the literature. The range included fifteen fluids² and pressures ranged from 4.7 kPa to 13500 kPa. Thus totally 500 experimental data points

²Acetic acid, Ammonia, Benzene, Butanol, Carbon tetrachloride, Ethanol, R-12, Helium, Hydrogen, Methanol, Methylene chloride, Neon, Nitrogen, Pentane, Water.

were evaluated. Some of their observations were as follows. The experimental data was characterized by a large scatter (- upto 100% variation between the bubble departure diameter from different references for the same fluid/surface conditions). All of the correlations that were tested, except the Fritz equation, generally showed correct trend in data. Those correlations which used heat flux in their expressions had a poorer agreement between their predictions and the experimental observations. Jensen and Memmel divided the correlations in two groups according to whether or not wall superheat ($\Delta T_e = T_s - T_{sat}$) is used in the prediction of the bubble departure diameter. They have not been able to conclude if the bubble departure diameter is a function of ΔT_e .

Jensen and Memmel used a non-linear regression analysis program in an attempt to develop a better correlation. Dynamic contact angle was not used as a independent parameter in their analysis because of the difficulties in its accurate prediction. One result of their analysis is that the ratio of solid to liquid thermal diffusivity is not a significant parameter in the prediction of bubble departure diameter. The expression they finally arrived at is

$$D_d = 0.19 (1.8 + K_1 \times 10^5)^{\frac{2}{3}} \left(\frac{\sigma}{g(\rho_l - \rho_v)} \right)^{\frac{1}{2}} \quad (1.1)$$

where

$$K_1 = \left(\frac{Ja}{Pr} \right)^2 \frac{g \rho_l (\rho_l - \rho_v)}{\mu^2} \left[\frac{\sigma}{g(\rho_l - \rho_v)} \right]^{3/2}$$

For the estimate of bubble departure diameter when the wall superheat is not available, they have arrived at the following correlation

$$D_d = 2.97 \times 10^4 \left(\frac{P}{P_{cr}} \right)^{-1.09} \left[\frac{P_{cr} \mathcal{M}}{K T_{cr}} \right]^{1/3} \quad (1.2)$$

where $K = 1.38 \times 10^{-23}$ J/°K (Boltzmann constant), \mathcal{M} is the molecular weight, and T_{cr} and P_{cr} represent the critical temperature and pressure respectively.

1.2.6 Temperature Distribution in the Bulk Fluid

Temperature distribution close to the wall in saturated nucleate pool boiling of water was measured by Marcus and Dropkin [56]. They found that the average temperature profile was linear for distance y less than $0.57\bar{\delta}_s$ and is expressed as $\frac{T-T_\infty}{\Delta T_s} = 1 - \frac{y}{\bar{\delta}_s}$, where boundary layer thickness ($\bar{\delta}_s$) is defined by $\Delta T_s / (-\frac{\partial T}{\partial y}|_{y=0})$. Beyond this region, the temperature profile followed a power law $\frac{T-T_\infty}{\Delta T_s} = D \left(\frac{y}{\bar{\delta}_s}\right)^{-a}$ where D and a are constants. $\bar{\delta}_s$ could be expressed in terms of heat transfer coefficient as $\bar{\delta}_s = C h^d$ (C and d constants). Due to the growth and departure of bubbles, the temperature fluctuated about the values given above. The fluctuations were minimal at the surface (~ 0.55 °C), were maximum at approximate distance $y = 0.64 \delta_s$, and then diminished as y increased. For example, the maximum fluctuation was 1.66 °C at $y = 0.0635$ cm, where the mean value of ΔT_s was 0.83 °C ($q'' = 3106$ W/m², $T_s = 119.4$ °C, $h = 1.215$ kW/m² K). At the surface, the fluctuation was only 0.14 °C.

Wiebe and Judd [57] and Zijl et al. [40] also find similar temperature profiles in boiling water. Wiebe and Judd found maximum fluctuation at about $\frac{1}{2}\bar{\delta}_s$ in subcooled boiling. Hsu [58] postulates that at the beginning of a cycle of bubble emission, relatively cool bulk liquid at temperature T_∞ surrounded the nucleus at an active site. As time progressed, the cool liquid was heated by transient conduction. The thickness of liquid layer heated increased with time, however, not without limit. The ultimate thermal layer thickness was governed by eddy diffusivity and turbulence which tended to hold the temperature constant at the bulk temperature

T_{∞} beyond a certain distance from the surface. Wiebe and Judd also found that in their experiments at various levels of subcooling that the boundary layer thickness is related to the nucleation site density by

$$\begin{aligned} \bar{\delta}_s &\sim \left[\frac{N}{A} f \right]^{-\frac{1}{2}} & \frac{N}{A} f < 55 \times 10^3 \frac{\text{bubbles}}{\text{in}^2 \text{sec}} \\ &\sim \left[\frac{N}{A} f \right]^{-\frac{1}{3}} & \frac{N}{A} f > 55 \times 10^3. \end{aligned}$$

At lower system pressure, however, the static pressure gradient can be significant, and then the saturation temperature is a linear function of distance from the wall. In this case, the bulk temperature curve may intersect the saturation temperature straight line at more than one point. Thus alternate occurrence of superheated and subcooled regions may be found as progressively traversed away from the wall [40] [54].

1.2.7 The Vapor Inside the Bubble

To address the question of pressure and temperature distribution inside the bubble, Plesset and Prosperetti [59] have considered a problem of vapor enclosure of arbitrary shape in fluid with prescribed temperature along its boundary. Assuming an inviscid flow, ideal gas behavior, and after accounting for conduction heat transfer as well as mass flux due to evaporation and condensation, they conclude that the vapor pressure must be nearly uniform in the enclosure. Further, the temperature distribution must be nearly equal to that at the hotter boundary except for a thin layer adjacent to the cooler liquid surface. This behavior is a consequence of the small thermal diffusivities of vapors and the fact that conduction effects cannot compete with even moderate convection of thermal energy. The only regions of flow where

rapid changes in velocity could take place are the thermal boundary layers in the vicinity of cooler portions of the surface. The thickness of this boundary layer is so small that their over all contribution to pressure drop is negligible.

Plesset and Prosperetti [60] suggest that since, as described before, the latent heat content of vapor in bubble is significantly less than required to explain the heat flux in nucleate boiling, the microconvection mechanism inside the bubble must be important. By analysis they conclude that in subcooled boiling, the latent heat transport *through* the bubble is significant.

van Stralen and Sluyter [28] measured the temperature of a vapor inside a bubble. They found that the temperature inside the bubble was at saturation value of the pressure of the environment (1 atm).

1.2.8 Statistical Characteristics

Sultan and Judd [61] observed spatial distribution of active nucleation sites for different heating rates in boiling of water on copper at atmospheric pressure. The results indicate that the active sites were located randomly on the heating surface. The distribution followed Poisson relationship

$$P(x) = \frac{e^{-U} U^x}{x!}$$

where $P(x)$ is the probability of event x occurring (probability of N active sites occurring), and U is the expected value of x (the expected value of active sites). Changes in heat flux and subcooling did not affect the distribution of active nucleation sites. Heat flux had a great effect on frequency while influence of subcooling was of lesser significance. The bubble flux density was found to be non-uniformly distributed over the heating surface contrary to expected (since heat flux was constant). Judd

and Hwang [29] also found that active site density was independent of subcooling and was proportional to a constant power of heat flux. Nishikawa [54] has found a relation between nucleation site density and ΔT_s , of the following type

$$\Delta T_s = C \left(\frac{N}{A} \right)^x (q'')^y$$

where C , x and y are constants. In depth discussion on nucleation site density is given by Yang and Kim [62], Shoukri and Judd [63], and Judd [64].

Bubble life time for various fluids³ ranges from 0.5 ms to 100 ms. These two extreme cases correspond to $T_s=116$ °C, 1 atm and $T_s=35$ °C, 9.6 kPa, respectively. The departure bubble size ranges from 0.5 mm to 40 mm (also corresponding to the above two cases). However, bubble life time of the order 5 ms and departure diameter of the order 1 mm are typical [25] [30] [11] [16] [39] and [20].

Judd and Hwang [29] found that the bubble frequency at a single site approximately obeyed the law $f = C q''^x$, where C may change according the level of subcooling. Typical frequency ranged from 2 to 33 sec⁻¹ [29] with q'' in the range 10⁴ to 10⁵ W/m². The theoretical minimum and maximum of initial size of the active site is discussed by Shoukri and Judd [63] and Hsu [1]. A typical active site in nucleate boiling is of the order 2 to 20 μm [63].

1.2.9 Computational Models

Analyses of of bubble growth that are completely numerical in nature are found only in recently published reports. All the models assume incompressible bulk fluid, neglect conduction from bubble interface to the bubble vapor, neglect interfacial

³water, Carbon tetrachloride, Methanol, Benzene, Methylene chloride, Pentane, Ammonia

motion on the bubble surface, neglect any effect from cooling of the heated surface during bubble growth (constant temperature boundary condition). They assume uniform properties in the vapor, and assume thermodynamic equilibrium between vapor and interface. The far field temperature boundary condition is usually taken to be that given by one dimensional heat conduction into a semi-infinite medium (solution to the Stoke's first problem), which also has been experimentally observed by Yesin and Jeffers [15].

Joosten et al. [38] have found initial temperature distribution for their numerical model by solving $\nabla^2 T = 0$ in a cylinder encompassing nucleation site whose walls are at T_s and the other surfaces are at T_∞ . Zijl et al. [40] used experimentally measured temperature profile for their computer program. During the bubble growth itself, the diffusion of heat was neglected and only convection caused by bubble growth was considered in both the above reports.

Joosten et al. [38] found numerically the growth of rotationally symmetric bubble in a gravitational field. In their model, the microlayer contribution has been neglected. To solve the temperature field, two regions were considered: thin thermal boundary layer around the bubble, and the remaining fluid. The thermal diffusion equation was solved in the thin layer while in the bulk region the heat transport was assumed to take place by convection only. Viscous effects were claimed negligible, hence a potential fluid flow was assumed. The pressure distribution was found from the Bernoulli equation. The effect from gravity entered through this equation. Combination of Bernoulli equation, Clapeyron equation and Laplace equation for surface tension led to a partial differential equation for velocity potential which was used to find compound radius ($R = R(\psi, t)$). They used the program to study oscillations in

growth rate during boiling of water. At 3 kPa pressure, they predict a large inertia controlled hemispherical bubble throughout its lifetime.

Guy and Ledwidge [65] used a finite difference analysis for growth and collapse of bubbles in subcooled boiling. Modified Rayleigh equation (which includes viscous effects) was used to find pressure difference $P_v - P_\infty$. This pressure difference was used to find local rate of growth of radius. The bubble shape was determined using local growth rate. Initial bubble shape was assumed to be hemispherical. They found that the shape remained hemispherical throughout the lifetime of the bubble ($\Delta T_s = 16$ and 29°C , $R_0 = 3\ \mu\text{m}$). The contribution from the microlayer is included in the following way. Initial microlayer thickness was taken to be the same as that given by Cooper and Lloyd, $\delta_o = 0.8\sqrt{\nu t}$. Evaporation of volume was found by assuming the microlayer to be of thickness $\frac{\delta_o}{2}$. From the evaporated volume, dry radius is found assuming that the microlayer profile remained linear at all time.

Lee and Nydahl [32] modeled an axisymmetric bubble of a truncated spherical shape and assumed that the microlayer profile remained linear. The velocity along the microlayer-vapor interface was assumed to be zero. The far field boundary condition was that provide by one-dimensional conduction into a semi-infinite media. The initial velocity was taken to be everywhere zero and the initial temperature field is assumed to be that given by one dimensional conduction into a semiinfinite media. The time before bubble growth begins was determined using the criteria that growth occurs when the fluid temperature at the bubble height from the wall equals the bubble temperature. A single non-orthogonal curvilinear grid was used in the region around the bubble and in the microlayer. Their simulation covered bubble growth since inception till its departure.

Due to its importance in the context of nucleate boiling, solution to potential flow due to growth of spherical bubble tangent to a solid surface has been found by Witze et al. [66]. They found that the inertial pressure is maximum at the top of the bubble which explains the flattening effect seen in rapidly growing bubbles. They also found a departure criterion based on balance of inertial and buoyancy force.

1.3 Scope of the Present Study

It is clear from the literature review that bubble growth is a complex phenomenon. Hughmark [67] has listed 32 variables that occur to him for nucleate boiling. Even after three or four decades of research, neither a general consensus on the the growth mechanism nor any reliable quantitative relationships have evolved. Contradictory hypotheses of growth mechanism (bulk convection theory against microlayer theory, for example) and observations of involved quantities (microlayer thickness, growth rate, for example) differing by one or even two orders of magnitude have been reported.

For the study of the mechanism, an experimental technique has the advantage of being the most realistic. Most experimental data available in the literature are very instructive. However, many difficulties have been encountered in the experimental method that make the process of conclusion difficult; few of these are:

- High temperature gradients close to the wall cause strong curvature of the light paths causing distortion of the image of the bubble near the wall, and produce 'mirage' effect [35] [41].
- Since the microlayer is extremely thin (few microns), the determination of its

thickness has been difficult.

- The temperature measurements in the vicinity of the bubble and in the heated surface have been difficult mainly due to the small size of the field (few microns to few millimeters).
- Since the temperature measurements were done with thermocouples, only non-conducting fluids could be used for boiling. This posed a restriction on the range of fluids that could be used.

The difficulties encountered in experimental methods do not occur in the numerical method. Repeatability, precision, and control over quantitative parameters are added advantages. Recent advances in computational power have made numerical methods more attractive. For this reason, the numerical method was chosen for the present study. The available experimental data were used as a guideline for the work. The disadvantages of numerical methods include truncation errors, difficulties in implementation of boundary conditions, and reliability of the results.

The chief objective of the present study was to develop a sufficiently general and also sufficiently accurate model of bubble growth, so that the qualitative nature of the mechanism involved in the bubble growth in nucleate boiling could be identified and also quantitative determinations could be made. The former includes study of micro-mechanisms in bubble growth, comparison with the simpler homogeneous boiling and the like, and the later includes identification of similarity parameters that dictate bubble growth and the determination of their relations etc.

The first generation numerical model of bubble growth has already been developed by Joshi [68], in which growth of a hemispherical bubble in an *inviscid* fluid on

an uniformly heated surface was studied neglecting the microlayer contribution. This model provided a clear insight into the geometry of the problem and the nature of parameters involved. With the help of the results of this model, a part of the results of the present study was verified. The next two generation models, i.e. the second and the third generation model form the scope of the present study.

The second generation model (Chapter 2) is based on bubble growth in a *viscous* medium. The other assumptions in this model are the same as that of Joshi. Since this model involved the solution of the complete set of Navier-Stokes equations, new governing equations as well as a new computer program were developed independent of the model of Joshi. A similarity transformation for the bubble growth problem in viscous fluid was identified. The importance of various non-dimensional parameters was determined and growth relationships were predicted. The problem of natural convection inside bubble is addressed in Appendix A.

In the third generation model (Chapter 3), governing equations for the microlayer, temperature distribution in the heated surface, and those for the non-condensable gas inside the bubble were added to the second generation model. The addition of these has made the problem more general in nature, and hence more realistic. These formulations were coupled with the Navier-Stokes equations of the region around the bubble (of the second generation model) with appropriate boundary conditions. The qualitative nature of mechanisms involved in the bubble growth as well as quantitative relationships between the various non-dimensional parameters were identified with the help of this model. A major role of microlayer in the bubble growth and the relative unimportance of microconvection in the vicinity of the bubble were established. A similarity nature of the bubble growth is again identified in

the third generation model. The coincidence of equal growth rates in homogeneous boiling and heterogeneous boiling (even with very different growth mechanisms) is noted. In Appendix B are derived the governing equations for relating quantities on both sides of the vapor-liquid interface. The flow field inside a bubble with a microlayer is described in Appendix C.

General conclusions and suggestions for future work are summarized in Chapter 4 and Chapter 5 respectively.

2. THE SECOND GENERATION MODEL OF BUBBLE GROWTH

2.1 Assumptions

Growth of a hemispherical bubble on an uniformly heated surface in a viscous medium is studied neglecting the microlayer in the present second generation model. Details of the model are described below.

A *hemispherical bubble shape* has been chosen for the computational model in the present work because many researchers have observed bubbles of this shape [7] [14] [39] [40] [38]. As described in Chapter 1, hemispherical shape is a result of high heat flux, high superheat, low system pressure, thick boundary layer on wall, smooth surface, and/or good wetting.

Based on the findings of Plesset and Prosperetti [59] *uniform vapor properties* are assumed inside the bubble. The calculation of flow-field inside the bubble in the present research (see Appendix A) also shows that this is a good approximation.

The presence of a microlayer underneath the bubble is an acknowledged fact, however, this second generation model is developed *without a microlayer*. The modeling of microlayer is incorporated in the third generation model, which is discussed in Chapter 3.

Since a small amount of surfactant has been found to stop interfacial motion of a surface of axisymmetric shape [47] [45] and significant amount of surfactant is found

to be present in boiling systems [48] [43] *tangential velocity along the bubble surface is taken as zero.*

The following additional assumptions are made to simplify the problem:

- Heated surface at uniform temperature T_s
- Semi-infinite extent of medium, initially at T_∞
- Vapor is saturated and an ideal gas
- Symmetry about vertical axis of bubble
- Constant property Newtonian fluid for liquid phase with negligible viscous dissipation
- Thermodynamic equilibrium at bubble interface
- Negligible conduction into the bubble

Thus this model consists of a hemispherical bubble growing on an isothermally heated surface in a semi-infinite extent of liquid. The liquid is assumed to be initially quiescent and at uniform temperature, T_∞ (Figure 2.1).

2.2 Formulation

The heat transfer takes place from the surface to the liquid which would cause evaporation at the bubble surface. The growth of the bubble would lead to convection in the bulk liquid. There are eight dependent variables in this model, namely: bubble radius (\bar{R}), pressure, temperature, density of the vapor inside the bubble ($\bar{P}_v, \bar{T}_v, \rho_v$), pressure, temperature, and velocity distribution in the liquid ($\bar{p}_l, \bar{T}_l, \bar{u}_l, \bar{v}_l$). The independent variables are time (\bar{t}), radial distance (\bar{r}), and angular distance ($\bar{\psi}$).

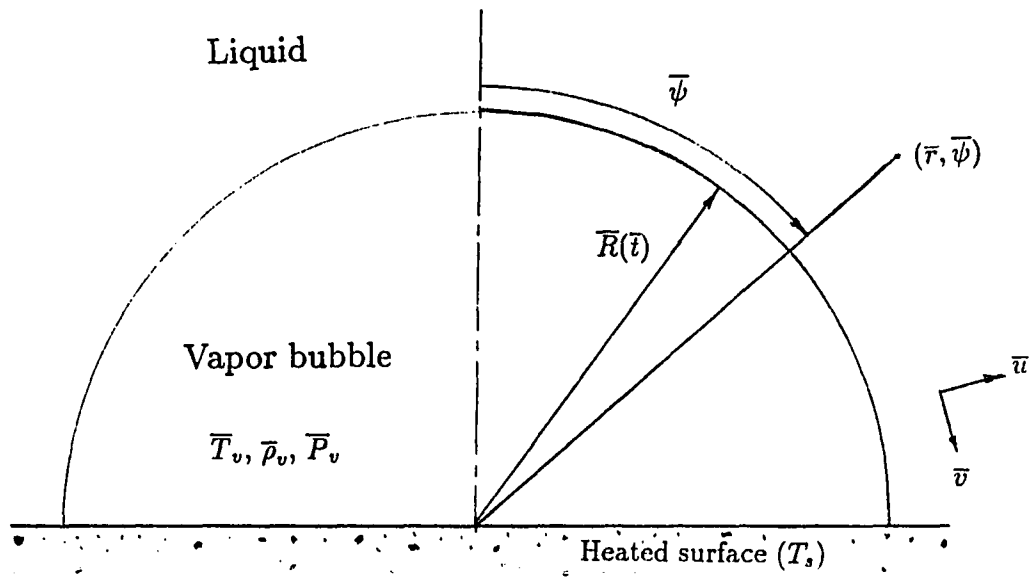


Figure 2.1: The second generation model in physical coordinates

2.2.1 Vapor in the Bubble

The equation of state of the vapor is given by the ideal gas law. The Clapeyron-Clausius equation (assuming $\bar{p}_v \ll \rho$) may be integrated from an initial state (P_{vo}, T_{vo}) to an arbitrary saturation state (\bar{P}_v, \bar{T}_v) assuming h_{fg} is constant (which is generally reasonable for a small enough change in saturation temperature – see Section 2.7) to give an additional governing equation for the vapor. Thus:

$$\bar{P}_v = \bar{p}_v R^* \bar{T}_v \quad (2.1)$$

$$\ln \left(\frac{\bar{P}_v}{P_{vo}} \right) = -\frac{h_{fg}}{R^*} \left(\frac{1}{\bar{T}_v} - \frac{1}{T_{vo}} \right). \quad (2.2)$$

Mass, momentum, and energy balances across the bubble interface are made to relate the state of vapor to that of liquid.

2.2.1.1 Mass Balance Consider an expanding hemispherical control volume of fixed quantity of mass, whose radius (\bar{R}_{cv}) is equal to the radius of bubble (Figure 2.2) at the given instant. Reynold's transport theorem for this control volume is written as:

$$0 = \frac{\partial}{\partial t} \int_{\mathcal{V}} \rho_v d\mathcal{V} + \int_{\mathcal{A}} \rho \vec{V} \cdot d\vec{\mathcal{A}} \quad (2.3)$$

where \mathcal{V} and \mathcal{A} represent volume and surface area of the control volume respectively. Since there is no efflux of mass from the control volume, the second term in the above equation is zero, thus,

$$0 = \frac{2}{3} \pi \bar{R}_{cv}^3 \dot{\bar{p}}_v + \bar{p}_v 2\pi \bar{R}_{cv}^2 \dot{\bar{R}}_{cv}.$$

Since there is no efflux of mass, \bar{u}_v at the bubble surface is equal to $\dot{\bar{R}}_{cv}$. Replacing \bar{R}_{cv} by \bar{R} (since they are equal at the given instant),

$$\bar{u}_v = -\frac{\bar{R} \dot{\bar{p}}_v}{3\bar{p}_v} = -\frac{\dot{\bar{R}}}{\bar{R}} \bar{R}. \quad (2.4)$$

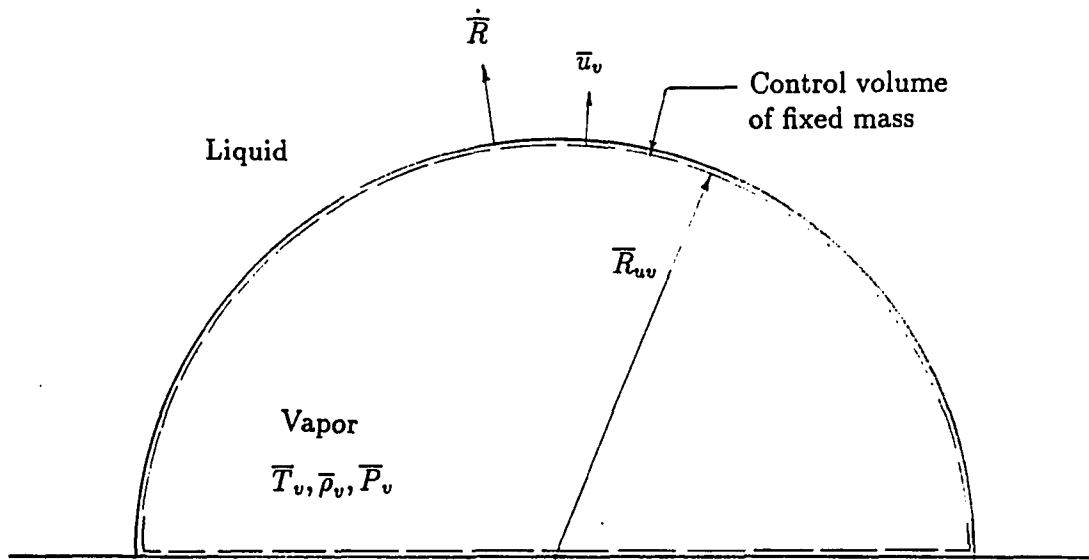


Figure 2.2: An expanding hemispherical control volume of a fixed quantity of mass

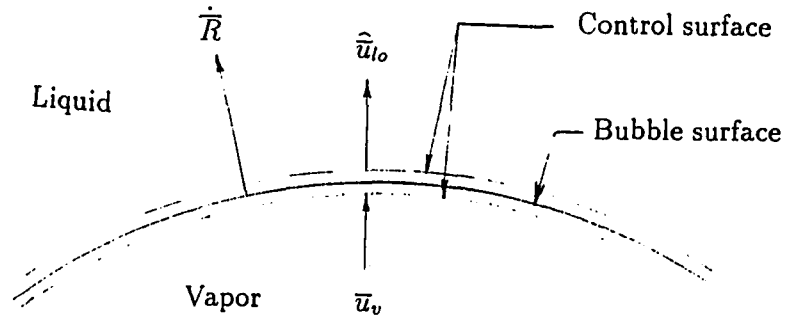


Figure 2.3: An infinitesimally thin control volume containing a portion of the bubble surface

Now consider mass balance for an infinitesimally thin control volume (Figure 2.3) containing a small portion of the surface of a bubble which is growing with mass inflow. Continuity yields

$$\bar{\rho}_v(\bar{u}_v - \dot{\bar{R}}) = \rho(\hat{u}_{l0} - \dot{\bar{R}})$$

where \bar{u}_v and \hat{u}_{l0} are velocities immediately inside and outside the bubble surface respectively. Substituting \bar{u}_v from Eq. (2.4),

$$\begin{aligned} \hat{u}_{l0} &= \dot{\bar{R}}(1 - \bar{\epsilon}) - \bar{\epsilon}\bar{R}/3 \\ &= \dot{\bar{R}} - \bar{\epsilon}\bar{\Gamma} \end{aligned} \quad (2.5)$$

where

$$\bar{\Gamma} = \dot{\bar{R}} + \frac{\bar{\epsilon}\bar{R}}{3}.$$

Equation (2.5) represents the mass balance on the bubble.

2.2.1.2 Momentum Balance Reynold's transport theorem for momentum balance for control volume in Figure 2.3 is:

$$\frac{D\vec{P}}{Dt} = \frac{\partial}{\partial t} \int_{\mathcal{V}} \vec{V}_1 \rho d\mathcal{V} + \int_{\mathcal{V}} \rho \vec{R} d\mathcal{V} + \int_{\mathcal{A}} \vec{V}_1 (\rho \vec{V}_2 \cdot d\vec{\mathcal{A}})$$

where \vec{P} is momentum, \vec{V}_1 is velocity in an inertial frame of reference, and $\rho \vec{V}_2 \cdot d\vec{\mathcal{A}}$ represents differential mass flux across interface. Note that \vec{V}_2 is the velocity relative to the control surface. The first two terms on the right hand side are zero since the control volume is infinitesimally thin. Consequently, the radial component becomes:

$$\left(\bar{P}_v - \hat{P}_{l_0} - \frac{2\sigma}{R} \right) 2\pi \bar{R}^2 = (\hat{u}_{l_0} - \bar{u}_v)(\bar{u}_v - \dot{R}) \bar{\rho}_v 2\pi \bar{R}^2$$

or,

$$\bar{P}_v - \hat{P}_{l_0} = \frac{2\sigma}{R} - \bar{\rho}_v (1 - \bar{\epsilon}) \bar{\Gamma}^2. \quad (2.6)$$

The left hand side in Eq. (2.6) is the pressure difference across the bubble surface and the terms on right hand side account for pressure due to surface tension and the dynamic pressure due to radial motion of fluid, respectively.

2.2.1.3 Energy Balance Reynold's transport theorem for energy is applied to the infinitesimal control volume in Figure 2.3 is:

$$\frac{dE}{dt} = \frac{\partial}{\partial t} \int_{\mathcal{V}} \left(u' + \frac{1}{2} |\vec{V}_1|^2 + pe_s \right) d\mathcal{V} + \int_{\mathcal{A}} \left(h + \frac{1}{2} |\vec{V}_1|^2 + pe_g \right) (\rho \vec{V}_2 \cdot d\vec{\mathcal{A}}) \quad (2.7)$$

where E , u' , and h stand for total energy, specific internal energy, and specific enthalpy of the interior of the control volume, respectively. pe_s represents the potential energy corresponding to the bubble surface tension. Since the control volume is infinitesimally thin, the contribution from u' and $|\vec{V}_1|^2$ in the first integral on the right hand side is zero, similarly in the absence of efflux of gravitational potential energy

into the control volume, p_{eg} in the second integral is set to zero. Equation (2.7) is therefore written as,

$$\dot{Q} - \dot{W} = 4\pi\sigma\bar{R}\dot{\bar{R}} + (\bar{u}_v - \dot{\bar{R}})\bar{\rho}_v \left[-h_{fg} + \frac{1}{2}(\widehat{u}_{l0}^2 - \bar{u}_v^2) \right] (2\pi\bar{R}^2)$$

where \dot{Q} is the rate of heat transfer into the control volume, and \dot{W} is the rate at which the control volume does work. Since the conductivity of vapor is usually very small compared with that of the liquid (by a factor 20 for water), the conduction of heat into the vapor is neglected. The only contribution to \dot{Q} is from conduction in the liquid. \dot{W} , the rate of work is equal to $(\widehat{P}_{l0} - \bar{P}_v)2\pi\bar{R}^2\dot{\bar{R}}$. Hence Eq. (2.7) is written as

$$k_l \left. \frac{d\widehat{T}}{d\bar{r}} \right|_{\bar{r}=\bar{R}} = \left(\widehat{P}_{l0} - \bar{P}_v + \frac{2\sigma}{\bar{R}} \right) \dot{\bar{R}} + \bar{\rho}_v \bar{\Gamma} \left[h_{fg} + \frac{1}{2}(\bar{u}_v^2 - \widehat{u}_{l0}^2) \right] \quad (2.8)$$

The left hand side of Eq. (2.8) represents the heat conducted into the bubble. The first term on the right hand side accounts for expansion work done by the bubble on the surrounding liquid. $\bar{\rho}_v \bar{\Gamma}$ represents mass flux across the interface, and the second term on the right hand side accounts for the influx of enthalpy and kinetic energy. After substitution of (2.5) and (2.6) and algebraic simplification, Eq. (2.8) becomes

$$k_l \left. \frac{d\widehat{T}}{d\bar{r}} \right|_{\bar{r}=\bar{R}} = \bar{\rho}_v \bar{\Gamma} \left\{ h_{fg} + \frac{1}{2}(1 - \bar{\epsilon}^2)\bar{\Gamma}^2 \right\}. \quad (2.9)$$

Note from the momentum equation that the value of the liquid pressure at the bubble surface is required to calculate the vapor pressure. This may be found by integrating the radial momentum equation along the heated surface (at $\psi = \pi/2$) from ∞ to the bubble surface and then integrating the momentum equation in the angular direction at $r = 0$ to determine the pressure $\bar{P}_{l0}(\bar{\psi})$ along the bubble surface. Then

an average pressure along the bubble surface is calculated as shown in Eq. (2.36).

$\frac{d\bar{T}}{d\bar{r}} \Big|_{\bar{r}=\bar{R}}$ in Eq. (2.8) denotes the average temperature gradient at the bubble surface.

2.2.2 Liquid in the Vicinity of the Bubble

The governing equations for the liquid around the bubble are based upon the usual differential forms for conservation of mass, momentum, and energy.

Continuity:

$$\frac{1}{\bar{r}^2} \frac{\partial}{\partial \bar{r}} (\bar{r}^2 \bar{u}) + \frac{1}{\bar{r} \sin \bar{\psi}} \frac{\partial}{\partial \bar{\psi}} (\bar{v} \sin \bar{\psi}) = 0 \quad (2.10)$$

Radial momentum transport:

$$\frac{D\bar{u}}{D\bar{t}} - \frac{\bar{v}^2}{\bar{r}} = -\frac{1}{\rho \bar{r}} \frac{\partial \bar{P}}{\partial \bar{r}} + \nu \left\{ \nabla^2 \bar{u} - \frac{2\bar{u}}{\bar{r}^2} - \frac{2}{\bar{r}^2} \frac{\partial \bar{v}}{\partial \bar{\psi}} - \frac{2\bar{v} \cot \bar{\psi}}{\bar{r}^2} \right\} \quad (2.11)$$

Tangential momentum transport:

$$\frac{D\bar{v}}{D\bar{t}} + \frac{\bar{u}\bar{v}}{\bar{r}} = -\frac{1}{\rho \bar{r}} \frac{\partial \bar{P}}{\partial \bar{\psi}} + \nu \left\{ \nabla^2 \bar{v} + \frac{2}{\bar{r}^2} \frac{\partial \bar{u}}{\partial \bar{\psi}} - \frac{\bar{v}}{\bar{r}^2 \sin^2 \bar{\psi}} \right\} \quad (2.12)$$

Energy transport:

$$\frac{D\bar{T}}{D\bar{t}} = \alpha \nabla^2 \bar{T} \quad (2.13)$$

where,

$$\nabla^2 = \frac{1}{\bar{r}^2} \frac{\partial}{\partial \bar{r}} \left(\bar{r}^2 \frac{\partial}{\partial \bar{r}} \right) + \frac{1}{\bar{r}^2 \sin \bar{\psi}} \frac{\partial}{\partial \bar{\psi}} \left(\sin \bar{\psi} \frac{\partial}{\partial \bar{\psi}} \right)$$

and

$$\frac{D}{D\bar{t}} = \frac{\partial}{\partial \bar{t}} + \bar{u} \frac{\partial}{\partial \bar{r}} + \frac{\bar{v}}{\bar{r}} \frac{\partial}{\partial \bar{\psi}}.$$

Equations (2.1 - 2.13) are subject to the initial conditions,

$$\bar{R} = R_0, \quad \bar{T} = T_\infty, \quad \text{and} \quad \bar{u} = \bar{v} = 0 \quad \forall (\bar{r}, \bar{\psi}) \quad \bar{r} > R_0 \quad (2.14)$$

and the boundary conditions,

$$\left. \begin{aligned}
 \bar{v} = \frac{\partial \bar{u}}{\partial \bar{\psi}} = \frac{\partial \bar{T}}{\partial \bar{\psi}} = 0 & \quad \text{at } \bar{\psi} = 0, \\
 \bar{u} = \bar{v} = 0 \text{ and } \bar{T} = T_s & \quad \text{at } \bar{\psi} = \pi/2, \\
 \bar{u} = \hat{u}_{l0}, \bar{v} = 0 & \\
 \text{and } \bar{T} = \bar{T}_v & \quad \text{at } \bar{r} = \bar{R}, \\
 \bar{u}, \bar{v} \rightarrow 0 \text{ and } \bar{T} \rightarrow T_\infty & \quad \text{as } \bar{r} \rightarrow \infty.
 \end{aligned} \right\} \quad (2.15)$$

The zero tangential velocity at the interface is a result of the presence of surfactants, however, other interface boundary conditions can easily be incorporated. The derivatives of temperature and velocities with respect to $\bar{\psi}$ are zero at $\bar{\psi} = 0$ because of the axial symmetry. The bubble surface is assumed to be at the saturation vapor temperature \bar{T}_v . The above equations constitute the formulation describing hemispherical bubble growth on a uniformly heated surface (heterogeneous boiling) with the mentioned assumptions.

2.2.3 Vorticity/Streamfunction Formulation

Streamfunction \bar{f} is defined in terms of \bar{u} and \bar{v} such that continuity is satisfied identically,

$$\bar{u} = \frac{-1}{\bar{r}^2 \sin \bar{\psi}} \frac{\partial \bar{f}}{\partial \bar{\psi}}, \quad \bar{v} = \frac{1}{\bar{r} \sin \bar{\psi}} \frac{\partial \bar{f}}{\partial \bar{r}}, \quad (2.16)$$

and a modified vorticity is defined

$$\vec{\omega} = \bar{r} \nabla \times \vec{V} = \left\{ \frac{\partial(\bar{r}\bar{v})}{\partial \bar{r}} - \frac{\partial \bar{u}}{\partial \bar{\psi}} \right\} \bar{e}_\phi. \quad (2.17)$$

Since the direction of $\vec{\omega}$ is always perpendicular to the radial and angular components of velocity, we define the scalar vorticity $\bar{\omega}$ to be the azimuthal component of $\vec{\omega}$.

Multiplying the tangential momentum equation (2.12) by \bar{r} and taking the derivative with respect to \bar{r} and then subtracting the result from the derivative with respect to $\bar{\psi}$ of radial momentum equation (2.11) eliminates the pressure term from those equations. Substitution of $\bar{\omega}$ then results in the vorticity transport equation. Finally, all velocity variables in the vorticity equation and in the energy equation (2.13) are replaced with appropriate derivatives of the streamfunction. Thus equations (2.10 - 2.13) become:

$$\bar{\omega} = \nabla_f^2 \bar{f} \quad (2.18)$$

$$\frac{\partial \bar{\omega}}{\partial \bar{t}} + \frac{1}{\bar{r}^2 \sin \bar{\psi}} \frac{\partial(\bar{f}, \bar{\omega})}{\partial(\bar{r}, \bar{\psi})} = \nu \nabla_{\omega}^2 \bar{\omega} \quad (2.19)$$

$$\frac{\partial \bar{T}}{\partial \bar{t}} - \frac{1}{\bar{r}^2 \sin \bar{\psi}} \frac{\partial \bar{f}}{\partial \bar{\psi}} \frac{\partial \bar{T}}{\partial \bar{r}} + \frac{1}{\bar{r}^2 \sin \bar{\psi}} \frac{\partial \bar{f}}{\partial \bar{r}} \frac{\partial \bar{T}}{\partial \bar{\psi}} = \alpha \nabla^2 T \quad (2.20)$$

where,

$$\begin{aligned} \nabla_f^2 &= \left(\frac{\partial^2}{\partial \bar{r}^2} - \frac{\cot \bar{\psi}}{\bar{r}^2} \frac{\partial}{\partial \bar{\psi}} + \frac{1}{\bar{r}^2} \frac{\partial^2}{\partial \bar{\psi}^2} \right) \div \sin \bar{\psi}. \\ \nabla_{\omega}^2 \bar{\omega} &= \frac{\partial^2 \bar{\omega}}{\partial \bar{r}^2} - \frac{1}{\bar{r}^2} \frac{\bar{\omega}}{\sin^2 \bar{\psi}} + \frac{\cot \bar{\psi}}{\bar{r}^2} \frac{\partial \bar{\omega}}{\partial \bar{\psi}} + \frac{1}{\bar{r}^2} \frac{\partial^2 \bar{\omega}}{\partial \bar{\psi}^2}. \\ \frac{\partial(\bar{f}, \bar{\omega})}{\partial(\bar{r}, \bar{\psi})} &= \frac{\partial \bar{f}}{\partial \bar{r}} \left(\frac{\partial \bar{\omega}}{\partial \bar{\psi}} - \bar{\omega} \cot \bar{\psi} \right) - \frac{\partial \bar{f}}{\partial \bar{\psi}} \left(\frac{\partial \bar{\omega}}{\partial \bar{r}} - \frac{2\bar{\omega}}{\bar{r}} \right) \end{aligned}$$

The initial conditions for Eq. (2.18) and (2.19) are:

$$\bar{f} = \bar{\omega} = 0 \quad \forall(\bar{r}, \bar{\psi}). \quad (2.21)$$

The boundary conditions for the streamfunction are:

$$\begin{aligned} \bar{f} = 0 \quad \text{at} \quad \bar{\psi} = \frac{\pi}{2}, \quad \bar{f} = (1 - \bar{\epsilon}) \dot{R} \bar{R}^2 \quad \text{at} \quad \bar{\psi} = 0 \\ \bar{f} = (1 - \bar{\epsilon}) \dot{R} \bar{R}^2 \cos \bar{\psi} \quad \text{at} \quad \bar{r} = \bar{R}, \quad \frac{\partial \bar{f}}{\partial \bar{r}} = 0 \quad \text{at} \quad \bar{r} = \bar{R} + \bar{\delta} \end{aligned} \quad (2.22)$$

Eq. 2.18 is used for the boundary condition for vorticity. The no-slip boundary conditions at the heated surface and at the bubble surface and the fact that $\frac{v}{u} \rightarrow 0$ as $\bar{r} \rightarrow \infty$ are incorporated into the vorticity equation, which is discussed in the non-dimensional form of these equations in Section 2.3.2.

Equations (2.1, 2.2, 2.6, 2.9) are the governing equations that must be solved after non-dimensionalization, which is described in the following section.

2.3 Non-dimensionalization

Assuming that hydrodynamic and thermal boundary layer thicknesses are the same order of magnitude (reasonable for $Pr \sim 1$), a single boundary layer thickness $\bar{\delta}$ is used as a length scale for the non-dimensionalization of radial coordinate. The non-dimensionalization is actually a transformation which maps $\bar{r} = \bar{R}$ to $r = 0$, and $\bar{r} = (\bar{R} + \bar{\delta})$ to $r = 1$. Consequently, the time varying domain of the physical space is mapped into a time invariant space in dimensionless space. Another critical length scale in the present problem is the instantaneous bubble radius, however, it is not constant. Hence the initial bubble radius is taken as a length scale for the non-dimensionalization. Fourier number (based on R_0) is used as non-dimensional time. Thus,

$$r = (\bar{r} - \bar{R})/\bar{\delta}, \quad \psi = \bar{\psi}, \quad t = \bar{t}\alpha/R_0^2 \quad (2.23)$$

The dependent variables are non-dimensionalized as:

$$R = \bar{R}/R_0, \quad \delta = \bar{\delta}/R_0, \quad \epsilon = \rho_v/\rho$$

$$P_v = \frac{\bar{P}_v - \hat{P}_{l0}}{2\sigma/R_0}, \quad \rho_v = \frac{\bar{\rho}_v - \rho_{sat}}{\rho_{v0} - \rho_{sat}}, \quad T_v = \frac{\bar{T}_v - T_{sat}}{T_s - T_{sat}}$$

$$P = \frac{\bar{P} - P_{\infty}}{\rho(\alpha/R_0)^2}, \quad T = \frac{\bar{T} - T_{sat}}{T_s - T_{sat}} \quad (2.24)$$

where $T_{sat} = T_{sat}(P_{\infty})$ is the saturation temperature corresponding to a vapor pressure of P_{∞} and $\rho_{sat} = P_{\infty}/(R^*T_{sat})$.

It will be shown that the streamfunction \bar{f} and vorticity $\bar{\omega}$ increase and decrease respectively proportional to \sqrt{t} during the later part of bubble growth. By factoring out \sqrt{t} in the following way, F and Ω are defined that become independent of time during this period. Thus,

$$F = \frac{\bar{f}}{\alpha R_0 \sqrt{t}}, \quad \Omega = \frac{\bar{\omega} R_0 \sqrt{t}}{\alpha} \quad (2.25)$$

The eight non-dimensional parameters which arise from the non-dimensionalization are:

$$\begin{aligned} Pr &= \nu/\alpha, & Ja &= C_l(T_s - T_{sat})/(\epsilon_0 h_{fg}), \\ We &= (\rho\alpha^2)/(\sigma R_0), & Sb &= (T_{sat} - T_{\infty})/(T_s - T_{sat}), \\ \epsilon_0 &= \frac{\rho v_0}{\rho}, & \pi_1 &= \frac{P_{v0}}{\rho v_0 h_{fg}}, & \pi_2 &= (\sigma/R_0)/P_{v0}, \\ \pi_3 &= T_{v0}/T_{sat}, & \pi_4 &= (T_s - T_{sat})/T_{sat} \end{aligned} \quad (2.26)$$

Ja is the ratio of sensible to latent heat per unit volume of the liquid and the vapor respectively. Note that Ja is a weak function of initial bubble radius through the value ϵ_0 . Sb is the measure of the initial subcooling of the liquid pool below the boiling point. The π terms represent ratios of various quantities at the initial state. π_1 is the ratio of stored energy of pressure to the latent heat. π_2 is the ratio of stored energy in the bubble surface to that of pressure. π_3 and π_4 are the two non-dimensional parameters that arise from three fixed temperatures in the problem.

2.3.1 Non-dimensional Equations

Substitution of the dimensionless variables (2.23 - 2.26) into equations (2.1, 2.2, 2.6, and 2.9) the governing equations for streamfunction, vorticity and liquid temperature (2.18-2.20) yields respectively,

$$\rho_v = \frac{(1 + \pi_2(P_v - 2) + \pi_2 We \widehat{P}_{l0})/T_v - \pi_3(1 - 2\pi_2)}{1 - \pi_3(1 - 2\pi_2)} \quad (2.27)$$

$$T_v = \left[\left(1 - \pi_1 \ln \left\{ \zeta \left[\frac{T_v \pi_4 + 1}{\pi_3} \right] \right\} \right)^{-1} \pi_3 - 1 \right] / \pi_4 \quad (2.28)$$

$$P_v = \frac{2}{R} - We \epsilon_o \dot{R}^2 \zeta (1 - \zeta \epsilon_o) \quad (2.29)$$

$$\dot{R} = \frac{Ja \frac{R}{\delta} \frac{dT}{dr} \Big|_{r=0} + 2\pi_1 \pi_2 \dot{R}}{R(1 + \frac{1}{2} \pi_1 \epsilon_o We \dot{R}^2) \zeta} \quad (2.30)$$

where,

$$\widehat{\frac{dT}{dr}} \Big|_{r=0} = \int_0^{\pi/2} \frac{dT}{dr} \Big|_{r=0} \sin \psi \, d\psi, \quad \widehat{P}_{l0} = \int_0^{\pi/2} P_{l0} \Big|_{r=0} \sin \psi \, d\psi,$$

and

$$\zeta = \rho_v + \pi_3(1 - 2\pi_2)(1 - \rho_v)$$

Streamfunction equation:

$$\frac{\partial^2 F}{\partial r^2} + \frac{\delta^2}{\gamma^2} \frac{\partial^2 F}{\partial \psi^2} - \frac{\delta^2 \cot \psi}{\gamma^2} \frac{\partial F}{\partial \psi} = \Omega \delta^2 \sin \psi \quad (2.31)$$

Vorticity transport equation:

$$\begin{aligned} & \delta^2 \left(\dot{\Omega} - \frac{\Omega}{2t} \right) - \left[\delta (\dot{R} + r\dot{\delta}) + \frac{\delta \sqrt{t}}{\gamma^2 \sin \psi} \frac{\partial F}{\partial \psi} \right] \frac{\partial \Omega}{\partial r} - \left[\frac{Pr \delta^2 \cot \psi}{\gamma^2} - \frac{\delta \sqrt{t}}{\gamma^2 \sin \psi} \frac{\partial F}{\partial r} \right] \frac{\partial \Omega}{\partial \psi} \\ & = Pr \frac{\partial^2 \Omega}{\partial r^2} + \frac{Pr \delta^2}{\gamma^2} \frac{\partial^2 \Omega}{\partial \psi^2} + \Omega \left[\frac{-Pr \delta^2}{\gamma^2 \sin^2 \psi} + \frac{\delta \sqrt{t} \cot \psi}{\gamma^2 \sin \psi} \frac{\partial F}{\partial r} - \frac{2\sqrt{t} \delta^2}{\gamma^3 \sin \psi} \frac{\partial F}{\partial \psi} \right] \end{aligned} \quad (2.32)$$

Energy transport equation:

$$\begin{aligned} \delta^2 \frac{\partial T}{\partial t} - \frac{\partial^2 T}{\partial r^2} - \frac{\delta^2}{\gamma^2} \frac{\partial^2 T}{\partial \psi^2} - \frac{\partial T}{\partial r} \left[\delta(\dot{R} + r\dot{\delta}) + \frac{\delta\sqrt{t}}{\gamma^2 \sin \psi} \frac{\partial F}{\partial \psi} + \frac{2\delta}{\gamma} \right] \\ - \frac{\partial T}{\partial \psi} \left[-\frac{\delta\sqrt{t}}{\gamma^2 \sin \psi} \frac{\partial F}{\partial r} + \frac{\delta^2 \cot \psi}{\gamma^2} \right] = 0 \end{aligned} \quad (2.33)$$

where

$$\gamma = R + r\delta$$

Note the appearance of $(\dot{R} + r\dot{\delta})$ in the radial convection term in vorticity and energy transport equations. It accounts for the effect of the moving bubble surface and the changing boundary layer thickness in physical coordinates.

The equation of state (2.27) explicitly requires the average dimensionless liquid pressure at the bubble liquid interface, \hat{P}_{l_0} , as an argument. The value of \hat{P}_{l_0} may be found by integrating the liquid momentum equation along the heated surface ($\psi = \pi/2$);

$$\frac{\partial P}{\partial r} = \frac{\delta Pr}{\gamma^2} \left(\frac{\partial^2 u}{\partial \psi^2} - 2 \frac{\partial v}{\partial \psi} \right) \quad (2.34)$$

and then along the bubble surface ($r=0$) for the case of interface with surfactant;

$$\frac{\partial P}{\partial \psi} = R \left\{ Pr \left[\frac{1}{\delta^2} \frac{\partial^2 v}{\partial r^2} + \frac{2}{R\delta} \frac{\partial v}{\partial r} + \frac{2}{R^2} \frac{\partial u}{\partial \psi} \right] + \frac{\dot{R}}{\delta} \frac{\partial v}{\partial r} - \frac{u}{\delta} \frac{\partial v}{\partial r} \right\}. \quad (2.35)$$

u and v may be found by differentiating the streamfunction. Because the bubble is assumed to be hemispherical in the present work, the velocity field will be uniform and one-dimensional very near the interface (except in a small neighborhood near the contact line at $\psi = \pi/2$). For this reason \hat{P}_{l_0} is determined in the present work by neglecting viscous effects [68].

$$\hat{P}_{l_0} = (1 - \epsilon) \left((2\dot{R}^2 + R\ddot{R}) - (1 - \epsilon)\dot{R}^2/2 \right) \quad (2.36)$$

2.3.2 Initial and Boundary Conditions

Since the initial pressure in the bubble is $P_{vo} = P_{\infty} + 2\sigma/R_0$, there will be a discontinuity in temperature at the bubble surface at $\bar{t} = 0$ if $T_{\infty} \neq T_{sat}(P_{vo})$. An approximate one-dimensional integral method [68] indicated that in this case the boundary layer around the bubble grows like

$$\delta = \beta\sqrt{t} \quad \text{as } t \rightarrow 0^+ \quad (2.37)$$

where β is a free parameter of order one. To resolve the temperature discontinuity at $t = 0$ at the bubble surface, (2.37) is substituted in (2.33). The limiting form of the resulting equation as $t \rightarrow 0^+$ is

$$\frac{\partial^2 T}{\partial r^2} + \frac{1}{2}r\beta^2 \frac{\partial T}{\partial r} = 0 \quad (2.38)$$

with boundary conditions:

$$T = (\pi_3 - 1)/\pi_4 \text{ at } r = 0 \text{ and } T = Sb \text{ at } r = 1. \quad (2.39)$$

The solution to this ordinary differential equation gives the initial condition for (2.33). The other initial conditions are,

$$P_v = 2, \quad T_v = \rho_v = R = 1, \quad \text{and } F = \Omega = 0 \quad \forall (r, \psi) \text{ at } t = 0. \quad (2.40)$$

The boundary conditions (2.15) become:

$$F = \frac{(1 - \epsilon)}{\sqrt{t}} \dot{R}R^2, \quad \Omega = 0, \quad \frac{\partial T}{\partial \psi} = 0 \quad \text{at } \psi = 0,$$

$$F = 0, \quad \Omega = \frac{t}{\gamma^2} \frac{\partial^2 F}{\partial \psi^2}, \quad T = 1 \quad \text{at } \psi = \pi/2$$

$$F = \frac{(1-\epsilon)\dot{R}R^2 \cos \psi}{\sqrt{t}}, \quad \Omega = \frac{t}{(\gamma^2 \sin \psi)} \frac{\partial^2 F}{\partial r^2}, \quad T = T_v \quad \text{at } r = 0$$

$$\frac{\partial F}{\partial r} = 0, \quad \Omega = -t \nabla_{R,\delta}^2 F, \quad \frac{\partial T}{\partial x} = 0 \quad \text{at } r = 1 \quad (2.41)$$

where x is the coordinate parallel to the heated surface. The boundary condition $\frac{\partial T}{\partial x} = 0$ is written in spherical coordinates as,

$$\frac{\partial T}{\partial r} = -\frac{\cot \psi}{1 + \frac{R}{\delta}} \frac{\partial T}{\partial \psi}$$

The streamfunction boundary condition along the bubble interface is again based upon a uniform radial flow there. For a hemispherical bubble, the error of this assumption is quite small, of order ϵ_0 .

2.4 Asymptotic Equations Appropriate for $t \rightarrow \infty$ Limit

If R were to increase proportional to square root of t , which will be shown to be true for large values of time, then substitution of $R = \eta \sqrt{t}$, ($\eta = \text{constant}$), and Eq. (2.37) in the governing equation for the liquid region (2.31 - 2.33) and the boundary conditions (2.41) yield equations that are independent of time. Thus, in the limit $t \rightarrow \infty$, the streamfunction, vorticity and energy transport equations become:
Streamfunction equation:

$$\frac{\partial^2 F}{\partial r^2} + \frac{\beta^2}{\gamma'^2} \frac{\partial^2 F}{\partial \psi^2} - \frac{\beta^2 \cot \psi}{\gamma'^2} \frac{\partial F}{\partial \psi} = \Omega \beta^2 \sin \psi \quad (2.42)$$

Vorticity transport equation:

$$\frac{\beta^2}{2} \Omega + \left[\frac{\beta \gamma'}{2} + \frac{\beta}{\gamma'^2 \sin \psi} \frac{\partial F}{\partial \psi} \right] \frac{\partial \Omega}{\partial r} + \left[\frac{Pr \beta^2 \cot \psi}{\gamma'^2} - \frac{\beta}{\gamma'^2 \sin \psi} \frac{\partial F}{\partial r} \right] \frac{\partial \Omega}{\partial \psi}$$

$$= -Pr \frac{\partial^2 \Omega}{\partial r^2} - \frac{Pr \beta^2}{\gamma'^2} \frac{\partial^2 \Omega}{\partial \psi^2} - \frac{\beta \cot \psi \Omega}{\gamma'^2 \sin \psi} \frac{\partial F}{\partial r} + \frac{Pr \beta^2 \Omega}{\gamma'^2 \sin^2 \psi} + \frac{2\beta^2 \Omega}{\gamma'^3 \sin \psi} \frac{\partial F}{\partial \psi} \quad (2.43)$$

Energy transport equation:

$$\begin{aligned} \frac{\partial^2 T}{\partial r^2} + \frac{\beta^2}{\gamma'^2} \frac{\partial^2 T}{\partial \psi^2} + \frac{\partial T}{\partial r} \left[\frac{\beta \gamma'}{2} + \frac{\beta}{\gamma'^2 \sin \psi} \frac{\partial F}{\partial \psi} + \frac{2\beta}{\gamma'} \right] \\ + \frac{\partial T}{\partial \psi} \left[-\frac{\beta}{\gamma'^2 \sin \psi} \frac{\partial F}{\partial r} + \frac{\beta^2 \cot \psi}{\gamma'^2} \right] = 0 \end{aligned} \quad (2.44)$$

where,

$$\gamma' = \eta + r\beta.$$

The boundary conditions are,

$$\begin{aligned} F &= \frac{(1-\epsilon)\eta^3}{2}, \quad \Omega = 0 \quad \text{at } \psi = 0 \\ F &= 0, \quad \Omega = \frac{1}{\gamma'^2} \frac{\partial^2 F}{\partial \psi^2} \quad \text{at } \psi = \pi/2 \\ F &= \frac{(1-\epsilon)\eta^3}{2} \cos \psi, \quad \Omega = \frac{1}{\gamma'^2 \sin \psi} \frac{\partial^2 F}{\partial r^2} \quad \text{at } r = 0 \\ \frac{\partial F}{\partial r} &= 0, \quad \Omega = -\nabla_{\eta, \beta}^2 F \quad \text{at } r = 1 \end{aligned} \quad (2.45)$$

The boundary conditions for (2.44) are the same as those in (2.41), and since T_v and P_v approach zero during this period, these are also independent of time, which implies that the viscous problem has a *similarity solution*.

2.5 Numerical Method

The full dimensionless formulation of the transient problem (section 2.3) is solved numerically using an implicit, point-iterative, finite difference method. This method, which is formally first order accurate in time and second order accurate in space is described next.

2.5.1 Finite Differencing

The three governing equations (2.31 – 2.33) are cast in generic form:

$$\delta^2 \frac{\partial \phi}{\partial t} - \frac{\partial^2 \phi}{\partial r^2} - \frac{\delta^2}{\gamma^2} \frac{\partial^2 \phi}{\partial \psi^2} - 2\lambda \frac{\partial \phi}{\partial r} - 2\mu \frac{\partial \phi}{\partial \psi} = S \quad (2.46)$$

where ϕ represents T , Ω , or F with the understanding that the term $\frac{\partial \phi}{\partial t}$ will be deleted while solving (2.31) and Pr will appear while solving (2.32). The corresponding μ , λ , and S are:

$$\begin{aligned} \lambda_{\Omega} &= \frac{\delta}{2} \left[(\dot{R} + r\dot{\delta}) + \frac{\sqrt{t}}{\sin \psi \gamma^2} \frac{\partial F}{\partial \psi} \right] \\ \lambda_T &= \frac{\delta}{2} \left[(\dot{R} + r\dot{\delta}) + \frac{\sqrt{t}}{\sin \psi \gamma^2} \frac{\partial F}{\partial \psi} + \frac{2}{\gamma} \right] \\ \mu_F &= -\frac{\delta^2 \cot \psi}{2\gamma^2} \\ \mu_{\Omega} &= \frac{\delta}{2\gamma^2} \left[-\frac{\sqrt{t}}{\sin \psi} \frac{\partial F}{\partial r} + Pr\delta \cot \psi \right] \\ \mu_T &= \frac{\delta}{2\gamma^2} \left[-\frac{\sqrt{t}}{\sin \psi} \frac{\partial F}{\partial r} + \delta \cot \psi \right] \\ S_F &= -\Omega \delta^2 \sin \psi / t \\ S_{\Omega} &= \frac{\Omega \delta^2}{\gamma^2 \sin \psi} \left[\frac{-Pr}{\sin \psi} + \frac{\cot \psi \sqrt{t}}{\delta} \frac{\partial F}{\partial r} - \frac{2\sqrt{t}}{\gamma} \frac{\partial F}{\partial \psi} + \delta^2 \frac{\Omega}{2t} \right] \\ S_T &= \lambda_F = 0 \end{aligned} \quad (2.47)$$

The temporal term is finite differenced first order accurate and the second order spatial derivatives are finite differenced second order accurate. The first order derivatives are written as,

$$2\lambda \frac{\partial \phi}{\partial r} = (\lambda - |\lambda|) \left(\frac{\phi_{i,j} - \phi_{i-1,j}}{\Delta r} + \left\{ \frac{\phi_{i+1,j} - 2\phi_{i,j} + \phi_{i-1,j}}{2\Delta r} \right\} \right)$$

$$+ (\lambda + |\lambda|) \left(\frac{\phi_{i+1,j} - \phi_{i,j}}{\Delta r} - \left\{ \frac{\phi_{i+1,j} - 2\phi_{i,j} + \phi_{i-1,j}}{2\Delta r} \right\} \right) \quad (2.48)$$

and a similar expression is written for ψ direction. The terms in curly parenthesis are then added to a source term so that the scheme represents upwind differencing which ensures diagonal dominance while retaining second order accuracy. Gauss-Seidel iteration method was preferred over ADI method to solve the resulting simultaneous equations because the later was found to take 10 to 15 percent more CPU time than the former. The boundary conditions for vorticity were finite differenced as follows:

$$\begin{aligned} \Omega_{I,NS} &= \frac{2tF_{I,NS-1}}{\gamma^2 \Delta \psi^2} \quad \text{at } \psi = \pi/2 \\ \Omega_{1,J} &= \frac{2t(F_{2,J} - F_{1,J})}{\delta^2 \sin \psi \Delta r^2} \quad \text{at } r = 0 \\ \Omega_{NR,J} &= \frac{t}{\sin \psi} \left[\frac{2(F_{NR-1,J} - F_{NR,J})}{\delta^2 \Delta r^2} - \frac{\cot \psi}{(R + \delta)^2} \frac{(F_{NR,J+1} - F_{NR,J-1})}{2\Delta \psi} \right. \\ &\quad \left. + \frac{F_{NR,J+1} - 2F_{NR,J} + F_{NR,J-1}}{(R + \delta)^2 \Delta \psi^2} \right] \quad \text{at } r = 1 \end{aligned} \quad (2.49)$$

The condition $v = 0$ is incorporated in the finite differencing of boundary condition at $r = 1$ because the flow is assumed to be radial far from the bubble ($\frac{v}{u} \rightarrow 0$ as $r \rightarrow \infty$).

The vorticity at $r = 1$ was found to be vanishingly small except at a very close portion near the heated surface. The conditions at the far field boundary were seen to have very small effect on the bubble growth. When the predictions of the program with the above boundary condition at $r = 1$ were compared with the case when Ω was set to zero at $r = 1$, the difference in bubble radius was less than 5%. However, the later case was found to save substantial amount of computer time. And hence the boundary condition $\Omega = 0$ was used at the far field boundary, $r = 1$.

The entire calculation was carried out in double precision. (The CPU time required for double precision is approximately 10 % more than that for single precision on the Apollo workstation.) The convergence criteria for temperature, streamfunction, vorticity, vapor pressure, vapor temperature, and vapor density were $\mathcal{T}_T < \epsilon_T$, $\mathcal{T}_F < \epsilon_F$, $\mathcal{T}_\Omega < \epsilon_\Omega$, $\mathcal{T}_{P_v} < \epsilon_{P_v}$, $\mathcal{T}_{\rho_v} < \epsilon_{\rho_v}$, $\mathcal{T}_{T_v} < \epsilon_{T_v}$, where

$$\mathcal{T}_T = \max_{i,j} \left| 2 \left(\frac{T_{i,j}^{k+1} - T_{i,j}^k}{T_{i,j}^{k+1} + T_{i,j}^k} \right) \right| \quad (2.50)$$

$$\mathcal{T}_F = \max_{i,j} \left| 2 \left(\frac{F_{i,j}^{k+1} - F_{i,j}^k}{F_{i,j}^{k+1} + F_{i,j}^k} \right) \right| \quad (2.51)$$

$$\mathcal{T}_\Omega = \max_{i,j} \left| \frac{\Omega_{i,j}^{k+1} - \Omega_{i,j}^k}{\Omega_{ave}} \right| \quad (2.52)$$

$$\mathcal{T}_{P_v} = \max_{i,j} \left| \frac{P_{v,i,j}^{k+1} - P_{v,i,j}^k}{P_v^{k+1}} \right| \quad (2.53)$$

$$\mathcal{T}_{\rho_v} = \max_{i,j} \left| \rho_{v,i,j}^{k+1} - \rho_{v,i,j}^k \right| \quad (2.54)$$

$$\mathcal{T}_{T_v} = \max_{i,j} \left| T_{v,i,j}^{k+1} - T_{v,i,j}^k \right| \quad (2.55)$$

where

$$\Omega_{ave} = \frac{\sum_{i=1}^{NR} \sum_{j=1}^{NS} |\Omega_{i,j}|}{NR \cdot NS}$$

The values of ϵ_T , ϵ_F , and ϵ_Ω were 10^{-6} , 10^{-5} , and 10^{-5} respectively. The values of ϵ_{P_v} , ϵ_{T_v} , ϵ_{ρ_v} were 10^{-6} each. These values were arrived at after noting that their increase by *two* orders of magnitude did not result in substantial change in the plot of bubble radius versus time as well as in the contour plots of the three dependent variables involved (T , F , and Ω). Since the vorticity was found to be negligibly small

everywhere except near heated and bubble surfaces, the average value of Ω has been used in the denominator for the test of vorticity. To save computer time, the above tests were performed only once after five iterations.

To resolve the gradients of dependent variables near the heated surface and near the bubble interface, more grid points were clustered in those regions (Figure 2.4) using the logarithmic transformation in [69], (page 247). The ratio of the lengths of the largest to the smallest cell was typically 40, however, in certain cases it was kept 10 or 90 depending on the gradients of the dependent variables. In order to capture the details of the transient during the initial period and still keep the number of steps to a minimum, the timestep Δt was successively increased in a manner such that $\frac{\Delta t}{t}$ remained small (typically 5×10^{-3}).

2.5.2 Dynamic Relaxation

The convergence of Gauss-Seidel iterations for the vorticity equation is very sensitive to any perturbations in streamfunction because vorticity is expressed in terms of the derivative of streamfunction at the boundaries (see equations 2.41). Note that if the vorticity computation is switched to a Dirichlet problem, that is, if the boundary values are fixed, Ω converges quickly). The relaxation of ϕ (which is any of the dependent variables, T , F , or Ω) has been defined according to the usual rule,

$$\phi^k = w \cdot \phi^k + (1 - w) \cdot \phi^{k-1}.$$

where w is the relaxation parameter. Too large w resulted in divergence of the iterative scheme either at the first timestep or later during the transient. Too small w resulted in too many iterations. A method of *dynamic relaxation* was developed, which was used separately for streamfunction, vorticity, and temperature.

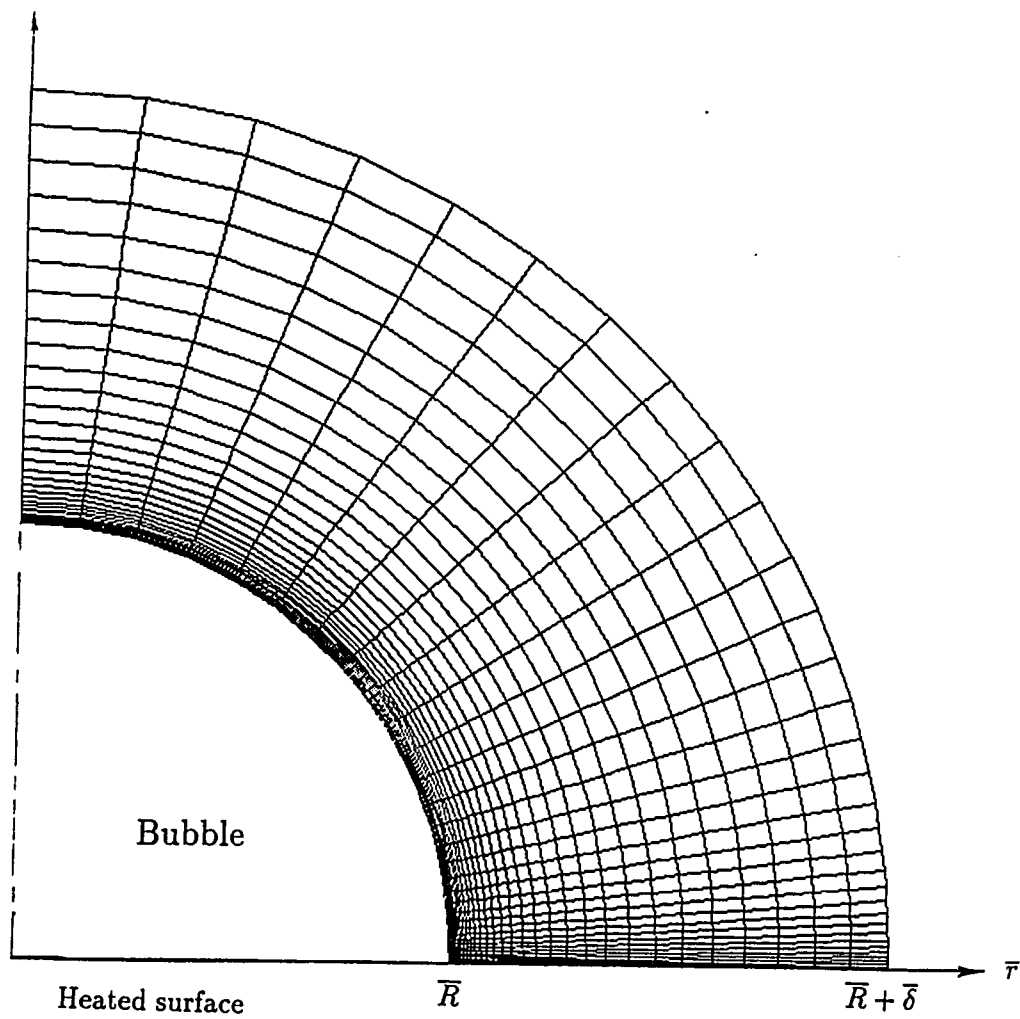


Figure 2.4: Typical computational grid

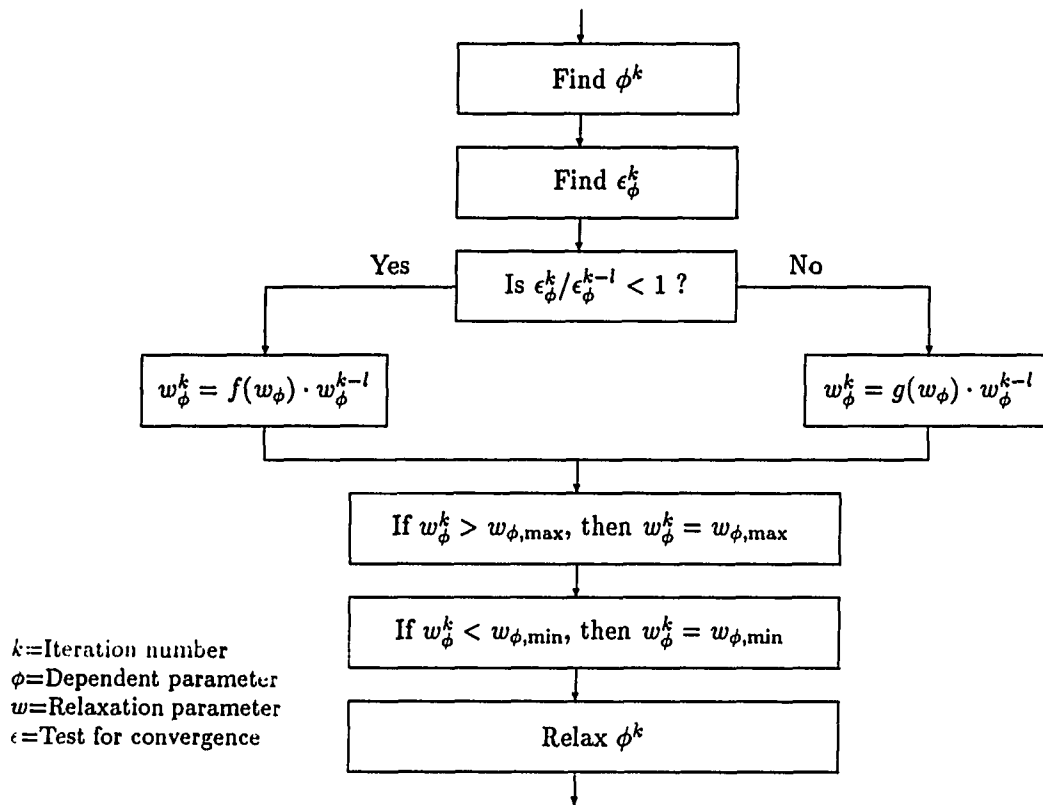


Figure 2.5: An algorithm for the method of dynamic relaxation

The flow chart for the scheme is depicted in Figure 2.5. ϵ is a test of convergence such that smaller value would imply convergence, f and g are two functions whose values are greater than and less than unity respectively. If ϵ^k is less than ϵ^{k-l} (i.e. value of ϕ converging), the scheme makes a small increase in the value of relaxation parameter and vice-versa. As the iterative process continued, w would assume a favorable value *dynamically*. l is a number greater than one, the purpose of which is to compare the value of ϵ of the current iteration with that l iterations before in

order to determine the trend of convergence. Selection of the exact form of f and g has been found to be unimportant. A step function such as the following may be employed:

$$f(w) = \begin{cases} 1.05 & \text{if } w_{\min} < w \leq 1.5 \\ 1.01 & \text{if } 1.5 < w \leq w_{\max} \end{cases}$$

$$g(w) = \begin{cases} 0.9 & \text{if } w_{\min} < w \leq 1.5 \\ 0.8 & \text{if } 1.5 < w \leq w_{\max}. \end{cases}$$

w_{\max} and w_{\min} are the maximum and minimum values of relaxation parameter that must be selected *a priori*. w_{\max} should be less than two else the scheme will diverge. The lower limit for w is necessary because a value of w too close to zero will result in unproductive iterations. The typical values of w_{\min} and w_{\max} were 0.05 and 1.75 respectively.

The value of w must be reset to some initial value w_{ini} (selected *a priori*) in the beginning of a steady state calculation or in the beginning of every timestep in case of a transient problem. This value has been found to be unimportant if it is smaller than unity but not too small.

This method exhibits a nature similar to that of a feed-back control mechanism. Too strong a feed-back produces oscillatory divergence in the output and too feeble feed-back is not effective. Hence values of f and g differing largely from unity may produce divergence while values too close to unity may not bring about sufficient variation in the relaxation parameter. The process of convergence in many circumstances is highly non-linear. The iterations may show a continuous trend of convergence, and then diverge suddenly. Since the value of w can only be changed by a small amount at one time, the dynamically assumed value of w displays nature similar to a quantity

characterized by inertia. The reason for limiting w to a maximum (w_{\max}) is this sluggish response. The values of (w_{\min}) and (w_{\max}) were chosen to be 0.2 and 1.6 respectively.

Figure 2.6 is an example of how the value of w_{Ω} varied at some typical timesteps. n is the timestep number and m is the iteration number. The curve for w_F shows that the relaxation parameter for streamfunction increased monotonically except during the first few iterations.

Figure 2.7 shows the cumulative number of iterations required with and without the dynamic relaxation. w_c denotes the constant value of the relaxation parameter as used in conventional method. For the present problem, this method reduced the number of iterations by as much as a factor of five (Figure 2.7) in addition (and most important), it reduced the chances of divergence.

2.5.3 Computational Resources

By and large, the computation were carried out on Apollo DN 10010 personal workstation, which is rated to perform 3 to 5 Mflops per second (14.9 Mwhets/second) with double precision. A typical run of saturated boiling for inviscid liquid with a 33x33 grid required about 100 minutes of CPU time irrespective of the value of Ja . For the viscous liquid however, with a 33x33 grid a $Ja = 1$ case required 110 minutes, where a $Ja = 80$ case required 8 hours and a $Ja = 320$ case required 12 hours of CPU time. A 17x17 grid typically took 8 times less CPU time, while a 65x65 grid took about 15 times more CPU time than the 33x33 grid. Subcooled boiling cases took less time than superheated boiling. The $Sb = 4$ case typically required about half as much CPU time as that of the saturated boiling case at all Jacob numbers. The

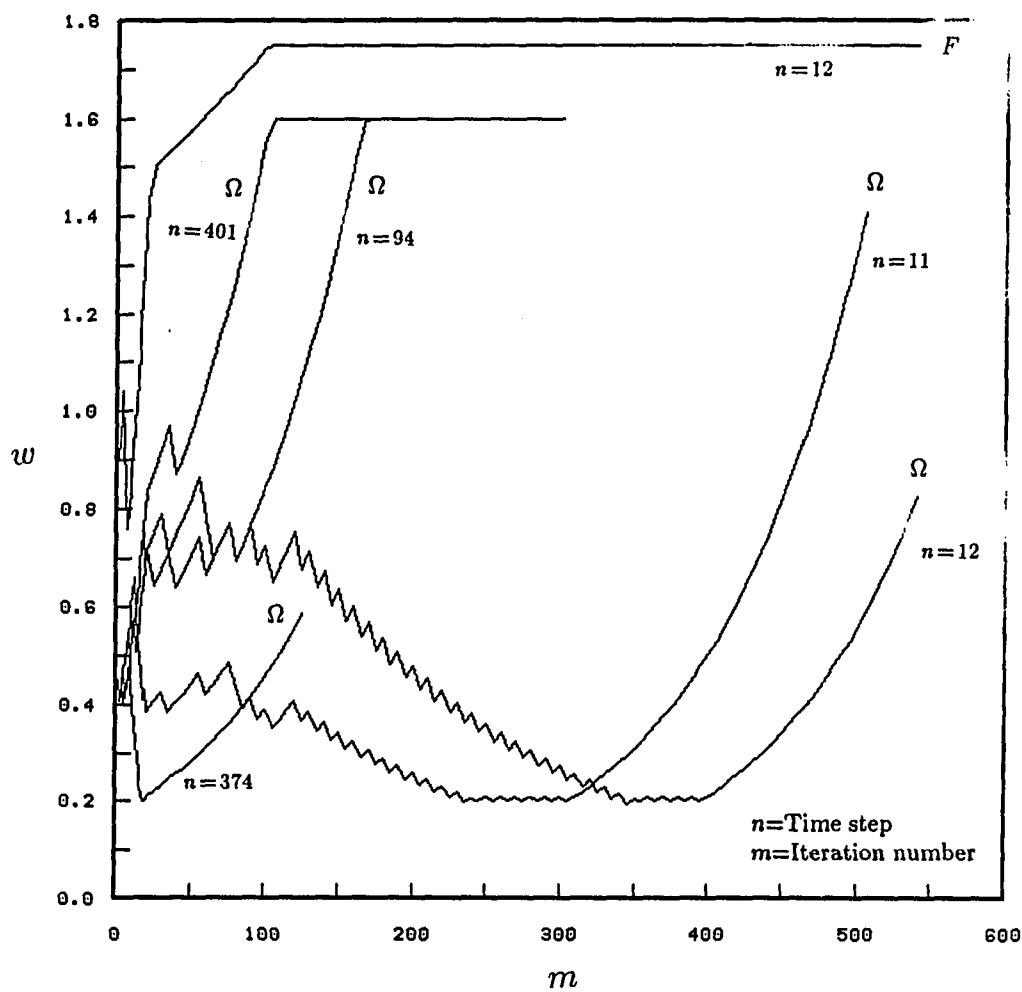


Figure 2.6: Variation of relaxation parameter against iteration number, $Ja=50$, $Sb=0$, Grid size: 17×17 , Viscous case

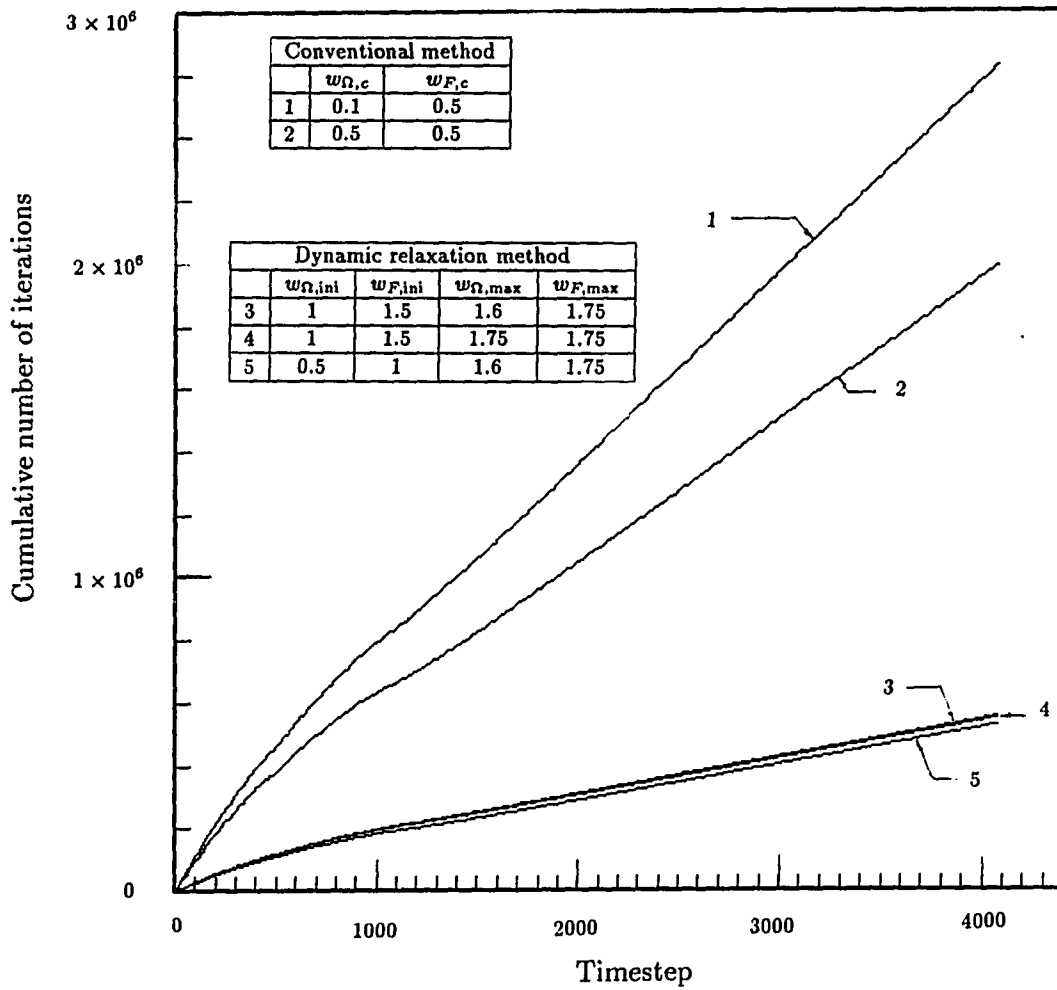


Figure 2.7: Cumulative number of iterations with and without dynamic relaxation, $Ja=50$, $Sb=0$, Grid size: 17×17 , Viscous case

inviscid superheated boiling case at $Ja = 10$ took approximately 1 hour while for $Ja = 320$ case took approximately 5 hours.

The similarity transformation defined in Eq. (2.25) helped reduce CPU time by about 50 % during the diffusion controlled period compared with a program that used a dimensionless streamfunction and vorticity proportional to \bar{f} and $\bar{\omega}$ as the dependent variables.

The extent of the boundary layer around the bubble defined by β in Eq. (2.37) is not known *a priori*. A trial and error method was adopted for finding an optimum value of β . Different values of β were used and temperature, streamfunction, and vorticity were plotted. β bigger than an optimum value did not produce substantial change in the dependent variables.

To study the effect of mesh size, 17x17, 33x33, and 65x65 node meshes were tried with a representative value of $Ja = 20$ and $Sb = 0$. The values of temperature, streamfunction, and vorticity given by these three cases showed convergence in that differences between values of any of the three dependent variables at any point in the domain given by the 33x33 and 65x65 cases were a lot smaller than differences between the values given by the 17x17 and 33x33 cases. The difference in the values of vorticity given by the 65x65 grid compared to 33x33 grid was about 5 percent at all points except those where vorticity was close to zero. The difference in the values of temperature never exceeded 5 percent anywhere in the computational domain. To find the truncation error due to finite size of time step, three different cases with the value of Δt one-third of the previous value were tried. The radius versus time plots were found to match extremely closely in the three cases and they clearly show convergence. If radius is expressed as $R = \eta\sqrt{t}$, then the value of η was always within

0.5 percent of other values in the three cases.

2.6 Verification of Method

Three test cases were carried out with the program with problems of known analytical solution.

2.6.1 Steady State Problem of Heat Diffusion Through a Spherical Shell

The following boundary conditions were chosen for this conduction heat transfer problem: $T = 1$ at $0 < \psi < \pi/4$ and $T = 0$ at $\pi/4 < \psi < \pi/2$ at $r = 1$, $T = 0$ at $0 < \psi < \pi/2$ and $r = 0$, and $\frac{\partial T}{\partial \psi} = 0$ at $\psi = 0$ and at $\psi = \pi/2$.

This problem was solved using the numerical method described before by holding R and δ constant in value equal to the inner radius and shell thickness respectively, and using the above boundary conditions. An analytical solution was found using series solution in terms of Legendre polynomials,

$$T(r, \psi) = s_1 \frac{1 - (\xi r + 1)^{-1}}{1 - (\xi + 1)^{-1}} + \sum_{n=1}^{\infty} \frac{1}{2} \{ P_{n+1}(s_1) - P_{n+1}(-s_1) - P_{n-1}(s_1) + P_{n-1}(-s_1) \} \left[\frac{(\xi r + 1)^n - (\xi r + 1)^{-(n+1)}}{(\xi + 1)^n - (\xi + 1)^{-(n+1)}} \right] P_n \cos \psi, \quad (2.56)$$

where $s_1 = \cos \pi/4$, $\xi = (R + \delta)/R - 1$, and P_n is a Legendre polynomial of n^{th} order. Due to the step in temperature profile at the boundary $r = 1$, the series solution, which was numerically evaluated, produced the "Gibbs jump", which is a profile exhibiting an overshooting at a discontinuity. 200 terms of the series were required to be evaluated before the Gibbs jump became narrower than the numerical

Table 2.1: Bubble growth in homogeneous boiling

Ja'	1	3	10	30	100	300
c (analytical result, [70])	1.1973	1.1078	1.0229	1.0043	1.0261	1.1305
c (numerical result, 33x33 grid)	1.3015	1.0901	1.0013	0.9823	0.9942	1.0379

grid spacing. The finite-difference solution and the Legendre series solution then matched within 1 percent.

2.6.2 Homogeneous Boiling

2.6.2.1 Analytical Solution Valid for $t \rightarrow \infty$ Limit A bubble growing in an infinite superheated medium in the absence of a surface is termed homogeneous boiling, in contrast to a bubble growing on a surface which is referred to as heterogeneous boiling. The numerical solution to the homogeneous boiling problem during the asymptotic period of growth was found using the finite difference algorithm. For this purpose, the temperature is non-dimensionalized as

$$T = \frac{\bar{T} - T_{sat}}{T_{\infty} - T_{sat}}$$

and vorticity is set to zero everywhere in the domain. The relevant boundary conditions are:

$$\frac{\partial T}{\partial \psi} = 0 \text{ at } \psi = 0 \text{ and at } \psi = \pi/2 \quad (2.57)$$

$$T = 1 \text{ at } r = 1, \text{ and } T = 0 \text{ at } r = 0. \quad (2.58)$$

The solutions from the numerical method for the value of the growth constant c in $R = 2cJa'\sqrt{t}$ are also given in Table 2.1.

The numerical and analytical results [70] lie within 2.5% of each other for the Ja' range from 3 to 100. The above values also compare reasonably well with values from several other references:

$c = 1.20$	Joshi [68]
$c = \sqrt{3/\pi} = 0.977$	Scriven [23]
$c = \sqrt{3/\pi} = 0.977$	Plesset and Zwick [71]
$c = \sqrt{\pi/2} = 1.253$	Forster and Zuber [72]

Values from the last three references are Ja' independent.

2.6.3 Flow-Field Due to Specified Growth Rate

The growth rate of the bubble was specified and vorticity was set to zero in the program in this test case. The solution from the program and the analytical solution $\bar{u} = \dot{\bar{R}} \bar{R}^2 / \bar{\tau}^2$ agreed within 1 percent.

2.7 Results

2.7.1 Thermophysical Properties and Dimensionless Parameters

Due to its industrial importance, water has been used as a model liquid for finding bubble growth characteristics. However, this should not be seen as restricting the utility of the present results, since all the terms in the governing equation that contain thermophysical similarity parameters (which carry the information on material properties) become negligible very soon after the initiation of growth. In particular, the two terms of the right hand side of Eq. (2.29) represent surface tension pressure and the inertial pressure respectively. The second term was found to be 4 to 6 orders

Table 2.2: Thermo-physical properties of water

Property	C	h_{fg}	R^*	α
Value	4220 J/kg/K	2256 kJ/kg	462 J/kg/K	$1.68 \times 10^{-7} \text{ m}^2/\text{s}$
Property	ρ	k	σ	
Value	958 kg/m ³	0.67918 W/m/K	0.0589 N/m	

Table 2.3: Non-dimensional parameters used in the second generation model

Parameter	π_1	π_2	π_3	π_4
Value	2.725×10^{-7}	5.746×10^{-3}	1.000884	1.948×10^{-2}
Parameter	We	Pr	ϵ_0	
Value	4.591×10^{-6}	1.0	6.8027×10^{-4}	

of magnitude smaller than the first. In Eq. (2.30), the two terms in the numerator represent rate of conduction heat transfer into the bubble and the rate of work required for the bubble to expand. The first term has been found to be 3 orders of magnitude larger than the second during the inertia controlled phase and 4 orders of magnitude larger during diffusion controlled growth. The $\frac{1}{2}\pi_1 We \dot{R}^2$ term in Eq. (2.30) represents the ratio of kinetic energy due to bubble growth to the latent heat, and was found to be 8 to 10 orders of magnitude smaller than unity.

The thermo-physical properties that were used are given in Table 2.2. h_{fg} has been assumed to be constant as its variation over the range of saturation temperature ($373 \pm 3 \text{ K}$) is less than a half percent. The initial radius of the bubble and P_∞ were selected to be 10^{-4} m and 101.32 kPa respectively. At $Ja = 20$ and $Sb = 0$, T_s and T_∞ were 380.41 K and 374.16 K respectively. As defined in Eq. (2.26), the non-dimensional parameters that were used are given in Table 2.3. Although Pr for water in the temperature range considered here is about 1.7, we elected to use the value of unity for Pr so that one boundary layer thickness could be used for both

the thermal and hydrodynamic fields about the bubble. This allows a greater degree of simplicity in the numerical algorithm. Later it will be shown that the effect of Pr on the predictions is extremely small.

2.7.2 Heterogeneous Boiling in an Inviscid Medium

Heterogeneous bubble growth in an inviscid medium was analyzed in order to compare the results of the much simpler inviscid flow model with those of the present viscous flow model so the utility of this simpler model can be examined.

Equations (2.27 – 2.33) were solved with Ω set to zero. Various cases with Ja ranging from 0.0001 to 300 and Sb ranging from -32 to 8 were analyzed. The extreme cases are chosen to make the various trends clear even though they may not have direct practical application. A 33×33 grid was used.

When the equation $R = \eta t^n$ was locally fitted to the growth curve, n was found to be close to $\frac{1}{2}$ (diffusion controlled growth) except in the beginning of the bubble's life in all cases. For example, n approached within 1 percent of $\frac{1}{2}$ at $t = 8.03$ for $Ja = 1$; whereas at $Ja = 1000$, it approached $\frac{1}{2}$ as early as at $t = 0.01$ for saturated boiling.

To find the dependence of η on Ja during the diffusion controlled growth period, the relation $\eta = c' Ja^m$ was tried. The value of m found using the relation

$$m = \frac{\log \eta_2 - \log \eta_1}{\log Ja_2 - \log Ja_1}$$

(where η_1 and η_2 are the values of η at Ja_1 and Ja_2 respectively), are depicted in Figure 2.14 with Ja as the abscissa. Note that a negative value of Sb represents superheated fluid while a positive value represents subcooled fluid. The figure shows that the value of m approaches 0.5 asymptotically as Ja is decreased in case of

Table 2.4: Bubble growth in heterogeneous saturated boiling

Ja	1	3	10	30	100	300
c , present results (inviscid, 33x33)	1.228	1.217	1.185	1.141	1.088	1.261
c , present results (viscous, 33x33)	1.476	1.473	1.531	1.612	1.821	
c , ref [68]		1.08	1.04	0.98	0.91	

boiling in superheated or subcooled fluid. In case of subcooled boiling, the value of m approaches zero asymptotically as Ja is increased; the more the subcooling, the smaller the value of m . In the case of superheated liquid, the plots diverge as Ja is increased. In this region, m grows linearly in Ja . Figure 2.8 shows the same values of m as in Figure 2.14, however with Sb as an abscissa. The contours at various Ja numbers cross at a common point $Sb = -0.0024$ and $m = 0.482 \pm 0.007$. It is believed that these values are not significantly different from 0 and $\frac{1}{2}$, respectively. This indicates that in the case of saturated boiling in an inviscid liquid, the radius grows according to the relation $R = c' \sqrt{Ja t}$, ($m = \frac{1}{2}$) in contrast with the homogeneous case where the dependence is proportional to Jakob number to the power unity. Values of c in $R = 2c \sqrt{Ja t}$ that were found during the asymptotic phase in case of saturated boiling are given in Table 2.4. At subcooling numbers other than zero however, the values of c varied from 0.33 to 2.72. Figure 2.9 shows the temperature contours around the bubble during the diffusion controlled period of growth at various values of subcooling and Jakob numbers. The ratio of R to δ in the figure is the same as that predicted by the computation. In all cases, the non-dimensional temperatures at the bubble surface, heated surface and infinity are zero, one, and $-Sb$ respectively. Note that point 'A' in some contour plots is a "saddle point". The direction of heat

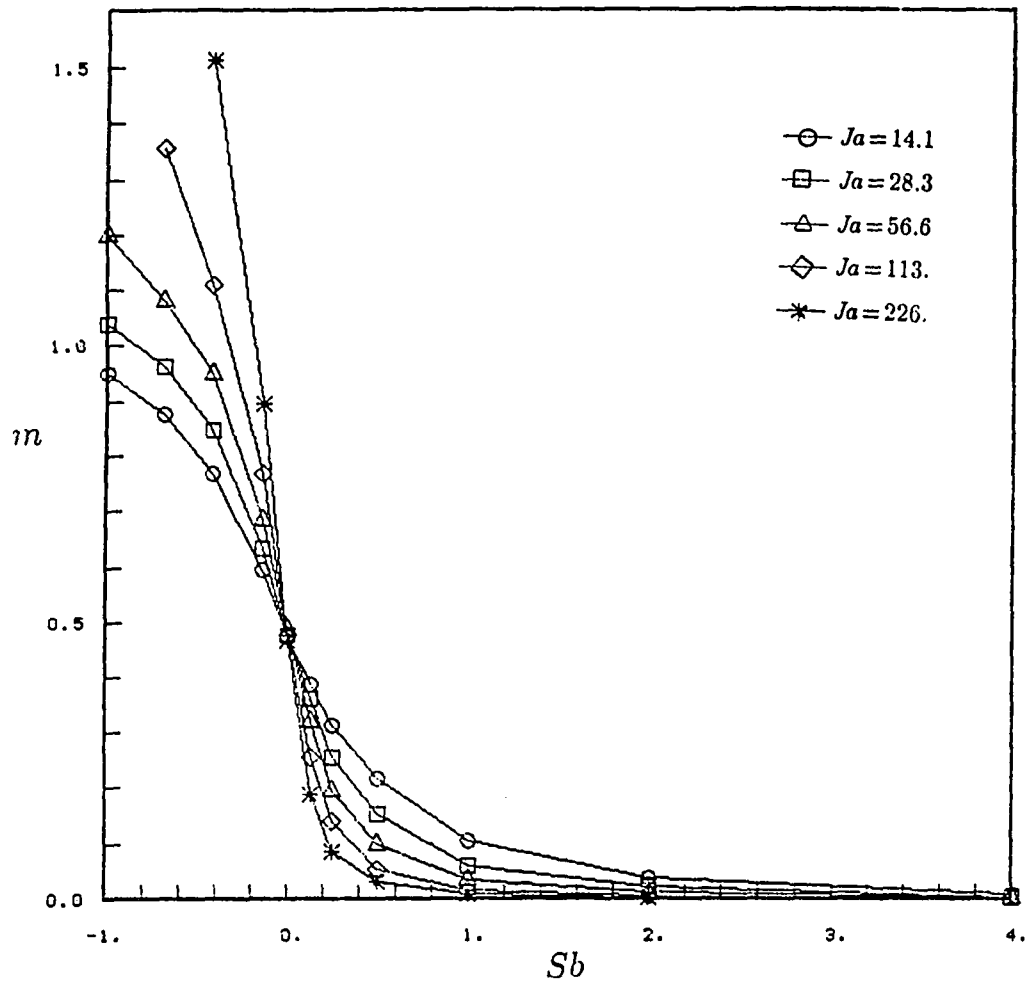


Figure 2.8: Exponent m versus subcooling number (inviscid medium)

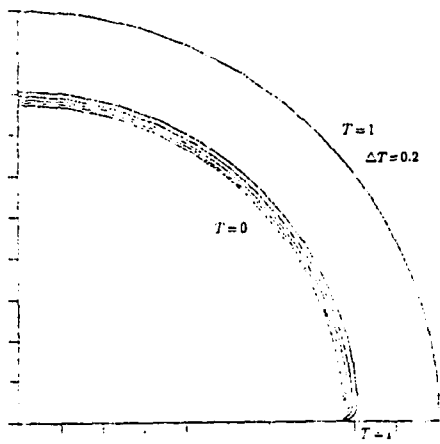
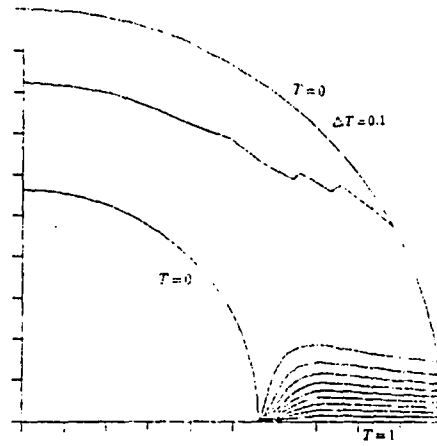
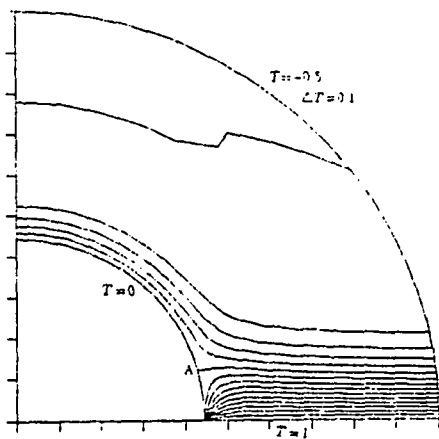
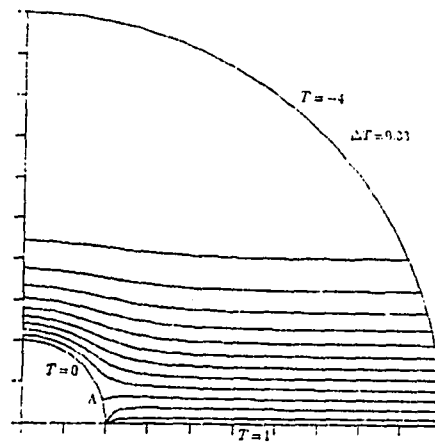
(a) $Ja=10, Sb=-1$ (b) $Ja=10, Sb=0$ (c) $Ja=10, Sb=0.5$ (d) $Ja=10, Sb=4$

Figure 2.9: Temperature contours around a bubble during diffusion controlled period of growth (Inviscid case)

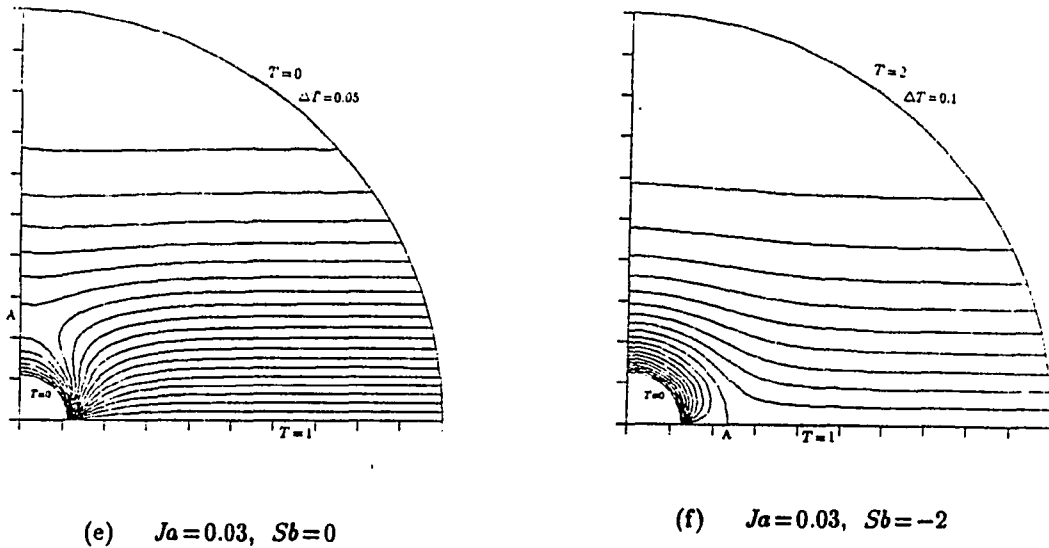


Figure 2.9 (Continued)

flow is opposite on either sides of the point. The direction of heat flow can be easily seen from Figure 2.10 in which temperature is plotted along the vertical (z) axis and the x - y plane forms the domain of computation ($Ja = 10, Sb = 0.25$). The temperature distribution away from the bubble where the velocity is negligible is close to that of a liquid of uniform temperature which is suddenly heated by a surface of constant temperature. This implies that the thickness of thermal boundary layer above the heated surface is proportional to the square root of time, and since the radius of bubble is also found to obey the same functional relation with time, the transformed domain has time-invariant boundary conditions, and hence the similarity solution.

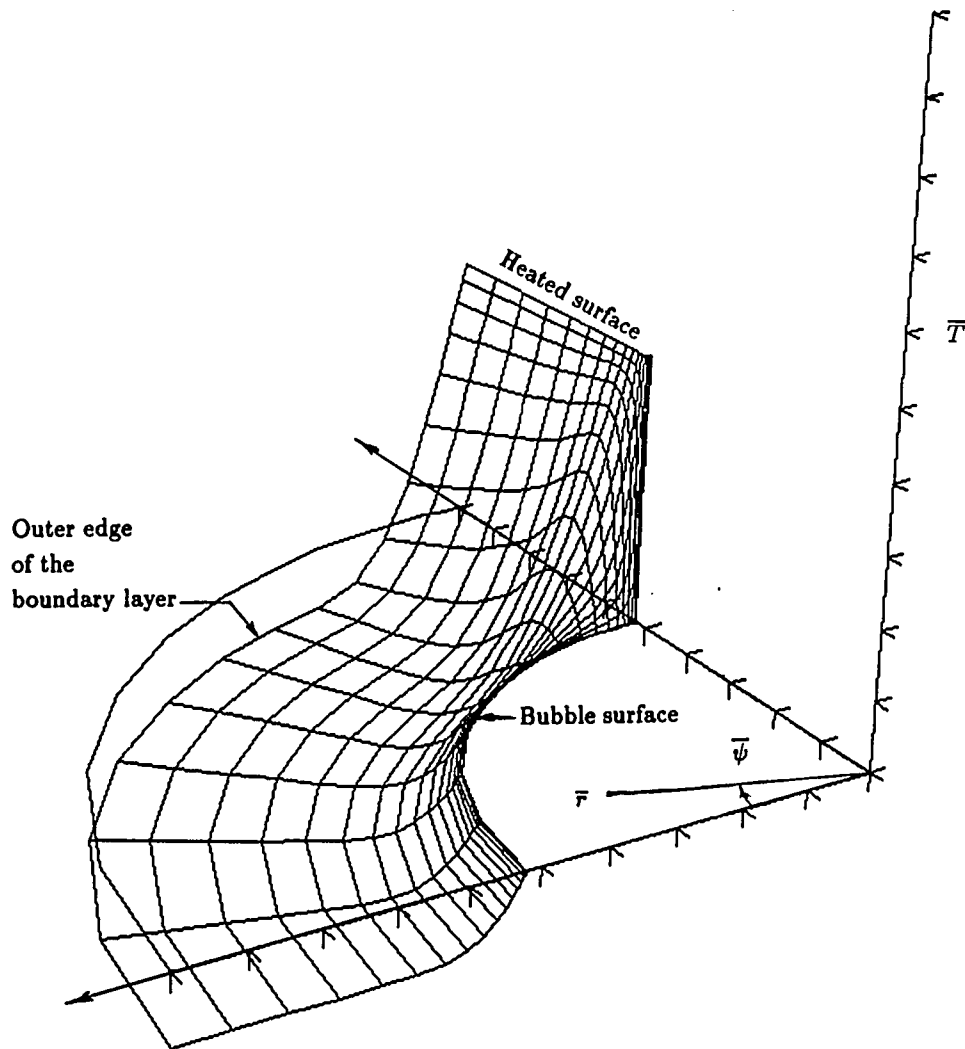


Figure 2.10: "Surface plot" of temperature against the computational domain, $Ja = 10$ $Sb = 0.25$, Inviscid case

2.7.3 Heterogeneous Boiling in a Viscous Medium

The boundary layer which exists along the heated surface in the viscous flow problem gives rise to a fundamental difference in the nature of flow as compared to the inviscid problem.

Bubble growth in viscous medium was analyzed for Ja ranging from 10 to 320 and Sb ranging from -1 to 4. Figure 2.11 and Figure 2.12 show plots of T and Ω at some selected points in the domain in a representative case of boiling ($Ja = 10$, $Sb = 0$).

The values of the two variables are seen to level off implying a similarity solution. In Figure 2.13, comparison is made of bubble growth in homogeneous medium and saturated growth on a surface in inviscid and viscous media. During the initial short period, \ddot{R} has been observed to depend on the initial bubble radius, the smaller the value of R_0 , the larger the value of \dot{R} . However, during the later period, the growth approached the relation $R = \eta \sqrt{t}$ in all cases.

The viscous predictions for the values of the growth exponent m are shown in Figure 2.14 along with those of inviscid fluid case. The values are somewhat larger compared to those of the inviscid medium; the trend of variation of m however, is seen to be the same. The major difference between inviscid case and the viscous case is that the no-slip condition at the heated surface gives rise to a velocity component in vertical direction which enhances convective mixing. At higher Ja , the growth rate and the additional mixing effect are larger, increasing the difference between the viscous and the inviscid case. A plot of m versus Sb for this case are shown in Figure 2.15. The coordinates of a common crossing point were found to be $Sb = 0.07$ and $m = 0.491 \pm .005$, and it is again concluded that $m = \frac{1}{2}$ when $Sb = 0$. Hence in the case of saturated boiling in viscous medium, the radius grows according to the

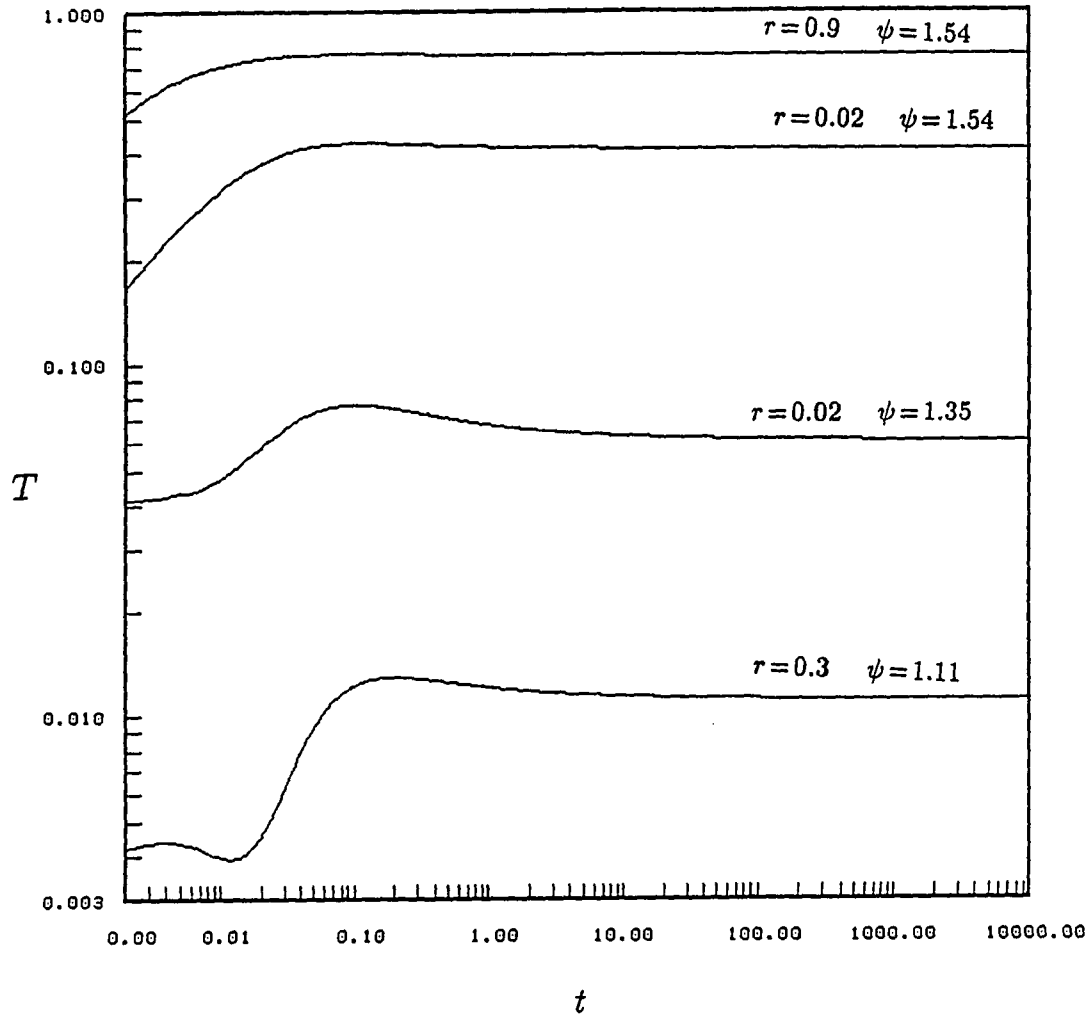


Figure 2.11: Asymptotic nature of temperature at various points in the computational domain against time, $Ja = 20$, $Sb = 0$, Grid size: 17×17 , Viscous case

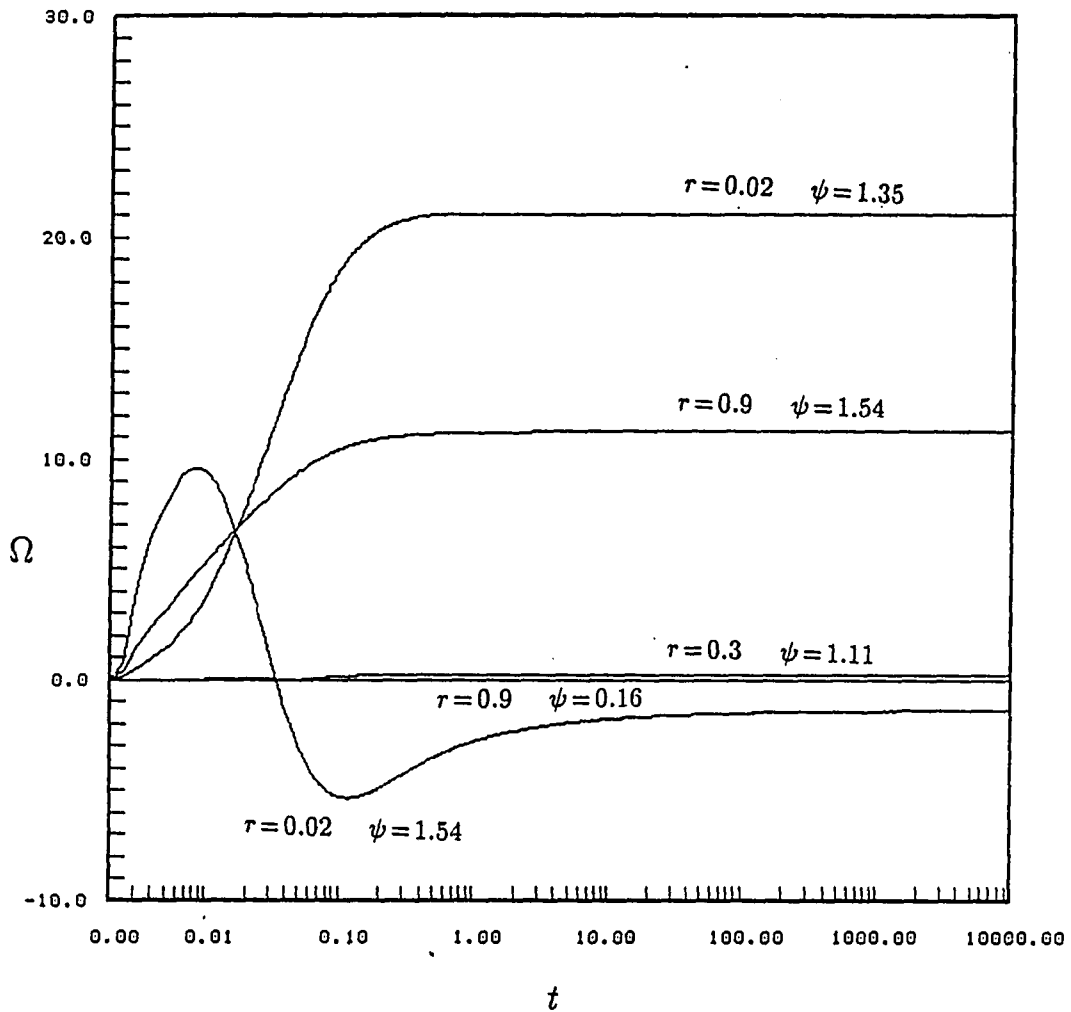


Figure 2.12: Asymptotic nature of vorticity at various points in the computational domain against time, $Ja = 20$, $Sb = 0$, Grid size 17×17 , Viscous case

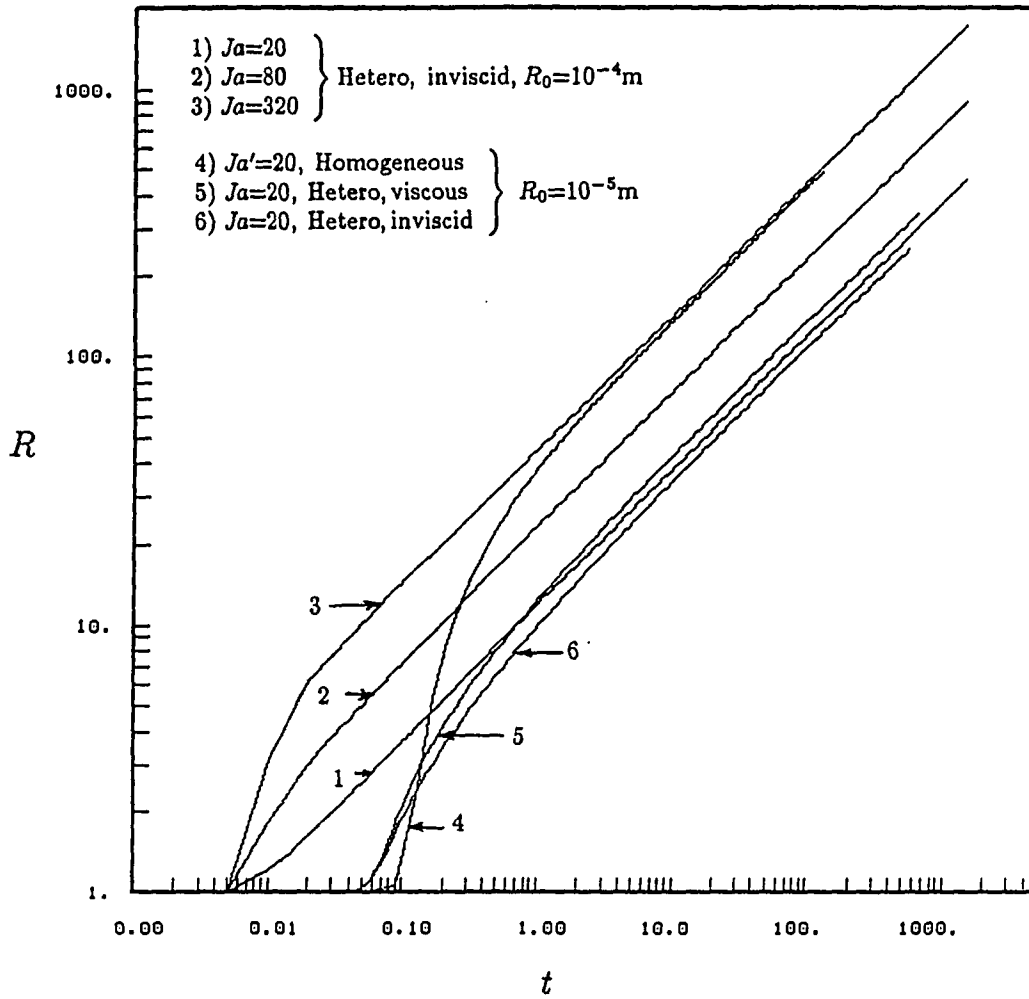


Figure 2.13: Comparison of bubble growth in viscous, inviscid, and homogeneous boiling

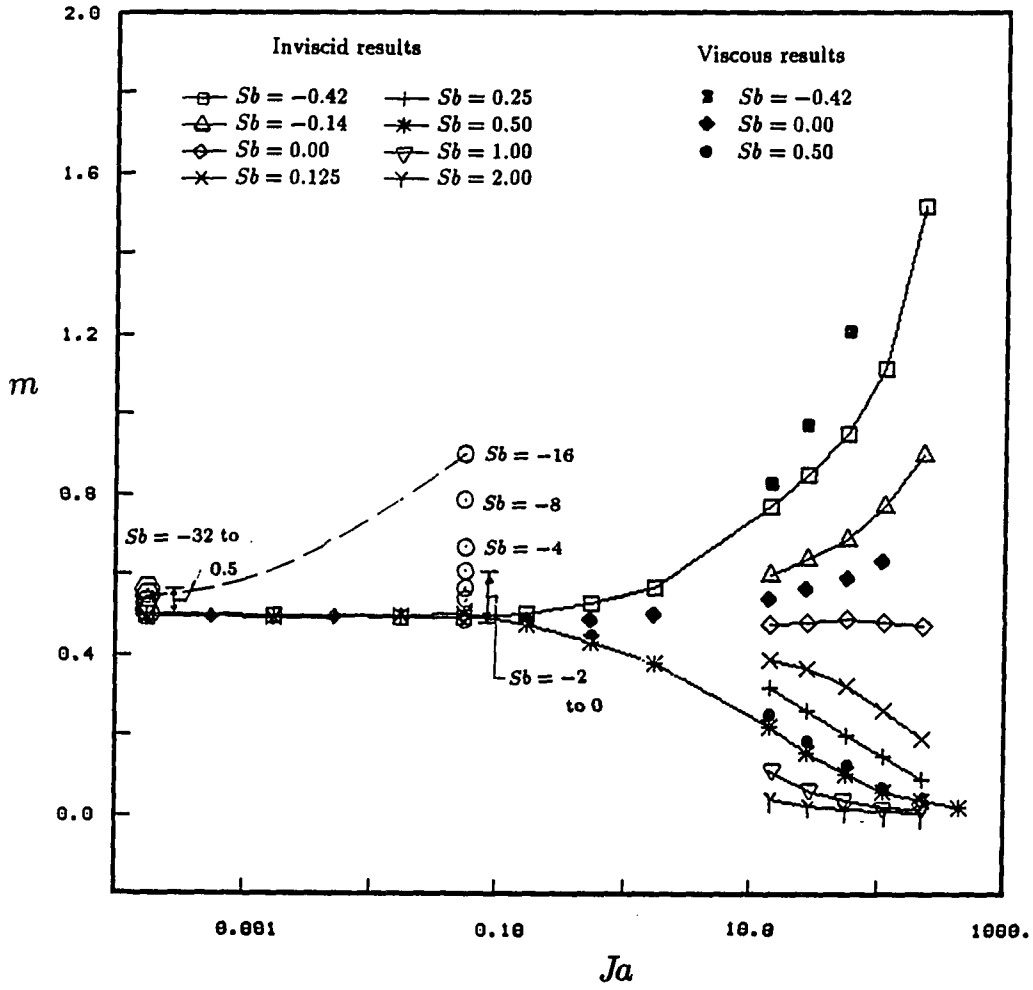


Figure 2.14: Exponent m in $R = 2c Ja^m \sqrt{t}$

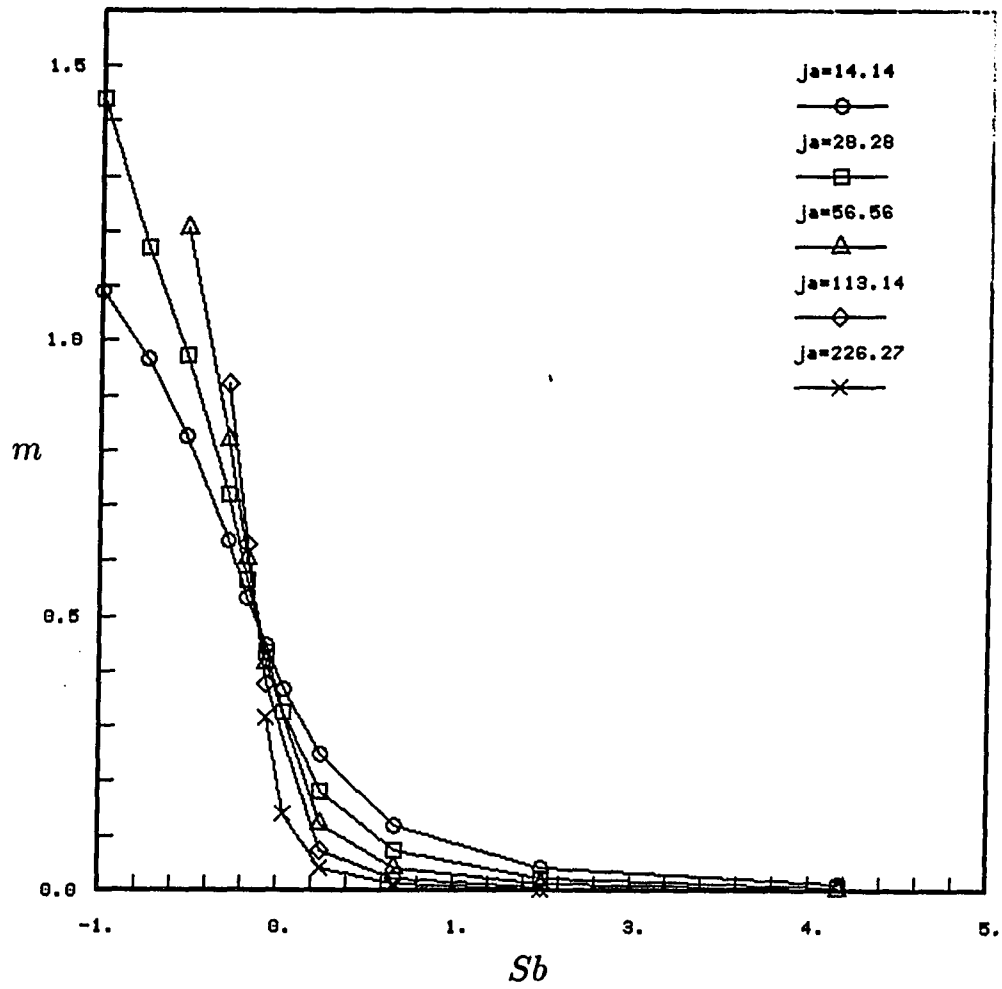


Figure 2.15: Exponent m versus subcooling number (viscous medium)

relation $R = 2c\sqrt{Ja t}$. Viscous values for c are given in Table 2.4.

The temperature, streamfunction and vorticity distribution obtained from the present numerical solution for viscous medium in the diffusion controlled phase (for bubble growth for saturated boiling at $Ja = 10$ and $Sb = .25$) is shown in Figure 2.16 to 2.18.

Note from Figure 2.16 that a uniform superheated layer surrounding the bubble was not observed in the second generation model as envisaged in the "bulk convection" theory discussed in Section 1.2.2. The heat transfer to the bubble is highly non-uniform around its periphery, with most of it occurring at the base.

The viscous and the inviscid results are compared in Figure 2.19. The ordinate $\eta = R/\sqrt{t}$ has been so chosen because the relation $R \sim \sqrt{t}$ has been found to describe the growth accurately except during the initial short period. The percent difference between the value of η from the viscous and inviscid results is shown in Table 2.5. Generally, for subcooled, saturated, and superheated boiling, the percent difference between viscous and inviscid values of η was of the order 5, 10, and 25 % respectively. The higher the Ja , the higher the percent difference in η , however, it was within 35 % for the cases covered in this study (see Table 2.5).

Comparison of the viscous and inviscid results in Figure 2.19 clearly shows that viscous effects are indeed fairly small - typically less than 10 to 20 % for moderate rates of boiling ($Ja < 100$), especially for the cases of subcooled liquid (which is more likely to be found in practice). Numerical experiments have been conducted directly on the effect of Pr . Computations with the viscous model using $Pr = 1, 1.7, 3, 10$ give almost identical results (difference between radius with $Pr = 1$ and $Pr = 10$ was within 0.03%) throughout the bubble life for the case $Ja = 20$ and $Sb = 0$.

Note that the heated surface is at higher temperature than the interior of the

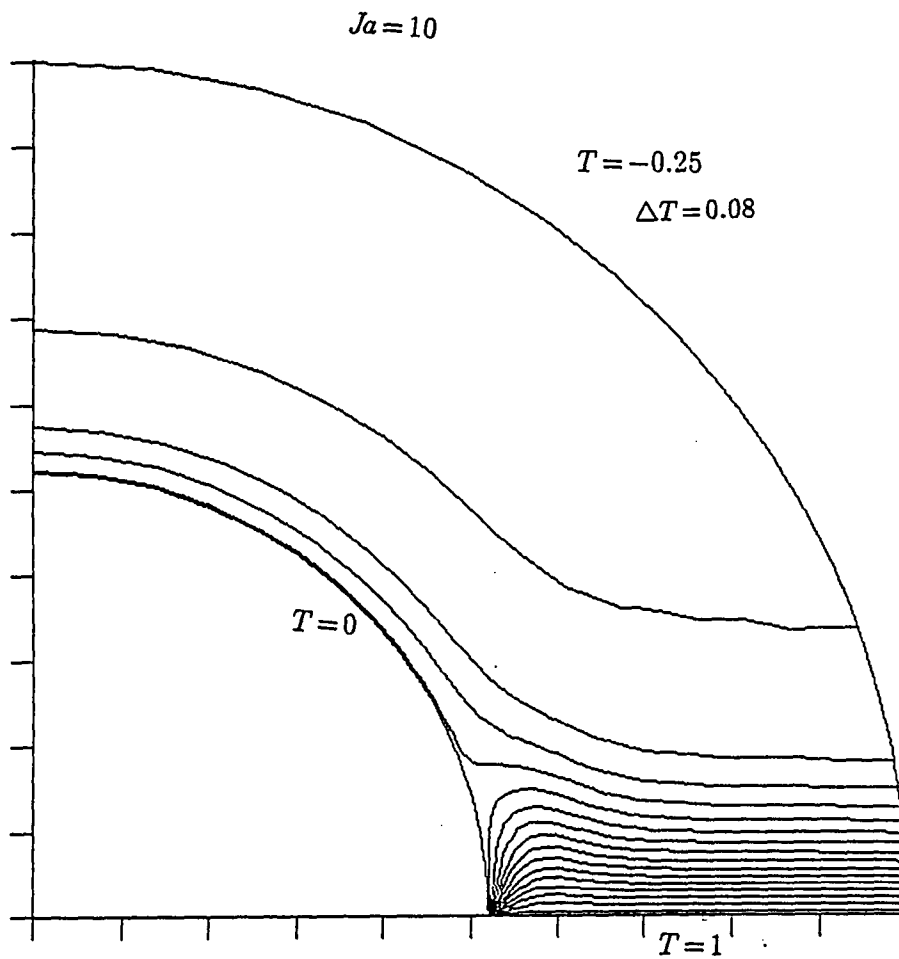


Figure 2.16: Temperature distribution in diffusion controlled phase, $Ja = 10$, $Sb = 0.25$, Viscous case

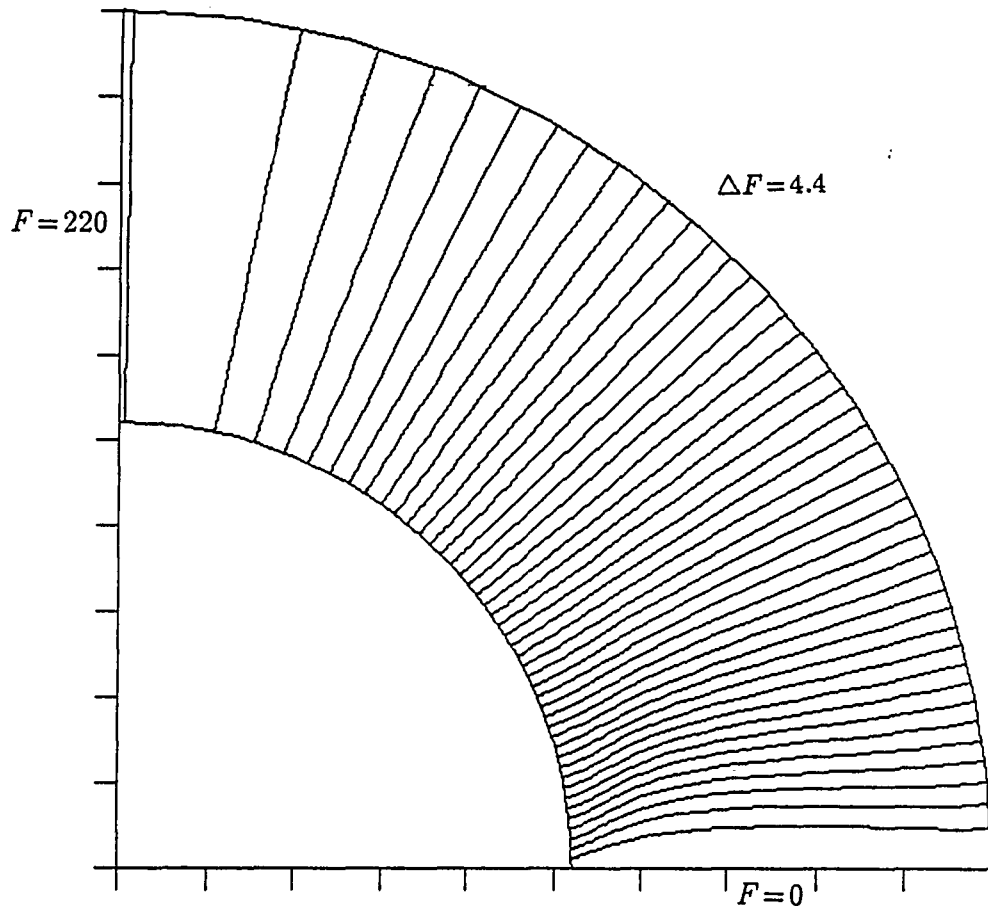


Figure 2.17: Streamfunction distribution in diffusion controlled phase, $Ja = 10$, $Sb = 0.25$, Viscous case

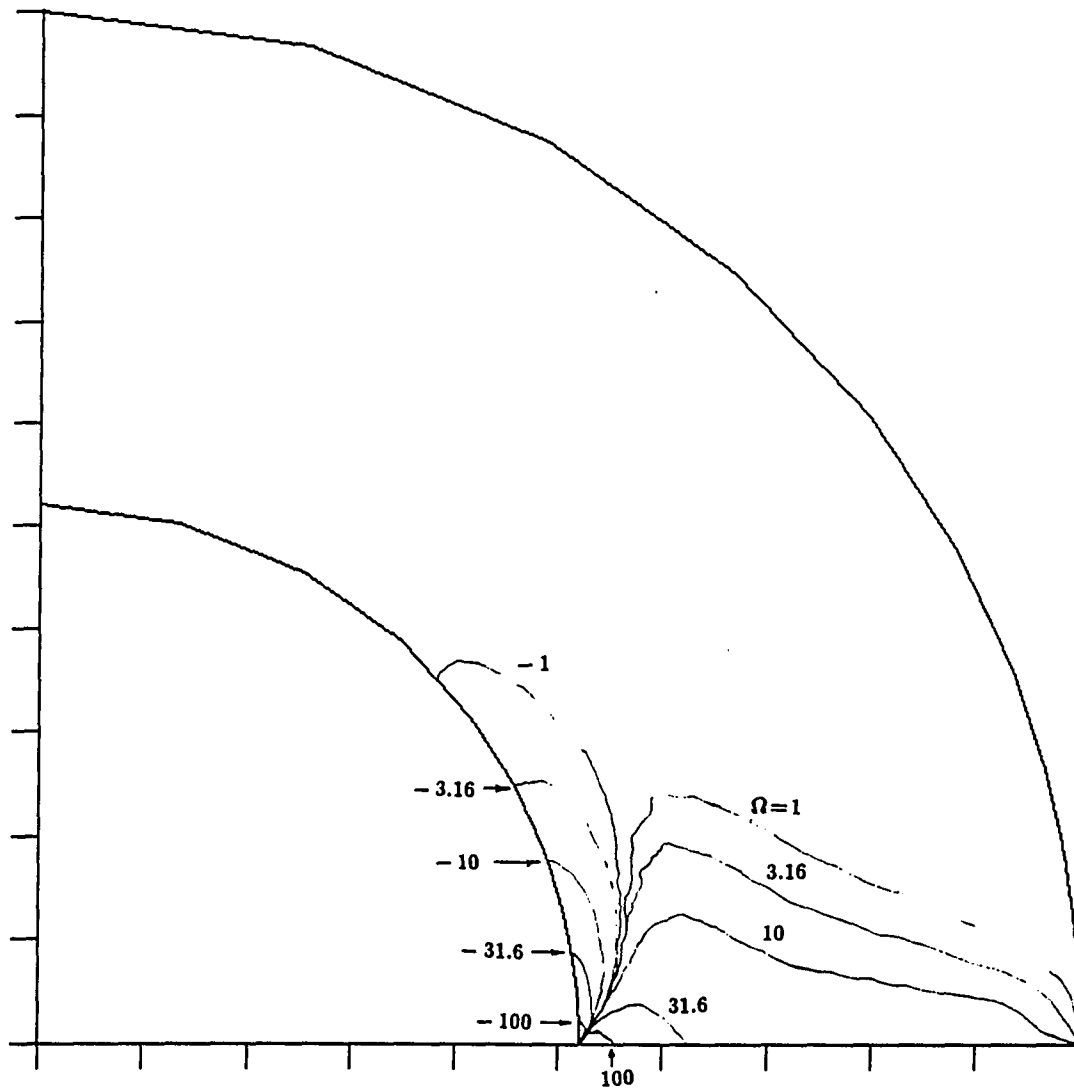


Figure 2.18: Vorticity distribution in diffusion controlled phase, $Ja = 10$, $Sb = 0.25$

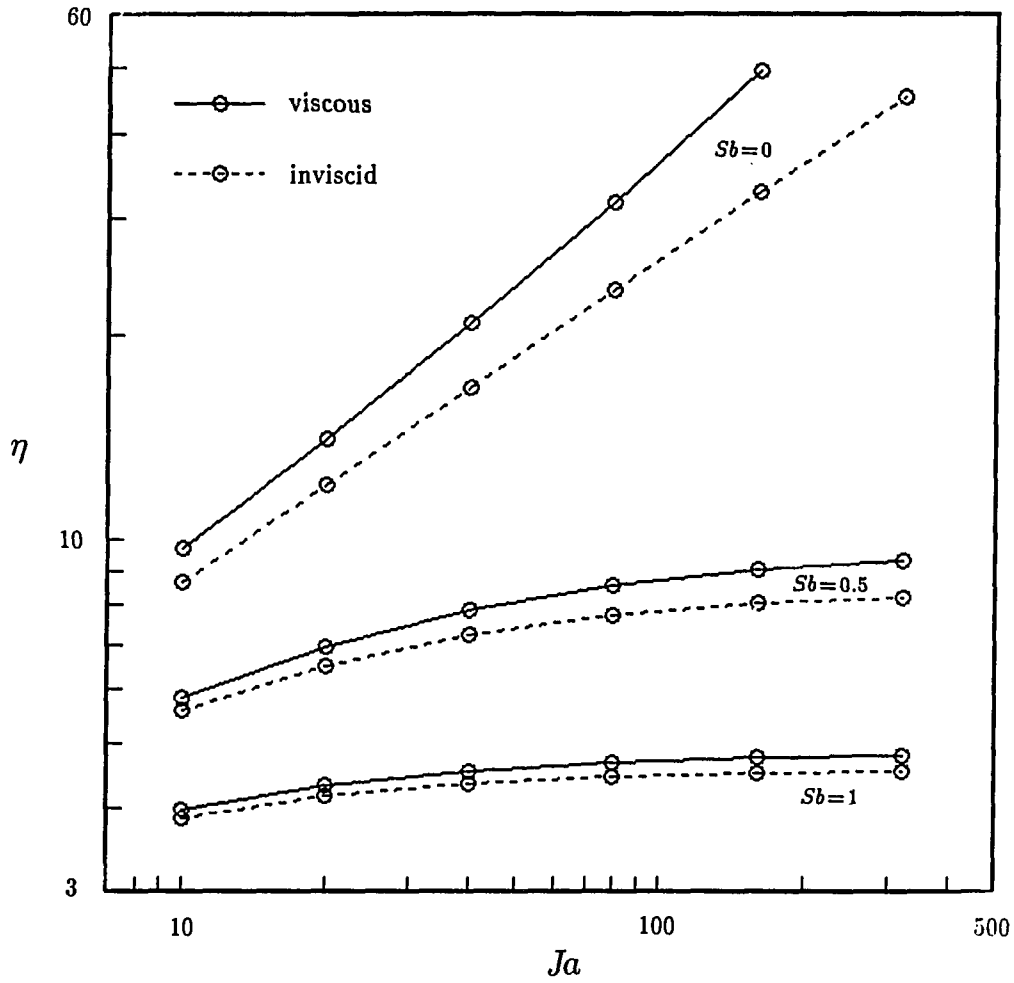


Figure 2.19: Comparison of the growth constants for viscous and inviscid cases

Table 2.5: The percent difference between the value of η from the viscous case and that from the inviscid case

Sb	$Ja \rightarrow$	10	20	40	80	160	320
-1.00		2.29	11.46	32.99	-	-	-
-0.69		2.33	8.17	20.55	-	-	-
-0.42		3.33	7.09	14.84	28.75	-	-
-0.14		5.25	7.98	13.25	20.83	28.72	-
0.00		7.84	11.74	17.04	23.58	31.20	-
0.125		8.27	12.02	16.52	21.82	28.12	34.18
0.25		8.56	11.99	16.11	-	23.79	26.55
0.50		3.99	6.03	8.03	9.59	10.77	11.45
1.00		2.82	3.74	4.48	4.91	5.26	5.35
2.00		2.82	2.90	2.96	2.95	2.98	2.98
4.00		4.08	4.16	4.21	4.23	-	-

bubble. The natural convection inside the bubble due to temperature gradients within it has been examined in Appendix A. For this purpose, a bubble of constant size has been assumed, and the set of transient Navier-Stokes equations have been solved. The maximum velocity in the bubble due to natural convection has been found to be extremely negligible, of the order 10^{-8} m/sec, which is about 8 orders of magnitude smaller than the rate of growth of radius. The dynamic pressure due to the velocity ($P = \rho v \frac{u^2}{2}$) was of the order 10^{-17} Pa, which is extremely small. The temperature distribution is completely governed by conduction as opposed to convection. Further, the time required to arrive at the steady state was found to be much larger than the bubble life time, and hence the above numbers, for maximum velocity and the dynamic pressure, are lesser during the life time of the bubble. It is argued in Appendix A that these findings indicate that the bubble must be at a uniform state.

2.8 Comparison with Available Experimental Data

The present computational viscous case results for saturated boiling are also compared in Figure 2.20 with observed data of from the literature. As mentioned before, the thermophysical similarity parameters drop out of the equations during this period and hence the growth characteristics are a function only of Ja and Sb . Each discrete point is an experimental finding from the literature representing growth of a single bubble. The description of the experimental points is given in Table 3.6. The value of η for the experimental data was found from the parabola of best fit using a regression analysis with help of a computer program. The regression analysis was done as follows. The experimental points in the diffusion controlled region of growth were chosen (since the inertia controlled growth period is extremely short, the above choice was not difficult). Subsequently, a linear regression was performed with R^2 as ordinate and t as the abscissa. The slope of the line of best fit is thus the growth constant η . The underprediction of the computational results (specially for $Ja > 20$) by a factor 1.5 to 2.5 may be due to the contribution to growth by a microlayer which was not accounted for in the present computational model. It is of interest to note that the disagreement between the computational and the experimental results is larger at larger Ja , and this condition favors microlayer formation.

2.9 Conclusions

The following conclusions can be drawn from the second generation model.

- Thermophysical similarity parameters which contain information on the material properties of the liquid are important only during the brief, initial period

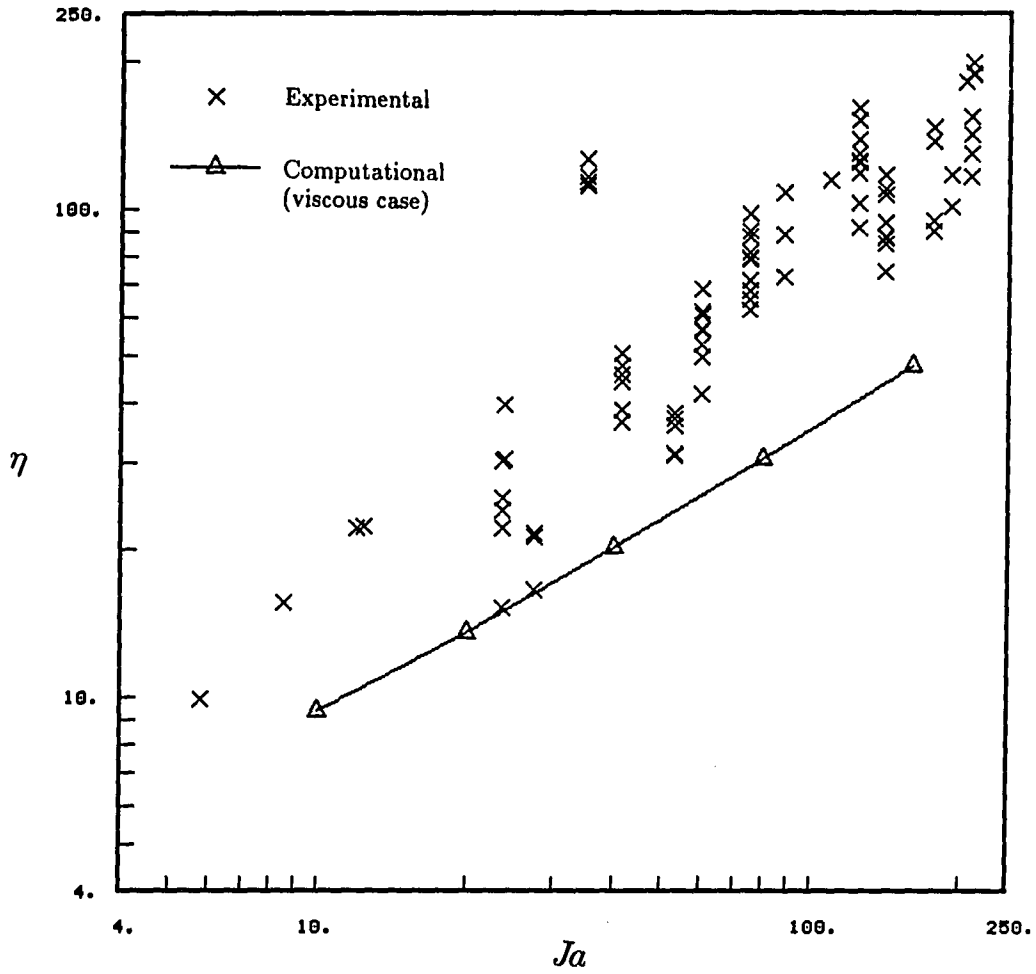


Figure 2.20: Comparison between experimental data from the literature and the predictions from the second generation model

of inertial bubble growth.

- An asymptotic nature (valid for $t \gg 1$) for the problem of hemispherical bubble growth on a heated surface in viscous as well as inviscid medium is identified. In this growth regime, only Ja and Sb affect bubble growth.
- Pr effect in the range $1 \leq Pr \leq 10$ is negligible for saturated boiling in viscous fluid at $Ja = 20$.
- The growth constant η for the viscous case was typically 2 to 35% larger than for the inviscid case. The smaller the Jakob number, and the larger the subcooling number the smaller the difference between the viscous and inviscid results.
- More generally, for asymptotic bubble growth in an inviscid or viscous medium the values of m in $R = 2c Ja^m \sqrt{t}$ are found to observe the following rules:
 1. In the case of growth in subcooled medium, m is generally less than 0.5, and approaches zero as Ja and/or Sb is increased.
 2. In the case of growth in superheated medium, m is generally larger than 0.5 and m increases linearly with Ja .
 3. In the case of bubble growth in either subcooled or superheated medium, m approaches 0.5 as Jakob number is decreased.
- The asymptotic behavior for saturated bubble growth in an inviscid or viscous medium is seen to approximately obey the growth rule:

$$R = 2c\sqrt{Ja t}$$

The values of c were found to be mild functions of Ja and clustered around a value of 1.2 in saturated boiling.

- The maximum velocity due to natural convection inside the bubble was found to be 8 orders of magnitude smaller than the rate of growth of the bubble radius.

3. THE THIRD GENERATION MODEL OF BUBBLE GROWTH

The second generation model neglected the microlayer contribution and comparison with experimental results showed that the model underpredicted the value of bubble growth (more so at $Ja > 20$). At large Jakob numbers, the growth rates are larger and the conditions favor microlayer formation.

It has been discussed in Section 2.3.2 of Chapter 2 that the initial pressure of the bubble is higher than the liquid pressure by an amount equal to the excess pressure by the curved bubble surface. Therefore, the initial temperature of the bubble, which is the saturation temperature, must be higher than the liquid temperature in absence of a non-condensable gas. Such a model (second generation model) thus corresponds to a mechanical equilibrium between the bubble and the surrounding liquid, but not a thermal equilibrium at $t = 0$. In the third generation model, some non-condensable gas is assumed to be present in the bubble, which causes the vapor pressure and the vapor temperature to lower and thus allows for both these equilibria. The initial temperature of the vapor (T_i) is thus the same as that of the surrounding fluid in this model.

From the analyses of Beer et al. (copper and steel) [73] it is clear that heated surface is not at uniform temperature during the bubble growth. There are considerable temperature gradients in the heated surface even with highly conductive surfaces

such as copper. The surface temperature is seen to drop [73] [7] [8] [11] [10], particularly close to the bubble, where the local heat flux is larger. The third generation model includes the formulation of transient conduction in the heated surface.

Thus, the following three assumptions of the previous model have been *removed* in this model, thus making the model more general. These are:

- negligible microlayer evaporation
- heated surface at uniform temperature
- bubble of *pure* vapor.

A schematic for the third generation model is shown in Figure 3.1. For the computation over the liquid around the bubble, the same formulation as in the second generation model has been used in this model. The governing equations for the microlayer, heated surface, and for the vapor and non-condensable gas mixture are then added to the algorithm of the second generation model.

3.1 Microlayer

Figure 3.2 shows a schematic of a microlayer. $\bar{\delta}_0$ is the height of the microlayer at the point of formation. \bar{z} denotes the height of the microlayer at an arbitrary radius. \bar{r}_d denotes the dry radius, i.e. the radial distance from the center over which the microlayer has dried. Since the upper surface of the microlayer undergoes evaporation, it is assumed to be at the vapor temperature, which is the saturation temperature at vapor pressure. The thermal capacity of the microlayer is neglected [7]. The temperature gradient in the microlayer can be related to the rate of its

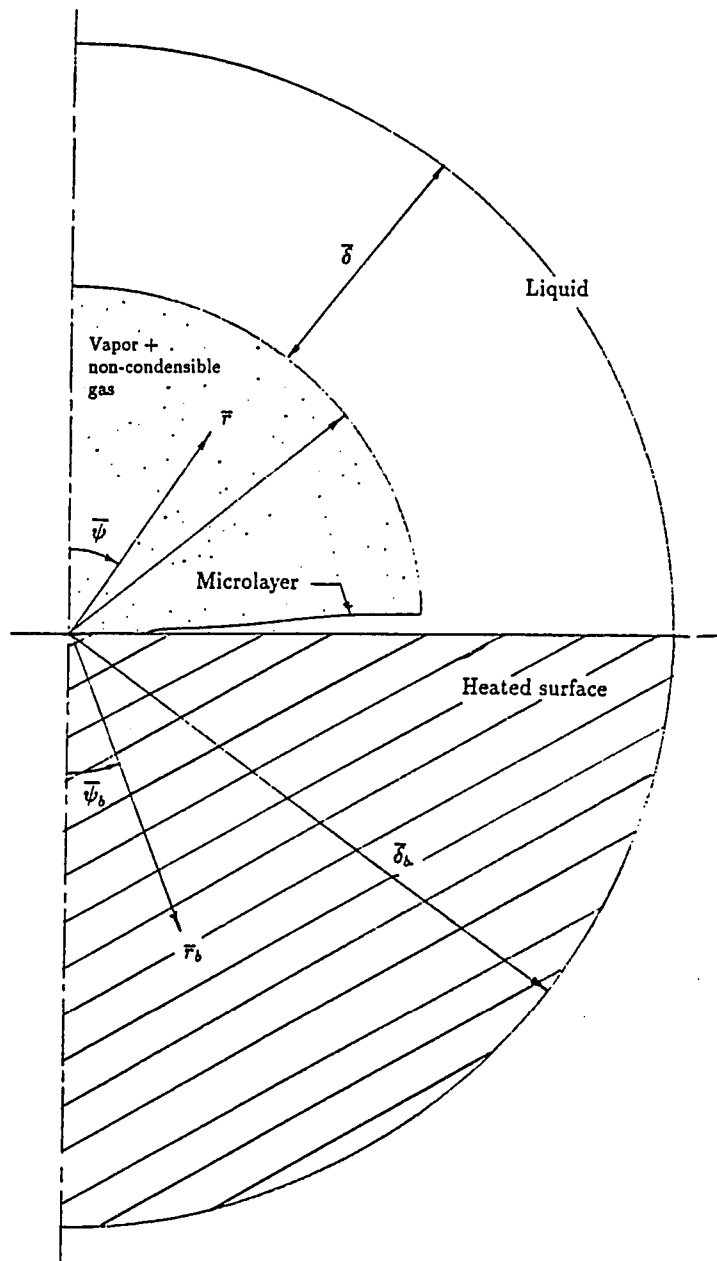


Figure 3.1: The third generation model in physical coordinates

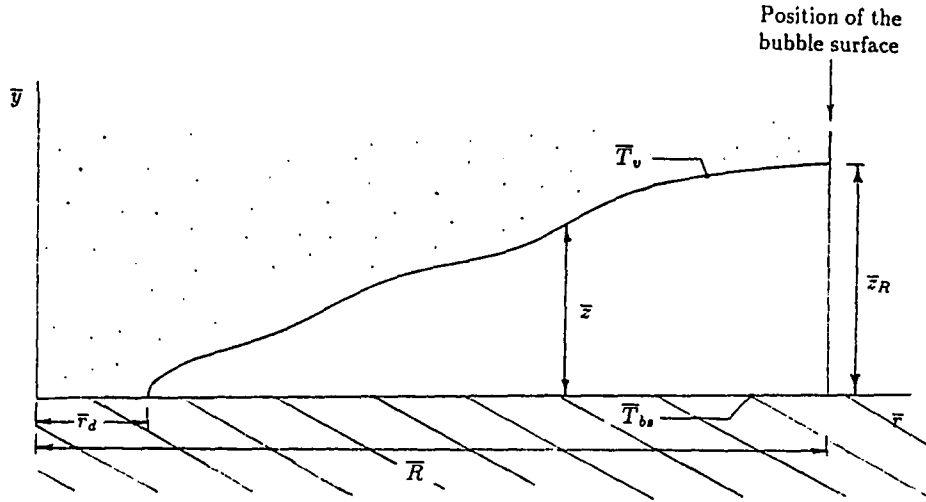


Figure 3.2: Schematic of a microlayer

evaporation by a heat balance:

$$\frac{\partial \bar{z}}{\partial \bar{t}} \rho h_{fg} = \frac{k}{\bar{z}} (\bar{T}_v - \bar{T}_{bs}) \quad \bar{z} \geq 0 \quad (3.1)$$

where \bar{T}_{bs} denotes the temperature of the heated surface immediately below the microlayer. Eq. 3.1 is the governing equation for the microlayer evaporation. Note that \bar{R} , \bar{r}_d , T_v are functions of time (\bar{t}) while \bar{z} , and \bar{T}_{bs} are functions of both time (\bar{t}) and radius (\bar{r}).

The following formula for the formation thickness of the microlayer has been suggested by many researchers [7] [19] [74] [17] [32] [22]

$$\bar{\delta}_o = C_z \sqrt{\nu \bar{t}_g} \quad (3.2)$$

where \bar{t}_g is the time elapsed after the beginning of growth, and C_z is a constant, the value of which has been reported to be ranging from 0.3 to 1.3. Since the exact value

of C_z was not known, C_z was parametrically varied in the present study, the details of which are discussed in Section 3.11.

3.2 Heated Surface

To solve for the temperature distribution in the heated surface, the heat equation is used:

$$\frac{\partial \bar{T}_b}{\partial t} = \alpha_b \left[\frac{1}{\bar{r}_b^2} \frac{\partial}{\partial \bar{r}_b} \left(\bar{r}_b^2 \frac{\partial \bar{T}_b}{\partial \bar{r}_b} \right) + \frac{1}{\bar{r}_b^2 \sin \bar{\psi}_b} \frac{\partial}{\partial \bar{\psi}_b} \left(\sin \bar{\psi}_b \frac{\partial \bar{T}_b}{\partial \bar{\psi}_b} \right) \right] \quad (3.3)$$

The boundary conditions for this equation are discussed in Section 3.4.

3.3 Vapor and the Non-condensing Gas in the Bubble

3.3.1 Initial State

As discussed before, thermal *and* mechanical equilibrium between the hemispherical bubble and the environment at initial state can only be achieved if some non-condensable gas is present along with the vapor. Note that if the bubble formation began at a microscopic crevice, then the vapor-fluid interface can be flat at the initial state and hence the pressure difference across the bubble surface can be zero. In that case, the presence of non-condensable gas is not a necessary condition for thermal and mechanical equilibrium. However, in the present model, with a hemispherical bubble at an initial state, presence of non-condensable gas is a necessary condition. The temperature of the non-condensable gas is assumed to be the same as that of the of the vapor, denoted by (\bar{T}_v) .

Given the initial bulk fluid temperature (T_i) , the vapor partial pressure at the

initial state ($P_{\text{sat}}(T_i)$) is the saturation pressure at T_i . Initial bubble pressure is given by $P_{B,o} = P_{\infty} + 2\sigma/R_0$. The last term in this equation arises due to the curvature of the bubble surface. If the bulk fluid is saturated or subcooled, i.e. if $T_i \leq T_{\text{sat}}(P_{\infty})$ (Figure 3.3), then it follows that P_{∞} must be greater than or equal to $P_{\text{sat}}(T_i)$. Following these facts, the initial partial pressure of non-condensable gas ($P_{g,o}$), necessary for equilibrium is,

$$P_{g,o} = P_{B,o} - P_{\text{sat}}(T_i).$$

And therefore,

$$P_{g,o} = P_{\infty} + \frac{2\sigma}{R_0} - P_{\text{sat}}(T_i).$$

In general T_i is less than $T_{\text{sat}}(P_{B,o})$. For saturated boiling, $T_i = T_{\text{sat}}(P_{\infty})$. $P_{v,o}$, the initial partial pressure of the vapor is defined as the saturation pressure at T_i , which is $P_{\text{sat}}(T_i)$. Thus the initial vapor fraction is given by

$$x_{v,o} = \frac{P_{v,o}}{P_{\infty} + 2\sigma/R_0}.$$

At the initial state, the vapor variables have the following values:

$$\bar{P}_B = P_{\infty} + \frac{2\sigma}{R_0}$$

$$\bar{x}_v = x_{v,o}$$

$$\bar{T}_v = T_i$$

$$\bar{\rho}_v = \rho_{v,\text{sat}}(T_i)$$

$$\bar{N}_v = N_{v,o}$$

$$\bar{P}_{l,o} = P_{\infty}$$

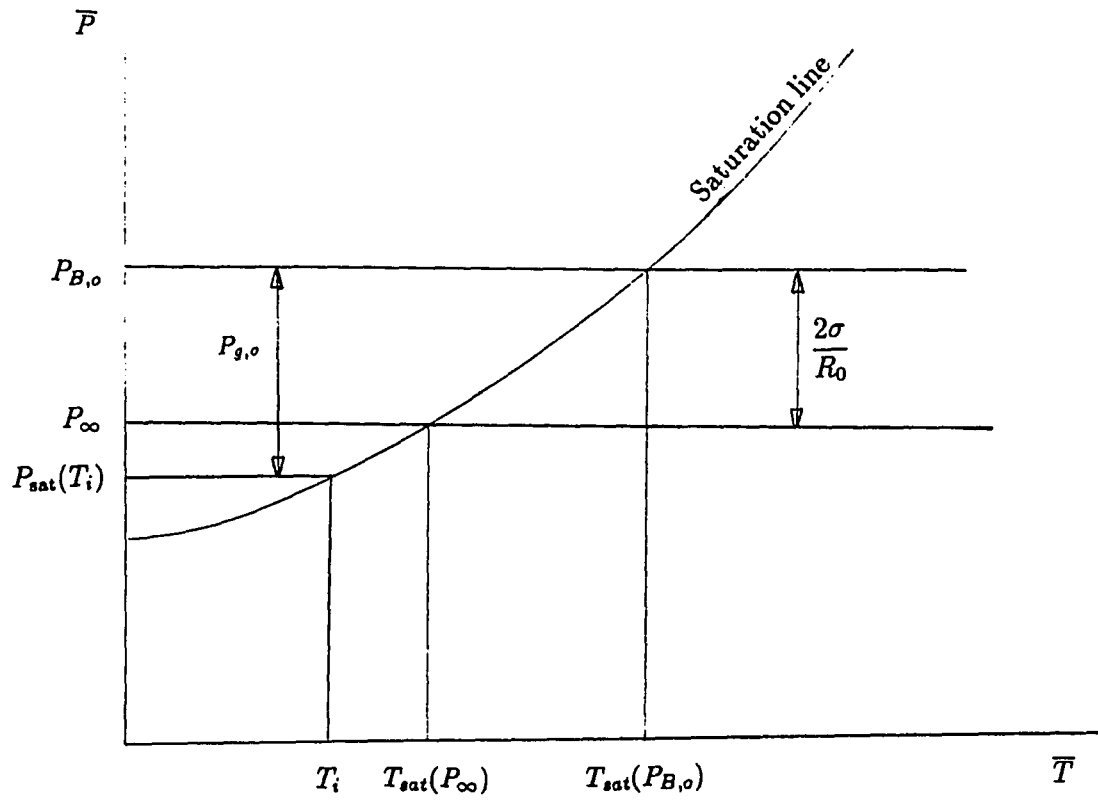


Figure 3.3: Illustration for the necessity of non-condensable gas in a bubble at the initial state

3.3.2 Governing Equations

3.3.2.1 The vapor and the non-condensable gas in the bubble The vapor density is given by the ideal gas relation

$$\bar{\rho}_v = \frac{\bar{P}_v}{R^* \bar{T}_v}. \quad (3.4)$$

The vapor temperature (which is also the bubble temperature) is found by integrating the Clapeyron-Clausius equation,

$$\frac{T_{vo}}{\bar{T}_v} = 1 - \frac{R^* T_{vo}}{h_{fg}} \ln \left(\frac{\bar{P}_v}{P_{vo}} \right). \quad (3.5)$$

The rate of increase of number of moles of vapor is found from the total rate of evaporation,

$$\dot{\bar{N}}_v = \dot{\bar{m}}_t / \mathcal{M}_v \quad (3.6)$$

Where \mathcal{M}_v is the molecular weight of the vapor.

Assuming that the vapor and the non-condensable gas behave as an ideal gas mixture, the partial pressure of the vapor is found using

$$\bar{P}_v = x_v \bar{P}_B \quad (3.7)$$

where $x_v = \bar{N}_v / (\bar{N}_v + N_{go})$, where N_{go} is the initial number of moles of the non-condensable gas.

The total number of moles of vapor is found from integrating the rate of addition of vapor moles,

$$\bar{N}_v = \int_0^{\bar{t}} \dot{\bar{N}}_v d\bar{t} + N_{vo} \quad (3.8)$$

3.3.2.2 Mass, momentum and energy balance The details of mass, momentum, and energy balance on an infinitesimal control volume containing vapor-liquid interface are shown in Appendix B and only the final results are presented in this section.

From the mass balance,

$$\dot{\bar{m}}_t = \bar{\rho}_g 2\pi \bar{R}^2 \dot{\bar{R}} + \frac{2}{3}\pi \bar{R}^3 \dot{\bar{\rho}}_v. \quad (3.9)$$

The relation between the bubble pressure and the liquid pressure just outside the bubble is got from the momentum balance

$$\bar{P}_B - \hat{P}_{l0} = \frac{2\sigma}{\bar{R}} - \frac{1}{\bar{\rho}_g} \left(\frac{\dot{\bar{m}}_c}{2\pi \bar{R}^2} \right)^2. \quad (3.10)$$

The first term on the right hand side is the pressure due to the curvature of the bubble and the second term is the dynamic pressure that arises due to the influx of vapor mass into the bubble. Note that $\dot{\bar{m}}_t$ represents the *total* mass flow into the bubble, i.e., including the flow from the cap and the microlayer. $\dot{\bar{m}}_c$ is the mass flow rate through the cap portion only.

The total rate of evaporation at the vapor-liquid interface is given by the energy balance

$$\dot{\bar{m}}_t = (\bar{q}_c + \bar{q}_m) / h_{fg}. \quad (3.11)$$

3.4 Boundary Conditions

At the initial state, the liquid is assumed to be at a uniform temperature T_i and the solid at a uniform temperature T_h . A quick order of magnitude calculation will reveal that the latent heat content of a hemispherical bubble is approximately

half that of the sensible heat content of a hemispherical portion of the heated surface of the same radius with $T_h - T_i$ equal to a typical value of 10 °C. This indicates that the heat content of the heated surface is sufficient to provide energy for the bubble growth. From the analyses of various researchers [73] [7] [8] [11] [10] it is clear after the departure of a bubble that the heat diffusion in the heated surface is very quick and the heated surface regains its superheat temperature almost instantaneously. After the departure of a bubble, its place is taken by fluid at the bulk temperature [28] [58] [25] [26]. From these findings, it follows that the far field boundary conditions for the liquid region and the solid region for a finite value of time are the solutions to the following conduction equations,

$$\frac{\partial \bar{T}_l}{\partial \bar{t}} = \alpha_l \frac{\partial^2 \bar{T}_l}{\partial \bar{y}^2} \quad \bar{y} > 0 \quad (3.12)$$

$$\frac{\partial \bar{T}_b}{\partial \bar{t}} = \alpha_b \frac{\partial^2 \bar{T}_b}{\partial \bar{y}^2} \quad \bar{y} \leq 0 \quad (3.13)$$

where \bar{T}_l and \bar{T}_b are the temperatures of liquid and heated surface respectively. The initial and the boundary conditions for the above equations are

$$\bar{T}_l = T_i, \quad \bar{y} > 0, \quad \bar{T}_b = T_h, \quad \bar{y} \leq 0 \quad \text{at } \bar{t} = 0$$

$$\bar{T}_l \rightarrow T_i \quad \text{as } \bar{y} \rightarrow \infty, \quad \bar{T}_b \rightarrow T_h, \quad \text{as } \bar{y} \rightarrow -\infty \quad \bar{t} > 0$$

At the interface between liquid and the heated surface, temperature gradients and the temperatures of the two regions are matched

$$\left. \begin{array}{l} \bar{T}_l = \bar{T}_b \\ k_l \frac{\partial \bar{T}_l}{\partial \psi_l} = -k_b \frac{\partial \bar{T}_b}{\partial \psi_b} \end{array} \right\} \quad \bar{R} \leq \bar{r} \leq \bar{R} + \bar{\delta}_b, \psi_l = \frac{\pi}{2}$$

At the junction between the microlayer and the heated surface, the temperature gradients, and the temperature in the microlayer and that in the heated surface are matched:

$$\left. \begin{aligned} k_l \frac{\bar{T}_{bs} - \bar{T}_v}{z} &= -\frac{k_b}{\bar{r}} \frac{\partial \bar{T}_b}{\partial \psi_b} \\ \bar{T}_{bs} &= \bar{T}_b \end{aligned} \right\} \quad \bar{R} \leq \bar{r} \leq \bar{R} + \bar{\delta}_b, \psi_b = \frac{\pi}{2}$$

Since the left hand side of the former of the above equations represents the heat flux, it is written in terms of the depletion of volume of the microlayer

$$d\dot{V}_m h_{fg} \rho_l = -2\pi d\bar{r} k_b \frac{\partial \bar{T}_b}{\partial \psi_b}$$

integration of which yields

$$\dot{V}_m = \frac{-2\pi k_b}{h_{fg} \rho_l} \int_{\bar{r}_d}^{\bar{R}} \frac{\partial \bar{T}_b}{\partial \psi_b} d\bar{r} \quad (3.14)$$

where \dot{V}_m is the rate of decrease of volume of the microlayer due to evaporation. The total rate of heat flow (\bar{q}_m) and the corresponding rate of decrease of mass (\dot{m}_m) of the microlayer are given by

$$\bar{q}_m = \dot{V}_m h_{fg} \rho_l \quad \text{and} \quad \dot{m}_m = \dot{V}_m \rho_l \quad (3.15)$$

The rate of evaporation of the liquid at the cap is found from

$$\dot{V}_c = \frac{2\pi \bar{R}^2 k_l}{h_{fg} \rho_l} \int_0^{\frac{\pi}{2}} \frac{\partial \bar{T}_l}{\partial \bar{r}} \sin \bar{\psi} d\bar{\psi} \quad (3.16)$$

Hence the total rate of heat flow (\bar{q}_c) and the corresponding rate of flow of mass (\dot{m}_c) into the bubble at the cap portion are given by

$$\bar{q}_c = \dot{V}_c h_{fg} \rho_l \quad \text{and} \quad \dot{m}_c = \dot{V}_c \rho_l \quad (3.17)$$

Due to the axial symmetry in the problem the boundary conditions at the symmetry line are

$$\frac{\partial \bar{T}_l}{\partial \bar{\psi}_l} = 0 \quad \text{and} \quad \frac{\partial \bar{T}_b}{\partial \bar{\psi}_b} = 0 \quad (3.18)$$

The upper surface of the microlayer and the cap portion of the bubble are assumed to be at the saturation temperature of the vapor pressure (\bar{P}_v) at all time.

3.5 Non-dimensionalization

The dimensionless dependent variables r , ψ , t , R , δ , ϵ , and P are defined in the same manner as in section 2.3. The other dependent variables are non-dimensionalized as

$$\begin{aligned} z &= \frac{\bar{z}}{\delta_o}, & \delta_o &= \frac{\bar{\delta}_o}{R_0} \\ r_d &= \frac{\bar{r}_d}{R_0}, & r_m &= \frac{\bar{r}}{R_0} \\ r_b &= \frac{\bar{r}_b}{\delta_b}, & t_b &= \frac{\alpha_b \bar{t}}{R_0^2}, & T_b &= \frac{\bar{T}_b - T_i}{T_h - T_i} \\ \psi_b &= \bar{\psi}_b, & \delta_b &= \frac{\bar{\delta}_b}{R_0}, & y &= \frac{\bar{y}}{R_0} \\ P_B &= \frac{\bar{P}_B - \bar{P}_{l0}}{\sigma/R_0}, & P_v &= \frac{\bar{P}_v - x_v \bar{P}_{l0}}{\sigma/R_0} \\ \rho_v &= \frac{\rho_v - \rho_{v0}}{\sigma/(R_0 R_v T_{sat})}, & T_v &= \frac{\bar{T}_v - T_i}{T_h - T_i} \\ \dot{m} &= \frac{\bar{m}}{\rho_{v0} \alpha R_0}, & N_v &= \bar{N}_v/N_{v0}, & V &= \bar{V}/R_0^3 \\ q &= \bar{q}/(k R_0 (T_h - T_{sat})) \end{aligned}$$

The initial bubble radius is used as the length scale for definition of the non-dimensional dry radius (r_d) and for the definition of non-dimensional microlayer radius (r_m).

The length scale for the non-dimensional radius (r_b) in the heated surface is δ_b . The height of the microlayer is non-dimensionalized based on the length scale equal to the formation height of the microlayer ($\bar{\delta}_o$). As a result, the non-dimensional microlayer height is of the order one. Fourier numbers based on the respective values of thermal diffusivities are used as the non-dimensional time for the liquid region and the heated surface. The term x_v appears in the non-dimensionalization of the vapor pressure since only an x_v fraction of P_{l0} is balanced by the vapor. The rest is balanced by the non-condensable gas. The temperature scale ($T_h - T_i$) was used for the non-dimensionalization of all temperatures because the differences between any two of T_h, T_i , and T_{sat} were of the same order of magnitude. The scale for non-dimensionalization of ρ_v , namely ($\frac{R_0 R_v T_{sat}}{\sigma}$), is based on the density difference of vapor corresponding to minimum and maximum possible pressure in the bubble.

3.6 The Dimensionless Governing Equations

Equations 3.1, 3.3, 3.4 - 3.6, and 3.11 are non-dimensionalized using the above definitions and the definitions in section 2.3 of Chapter 2. The results are

$$z \delta_o \frac{\partial}{\partial t} (z \delta_o) = -\epsilon_c Ja (1 + Sb) (T_{bs} - T_v) \quad (3.19)$$

$$\delta_o = C_z (Pr t_g)^{\frac{1}{2}} \quad (3.20)$$

$$\delta_b^2 \frac{\partial T_b}{\partial t_b} - \frac{\partial^2 T_b}{\partial r_b^2} - \frac{1}{r_b^2} \frac{\partial^2 T_b}{\partial \psi_b^2} - \left(r_b \delta_b \dot{\delta}_b + \frac{2}{r_b} \right) \frac{\partial T_b}{\partial r_b} - \frac{\cot \psi_b}{r_b^2} \frac{\partial T_b}{\partial \psi_b} = 0 \quad (3.21)$$

$$\dot{R} = \left(\frac{\dot{m}_t}{2\pi R^2} - \pi_4 \rho_v \frac{R}{3} \right) / (1 + \pi_4 \rho_v) \quad (3.22)$$

$$P_B = \frac{2}{R} - \frac{We \epsilon_o}{1 + \pi_4 \rho_v} \left(\frac{\dot{m}_c}{2\pi R^2} \right)^2 \quad (3.23)$$

$$\dot{m}_c = (1 + Sb) \frac{2\pi R^2 Ja \epsilon_c}{\delta \epsilon_o} \int_0^{\pi/2} \frac{\partial T}{\partial r} \sin \psi \Delta \psi \quad (3.24)$$

$$\dot{m}_m = (1 + Sb) \frac{2\pi \delta_b^2 Ja \epsilon_c}{\epsilon_o \delta_o} \int_{r_d}^R \frac{(T_{bs} - T_v)}{z} r_b dr_b \quad (3.25)$$

$$\dot{m}_t = \dot{m}_m + \dot{m}_c \quad (3.26)$$

$$\dot{N}_v = \frac{3}{2\pi} \dot{m}_t \quad (3.27)$$

$$P_v = x_v P_B \quad (3.28)$$

$$x_v = \frac{N_v}{N_v + \left(\frac{1 - x_{vo}}{x_{vo}} \right)} \quad (3.29)$$

$$N_v = \int_0^t \dot{N}_v dt + 1 \quad (3.30)$$

$$T_v = \left[(1 - \pi_1 \ln [(\pi_4 \rho_v + 1)(\pi_3 T_v + 1)])^{-1} - 1 \right] \div \pi_3 \quad (3.31)$$

$$\rho_v = \left\{ \frac{x_v}{\pi_3 T_v + 1} \left[\pi_2 (P_B - 2 + We P_{lo}) + \frac{1}{x_{vo}} \right] - 1 \right\} \div \pi_4 \quad (3.32)$$

where $\epsilon_c = \frac{\rho_{vo} c}{\rho}$. The choice of this parameter is explained in this section later.

The rate of evaporation of liquid at the microlayer (\dot{V}_m) and at the cap (\dot{V}_c) are found from

$$\dot{V}_m = \dot{m}_m \epsilon_o \quad \text{and} \quad \dot{V}_c = \dot{m}_c \epsilon_o$$

The rates of heat flow at the cap and at the microlayer are found from

$$q_c = \frac{\dot{m}_c \epsilon_o}{Ja \epsilon_c} \quad \text{and} \quad q_m = \frac{\dot{m}_m \epsilon_o}{Ja \epsilon_c}$$

Note that the Eq. 3.25 is singular at the tail point of the microlayer since the microlayer thickness is zero at that point. A non-singular formulation for the determination of z is discussed later in this chapter. Thus the value of \dot{m}_m is found from the following equation which makes use of the available values of z .

$$\dot{m}_m = \frac{2\pi R^2}{\epsilon_o} \int_{r_d}^R \frac{\partial (z \delta_o)}{\partial t} r_m dr_m \quad (3.33)$$

As explained in Section 2.3.1 of Chapter 2, \hat{P}_{l0} is determined by neglecting viscous effects,

$$\hat{P}_{l0} = \frac{3}{2} \dot{R}^2 + R\ddot{R}.$$

The term ϵ from Eq. 2.36 has been dropped since it was three orders of magnitude smaller than unity.

The new non-dimensional parameters that arise in the above formulation are:

$$\begin{aligned} \pi_1 &= \frac{P_{vo}}{\rho_{vo} h_{fg}} & \pi_2 &= \frac{\sigma}{R_0 P_{vo}} & \pi_3 &= \frac{T_h - T_i}{T_i} \\ S_b &= \frac{T_{sat} - T_i}{T_h - T_{sat}} & \epsilon_c &= \frac{\rho_{vo,c}}{\rho_{vo}} & \epsilon_o &= \frac{\rho_{vo}}{\rho_l} \\ Ja &= \frac{\rho_l C_{pl} (T_h - T_{sat})}{\rho_{vo,c} h_{fg}} & \lambda &= \frac{\alpha_l}{\alpha_b} & K &= \frac{k_l}{k_b} & x_{vo} &= \frac{P_{vo}}{P_{B,o}} \end{aligned}$$

The Jakob number is defined differently from the Chapter 2. It has a definition similar to that in the second generation model, however, since a unique temperature cannot be ascribed to the heated surface, it is based on the initial temperature of the heated surface. $\rho_{vo,c}$ designates the initial vapor density with a given bubble radius (10^{-5} m) and thus the dependence of Ja on the initial bubble radius is removed.

The non-dimensional parameters represent ratios of various quantities at the initial state. π_1 and π_2 are defined in a same manner as in the second generation model. π_3 represents the ratio of superheat of the heated surface (above the bulk temperature) to the initial absolute temperature. π_4 , which is $\frac{\sigma}{R_0 R_v T_i \rho_{vo}}$ can be expressed in terms of the other non-dimensional parameters in the following way

$$\pi_4 = \frac{2\pi_2 (1 + S_b)}{S_b(\pi_3 + 1) + 1}.$$

The subcooling number is a ratio of the subcooling of the bulk fluid below T_{sat} to the superheat of the heated surface above the saturation temperature. For saturated boiling, the subcooling number is equal to zero.

The same governing non-dimensional equations and the boundary conditions for the liquid region of Chapter 2 have been used in the third generation model.

In order to solve Eq. 3.19, it is first integrated with respect to time to yield

$$(z \delta_o)^2 = -2 \epsilon_c Ja (1 + Sb) \int_{t_1(r_m)}^t (T_{bs} - T_v) dt + \text{const.} \quad (3.34)$$

where $t_1(R)$ is the time required for the radius of the bubble to reach the value R . Thus t_1 is an inverse function of R such that $R = R(t_1(R))$. The constant of integration is found by noting that the height of the microlayer is δ_o (initial height, which is the height of formation) at time $t_1(R)$. Thus the constant is equal to δ_o^2 , and therefore

$$z^2 = \frac{-2 \epsilon_c Ja}{\delta_o^2} (1 + Sb) \int_{t_1(r_m)}^t (T_{bs} - T_v) dt + 1 \quad z^2 \geq 0 \quad (3.35)$$

Note that $\bar{z} = 0$ at $\bar{r} = \bar{r}_d$ (tail point), and hence, from Eq. 3.1, $\frac{\partial \bar{z}}{\partial t}$ is unbounded at that point. Since at any point in time, $\frac{\partial \bar{r}}{\partial t}$ must be finite, $\frac{\partial \bar{z}}{\partial \bar{r}}$ is also unbounded at the tail point. These unbounded derivatives at the tail point pose difficulties for differential formulations of the microlayer. Equation 3.35 works because it involves *integration*.

3.7 Dimensionless Boundary Conditions

The non-dimensional solution to the far field boundary conditions (Eq. 3.12 and 3.13) [75] is

$$T_l = \frac{\sqrt{\lambda}}{K + \sqrt{\lambda}} \operatorname{erfc} \left(\frac{y}{2\sqrt{t}} \right) \quad (3.36)$$

$$T_b = 1 - \frac{\sqrt{\lambda}}{K + \sqrt{\lambda}} \operatorname{erfc} \left(\frac{y}{2\sqrt{t/\lambda}} \right) \quad (3.37)$$

Equations 3.36 and 3.37 describe the far field boundary temperature in the liquid and solid regions.

The other boundary conditions are non-dimensionalized as

$$\begin{aligned} \frac{\partial T_b}{\partial \psi_b} &= \frac{-K}{Ja \epsilon_c 2\pi (1 + Sb) \delta_b} \frac{\partial \dot{V}_m}{\partial r_b} & \frac{r_d}{\delta_b} < r_b < \frac{R}{\delta_b}, \psi_b = \frac{\pi}{2} \\ \frac{\partial T_b}{\partial \psi_b} &= 0 & 0 < r_b < \frac{r_d}{\delta_b}, \psi_b = \frac{\pi}{2} \\ \frac{\partial T_b}{\partial \psi_b} &= -K \frac{\partial T_l}{\partial \psi_l} & 0 < r < 1, \psi_b = \frac{\pi}{2}, \psi_l = \frac{\pi}{2} \\ \frac{\partial T_b}{\partial \psi_b} &= 0 & \psi_b = 0 \\ \frac{\partial T_l}{\partial \psi_l} &= 0 & \psi_l = 0 \end{aligned}$$

3.8 Dimensionless Initial Conditions

The initial conditions for temperature inside the liquid and solid region are:

$$T_l = 0 \quad 0 \geq r \geq 1, 0 < \psi_l < \frac{\pi}{2} \quad (3.38)$$

$$T_b = 1 \quad 0 \geq r_b \geq 1, 0 < \psi_b < \frac{\pi}{2} \quad (3.39)$$

The initial conditions for the streamfunction and vorticity are:

$$F = 0 \quad 0 \geq r \geq 1, 0 < \psi_l < \frac{\pi}{2} \quad (3.40)$$

$$\Omega = 0 \quad 0 \geq r \geq 1, 0 < \psi_l < \frac{\pi}{2} \quad (3.41)$$

The other initial conditions are $N_v = 1, P_B = 2, T_v = 0, \rho_v = 1, P_{l0} = 0, z = 0$ and $\delta_o = 0$.

3.9 Numerical Method

Numerical integration in Eq. 3.35 is done by defining P according to

$$P = z^2(t) - Q$$

where

$$Q = \frac{2 \epsilon_c Ja}{\delta_0^2} (T_v - T_{bs}) \Delta t.$$

Eq. 3.35 is written as

$$z^2(t + \Delta t) = \begin{cases} P & \text{if } P \geq 0 \\ 0 & \text{if } P < 0 \end{cases} \quad (3.42)$$

The initial condition for Eq. 3.42 is

$$z(t_1, r_m) = 1.$$

The second clause in Eq. 3.42 is a mathematical expression of the physical requirement that z be non-negative. At a given radius r_m , the decrease in z^2 is given by Q at any time interval Δt except in the last time interval. During this final time interval, $Q > z^2(t)$, and the decrease is $z^2(t)$ itself, since there is not enough liquid left in the microlayer at the given radial location to evaporate throughout the interval.

Equation 3.21 is written in generic form (similar to Eq. 2.46 of Chapter 2)

$$\delta_b^2 \frac{\partial T_b}{\partial t_b} - \frac{\partial^2 T_b}{\partial r_b^2} - \frac{1}{r_b^2} \frac{\partial^2 T_b}{\partial \psi_b^2} - 2\lambda \frac{\partial T_b}{\partial r_b} - 2\mu \frac{\partial T_b}{\partial \psi_b} = S \quad (3.43)$$

where

$$\lambda = \frac{r_b \delta_b \dot{\delta}_b}{2} + \frac{1}{r_b}, \quad \mu = \frac{\cot \psi_b}{2 r_b^2}, \quad S = 0.$$

Eq. 3.43 has been finite differenced in a similar manner as Eq. 2.46, the details of which have been given in Section 2.5.1 of chapter 2

3.10 Computational Method

Viscous effects are critically important in the microlayer formation mechanism. In the third generation model, however, the microlayer has been built in, a priori. As a result, viscous effects in the liquid near the bubble base do not directly affect microlayer formation and are confined to the microconvection around the bubble. From the comparison of viscous and inviscid cases of the second generation model this, microconvection effect has been found to be quite limited. In order to obtain more results with the given computational resources, the vorticity was thus set to zero (that is, inviscid flow was set) for all computations with the third generation model. Lee and Nydahl [32] have also observed through their computational simulation that virtually 100% of the energy transferred to the bubble up to the departure has been provided by the microlayer, and have pointed to the unimportance of microconvection. For the same reason, only a 17x17 grid was used in the liquid region. These helped reduce the computation time by a factor of 20 to 50.

The clustering of grid points for the liquid region near the heated surface and near the bubble surface was such that the ratio of the size of the smallest to the largest cell was 42 in each direction. A uniform orthogonal grid was used for the computation in the heated surface. Linear interpolation was used to match the temperature and the temperature gradients at the interface between the liquid region and the heated surface. When solving for the liquid region, temperature of the heated surface at $\psi_b = \frac{\pi}{2}$ has been used as a boundary condition. The temperature gradient at $\psi_l = \frac{\pi}{2}$ in the liquid region was used as boundary condition while solving for the region of heated surface. A fixed relaxation parameter equal to 0.2 was used at these matching boundaries. Strong underrelaxation for matching boundary conditions at the contact

of two computational domains is recommended in [76].

A grid with 33 radial nodes and 17 angular nodes was used for the heated surface. The nodes in the microlayer were matched with those of the heated surface. Since the location of the nodes in the heated surface (therefore those in the microlayer) changed at every timestep due to the increasing size of the thermal penetration in the heated surface, linear interpolation was used to find the microlayer height at the new location of grid points in the microlayer at every timestep based on the location of nodes at the previous timestep. When 33 radial nodes were used for the heated surface, typically, the microlayer covered approximately 20 nodes. When solving the microlayer equation, the temperature of the heated surface immediately below the bubble was used as a boundary condition, while the temperature gradient in the microlayer was used as a boundary condition while solving for the heated surface.

The similar computational method as in the second generation model was used for calculation of temperature and streamfunction in the liquid around the bubble in this model. The flowchart for the algorithm is given in Figure 3.4. The relaxation in each step represents the dynamic relaxation (Section 2.5.2). After checking for overall convergence, only T_l , ρ_g , T_v , and T_b were relaxed, P_B was not relaxed because it was found to be strongly dependent on the other variables. The convergence test was carried out only once in five iterations except for the test of overall convergence, which was carried out at every iteration. Just as in the second generation model, double precision was used for the calculation. The tests for convergence for T_l , f , P_g , ρ_g and T_v were the same as those for T_l , F , P_v , ρ_v , and T_v in the second generation model (see Eq. 2.50, Eq. 2.51, and Eq. 2.53 through Eq. 2.55). The convergence

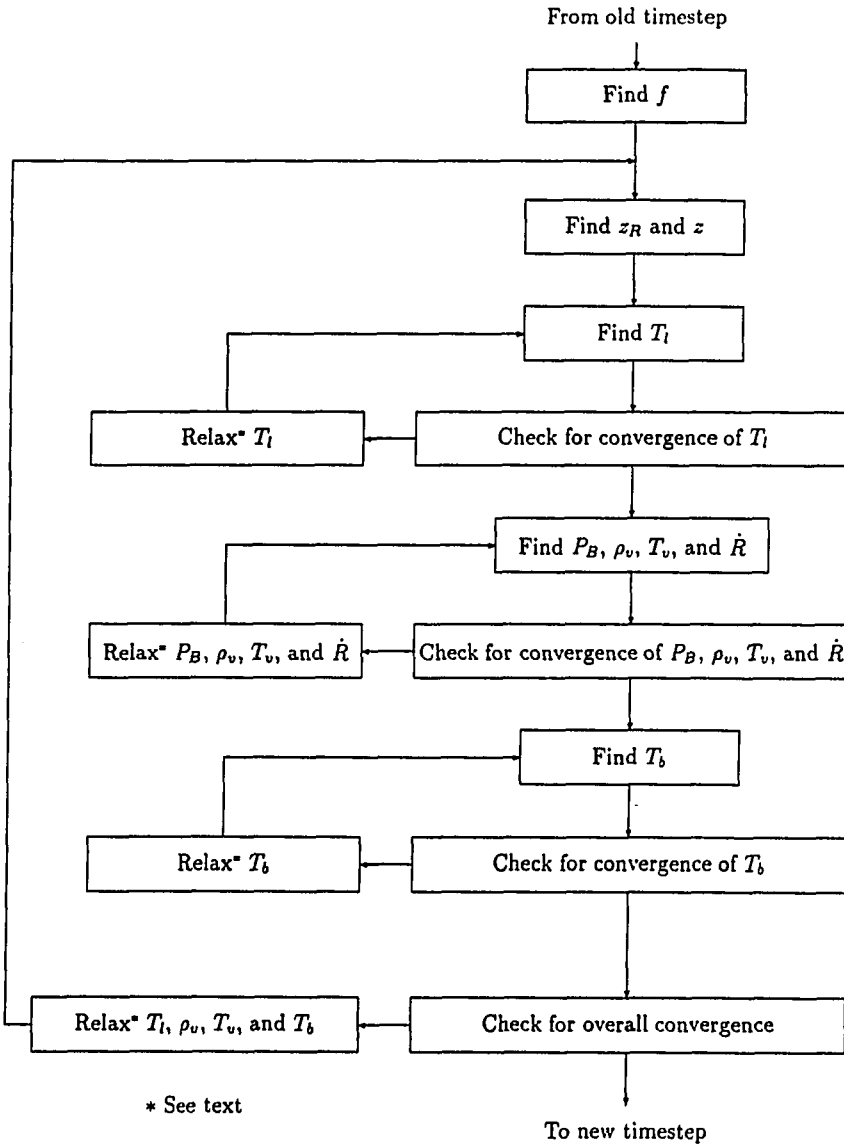


Figure 3.4: The flowchart for the third generation model

test for T_b was

$$\mathcal{T}_{T_b} = \max_{i,j} \left| 2 \left(\frac{T_{b,i,j}^{k+1} - T_{b,i,j}^k}{T_{b,i,j}^{k+1} + T_{b,i,j}^k} \right) \right| \quad (3.44)$$

The convergence criterion for all the variables was $\mathcal{T}_\phi < 10^{-5}$, where ϕ represents any of the above dependent variables. The convergence criterion for the overall loop was however, $\mathcal{T}_\phi < 3 \times 10^{-5}$.

The subroutine for finding the temperature distribution in the heated surface was verified by solving one dimensional problems of known solutions, such as diffusion of heat in a semi-infinite medium (Stoke's first problem), heat flow with constant temperature gradients etc.

The entire program required approximately 80 minutes of CPU time on a Apollo, DN 10000 workstation.

3.11 Results and Discussion

3.11.1 The Non-dimensional Parameters and Description of the Computational Runs

The heated surface was assumed to be plain carbon steel. Water was used as a model liquid for the computation of the bubble growth, like in the second generation model. Again, this should not be seen as restricting the applicability of results because the terms carrying the thermophysical properties (except the Prandtl number) become negligible very soon after the initiation of growth. Only Ja , Sb , and Pr were seen to dictate the growth during the later period of bubble's life. The Prandtl number is an extra factor that governs the bubble growth in this model compared

Table 3.1: Non-dimensional parameters used in the third generation model

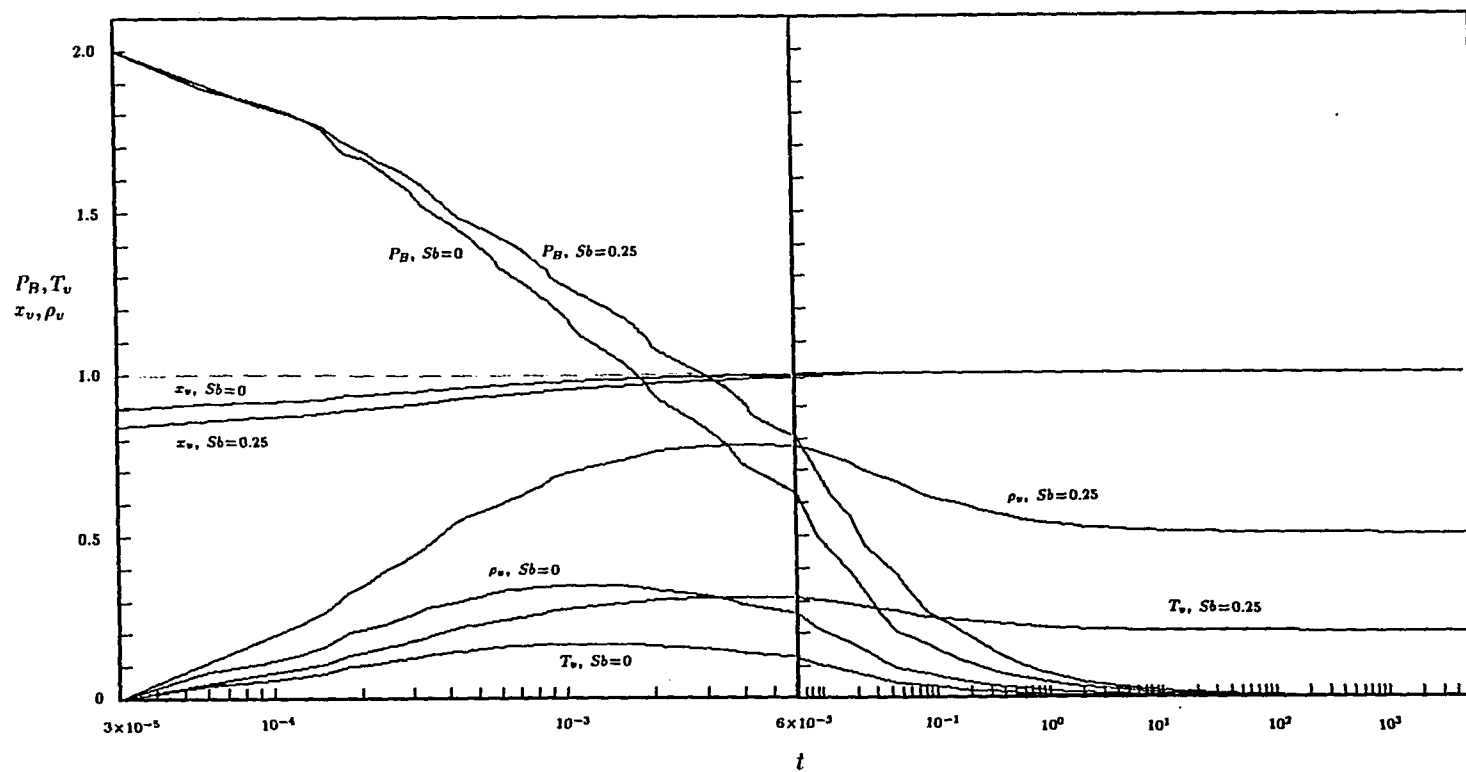
Parameter	π_1	π_2	π_3	π_4
Value	2.725×10^{-7}	5.746×10^{-3}	0.07719	1.948×10^{-2}
Parameter	We	ϵ_0	K	λ
Value	4.591×10^{-6}	6.8027×10^{-4}	0.012	0.0095

with the second generation model, and its effect on the growth comes through the microlayer formation equation (Eq. 3.20). The non-dimensional parameters used for the case of saturated boiling are given in Table 3.1.

Since Pr is the only thermophysical similarity parameter governing the bubble growth except in the initial short period, it was varied independently of the other non-dimensional parameters to simulate bubble growth in various fluids. Initial radii ranging from 1 to 5 microns have been reported in the literature [54] [65]. The growth in the later part of bubble's life has been found to be independent of the initial radius, for this reason initial bubble radius was chosen to be 10^{-5} m for all runs.

3.11.2 The Vapor Variables

The variation of bubble pressure, temperature, vapor density, and vapor mole fraction against time for $Ja = 20$ and $Sb = 0$ and $Sb = 0.25$ are shown in Figure 3.5. Note that the scales on the abscissa are different on either sides of $t = 6 \times 10^{-3}$. The dependent variables in the figure reach their asymptotic values approximately at $t = 50$. The vapor fraction reached within 1% of its final value (unity) approximately at time $t=0.01$. Beyond this time, the non-condensable gas does not play a significant role.



111

Figure 3.5: Vapor variables versus time (Third generation model)

3.11.3 Various Bubble Growth Theories

In Figure 3.6 are shown the plots of radius versus time. Note that higher sub-cooling results in lower growth and higher Ja results in higher growth. Surprisingly, *the homogeneous boiling model is seen to predict the same growth rate as that of the third generation model* during the later part of the growth for the case of saturated boiling. Cooper [17] has pointed out that his expression of bubble growth with microlayer and Scriven's [23] expression of homogeneous boiling would yield the same results if the wall temperature in his expression is the same as the superheat temperature in the later case, although the mechanism and the theory are quite different in the respective cases.

Mikic and Rohsenow [27] have stated that if evaporation of the microlayer is the governing mechanism, then one would expect that the bubble growth on a heated surface (with microlayer) should have exhibited different characteristics than the bubble growth in a uniformly superheated liquid. However, the opposite is true. They have supported the theory called 'bulk convection' for bubble growth on surface, which had been postulated by Han and Griffith [25] and Han and Griffith [26]. According to this theory, the bubble is surrounded by a uniformly superheated fluid, similar to that in homogeneous boiling. This thermal layer is carried away as the bubble departs. By this kind of transportation of the thermal layer, heat is transferred to the fluid from the heated wall. The bulk convection theory has been accepted by Yu and Mesler [10], Judd and Hwang [29], van Stralen [30], and van Stralen [31].

The present study, which modeled the relevant physics rather than *presuming* the dominance of either bulk convection or microlayer theory have yielded results that match the experimental data reasonably well (discussed later). From the temperature

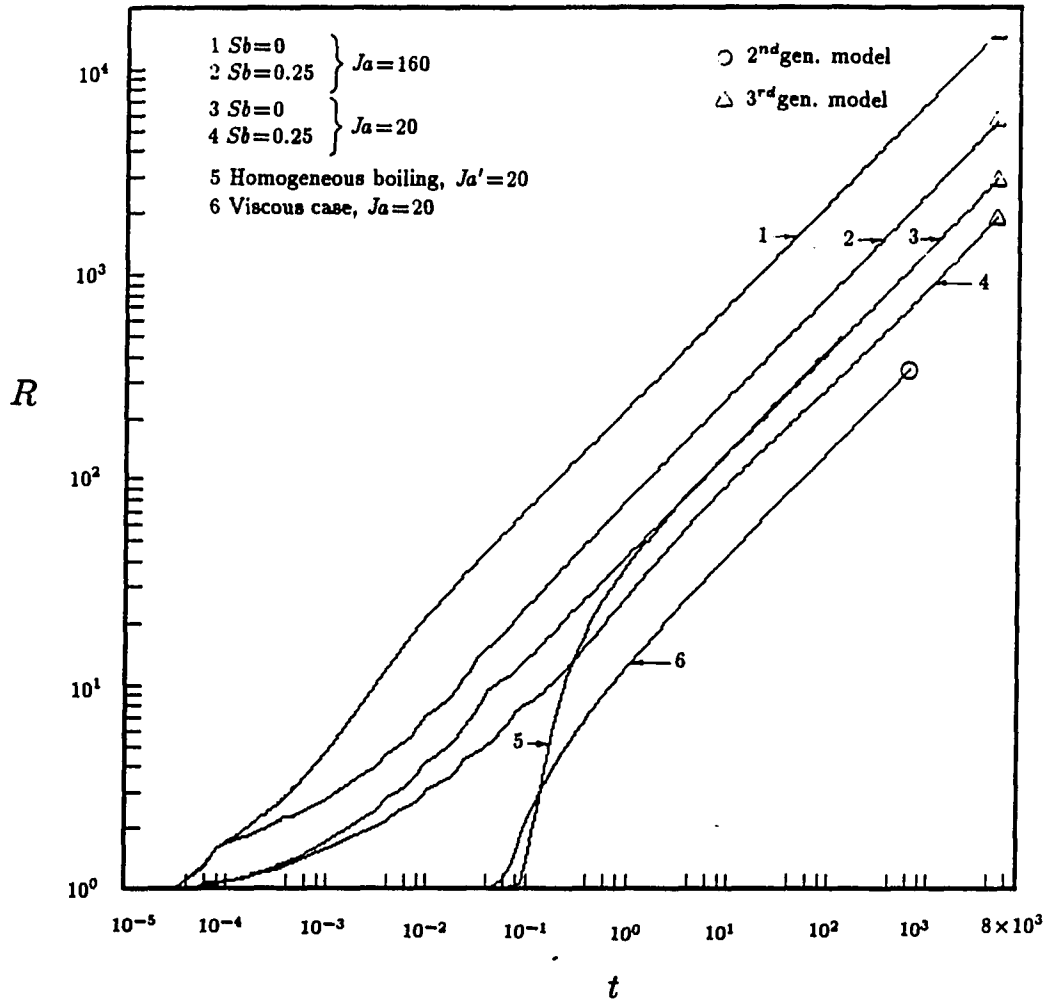


Figure 3.6: Comparison of predictions of bubble growth from the homogeneous boiling, second, and third generation models

contour plots of Ja ranging from 10 to 640, Sb ranging from 0 to 1, and Pr in the range 0.25 to 5.25, it is clear that there is no uniform wrapping of superheated fluid around the bubble at any time in the bubble's life. For example, in Figure 3.7 and Figure 3.8 are shown the temperature contours at Jakob number equal to 20 for $Sb = 0$ and $Sb = 0.25$ respectively. In fact most of the heat for the bubble growth was observed to have been transferred from the microlayer. Note that the initial condition in the present study (uniformly heated liquid and uniformly heated supporting surface) is the same as that of the models of researchers who propose bulk convection. It is also clear from the second generation model, Figure 2.9 and Figure 2.16, that a bubble is not surrounded by a superheated thermal boundary layer. Lee and Nydahl [32] have also observed through their computational modeling, that there is essentially no wrapping of thermal boundary layer around the bubble and almost all the heat was transferred by the microlayer. The above facts indicate that the equal growth rates of a bubble in uniformly superheated medium (homogeneous boiling) and that on surface (heterogeneous boiling) is perhaps only a coincidence. The mechanisms in respective cases are very different. For this reason the bulk convection theory must be seriously questioned. The alternative, the microlayer theory, is accepted by many researchers: Cooper and Vijuk [74], Rogers and Mesler [8], Kotake [77], Cooper [17], Hospeti and Mesler [11], Cooper and Lloyd [7], Sernas and Hooper [14], Yesin and Jeffers [15]. Katto and Shoji [12], Mesler [9], Yu and Mesler [10], Cooper, Judd, and Pike [22], Cooper and Chandratilleke [35], and Cooper [37].

Figures 3.7 and Figure 3.8 show the temperature contours around the bubble. It can be seen that most of the heat flow in the heated surface is directed toward the tail

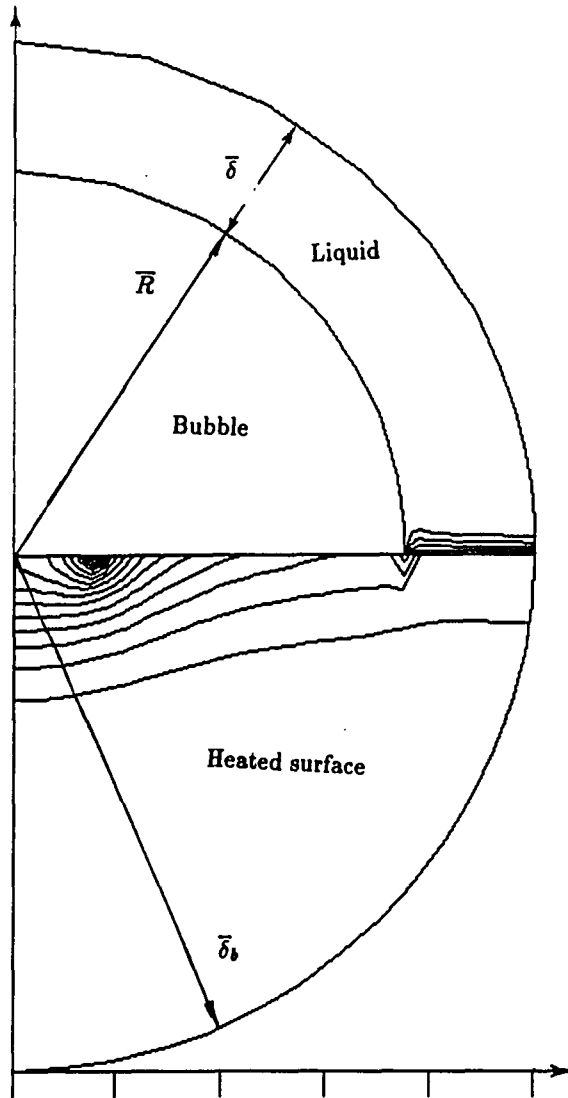


Figure 3.7: Temperature contours in the liquid and in the solid during the diffusion controlled growth period (Saturated boiling)

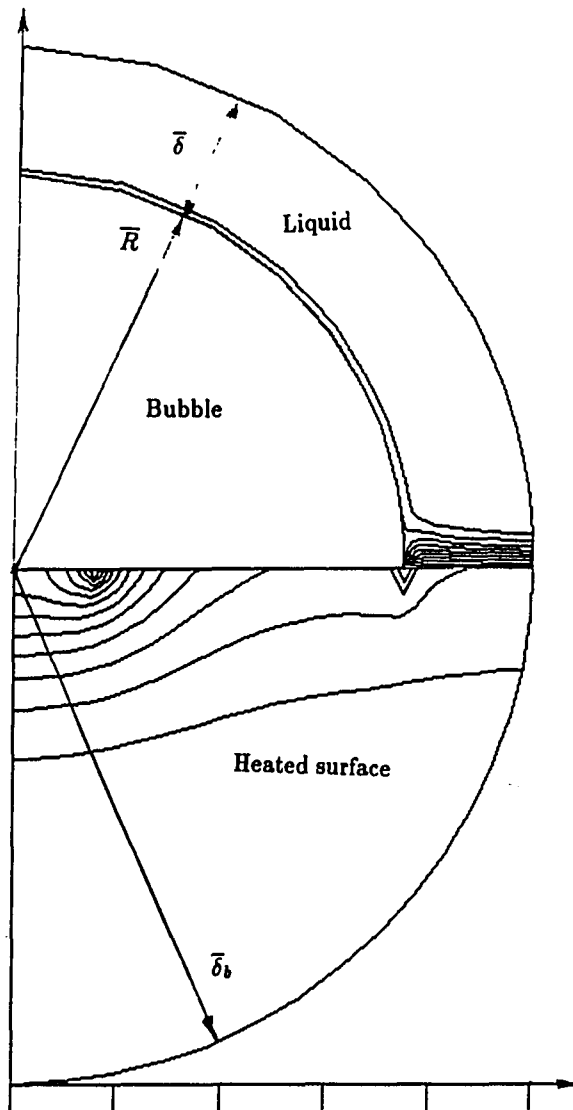


Figure 3.8: Temperature contours in the liquid and in the solid during the diffusion controlled growth period (Subcooled boiling)

of the microlayer and at the junction of the bubble and the heated surface. Note that there is a local minimum in the temperature of the heated surface at the corner of bubble and the heated surface. This is due to the higher rate of heat flow at the corner of the bubble and the heated surface. In the case of subcooled boiling, the bubble is surrounded by concentric contours around most of the bubble, showing that the bubble loses heat from most of the cap portion in subcooled boiling. The "surface plots" of temperature are shown in Figure 3.9 and Figure 3.10 where temperature is plotted on the vertical axis while the computational domain is shown in the horizontal plane. The direction of the flow of heat can be clearly seen in the figures. The large drop on the temperature at the tail of the microlayer as in the present study has also been observed by Cooper and Lloyd [7], Rogers and Mesler [8], Hospeti and Mesler [11], Yu and Mesler [10] by way of surface temperature measurements, and in addition, has been supported by way of analysis in some cases.

3.11.4 The Microlayer Profile

The microlayer profiles for Ja ranging from 10 to 320 are shown in Figure 3.11 ($Sb = 0$) and in Figure 3.12 ($Sb = 0.25$). The profiles are linear towards the bubble surface, the extent of linear part increasing with Ja decreasing. The profile is extremely steep close to the dry point as expected. The volume added by the microlayer was found to be a constant function of radius except at the tail point, where its value was higher indicating that the local heat flux at the base of the microlayer is inversely proportional to the square of the radius. It can be proved by asymptotic analysis that the microlayer profile is quadratic ($\bar{z} = \sqrt{\bar{r} - \bar{r}_d}$) at the tail. The microlayer profiles observed with the help of laser interferometry by Koffman

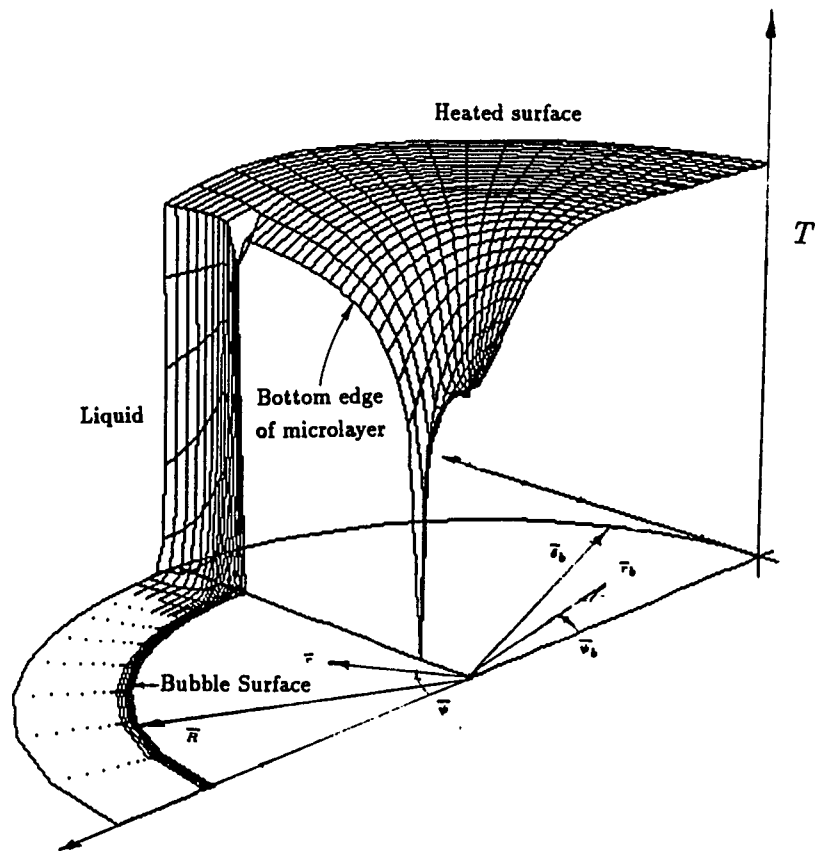


Figure 3.9: "Surface plot" of temperature. Third generation model (Saturated boiling)

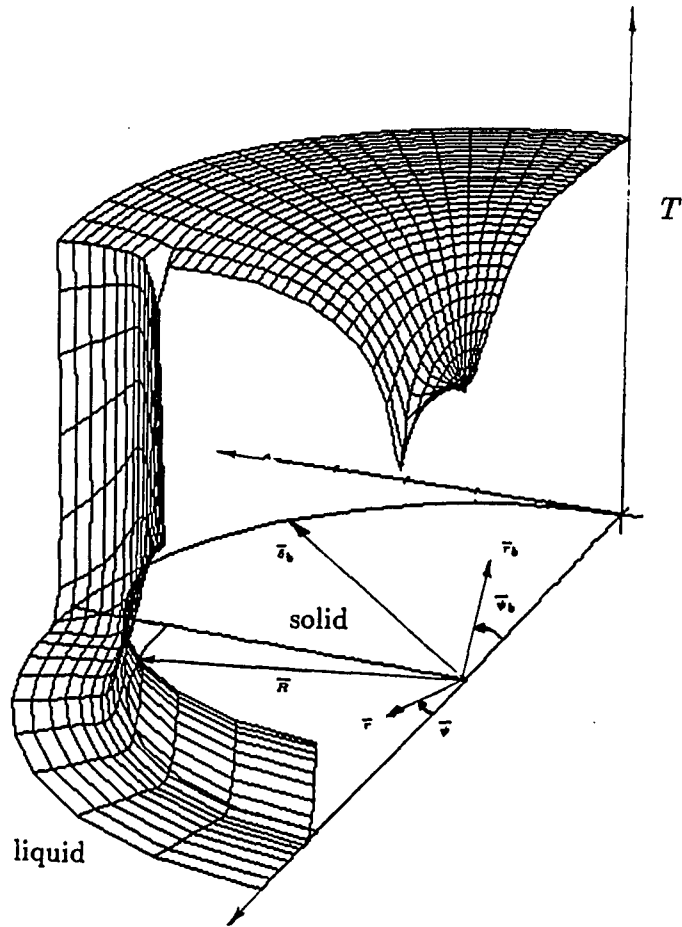


Figure 3.10: "Surface plot" of temperature. Third generation model (Subcooled boiling)

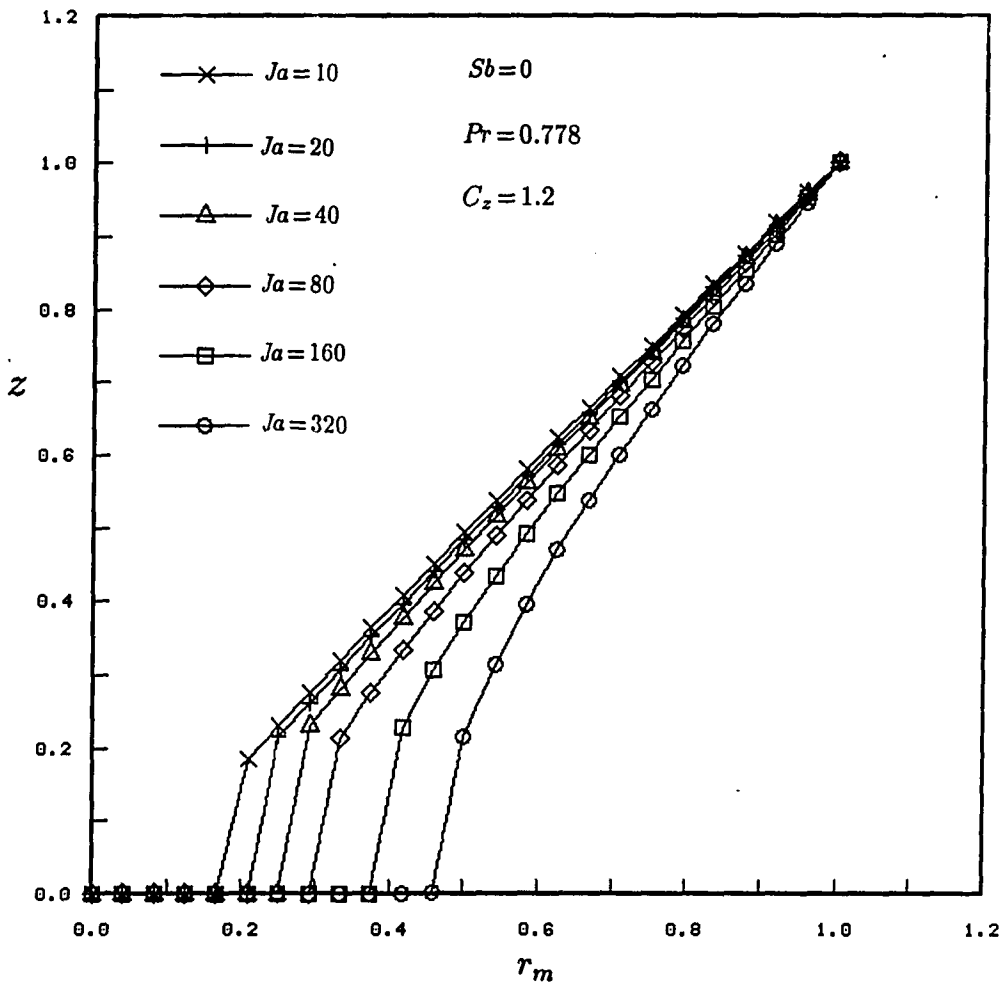


Figure 3.11: Microlayer profile (Saturated boiling)

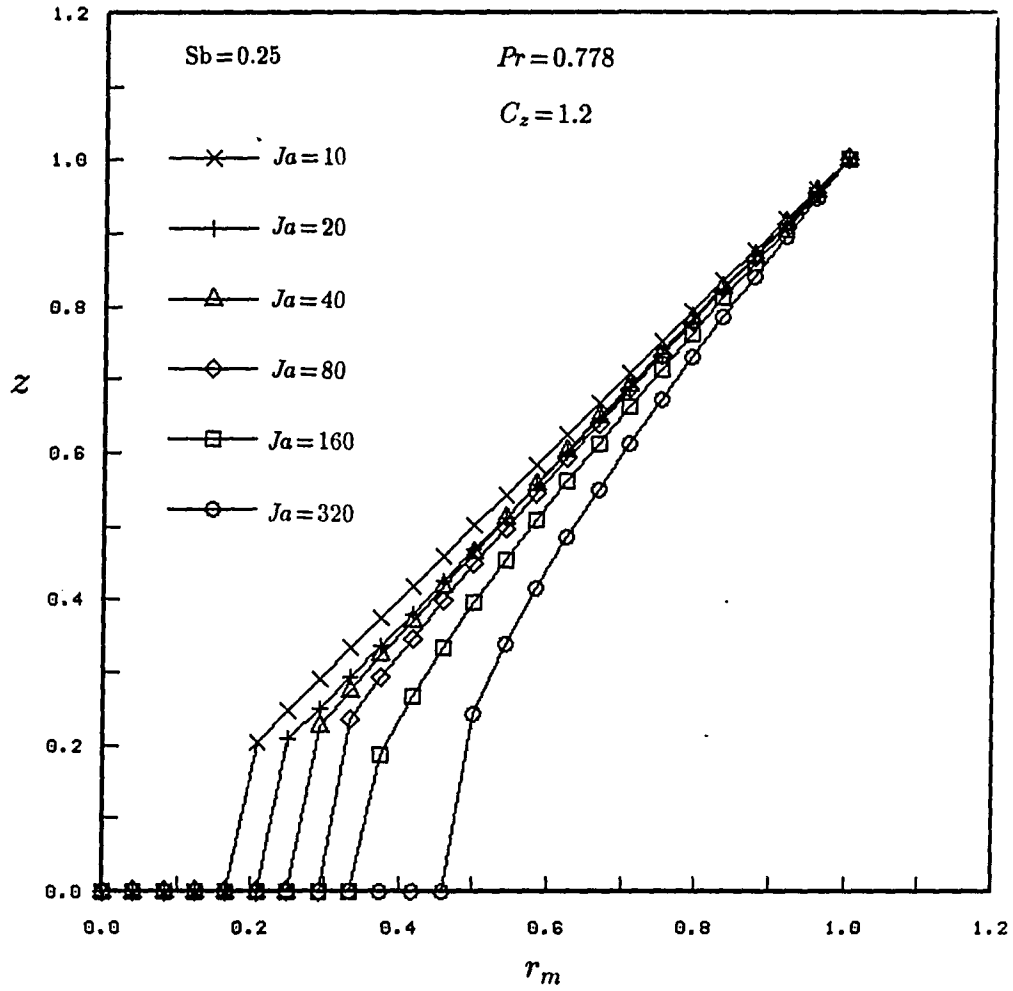


Figure 3.12: Microlayer profile (Subcooled boiling)

and Plesset (water, 1 atm, $T_{sat} - T_{\infty} = 5.7$ and 21.7 °C, $q'' = 26.5$ and $204 \frac{\text{kW}}{\text{m}^2}$, respectively) do appear linear towards the bubble surface end of the microlayer and are steeper toward the tail. The Ja in their work, however, is not available, the knowledge of which would be instructive for comparison purpose. Voutsinos and Judd [20] have compared the microlayer profile of their work with those of Jawurek (methanol, $240 \frac{\text{kW}}{\text{m}^2}$ $T_{sat} - T_{\infty} = 7.1$ °C, $q'' = 62.3 \frac{\text{kW}}{\text{m}^2}$), and that of Sharp [78] (water, $q'' = 41.0 \frac{\text{kW}}{\text{m}^2}$). All the above profiles are wedge like and have a little curvature so they appear convex from the top.

3.11.5 The Similarity Solution

An important finding of the present study is that the entire solution of this problem showed similarity for large values of time, i.e., for example, the temperature contours in the liquid and the solid region and the microlayer profiles are self similar when plotted on a normalized scale at large values of time. The microlayer profiles at various values of time by Koffman and Plesset do seem to show this similitude. Cooper and Lloyd [7] have analytically proven that the dry radius must be a constant fraction of the bubble radius during the diffusion controlled growth. Since the solution to the third generation model in the present study exhibited similarity for large values of time, the above fact is verified. The ratio of dry radius to the bubble radius in the present solution varied from 0.15 ($Ja=10$) to 0.45 ($Ja=640$).

3.11.6 Comparison of Heat Flow Through the Cap and Through the Microlayer

The local rate of volume added to the bubble as a function of angle ψ is shown in Figure 3.13. Most evaporation is seen to occur near $\psi = \frac{\pi}{2}$ (near the heated surface). At higher Jakob numbers, the volume added is large as is expected from Eq. 3.24. Note that the abscissa is logarithmic. The higher the Jakob number, the higher the q_c . If the liquid is subcooled, then there is condensation in some part of the cap portion (Figure 3.14). Again, the higher the Jakob number, the higher are the rates of evaporation and condensation. The angle of nil condensation is seen to remain more or less independent of Ja for the range of Ja tried, and is approximately given by $\frac{\pi}{2} - \psi = 4.6 \times 10^{-2}$.

In Figure 3.15 is shown the ratio of total heat added by the microlayer (q_m) to the total heat added by the cap (q_c) against the Jakob number. This ratio is seen to fall between 7 and 800 for the cases shown. This finding indicates that the microlayer dominates the bubble growth. The heat added from the cap portion is negligible, especially in saturated boiling. Increase of Ja and decrease of Pr increases the ratio $\frac{q_m}{q_c}$.

3.11.7 Mass Flow Through the Bubble

In Table 3.2 and Table 3.3 is given the cap mass flow ratio \mathcal{R}_1 which is defined as

$$\mathcal{R}_1 = \frac{\dot{m}_c^+}{\dot{m}_c}$$

where \dot{m}_c^+ is the positive component (inward flow) of influx of liquid mass and \dot{m}_c is the net influx of liquid mass through the cap. For saturated boiling, the ratio is close

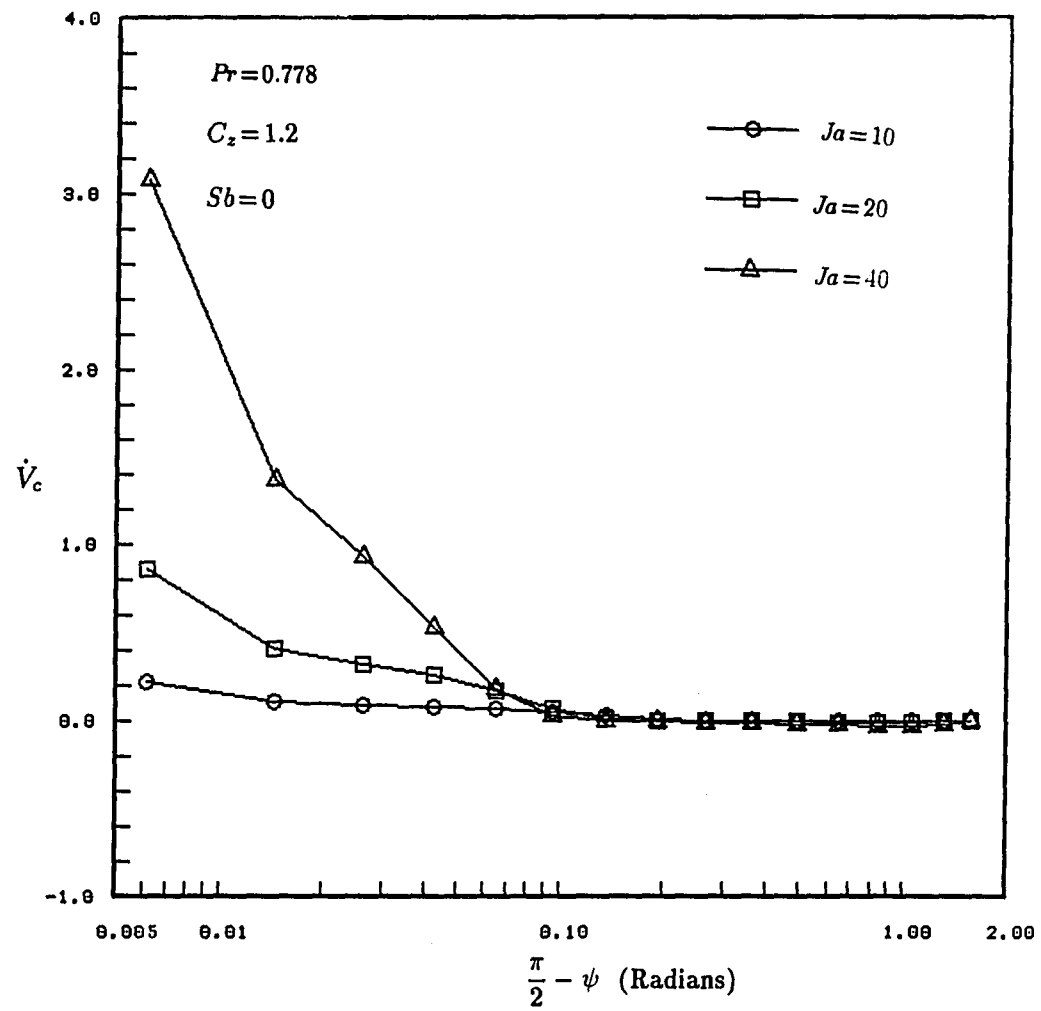


Figure 3.13: Local rate of evaporation at the cap portion of the bubble,
Saturated boiling

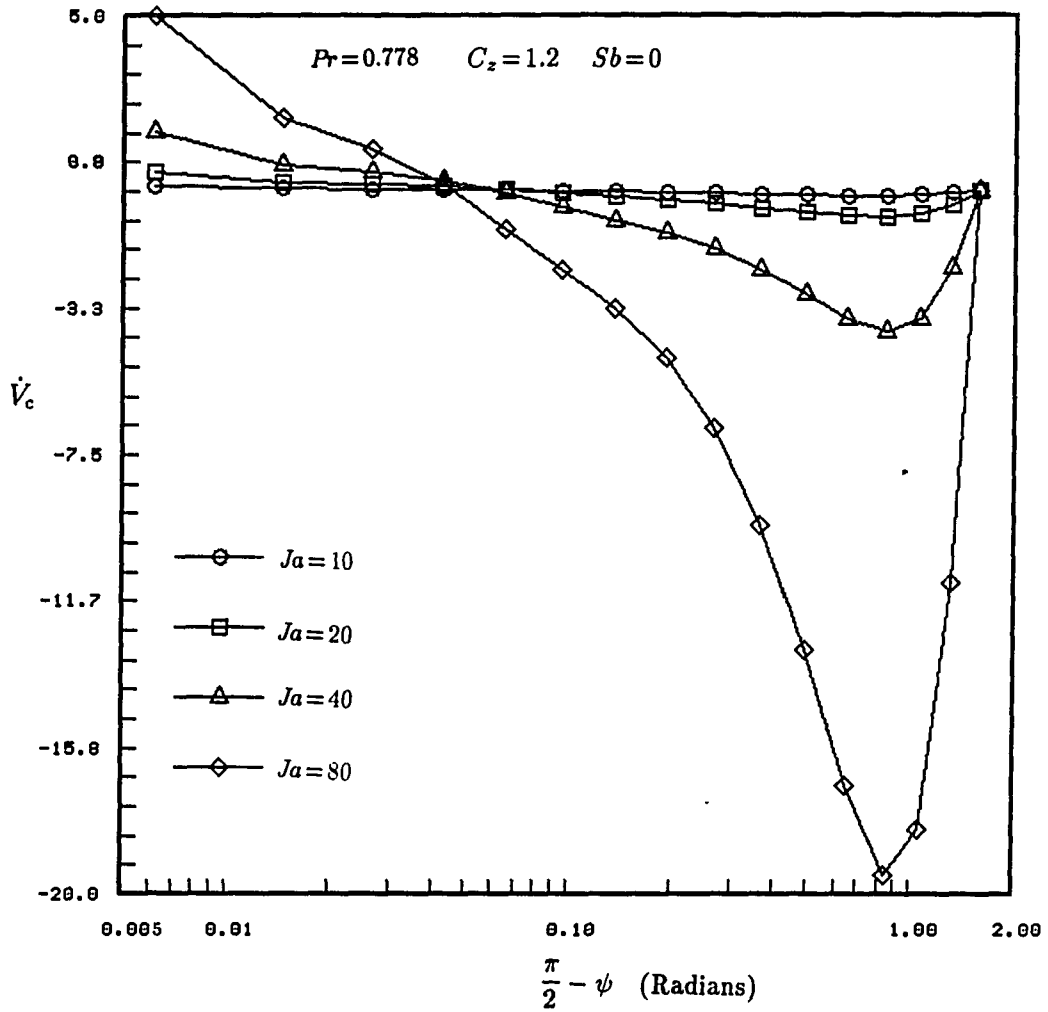


Figure 3.14: Local rate of evaporation at the cap portion of the bubble, Subcooled boiling

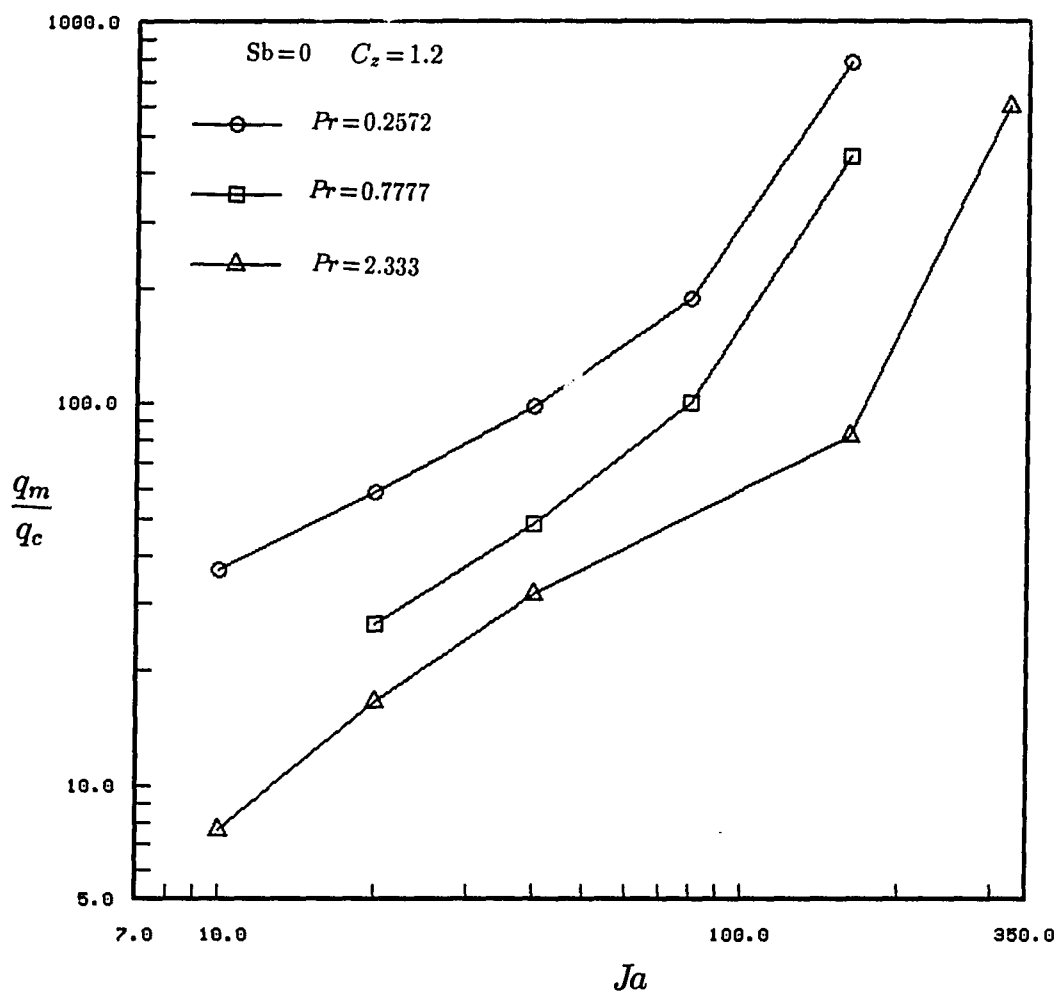


Figure 3.15: The ratio of heat added to the bubble from the microlayer to that from its cap portion

to unity indicating negligible condensation at the cap. Increase of Ja , and decrease of Pr increases \mathcal{R}_1 . With subcooled boiling, the ratio is negative. Thus there is a net condensation in subcooled boiling.

In Table 3.4 and Table 3.5 is given the the ratio \mathcal{R}_2 which is defined as

$$\mathcal{R}_2 = \frac{(\dot{m}_m + \dot{m}_c^+)}{\rho_v \dot{V}_B}$$

The numerator in the above equation is the positive contribution of the mass flow to the bubble from the microlayer and the cap, while the denominator, $\rho_v \dot{V}_B$ represents the rate of increase of the mass of the bubble. Again the ratio for saturated boiling is near unity since the condensation in this case is negligible. In case of subcooled boiling, the ratio is as high as 15 (high Ja , high Sb). Higher \mathcal{R}_2 represents large flow *through* the bubble as conjectured by Gunther and Kreith [4]. From Table 3.5 it is clear that the ratio is not very high at Ja and Sb in the lower range.

Gunther and Kreith [4] ($q'' = 908 \frac{\text{W}}{\text{m}^2}$, $T_s - T_\infty = 77.7^\circ\text{C}$, $Ja = 214$, 1 atm) observed that the latent heat content of a bubble was only 2% of the total heat flux and postulated heat flow through the bubble by mass transfer. The present study is in support of their finding. Cooper and Lloyd [7] (toluene, $13.8 \frac{\text{kN}}{\text{m}^2}$, $q'' = 47.3 \frac{\text{kW}}{\text{m}^2}$) note that the volume of evaporation from the microlayer in their experiments was 16% and 3.3 times larger than the bubble volume for cases $T_{sat} - T_\infty = 1.7$ and 7.8°C respectively. The findings of the above reporters are similar to that in the present study. Details of the flowfield through the bubble are given in Appendix C.

Table 3.2: Ratio \mathcal{R}_1 in saturated boiling

<i>Ja</i>	<i>Pr</i>	0.2572	0.7777	2.333
10		1.012	1.009	1.008
20		1.017	1.013	1.012
40		1.030	1.024	1.018
80		1.074	1.044	1.027
160		1.384	1.184	1.068

Table 3.3: Ratio \mathcal{R}_1 in subcooled boiling ($Pr = 0.7777$)

<i>Ja</i>	<i>Sb</i>	0.0625	0.125	0.25	0.5
10			-7.18	-1.15	-0.57
20		-4.24	-0.66	-0.36	-0.54
40		-0.52	-0.23	-0.17	-0.29
80		-0.15	-0.091	-0.087	-0.22
160		-0.033	-0.031	-0.052	-0.11

Table 3.4: Ratio \mathcal{R}_2 in saturated boiling

<i>Ja</i>	<i>Pr</i>	0.2572	0.7777	2.333
10		1.00145	1.00032	1.00089
20		1.00049	1.00029	1.00068
40		1.00043	1.00030	1.00054
80		1.00044	1.00039	1.00069
160		1.00041	1.00049	1.00082
320		1.00093	1.00059	1.00076
640		1.00633	1.00263	1.00020

Table 3.5: Ratio \mathcal{R}_2 in subcooled boiling ($Pr = 0.7777$)

<i>Ja</i>	<i>Sb</i>	0.0625	0.125	0.25	0.5	1
10		1.04	1.26	1.67	1.78	1.99
20		1.12	1.34	1.90	2.48	6.41
40		1.16	1.45	2.31	3.32	14.97
160		1.35	1.40	2.42	7.56	

3.11.8 Height of Formation of Microlayer

Olander and Watts [21] have derived the following relation for the ratio $\frac{\delta_o}{R}$

$$\frac{\delta_o}{R} = \frac{\sqrt{\pi}}{2\eta} \sqrt{Pr} \quad (3.45)$$

where η is the growth constant according to the relation $R = \eta \sqrt{t}$. The value of η from the present study which best matched the experimental data (discussed later in this chapter), was found to be obeying the relation

$$\eta = 4.5 \frac{Ja^{\frac{3}{4}}}{Pr^{\frac{1}{4}}}$$

Substitution of this growth constant in Eq. 3.45 yields

$$\frac{\delta_o}{R} = \frac{\sqrt{\pi}}{9} \left(\frac{Pr}{Ja}\right)^{\frac{3}{4}} = 0.20 \left(\frac{Pr}{Ja}\right)^{\frac{3}{4}}$$

A multiple regression analysis of the data from the computational predictions showed that

$$\frac{\delta_o}{R} = 0.279 \frac{Pr^{0.741}}{Ja^{0.737}} \quad (3.46)$$

The exponent of Pr , however, decreased from 0.804 to 0.5634 for Ja in the range 10 to 640, and the above value (0.741) represents an average. When a power of $\frac{3}{4}$ was forced on the ratio $\frac{Ja}{Pr}$, regression analysis revealed the following relation

$$\frac{\delta_o}{R} = 0.163 \left(\frac{Pr}{Ja}\right)^{\frac{3}{4}} \quad (3.47)$$

The value $\frac{\delta_o}{R} Ja^{-\frac{3}{4}}$ predicted by the present computation was plotted against Pr on logarithmic axes (Figure 3.16), the data merged approximately into one single line. This finding indicates that the present study is in reasonable agreement with that of Olander and Watts.

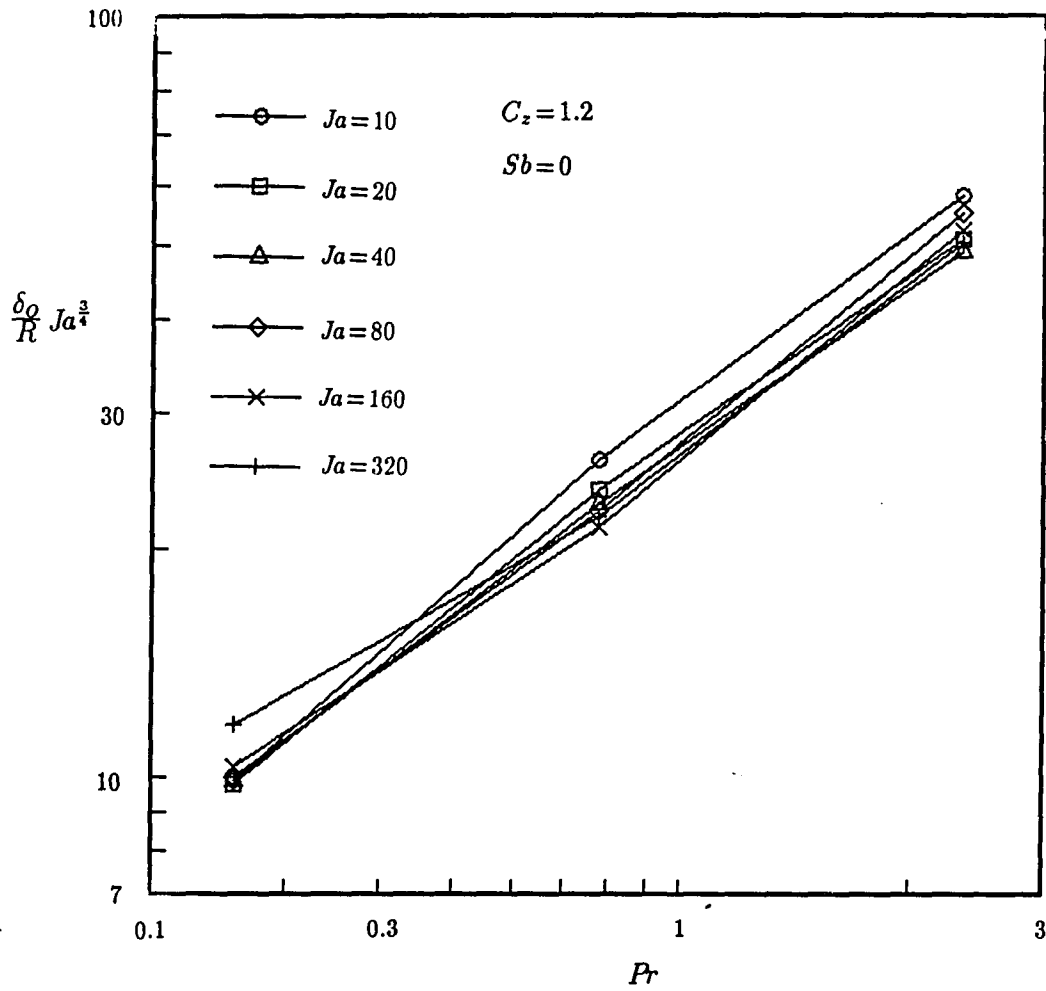


Figure 3.16: Graph illustrating the relationship between $\frac{\delta_0}{R}$, Ja , and Pr

3.11.9 The Relationship of R and t

The question of determination of bubble radius as a function of time can be seen to be the most important question in the literature. Based on dimensional analysis, Cooper, Judd, and Pike [22] have established that the factor $\frac{Ja}{\sqrt{Pr}}$ must be one of the important parameters determining any of the bubble characteristics. They state that the role of Pr in bubble growth has not been clear from their research. They have adopted the relation

$$R = \text{constant } Ja \sqrt{t} \quad (3.48)$$

(without Pr) where the constant is equal to 2 ($\pm 10\%$). This relation has also been found to hold true in the present study and by other researchers for homogeneous boiling (see Section 2.6.2). After extensive testing in positive, negative, and zero gravity in saturated and subcooled boiling, Cooper and Chandratilleke [35] and also Cooper [37] have again suggested Eq. 3.48. However, Cooper, Judd, and Pike note that some details are lost in adoption of Eq. 3.48 since the Prandtl number *does* enter into the determination of R through the equation of microlayer formation (Eq. 3.20).

Assuming $q_c \ll q_m$, Cooper [17] has derived the following relations for the cases $T_h - T_{sat} \gg T_h - T_{bs}$ and $T_h - T_{sat} \gg T_{bs} - T_{sat}$ respectively:

$$R \doteq 2.5 \frac{Ja}{\sqrt{Pr}} \sqrt{t} \quad T_h - T_{sat} \gg T_h - T_{bs} \quad (3.49)$$

and

$$R \doteq 1.12 \frac{Ja}{K} \sqrt{\lambda t} \quad T_h - T_{sat} \gg T_{bs} - T_{sat} \quad (3.50)$$

The former case represents a poorly conducting liquid on a highly conducting wall in which case the wall temperature will remain nearly constant (equal to T_h) during the

bubble's life time. The later case represents sufficiently conducting liquid in which case wall temperature will soon fall nearly to saturation temperature during bubble growth.

The present results, along with experimental findings of various researchers were plotted with equations 3.48–3.50 in mind. Figure 3.17 is a plot of η_1 (which is equal to $\eta \sqrt{Pr}$) against Ja . The lines represent computational results of the present study and each discrete point is an experimental finding from the literature and represents growth of a single bubble (same as in Figure 2.20). Each line segment connecting experimental points represents many bubbles with same experimental conditions (a single experiment). As mentioned in Chapter 2, the values of η for experimental data were found from the parabola of best fit using a regression analysis with help of a computer program. The description of the experimental data is given in Table 3.6. ΔT_e is the excess surface temperature above the saturation temperature of liquid at the system pressure.

The values of η_2 (which is equal to $\eta Pr^{\frac{1}{4}}$) is plotted against Ja in Figure 3.18. When the quantity η was plotted against Ja , the scatter was more than the above two plots.

In order to determine the constants C and m in the relation $\eta = C Ja^m$, a linear regression analysis was performed with the logarithm of values of the independent and dependent coordinates in Figure 3.17 and Figure 3.18. In Table 3.7 is given the best fit values of C and m along with the number of data points (N), and the standard correlation coefficient (ρ). The correlation coefficient is an indicator of the deviation of the data points from the best fit straight line. Note that the lines of computational results in Figure 3.17 are moving up as Ja is increased. In Figure

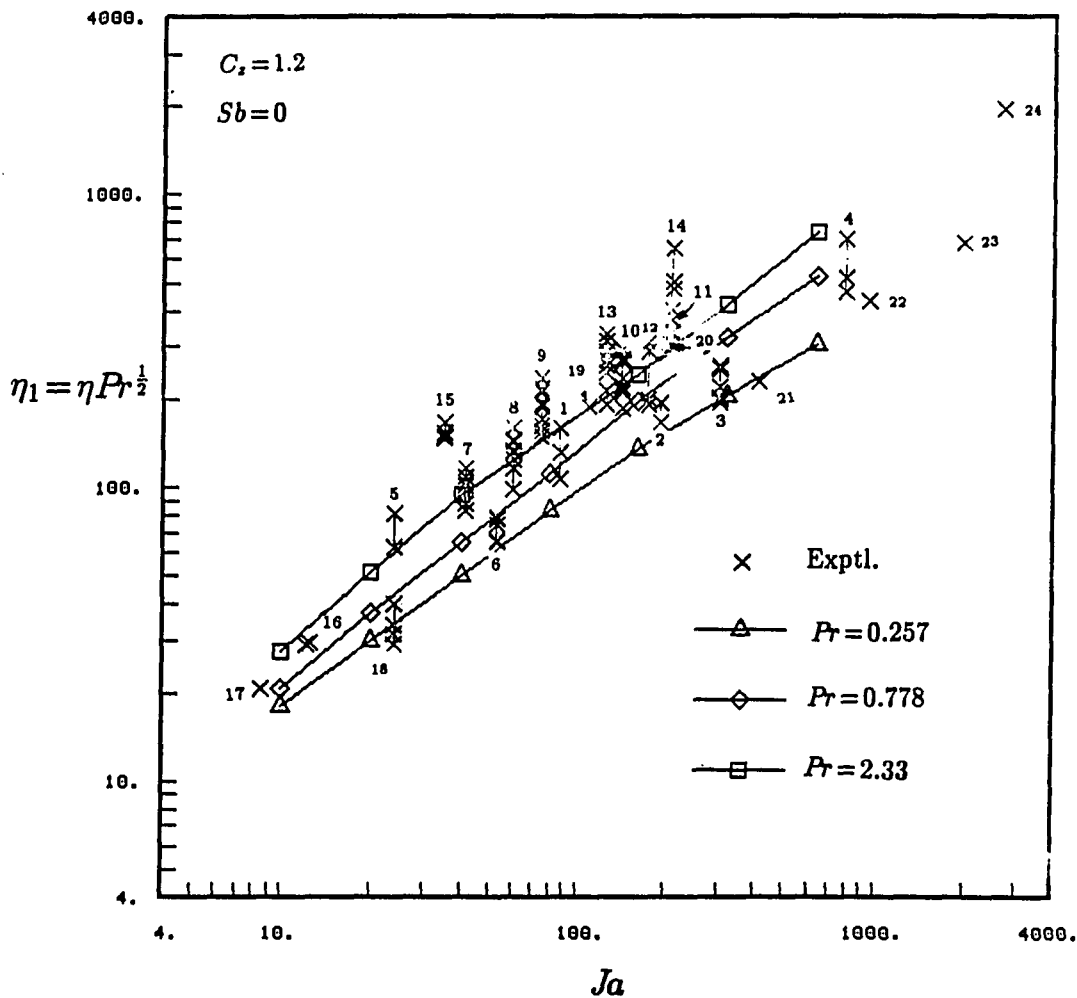


Figure 3.17: Relationship of $\eta_1 = \eta Pr^{\frac{1}{2}}$ with Ja (experimental and computational) where $\eta = \bar{R} / \sqrt{\alpha_l \bar{t}}$

Table 3.6: Description of bubble growth data from the literature

	Reference	Fluid	Ja	P atm	ΔT_e °C	$q'' \frac{W}{m^2 \times 10^4}$	Pr
1	Cole and Shulman [34]	Water	87.7	0.47	15.0	6.28	2.21
2	— " —	Water	191.0	0.26	18.3	4.76	2.75
3	— " —	Water	301.0	0.13	15.0	3.74	3.65
4	— " —	Water	792.0	0.07	20.6	6.62	4.25
5	— " —	N-pentane	239.0	1.00	17.2	2.92	4.2
6	— " —	N-pentane	528.0	0.69	27.8	2.46	4.43
7	— " —	Methanol	41.2	0.71	17.8	2.90	5.3
8	— " —	Methanol	59.6	0.52	20.0	2.89	5.6
9	— " —	Methanol	74.6	0.40	20.0	2.33	5.8
10	— " —	Methanol	140.5	0.27	26.7	2.81	6.28
11	— " —	Methanol	209.0	0.18	27.8	3.31	6.91
12	— " —	C-tetracloride	175.0	0.18	28.9	2.24	4.5
13	— " —	Acetone	124.0	0.29	27.2	4.23	4.37
14	— " —	Toluene	210.0	0.06	13.3	1.88	6.46
15	Sernas and Hooper [14]	Water	34.9	N.A. ^a	N.A.	N.A.	1.75
16	Plesset and Zwick [71]	Water	12.0	N.A.	N.A.	N.A.	1.75
17	Forster and Zuber [72]	Water	8.53	N.A.	N.A.	N.A.	1.75
18	Lee and Nydahl [32]	Water	23.7	N.A.	N.A.	N.A.	1.75
19	van Stralen et al [39]	Water	108.0	0.26	N.A.	5.32	2.73
20	— " —	Water	203.0	0.20	N.A.	3.84	2.95
21	— " —	Water	412.0	0.13	N.A.	5.46	3.65
22	— " —	Water	956.0	0.08	N.A.	5.89	4.17
23	— " —	Water	1982.0	0.04	N.A.	5.38	4.55
24	— " —	Water	2689.0	0.02	N.A.	14.0	4.75

a: Not available

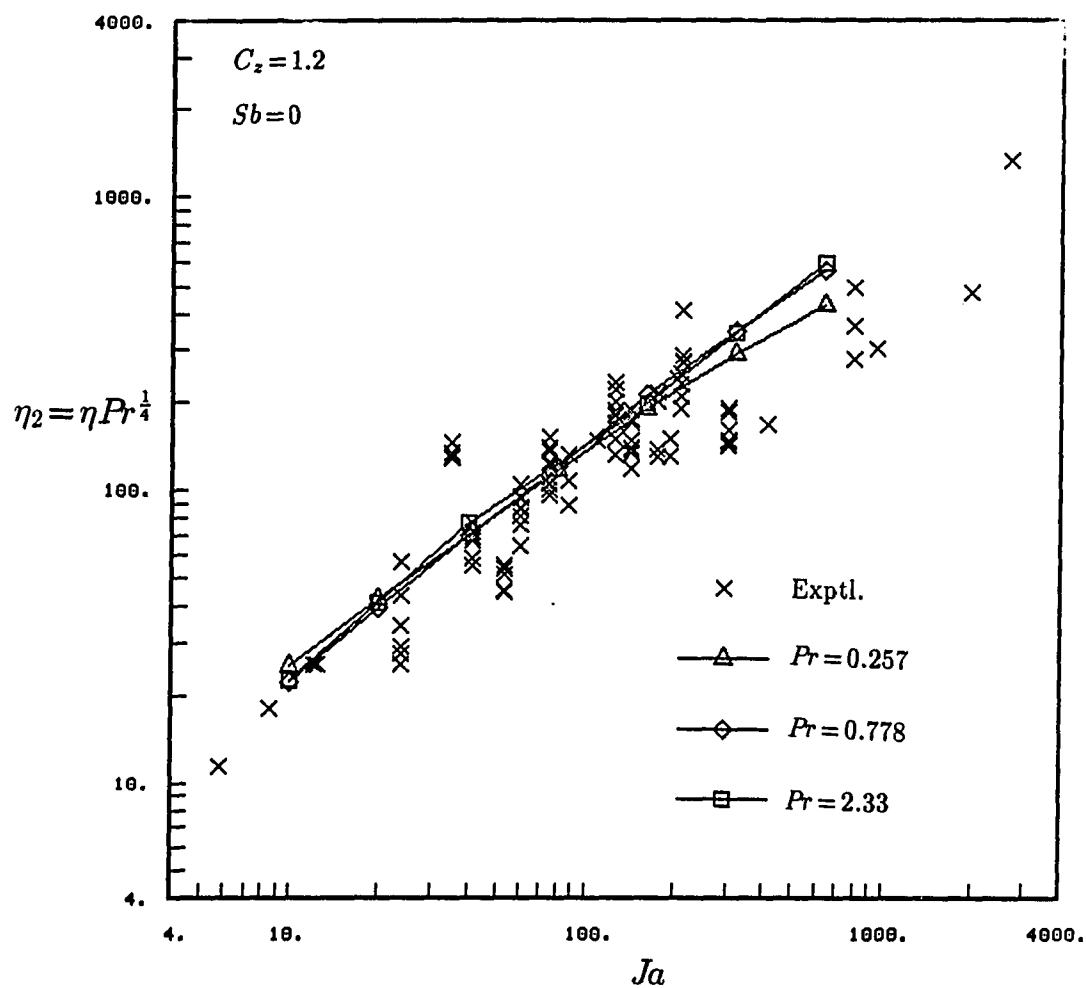


Figure 3.18: Relationship of $\eta_2 = \eta Pr^{\frac{1}{4}}$ with Ja (experimental and computational), where $\eta = \bar{R} / \sqrt{\alpha_1 t}$

Table 3.7: Regression analysis with the data in Figures 3.17 and 3.18

Figure	Description	N	C	m	ρ
3.17	Experimental points	97	9.83	0.61	0.840
3.17	Computational points	20	4.06	0.75	0.971
3.18	Experimental points	97	6.22	0.64	0.890
3.18	Computational points	20	4.38	0.75	0.997

3.18 the computational lines have more or less merged into each other. The values of C (which indicates intercept of best fit line with the vertical axis) in third and fourth rows in Table 3.7 are closer than those in first and second rows, and similar observation holds for the values of m (slope of the best fit line). This indicates that η_2 correlates bubble growth better than η_1 . The true value of power of the Prandtl number in the radius growth relation must be closer to $\frac{1}{4}$ than to either $\frac{1}{2}$ or 0.

Cole and Shulman [34] have arrived at the value of m to be 0.75. The present computational findings point to the same value. The underprediction of the value of m from the experimental data may be due to insufficient number of data. More experimental data points may perhaps allow more accurate conclusions. If the true value of m is believed to be $\frac{3}{4}$, the bubble growth relation in saturated boiling is

$$R = \text{const} \frac{Ja^{\frac{3}{4}}}{Pr^{\frac{1}{4}}} \sqrt{t}. \quad (3.51)$$

Thus the dependence of R on Ja and Pr is inbetween the predictions of Eq. 3.49 and Eq. 3.50 wherein the powers of Pr are $-\frac{1}{2}$ and zero respectively. From figures 3.9 and 3.10 it is clear that neither of the two assumptions ($T_h - T_{sat} \gg T_h - T_{bs}$ and $T_h - T_{sat} \gg T_{bs} - T_{sat}$) hold strictly, and hence, perhaps the power of Pr is in between zero and one-half.

The trend in the experimental data points shows a downward bending at both

ends. This may be explained if the bulk fluid is assumed to be slightly subcooled. In Figure 3.19, the computational results are shown for various subcooling numbers. Note that even for a small subcooling number, the plots are curved. The subcooling number is the ratio of $T_{sat} - T_{\infty}$ to $T_h - T_{sat}$, and hence at subcooling number as small as 0.0625, T_{∞} is within 1 °C of T_{sat} if $T_h - T_{sat}$ is at least 16 °C.

A plot of m against Ja at various values of subcooling number (similar to Figure 2.14) for the third generation model is shown in Figure 3.20. In the same manner as in the second generation model, the values of m decrease as Ja is increased and subcooling is increased for the range of Ja in the figure. The higher the Jakob number, the smaller is m . For sufficiently large values of Ja and Sb the value of m may become quite small as predicted in the second generation model. The high subcooling case may be of industrial importance under certain cases when liquid is preheated and boiled in the same vessel.

One interesting comparison with the present work can be made using the relationship for bubble growth on a surface as given by Mikic et al. [24]. When used for saturated boiling it yields a radius versus time relation such that radius asymptotically approaches a fixed value in case $\frac{t_w}{\tau} \rightarrow 0$ with a finite value of waiting time, t_w . The present work predicts that R is seen to grow proportional to the square root of time for saturated boiling on a surface as $t \rightarrow \infty$, however.

3.11.10 The Constant C_z of Microlayer Formation

The microlayer formation constant (C_z) has been cast as a free parameter in the present study (see Eq. 3.2). Cooper and Lloyd [7] have predicted analytically that the value of C_z must be unity. However, they point out that $C_z = 0.8$ best

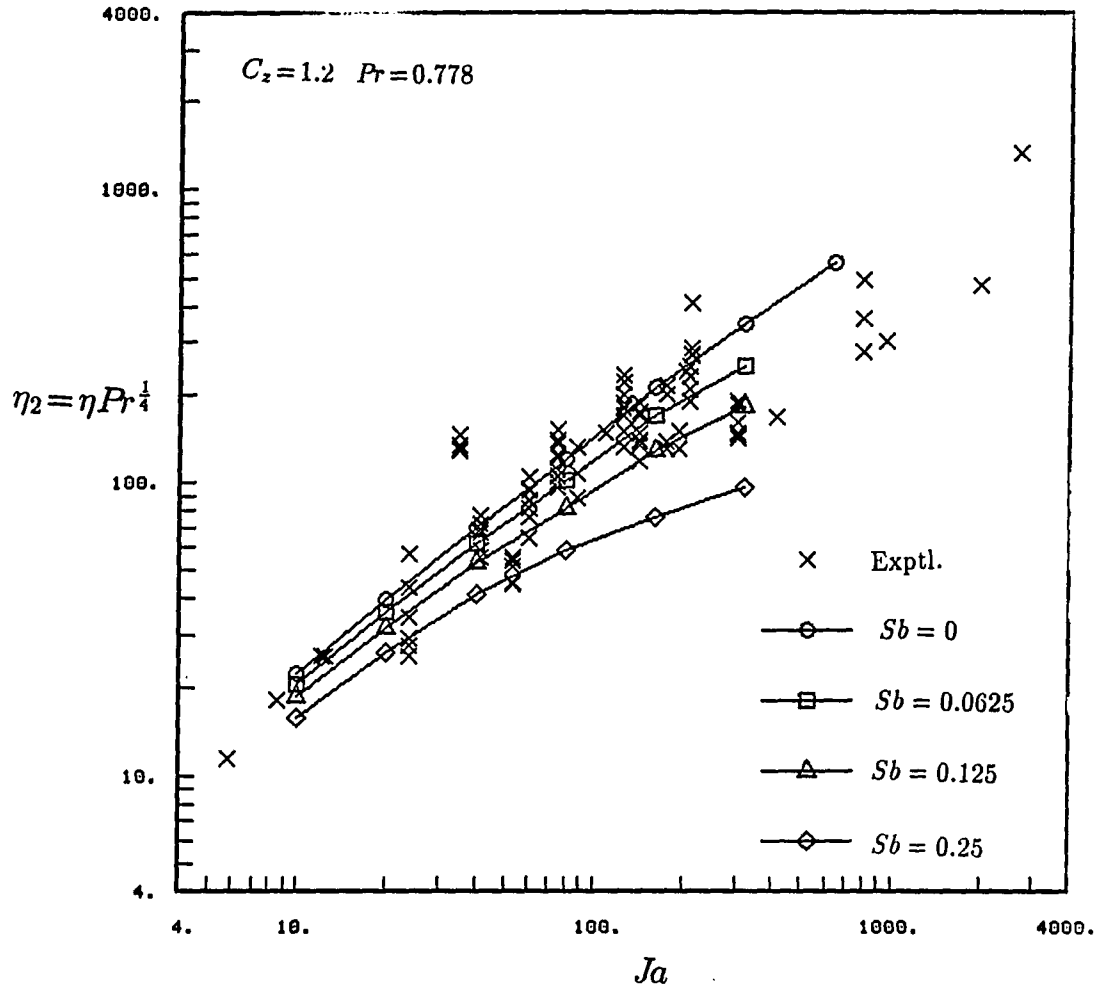
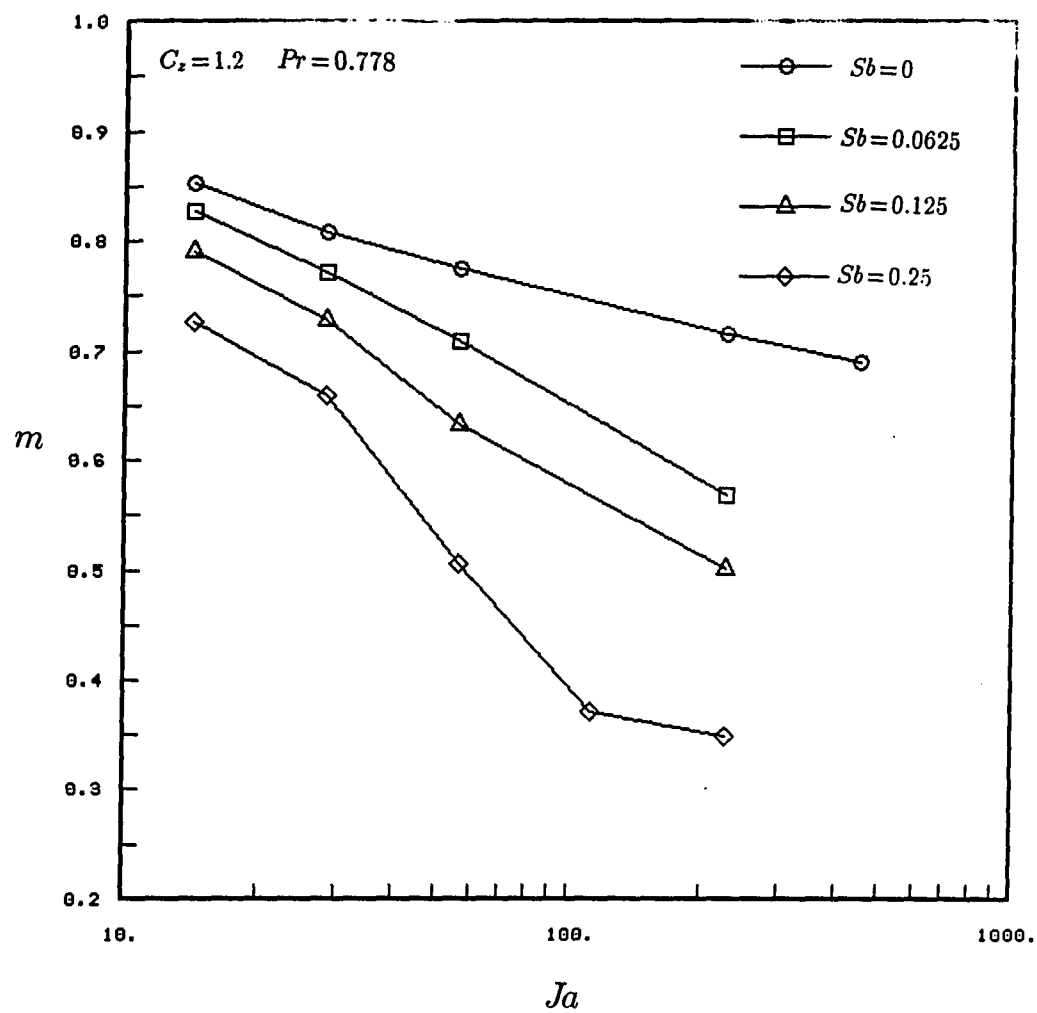


Figure 3.19: Relationship of $\eta_2 = \eta Pr^{\frac{1}{4}}$ with Ja in subcooled boiling where $\eta = \bar{R} / \sqrt{\alpha_l t}$

Figure 3.20: The exponent m versus Ja

explained their experimental findings. Dwyer and Hsu have analytically predicted the value of C_z to be 0.886. van Ouwerkerk [16] analytically derived the value to be 1.2728. Lee and Nydahl have reported that their computational results with value of $C_z = 1$ fitted the experimental data very well. The matching of computation and the experimental data in Figure 3.18 suggests that the best value of C_z is at least as large as 1.2. When $C_z = 1$ and $C_z = 0.8$ were tried, the computational lines moved up by an approximate factor of 1.08 each case respectively (the experimental points do not change). In Figure 3.21 are shown the values of $\eta Pr^{\frac{1}{4}}$ versus Jakob number of the computational results of the third generation model with various values of C_z . The experimental data points and the computational results of the second generation model of $Pr = 1$ are also shown for comparison.

3.12 Conclusions

The following conclusions were drawn from the third generation model.

- The homogeneous boiling model predicted the same amount of bubble growth as the heterogeneous model with microlayer in saturated boiling when T_∞ in the former was equal to T_h in the later.
- The pressure in the bubble was almost equal to the P_∞ except in the extremely short initial period.
- The solution to the problem exhibited similarity at large values of time.
- For Ja ranging from 10 to 640, the bubble was found to grow well beyond the thermal boundary layer on the heated surface in saturated or subcooled boiling.

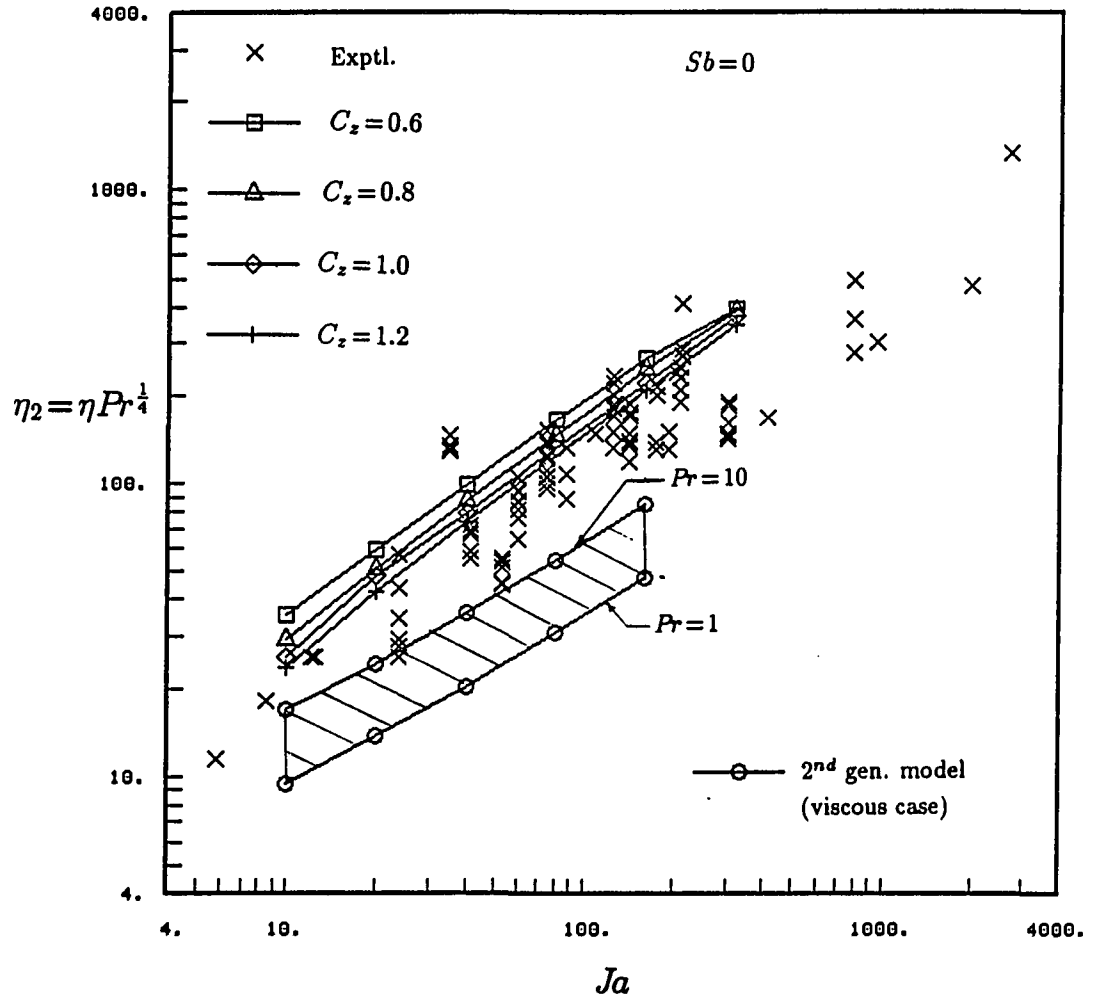


Figure 3.21: Relationship of $\eta_2 = \eta Pr^{\frac{1}{4}}$ with Ja with various values of C_z where $\eta = \bar{R} / \sqrt{\alpha_1 \bar{t}}$

- Most evaporation at the cap portion occurs close to the heated surface.
- There is negligible condensation at the bubble cap in saturated boiling. In subcooled boiling the ratio of evaporation at the cap (which occurs close to the heated surface) to the net condensation at the cap ranged from 0.0011 to 7.18 ($10 \leq Ja \leq 640, 0.0625 \leq Sb \leq 1, 0.26 \leq Pr \leq 2.33$).
- The ratio of positive component of the mass flow into the bubble at the liquid vapor interface (at the microlayer and at the cap) to the net mass flow into the bubble in saturated boiling is close to unity. In subcooled boiling, the above ratio ranged from 1.038 to 7.56 ($10 \leq Ja \leq 640, 0.0625 \leq Sb \leq 1, 0.26 \leq Pr \leq 2.33$). The higher the Ja and/or Sb , the higher the ratio.
- The local rate of volume evaporated per unit radius ($\frac{\partial \dot{V}_m(r)}{\partial r}$) from the microlayer was a constant function of radius (except at the tail where it was large), indicating that the local heat flux at the base of the microlayer is inversely proportional to the square of the radius.
- The ratio of microlayer evaporation to the evaporation at the cap in saturated boiling is of the order 10 at Ja in the lower range and Pr in the higher range of those presently studied (i.e. $Ja \simeq 10, Pr \simeq 2.5$), but increases to 100 ($Ja \simeq 80, Pr \simeq 1$) and even to 500 ($Ja \simeq 320, Pr \simeq 0.2$) as Ja increases and Pr decreases.
- At subcooling number from 0.0625 to 1 the above ratio is negative and ranges approximately from -1 to -5 for Ja in the range 10 to 320.
- The microlayer profiles were wedge like in shape, almost linear, except at the tail where they were steep. At Ja approximately higher than 160, the profile

appeared slightly curved such that they appeared convex from the top.

- The ratio of initial microlayer height to the bubble radius obey the following relationship

$$\frac{\delta_o}{R} = 0.279 \left(\frac{Ja}{Pr} \right)^{\frac{3}{4}}.$$

- The region close to the tail of the microlayer was the coolest in the heated surface. Small local minimum was seen in the temperature in the heated surface at the corner of the heated surface and the bubble. Most of the heat flow in the heated surface was directed toward the tail of the microlayer.
- There was no “uniform wrapping” of superheated thermal boundary layer in the computational results as postulated in the “bulk convection” or “liquid-vapor exchange” theories proposed by some researchers in the literature.
- The following relation was found to fit best the present computational data and also the experimental data in the literature.

$$R = \text{const} \frac{Ja^{\frac{3}{4}}}{Pr^{\frac{1}{4}}} \sqrt{t}.$$

- The best value of growth constant C_z in the microlayer formation equation $\delta_o = C_z \sqrt{t}$ is at least 1.2.

4. GENERAL CONCLUSIONS

An in-depth analysis of the problem of bubble growth on a heated surface has been made in the present study. The investigation comprised of three different numerical models developed in sequence such that each successive model increased in complexity. The first generation model (growth of a hemispherical bubble in an *inviscid* medium on an uniformly heated surface) had already been developed by Joshi [68]. The second and third generation models form the scope of the present study. Hemispherical bubble growth in *viscous* fluid on an uniformly heated surface was analyzed in the second generation model. The major findings from the second generation model are that the problem has a similarity solution, and *only* Ja and Sb dictate growth of a bubble without a microlayer at large values of time. The difference in the growth rates of viscous and inviscid medium was found to be fairly small; of the order 10% for many cases of practical interest. The Pr number effect was found to be negligible in the second generation model. When compared with the experimental data, the second generation model underpredicted the growth. This suggested that microlayer contribution was important.

The governing equations for the microlayer, for the temperature distribution in the heated surface, and for the non-condensing gas inside the bubble were added to the second generation model to form the third generation model. For computational

ease, the third generation model was only run with the vorticity set equal to zero, *a priori* (inviscid flow). This helped reduce the execution time to a large extent, and allowed a reasonable number of runs within the computational resources. Given the results from the second generation model, the inviscid calculations should be quite reasonable.

The major finding of the third generation model is that the microlayer evaporation is a predominant mechanism for bubble growth. Microconvection is negligible at Jakob numbers approximately higher than 100 (see Figure 3.15). The "bulk convection" theory (see Section 1.2.2 and Section 3.11.3) was found to be questionable from the results of both the second and the third generation models. As in the second generation model, the third generation model also exhibits a similarity solution at large times. In this asymptotic regime, the homogeneous boiling and heterogeneous saturated boiling predicted very similar growth rates for equal Jakob numbers as reported in the literature. The predicted microlayer shape appeared wedgelike except at the tail of the microlayer, where the profile was very steep. The bubble growth in the asymptotic phase was dictated only by Jakob, Prandtl, and subcooling numbers. The constant C_z in the microlayer formation equation was found to be at least 1.2. Finally, the asymptotic bubble growth relation in heterogeneous saturated boiling for $Ja > 20$ was found to be

$$R = \text{const} \frac{Ja^{\frac{3}{4}}}{Pr^{\frac{1}{4}}} \sqrt{t}. \quad (4.1)$$

The value of exponent of Ja generally decreased as Sb or Ja were increased. The value of the constant was approximately 5.

5. LIMITATIONS OF THE PRESENT STUDY AND SCOPE OF THE FUTURE WORK

The present study has covered nucleate boiling over a wide range of applications, however, due to the complexity of the process, the results may not be applicable in all cases. The limitations that arise due to various assumptions that form the base of the model are discussed below as also some possible future work for better understanding of nucleate boiling.

The temperatures in the fluid and in the heated surface at the beginning of growth may not be uniform as assumed in the present model. Due to the repeated growth and detachment of bubbles, an approximate cyclic pattern in the temperature distribution in the fluid has been reported by some researchers [73] [56] [57]. The heated surface, however, has been observed to reach uniform temperature quickly in the waiting period due to its high thermal diffusivity [73]. If available, actual temperature distribution in the fluid and the heated surface, can be used in the present computational model.

The bubble growth is usually observed to begin at a crevice. The present study modeled growth on a flat surface, however, this should not be seen as a limitation of the present model because the bubble growing on a crevice does assume a hemispherical shape as soon as it grows larger than the crevice. Further, from the third

generation model, the effect of non-condensable gas has been seen to diminish very soon.

The knowledge of formation mechanism of the microlayer is very important before accurate predictions of bubble growth can be made. Cooper, Judd, and Pike [22] have pointed out that surface tension may be an important parameter in the formation. This parameter has been omitted in most analyses in the literature, and only viscous forces and inertia forces are accounted for. A numerical technique may be developed either to model the dynamics at the formation of the microlayer or to predict the shape of entire bubble including the microlayer. Kenning and Cooper [47], Scriven [51], and Sternling and Scriven [42] have described equations of dynamics of fluid interface. However, accurate predictions of pressure and shear at the bubble surface will be required for which a viscous model is essential for calculation over the fluid region. The Marangoni effect may be important *locally* at the point of formation of the microlayer. Groenveld [79], Kenning [44], Kenning and Cooper [47] have described governing equation of the marangoni effect.

The present model does not take into account the effect of neighboring bubbles. The locations of bubble growth are known to exhibit a statistical nature, about which sufficient information is not available. The present model also does not account for motion in the bulk fluid imposed by external means, such as a cross flow. The bubble surface will not get "locked" (Figure 1.3) in this case. Kenning and Cooper [48] have observed flow on a bubble surface in case of a cross flow. Due to the non-axisymmetric temperature distribution, the Marangoni effect may be important in this situation.

Additional experimental work would be extremely useful in the understanding of nucleate boiling. The areas of verification of the present hypotheses or additional

study are:

- Temperature distribution in the heated surface
- Bubble shape
- Importance of Marangoni effect
- Formation mechanism of the microlayer
- Microlayer thickness
- Flow field within the microlayer (does the liquid in the microlayer get 'squeezed out' into the bulk fluid?)
- Departure mechanism of the bubble
- "Scavenging effect" (increased heat transfer during the detachment process)

Due to the small size of the bubble, difficulties have been reported in making the above-mentioned measurements. Hopefully, better experimental techniques will be available in the near future.

With the help of systematic experimentation progressively increasing in complexity, similar to that of Cooper [17], Cooper [37] Cooper and Chandratilleke [35], Cooper, Judd, and Pike [22], the relationship between important non-dimensional parameters can be identified. Most of the above description pertains to growth of a single bubble. As depicted in Figure 1.2, many other data are needed before results can be applied in practice.

BIBLIOGRAPHY

- [1] Hsu, Y. Y. and Graham, R. W. *Transport Processes in Boiling and Two-Phase Systems*. Americal Nuclear Society, Inc., 1986.
- [2] Rayleigh, Lord. On the pressure developed in a liquid during the collapse of a spherical cavity. *Philosophical Magazine*, 34:94-98, 1917.
- [3] Engelberg-Forster, Kurt and Greif, R. Heat transfer to a boiling liquid - mechanism and correlations. *J. Heat Transfer*, page 43, Feb 1959.
- [4] Gunther, F. C. and Kreith, F. Photographic study of bubble formation in heat transfer to subcooled water. In *Progress Report No. 4-120*, California Institute of Technology, March 1950. Jet Propulsion Laboratory.
- [5] Snyder, N. W. and Robin, T. T. Mass-transfer model in subcooled nucleate boiling. *Trans. A.S.M.E.*, page 404, Aug 1969.
- [6] Moore, F. D. and Mesler, R. B. The measurement of rapid surface temperature fluctuations during nucleate boiling. *A.I.Ch.E. Journal*, 7:629, 1961.
- [7] Cooper, M. G. and Lloyd, A. J. P. The microlayer in nucleate pool boiling. *Int. J. Heat Mass Transfer*, 12:895-913, 1969.
- [8] Rogers, Thomas F. and Mesler, Russell B. An experimental study of surface cooling by bubbles during nucleate boiling of water. *A.I.Ch.E. Journal*, page 656, Sept 1964.
- [9] Mesler, Russell. A mechanism supported by extensive experimental evidence to explain high heat fluxes observed during nucleate boiling. *A.I.Ch.E. Journal*, 22:246, Mar 1976.
- [10] Yu, Chi-Liang and Mesler, Russell B. A study of nucleate boiling near the peak heat flux through measurement of transient surface temperature. *Int. J. Heat Mass Transfer*, 20:827-840, 1977.

- [11] **Hospeti, N. B. and Mesler, R. B.** Vaporization at the base of bubbles of different shape during nucleate boiling of water. *A.I.Ch.E. Journal*, page 214, Mar 1969.
- [12] **Katto, Y. and Shoji, M.** Principal mechanism of Micro-Liquid-Layer formation on a solid surface with a growing bubble in nucleate boiling. *Int. J. Heat Mass Transfer*, 13:1299-1311, 1970.
- [13] **Kotake, Susumu.** On the liquid film of nucleate boiling. *Int. J. Heat Mass Transfer*, 13:1595-1606, 1970.
- [14] **Sernas, V. and Hooper, F. C.** The initial vapor bubble growth on a heated wall during nucleate boiling. *Int. J. Heat Mass Transfer*, 12:1627-1639, 1969.
- [15] **Yesin, A. O. and Jeffers, D. E.** Bubble growth in transient pool boiling. *J. Br. Nuc. Energy Soc.*, 8(4):267-274, 1969.
- [16] **van Ouwerkerk, H. J.** The rapid growth of vapor bubble at a liquid-solid interface. *Int. J. Heat Mass Transfer*, 14:1415-1431, 1971.
- [17] **Cooper, M. G.** The microlayer and bubble growth in nucleate pool boiling. *Int. J. Heat Mass Transfer*, 12:915-933, 1969.
- [18] **Koffman, L. D. and Plesset, M. S.** Experimental observations of the microlayer in vapor bubble growth on a heated solid. *J. Heat Transfer*, 105:625, Aug 1983.
- [19] **Dwyer, O. E. and Hsu, C. J.** Liquid microlayer thickness in nucleate boiling on a heated surface. *Letters in Heat Mass Transfer*, 2:179, 1975.
- [20] **Voutsinos, C. M. and Judd, R. L.** Laser interferometric investigations of the microlayer evaporation phenomenon. *Trans. A.S.M.E.*, page 88, Feb 1975.
- [21] **Olander, R. R. and Watts, R. G.** An analytical expression of microlayer thickness in nucleate boiling. *Trans. A.S.M.E.*, page 178, Feb 1969.
- [22] **Cooper, M. G. and Judd, A. M. and Pike, R. A.** Shape and departure of single bubbles growing at a wall. In *Sixth Int. Heat Transfer Conference, Toronto, Canada*, pages 115-120, Aug 7-11 1978.
- [23] **Scriven, L. E.** On the dynamics of phase growth. *Chemical Engineering Science*, 10:1-13, 1959.

- [24] Mikic, B. B. and Rohsenow, W. M. and Griffith, P. On bubble growth rates. *Int. J. Heat Mass Transfer*, 13:657-666, 1970.
- [25] Han, Chi-Yeh and Griffith, Peter. The mechanism of heat transfer in nucleate pool boiling-Part I. *Int. J. Heat Mass Transfer*, 8:887-904, 1965.
- [26] Han, Chi-Yeh and Griffith, Peter. The mechanism of heat transfer in nucleate pool boiling-Part II. *Int. J. Heat Mass Transfer*, 8:905-914, 1965.
- [27] Mikic, B. B. and Rohsenow, W. M. A new correlation of pool-boiling data including the effect of heating surface characteristics. *J. Heat Transfer*, 91:245-250, 1969.
- [28] van Stralen, S. J. D. and Sluyter, W. M. Local temperature fluctuations in saturated pool boiling of pure liquids and binary mixtures. *Int. J. Heat Mass Transfer*, 12:187-198, 1969.
- [29] Judd, R. L. and Hwang, K. S. A comprehensive model for nucleate pool boiling heat transfer including microlayer evaporation. *J. Heat Transfer*, page 623, Nov 1976.
- [30] van Stralen, S. J. D. The mechanism of nucleate boiling in pure liquids and in binary Mixtures-Part I. *Int. J. Heat Mass Transfer*, 9:995-1020, 1966.
- [31] van Stralen, S. J. D. The mechanism of nucleate boiling in pure liquids and in binary Mixtures-Part II. *Int. J. Heat Mass Transfer*, 9:1021-1046, 1966.
- [32] Lee, R. C. and Nydahl, J. E. Numerical calculation of bubble growth in nucleate boiling from inception through departure. In A. F. Emery, editor, *The Winter Annual Meeting of A.S.M.E.*, pages 25-30, United Engineering Centre, 345 East 47th street, New York, N.Y. 10017, Dec 13-18 1987. Heat Transfer Division, The Americal Society of Mechanical Engineers.
- [33] Fath , H. S. and Judd , R. L. Influence of system pressure on microlayer evaporation heat transfer. *J. Heat Transfer*, 100:49, Feb 1978.
- [34] Cole, R. and Shulman H. L. Bubble growth rates at high jakob numbers. *Int. J. Heat Mass Transfer*, 9:1377-1390, 1966.
- [35] Cooper, M. G. and Chandratilleke, T. T. Growth of diffusion-controlled vapor bubbles at a wall in a known temperature gradient. *Int. J. Heat Mass Transfer*, 24:1475-1492, 1981.

- [36] Saini, J. S., and Gupta, C. P. and Lal, S. Evaluation of microlayer contribution to bubble growth in nucleate pool boiling using a new bubble growth model. *Int. J. Heat Mass Transfer*, 18:469-472, 1975.
- [37] Cooper, M. G. Growth and departure of individual bubbles at a wall. *Applied Scientific Research*, 38:77-84, 1982.
- [38] Joosten, J. G. and Zijl, W. and van Stralen, S. J. D. Growth of a vapor bubble in combined gravitational and Non-Uniform temperature fields. *Int. J. Heat Mass Transfer*, 21:15-23, 1978.
- [39] van Stralen, S. J. D. and Cole, R. and Sluyter W. M. and Sohal, M. S. Bubble growth rates in nucleate boiling of water at subatmospheric pressures. *Int. J. Heat Mass Transfer*, 18:655-669, 1975.
- [40] Zijl, W. and Ramakers, F. J. M. and van Stralen, S. J. D. Global numerical solutions of growth and departure of a vapour bubble at a horizontal superheated wall in a pure liquid and a binary mixture. *Int. J. Heat Mass Transfer*, 22:401-420, 1979.
- [41] Zysin, L. V. and Feldberg, L. A. and Dobkes A. L. and Sazhenin, A. G. Allowance for optical distortion produced by temperature gradients, in investigating the shape of vapor bubbles generated on a flat wall. *Heat Transfer Sov. Res.*, 12(2), Mar-Apr 1980.
- [42] Sternling, C. V. and Scriven, L. E. Interfacial turbulence: Hydrodynamic instability and the marangoni effect. *A.I.Ch.E. Journal*, page 514, Dec 1959.
- [43] Groenveld, P. Low capillary number withdrawal. *Chem. Eng. Sc.*, 25:1259-1266, 1970.
- [44] Kenning, D. B. R. Two-phase flow with nonuniform surface tension. *Applied Mechanics Review*, 21:1101, Nov.1968.
- [45] Huplic, V. and Raithby, G. D. Surface-tension effects in boiling from a Downward-facing surface. *J. Heat Transfer*, page 403, Nov 1972.
- [46] Kenning, D. B. R. Hydrodynamics of surface films: Modelling laws for two-phase flows containing dilute surfactant. *Proc Instn Mech Engrs*, 182:320, 1967.
- [47] Kenning, D. B. R. and Cooper, M. G. Interfacial circulation due to surface-active agents in steady two-phase flows. *J. Fluid Mech*, 24:293-306, 1966.

- [48] Kenning, D. B. R. and Cooper, M. G. Flow patterns near nuclei and the initiation of boiling during forced convection heat transfer. *Proc Instn Mech Engrs*, 180:112, 1965.
- [49] Scriven, L. E. and Sternling, C. V. On cellular convection driven by surface-tension gradients: Effects of mean surface tension and surface viscosity. *J. Fluid Mech.*, 19:321, 1964.
- [50] Yih, Chia-Shun. Fluid motion induced by surface-tension variation. *The Physics of Fluids*, 11:477, Mar 1968.
- [51] Scriven, L. E. Dynamics of a fluid interface. *Chemical Engineering Science*, 12:98, 1960.
- [52] Fritz. Maximum volume of vapor bubbles. *Physik Zeitschr*, 36:379-384, 1935.
- [53] Cole, R. and Shulman, H. L. Bubble departure diameters at subatmospheric pressures. *Chem. Eng. Prog. Symp.*, 64:series 62, 6-16, 1966.
- [54] Nishikawa, Kaneyasu and Fujita, Yasunobu. Correlation of nucleate boiling heat transfer based on bubble population density. *Int. J. Heat Mass Transfer*, 20:233-245, 1977.
- [55] Jensen, M. K. and Memmel, G. J. Evaluation of bubble departure diameter correlations. In *Proc. Eighth Int. Heat Transfer Conf., San Francisco, U.S.A.*, volume 4, pages 1907-1912, Aug 17-22 1986.
- [56] Marcus, B. D. and Dropkin, D. Measured temperature profiles within the superheated boundary layer above a horizontal surface in saturated nucleate pool boiling of water. *J. Heat Transfer*, page 333, Aug 1965.
- [57] Wiebe, J. R. and Judd, R. L. Superheat layer thickness measurements in saturated and subcooled nucleate boiling. *J. Heat Transfer*, page 455, Nov 1971.
- [58] Hsu, Y. Y. On the size range of active nucleation cavities on a heating surface. *J. Heat Transfer*, 84:No. 3, 207-216, 1962.
- [59] Plesset, Milton and Prosperetti, Andrea. Flow of vapour in a liquid enclosure. *J. Fluid Mech*, 78:433-444, 1976.
- [60] Plesset, Milton S. and Prosperetti, Andrea. The contribution of latent heat transport in subcooled nucleate boiling. *Int. J. Heat Mass Transfer*, 21:725-734, 1978.

- [61] Sultan, M. and Judd, R. L. Spatial distribution of active sites and bubble flux density. *Trans. A.S.M.E.*, 100:56, Feb 1978.
- [62] Yang, S. R. and Kim, R. H. A mathematical model of the pool boiling nucleation site density in terms of the surface characteristics. *Int. J. Heat Mass Transfer*, 31:1127-1135, 1988.
- [63] Shoukri, M. and Judd, R. L. Nucleation site activation in saturated boiling. *J. Heat Transfer*, page 93, Feb 1975.
- [64] Judd, R. L. The influence of subcooling on the frequency of bubble emission in nucleate boiling. *J. Heat Transfer*, 111:747-751, 1989.
- [65] Guy, T. B. and Ledwidge, T. J. Numerical approach to non-spherical vapor bubble dynamics. *Int. J. Heat Mass Transfer*, 16:2393-2406, 1973.
- [66] Witze, C. P. and Schrock, W. E. and Chamber, P. L. Flow about a growing sphere in contact with a plane surface. *Int. J. Heat Mass Transfer*, 11:1637-1652, 1968.
- [67] Hughmark, G. A. A statistical analysis of nucleate boiling. In *A.I.Ch.E. National Meeting*, Cleveland, Ohio, May 1961. Heat Transfer Division, The American Society of Mechanical Engineers.
- [68] Joshi A. A numerical model for nucleate pool boiling. *M.S. Thesis, Mechanical Engineering Dept., Iowa State University*, 1987.
- [69] Anderson D. A., Tannehill J. C., and Pletcher R. H. *Computational Fluid Mechanics and Heat Transfer*. Hemisphere Publishing Corp., New York, 1984.
- [70] Patil, R. K. and Prusa, J. Numerical solutions for asymptotic diffusion controlled growth of a hemispherical bubble on an isothermally heated surface. Minneapolis, July 28-31 1991. A.S.M.E./A.I.Ch.E. National Heat Transfer Conf.
- [71] Plesset, M. S. and Zwick, S. A. The growth of vapor bubbles in superheated liquids. *Journal of Appl. Phys.*, 25:493-500, 1954.
- [72] Forster, H. K. and Zuber, N. Growth of a vapor bubble in a superheated liquid. *Journal of Appl. Phys.*, 25:474-478, 1954.

- [73] Beer, H. and Burow, P. and Best, R. *Bubble Growth, Bubble Dynamics, and Heat Transfer in Nucleate Boiling, Viewed with a Laser Interferometer*. Hemisphere Publishing Corporation, 1977.
- [74] Cooper, M. G. and Vijuk, R. M. Bubble growth in nucleate pool boiling. *Int. J. Heat Mass Transfer*, 26:1091-1097, 1969.
- [75] Carslaw, H. S. and Jaeger. *Conduction of Heat in Solids*. Oxford University Press, London, 1950.
- [76] Prusa, J. and Vande Kamp, L. A numerical solution for melting around multiple horizontal heated cylinders. pages 85-HT-12, 25-30, Denver, Colorado, August 4-7 1985. National Heat Transfer Conference.
- [77] Kotake, Susumu. On the mechanism of nucleate boiling. *Int. J. Heat Mass Transfer*, 9:711-728, 1966.
- [78] Sharp, R. R. The nature of liquid film evaporation during nucleate boiling. *NASA TN-D 1997*, 1964.
- [79] Groenveld, P. Laminar withdrawal with appreciable inertial forces. *Chem. Eng. Sc.*, 25:1267-1273, 1970.
- [80] Levy, S. Generalized correlation of boiling heat transfer. *J. Heat Transfer*, page 37, Feb 1959.
- [81] Moissis, Raphael and Berenson, Paul J. On the hydrodynamic transitions in nucleate boiling. *J. Heat Transfer*, page 221, Aug 1963.
- [82] Scriven, L. E. and Sternling, C. V. On cellular convection driven by surface-tension gradients: Effects of mean surface tension and surface viscosity. *J. Fluid Mech.*, 19:321, 1964.
- [83] Gaertner, R. F. Photographic study of nucleate pool boiling on a horizontal surface. *J. Heat Transfer*, page 17, Feb 1965.
- [84] Han, Chi-Yeh and Griffith, Peter. The mechanism of heat transfer in nucleate pool boiling-Part I. *Int. J. Heat Mass Transfer*, 8:887-904, 1965.
- [85] Han, Chi-Yeh and Griffith, Peter. The mechanism of heat transfer in nucleate pool boiling-Part II. *Int. J. Heat Mass Transfer*, 8:905-914, 1965.
- [86] McGrew, J. L. and Bamford, F. L. and Rehm, T. R. Marangoni flow: An additional mechanism in boiling heat transfer. *Science*, 153:1106-1107, 1966.

- [87] **Harper, J. F. and Moore, D. W. and Pearson, J. R. A.** The effect of variation of surface tension with temperature on the motion of bubbles and drops. *J. Fluid Mech.*, 27:361-366, 1967.
- [88] **Katto, Y. and Yokoya, S.** Principal mechanism of boiling crisis in pool boiling. *Int. J. Heat Mass Transfer*, 11:993-1002, 1968.
- [89] **Cooper, M. G. and Merry, J. M. D.** A general expression for the rate of evaporation of a layer of liquid on a solid body. *Int. J. Heat Mass Transfer*, 16:1811-1815, 1973.
- [90] **van Stralen, S. J. D. and Sohal, M. S. and Cole, R. and Sluyter W. M.** Bubble growth rates in pure and binary systems: Combined effect of relaxation and evaporation microlayers. *Int. J. Heat Mass Transfer*, 18:453-467, 1975.
- [91] **Dalle Donne, M. and Ferranti, M. P.** The growth of vapor bubbles in superheated sodium. *Int. J. Heat Mass Transfer*, 18:477-493, 1975.
- [92] **Yermakov, G. V. and Semenova, N. M.** Dependence of the surface tension and pressure of supersaturated vapor on the radius of curvature of an embryonic droplet. *Heat Transfer Sov. Res.*, 12(2), Mar-Apr 1980.
- [93] **Baranenko, V. I. and Chichkan, L. A.** Thermocapillary convection in the boiling of various fluids. *Heat Transfer Sov. Res.*, 12(2), Mar-Apr 1980.
- [94] **Coutanceau, Madeleine and Thizon, Patrick.** Wall effect on the bubble behaviour in highly viscous liquids. *J. Fluid Mech.*, 107(2):339-373, 1981.
- [95] **Kopp, I. Z.** A new model of nucleation in the boiling of liquids. *Heat Transfer Sov. Res.*, 13(1), Jan-Feb 1981.
- [96] **Buyevich, Yu. A. and Kazenin, D. A. and Mankevich, V. N.** Perturbation methods in the problem of growth of a vapor bubble. *Heat Transfer Sov. Res.*, 14(1), Jan-Feb 1982.
- [97] **Coutanceau, Madeleine and Hajjam, Mohamed.** Viscoelastic effect on the behaviour of an air bubble rising axially in a tube. *Applied Scientific Research*, 38:199-207, 1982.
- [98] **Bhat, A. M. and Prakash, R. and Saini, J. S.** Heat transfer in nucleate pool boiling at high heat flux. *Int. J. Heat Mass Transfer*, 26:833-840, 1983.
- [99] **Glaser, H.** Equilibrium radii of small vapour bubbles and liquid droplets. *Int. J. Heat Mass Transfer*, 27:1439-1443, 1984.

- [100] Nukiyama, Shiro. Memories of my research on boiling. *Int. J. Heat Mass Transfer*, 27:955-957, 1984.
- [101] Nukiyama, Shiro. The maximum and minimum values of the heat q transmitted from metal to boiling water under atmospheric pressure. *Int. J. Heat Mass Transfer*, 27:959-970, 1984.
- [102] Chahine, G. L. and Liu, H. L. Collective effects on the growth of vapor bubbles in a superheated liquid. *Trans. A.S.M.E.*, 106:486, Dec 1984.
- [103] Rajendra Prasad, N. and Saini, J. S. and Prakash, R. The effect of heater wall thickness on heat transfer in nucleate pool-boiling at high heat flux. *Int. J. Heat Mass Transfer*, 28:1367-1375, 1985.
- [104] Abdelghaffar, M. A. and Cornwell, K. On the flow field generated by a growing sphere near a solid plane with application to nucleate boiling. *Int. J. Heat Mass Transfer*, 28:1131-1146, 1985.
- [105] Bhat, A. M. and Saini, J. S. and Prakash, R. Role of microlayer evaporation in pool boiling at high heat flux. *Int. J. Heat Mass Transfer*, 29:1953-1961, 1986.
- [106] Chyu, M.-C. Evaporation of macrolayer in nucleate boiling near burnout. *Int. J. Heat Mass Transfer*, 30:1531-1538, 1987.
- [107] Nishikawa, Kaneyasu. Historical developments in the research of boiling heat transfer. *J.S.M.E. Int. Journal*, 30(264):897-905, 1987.
- [108] Fyodorov, M. V. and Klimenko, V. V. Vapour bubble growth in boiling under quasistationary heat transfer conditions in a heating wall. *Int. J. Heat Mass Transfer*, 32:227-242, 1989.
- [109] Plesset M. S. and Zwick, S. A. The growth of vapor bubbles in superheated liquids. *Journal of Appl. Phys.*, 25:493-500, 1954.
- [110] Lezak, D. and Brodie, L. C. and Semura, J. S. Photographic studies of light induced nucleation of boiling at the interphase of a solid and superheated liquid helium. *Cryogenics*, pages 659-661, 1983.
- [111] Jensen, M. K. and Jackman, D. L. Prediction of nucleation pool boiling heat transfer coefficients of refrigerant-oil mixtures. *J. Heat Transfer*, 106:184-190, 1984.

- [112] **Ibrahim, E. A. and Judd, R. L.** An experimental investigation of the effect of subcooling on bubble growth and waiting time in nucleate boiling. *J. Heat Transfer*, 107:168-174, 1985.
- [113] **Lienhard, J. H.** On the two regimes of nucleate boiling. *J. Heat Transfer*, 107:262-264, 1985.
- [114] **Witzke, M. D. and Schroeder, J. E. and Sgheiza, J. E. and Myers, J. E.** Nucleate boiling site activation by vapor injection. *A.I.Ch.E. Journal*, 31:1229-1230, July 1985.
- [115] **Myers, J. E.** Short-lived sites in nucleate boiling. *A.I.Ch.E. Journal*, 31:1441-1445, Sept 1985.
- [116] **Raina, G. K. and Wanchood, R. K.** Direct contact heat transfer with phase change: Bubble growth and collapse. *Canadian J. Chem. Eng.*, 64:393-398, 1986.
- [117] **Inada, S. and Miyasaka, Y.** Disappearance of a coalescent vapor bubble detached into subcooled water. *J.S.M.E. Int. Journal*, 52:2222-2227, 1986.
- [118] **Creza, M. and Sernas, V.** Nucleate boiling in thermally developing and fully developed laminar falling films. *J. Heat Transfer*, 110:221-228, 1988.
- [119] **Keller, J. R. and Bergman, T. L.** Prediction of conjugate heat transfer in a solid-liquid system: Inclusion of buoyancy and surface tension forces in the liquid phase. *J. Heat Transfer*, 111:690-698, 1989.
- [120] **Dhir, V. K. and Liaw, S. P.** Framework for a unified model for nucleate and transition pool boiling. *J. Heat Transfer*, 111:739-746, 1989.
- [121] **Samant, K. R. and Simon, T. W.** Heat transfer from a small heated region to r-113 and fc-72. *J. Heat Transfer*, 111:1053-1059, 1989.
- [122] **Cooper, P.** Ehd enhancement of nucleate boiling. *J. Heat Transfer*, 112:458-464, 1990.
- [123] **Ulucakli, M. E. and Merte Jr., H.** Nucleate boiling with high gravity and large subcooling. *J. Heat Transfer*, 112:451-457, 1990.
- [124] **Dix, D. and Orozco, J.** An experimental study in nucleate boiling heat transfer from a sphere. *J. Heat Transfer*, 112:258-263, 1990.

- [125] Mikic, B. B. and Rohsenow, W. M. A new correlation of pool-boiling data including the effect of heating surface characteristics. *J. Heat Transfer*, pages 245-250, May 1969.
- [126] Forster, H. K. and Zuber, N. Dynamics of vapor bubbles and boiling heat transfer. *A.I.Ch.E. Journal*, 1(4):531-535, Dec 1955.
- [127] Sakurai, A. and Shiotsu, M. and Kataoka, I. and Hata, K. Sodium pool boiling heat transfer. In *Sixth Int. Heat Transfer Conference, Toronto, Canada*, volume 1, pages 193-198, Aug 7-11 1978.
- [128] Thibault, Jules and Hoffman, Terrence W. Local boiling heat flux density around a horizontal cylinder under saturated and subcooled conditions. In *Sixth Int. Heat Transfer Conference, Toronto, Canada*, volume 1, pages 199-204, Aug 7-11 1978.
- [129] Kovalev, S. A. and Rybchinskaja, G. B. Analysis of conditions for transition to film boiling upon incipient boiling. In *Sixth Int. Heat Transfer Conference, Toronto, Canada*, volume 1, pages 205-208, Aug 7-11 1978.
- [130] Hahne, E. and Diesselhorst, T. Hydrodynamic and surface effects on the peak heat flux in pool boiling. In *Sixth Int. Heat Transfer Conference, Toronto, Canada*, volume 1, pages 209-214, Aug 7-11 1978.
- [131] Grigoriev, V. A. and Klimenko, V. V. and Pavlov, Yu. M. and Ametistov, V. The influence of some heating surface properties on the critical heat flux in cryogenic liquids boiling. In *Sixth Int. Heat Transfer Conference, Toronto, Canada*, volume 1, pages 215-220, Aug 7-11 1978.
- [132] Labuntsov, D. A. and Jagov, V. V. and Gorodov, A. K. Critical heat fluxes in boiling at low pressure region. In *Sixth Int. Heat Transfer Conference, Toronto, Canada*, volume 1, pages 221-226, Aug 7-11 1978.
- [133] Mohan Rao, P. K. and Andrews, D. G. Post-nucleate boiling and critical heat flux from horizontal heated surfaces. In *Sixth Int. Heat Transfer Conference, Toronto, Canada*, volume 1, pages 227-232, Aug 7-11 1978.
- [134] Berghmans, J. The minimum heat flux during film boiling. In *Sixth Int. Heat Transfer Conference, Toronto, Canada*, volume 1, pages 233-238, Aug 7-11 1978.
- [135] Styricovich, M. A. and Baryshev, Yu. V. and Tsiklauri, G. V. and Grigorieva, M. E. The mechanism of heat and mass transfer between a water

- drop and a heated surface. In *Sixth Int. Heat Transfer Conference, Toronto, Canada*, volume 1, pages 239-244, Aug 7-11 1978.
- [136] **Nishio, S. and Hirata, M.** Direct contact phenomenon between a liquid droplet and high temperature solid surface. In *Sixth Int. Heat Transfer Conference, Toronto, Canada*, volume 1, pages 245-250, Aug 7-11 1978.
- [137] **Rhodes, T. R. and Bell, K. J.** The leidenfrost phenomenon at pressures up to the critical. In *Sixth Int. Heat Transfer Conference, Toronto, Canada*, volume 1, pages 251-256, Aug 7-11 1978.
- [138] **Rao, P. S. V. K. and Sarma, P. K.** Film boiling heat transfer method of partial evaporation of extended liquid masses. In *Sixth Int. Heat Transfer Conference, Toronto, Canada*, volume 1, pages 257-263, Aug 7-11 1978.
- [139] **Yao, S. C. and Henry, R. E.** Experiments of quenching under pressures. In *Sixth Int. Heat Transfer Conference, Toronto, Canada*, volume 1, pages 263-268, Aug 7-11 1978.
- [140] **Bankoff, S. G. and Maeshima, M. and Segev, A. and Sharon, A.** Destabilization of film boiling in liquid-liquid systems. In *Sixth Int. Heat Transfer Conference, Toronto, Canada*, volume 1, pages 269-274, Aug 7-11 1978.
- [141] **Oker, E. and Merte, jr., H.** A study of transient effects leading up to inception of nucleate boiling. In *Sixth Int. Heat Transfer Conference, Toronto, Canada*, volume 1, pages 139-144, Aug 7-11 1978.
- [142] **Singh, A. and Mikic, B. B. and Rohsenow, W. M.** Relative behavior of water and organics in boiling. In *Sixth Int. Heat Transfer Conference, Toronto, Canada*, volume 1, pages 163-168, Aug 7-11 1978.
- [143] **Aksyonova, E. S. and Diev, M. D. and Mironov, B. M.** Internal characteristics of squeezed boiling. In *Sixth Int. Heat Transfer Conference, Toronto, Canada*, volume 1, pages 169-173, Aug 7-11 1978.
- [144] **Bier, K. and Gorenflo, D. and Salem, M. and Tanes, Y.** Pool boiling heat transfer and size of active nucleation centers for horizontal plates with different surface roughness. In *Sixth Int. Heat Transfer Conference, Toronto, Canada*, volume 1, pages 151-156, Aug 7-11 1978.
- [145] **Jawurek, H. H.** Simultaneous determination of microlayer geometry and bubble growth in nucleate boiling. *Int. J. Heat Mass Transfer*, 12:843-848, 1969.

- [146] **Stphan, K.** *Bubble Formation and Heat Transfer in Natural Convection Boiling*. Hemisphere Publishing Corporation, 1977.
- [147] **von Ceumern-Lindenstjerna, W.-C.** *Bubble Departure Diameter and Release Frequencies during Nucleate Pool Boiling of Water and Aqueous Sodium Chloride Solutions*. Hemisphere Publishing Corporation, 1977.
- [148] **Diesselhorst, T. and Grigull, U. and Hahne, E.** *Hydrodynamic and Surface Effects on the Peak Heat Flux in Pool Boiling*. Hemisphere Publishing Corporation, 1977.
- [149] **Yao, Shi-Chune and Chang, Yung.** Pool boiling heat transfer in a confined space. *Int. J. Heat Mass Transfer*, 26(6):841-848, 1983.
- [150] **Nakayama, W. and Daikoku, T. and Nakajima, T.** Effects of pore diameters and system pressure on saturated pool nucleate boiling heat transfer from porous surfaces. *Trans. A.S.M.E.*, 104:286-291, May 1982.
- [151] **Choi, K. J. and Yao, S. C.** Mechanisms of film boiling heat transfer of normally impacting spray. *Int. J. Heat Mass Transfer*, 30(2):311-318, 1987.
- [152] **Wayner, Jr., P. C.** Adsorption and capillary condensation at the contact line in change of phase heat transfer. *Int. J. Heat Mass Transfer*, 25(5):707-713, 1982.
- [153] **Karagozian, A. R. and Eastes, T. W.** A two-dimensional study of liquid droplet breakup. In *Winter Annual Meeting of A.S.M.E., Anaheim, California*, Dec 7-12 1986.
- [154] **Graham, Robert W. and Hendricks, Robert C.** Assessment of convection, conduction, and evaporation in nucleate boiling. Technical Report NASA Technical Note TN D-3943, NASA, May 1967.
- [155] **Reda, D. C.** Natural convection experiments in a stratified liquid-saturated porous medium. *Trans. A.S.M.E.*, 108:660-664, Aug 1986.
- [156] **Bergles, A. E. and Rohsenow, W. M.** The determination of forced-convection surface-boiling heat transfer. *J. Heat Transfer*, pages 365-372, Aug 1964.
- [157] **Anderson, G. H. and Abayawardana, S. A. K.** Bubble dynamics in nucleate boiling. In *sixth Int. Heat Transfer Conference, Toronto, Canada*, volume 1, pages 121-126, Aug 7-11 1978.

- [158] **Schultz, Robert R. and Cole, Robert.** Bubble nucleation and growth instabilities in transient boiling. In *Sixth Int. Heat Transfer Conference, Toronto, Canada*, volume 1, pages 133-138, Aug 7-11 1978.
- [159] **Cooper, M. G.** The mirage boiling. *Int. J. Heat Mass Transfer*, 26(7):1088-1090, 1983.
- [160] **Cornwell, K. and Brown, R. D.** Boiling surface topography. In *Sixth Int. Heat Transfer Conference, Toronto, Canada*, volume 1, pages 157-161, Aug 7-11 1978.
- [161] **Shoukri, M. S. M. and Judd, R. L.** A theoretical model for bubble frequency in nucleate pool boiling including surface effects. In *Sixth Int. Heat Transfer Conference, Toronto, Canada*, volume 1, pages 145-150, Aug 7-11 1978.
- [162] **Bergles, A. E. and Chyu, M. C.** Characteristics of nucleate pool boiling from porous metallic coating. *J. Heat Transfer*, 104:279-285, May 1982.
- [163] **Ivey, H. J.** Relationships between bubble frequency, departure diameter and rise velocity in nucleate boiling. *Int. J. Heat Mass Transfer*, 10:1023-1040, 1967.
- [164] **Westwater, J. W.** *Nucleate Pool Boiling*. Univ. of Illinois Press, 1969.
- [165] **Slattery, John C.** General balance equation for a phase interface. *Industrial Engineering Chemistry Fundamentals*, 6:108-115, 1967.
- [166] **Kwak, Ho-Young and Panton, R. L.** Tensile strength of simple liquids predicted by a model of molecular interactions. *J. Phys. D: Appl. Phys.*, 18:647-659, 1985.
- [167] **Kwak, Ho-Young and Panton, R. L.** Gas bubble formation in nonequilibrium -gas solutions. *J. Chem. Phys.*, 78(9):5705-5799, May 1983.
- [168] **Theofanous, T. and Biasi, L. and Isbin, H. S. and Fauske, H.** A theoretical study on bubble growth in constant and time-dependent pressure fields. *Chem. Eng. Sc.*, 24:885-897, 1969.
- [169] **Mathieu, Ph. and Lebon, G.** A non-equilibrium thermodynamic model of two-phase fluids with mass transfer. *Journal of Non-Equilibrium Thermodynamics*, 7:129-144, 1982.

- [170] **Bornhorst, W. J. and Hátsopoulos, G. N.** Bubble growth calculation without neglect of interfacial discontinuities. *Journal of Appl. Mech.*, pages 847-853, Dec 1967.
- [171] **Jensen, M. K. and Jackman, D. L.** Prediction of nucleate pool boiling heat transfer coefficients of refrigerant-oil mixture. *Trans. A.S.M.E.*, 106:184-190, Feb 1984.
- [172] **Barakat, S. A. and Sims, G. E.** Heat transfer in pool barbotage. In *Sixth Int. Heat Transfer Conference, Toronto, Canada*, volume 1, pages 127-132, Aug 7-11 1978.
- [173] **Jemison, T. R. and Rivers, R. J. and Cole, R.** Incipient vapor nucleation of methanol from an artificial site- uniform superheat. *J. Heat Transfer*, 104:567-569, Aug 1982.
- [174] **Takenaka, N. and Murata, T. and Takahashi, O. and Michiyoshi, I.** Boiling heat transfer from a horizontal plane heater to a potassium layer. *Int. J. Heat Mass Transfer*, 26(1):154-156, 1983.
- [175] **Sinitsyn, Ye. N. and Muratov, G. N. and Skripov, V. P.** The surface tension of f-11, 21 and 113. *Heat Transfer Sov. Res.*, 4(4):79-80, July-Aug 1972.
- [176] **Paul, D. D. and Abdel-Khalik S. I.** A statistical analysis of saturated nucleate boiling along a heated wire. *Int. J. Heat Mass Transfer*, 26(4):509-519, 1983.
- [177] **Jacobs, H. R. and Major, B. H.** The effect of noncondensable gases on bubble condensation in an immiscible liquid. *J. Heat Transfer*, 104:487-492, Aug 1982.
- [178] **Firth, R. J. and Meyer, L.** A comparison of the heat transfer and friction factor performance of four different types of artificially roughened surface. *Int. J. Heat Mass Transfer*, 26(2):175-183, 1983.
- [179] **Kocamustafaogullari, G. and Ishii, M.** Interfacial area and nucleation site density in boiling systems. *Int. J. Heat Mass Transfer*, 26(9):1377-1387, 1983.
- [180] **Matsumura, Hiroaki.** The influence of sound on natural convection from vertical flat plates. *Int. J. Heat Mass Transfer*, 26(5):790-792, 1983.
- [181] **Cole, Robert.** A photographic study of pool boiling in the region of the critical heat flux. *A.I.Ch.E. Journal*, 6(4):533-538, 1960.

- [182] **Katto, Y. and Haramura, Y.** A new hydrodynamic model of critical heat flux, applicable widely to both pool and forced convection boiling on submerged bodies in saturated liquids. *Int. J. Heat Mass Transfer*, 26(3):389-399, 1983.
- [183] **Mollendorf, J. C. and Arif, H. and Ajiniran, E. B.** Developing flow and transport above a suddenly heated horizontal surface in water. *Int. J. Heat Mass Transfer*, 27(2):273-289, 1984.
- [184] **Monde, M. and Kusuda, H. and Uehara, H.** Critical heat flux during natural convective boiling in vertical rectangular channels submerged in saturated liquid. *Trans. A.S.M.E.*, 104:300-303, May 1982.
- [185] **Chongrungreong, S. and Sauer, Jr., H. J.** Nucleate boiling performance of refrigerants and refrigerant-oil mixtures. *J. Heat Transfer*, 102:701-705, Nov 1980.

APPENDIX A. NATURAL CONVECTION INSIDE THE BUBBLE

Since the heated surface is at a higher temperature than the cap portion of the bubble, some natural convection is expected inside the bubble. A separate program has been developed to simulate the natural convection inside the bubble the purpose of which was to find the *order of magnitude* of the velocities and the nature of flow field. As the bubble expands to large sizes, its rate of growth decreases markedly (like $\frac{1}{t^2}$). Thus a quasi-steady assumption for flow inside the bubble becomes reasonable. For this reason a bubble of constant radius (R_{rep}) and constant mass has been considered to simulate the natural convection. The vapor properties are assumed to be constant except the vapor density is a function of temperature $\bar{\rho}_v = \bar{\rho}_v(\bar{T})$ in the buoyancy terms of the momentum equation (Boussinesq approximation). Due to the spherical geometry, the same equations as that for the liquid region (2.18, 2.19 and 2.20) have been used, however, the terms accounting for the natural convection have been added in the vorticity transport equation, the description of which is given below.

A.1 Formulation

The radial and tangential components of momentum due to buoyancy (in equations 2.11 and 2.12) are $\bar{g}_r \frac{\Delta \bar{\rho}}{\rho}$ and $\bar{g}_\psi \frac{\Delta \bar{\rho}}{\rho}$ respectively, where ρ is the density at

a reference temperature (T_i), $\bar{g}_r = g \sin \bar{\psi}$ and $\bar{g}_\psi = -g \cos \bar{\psi}$, $\bar{\rho} = \bar{\rho}(\bar{T})$, and $\rho = \rho(T_i)$. From the discussion in Section 2.2.3 it is clear that this would result in the following additional term in the vorticity transport equation

$$\frac{\partial}{\partial \bar{r}} \left(\bar{r} \bar{g}_\psi \frac{\bar{\rho}}{\rho} \right) - \frac{\partial}{\partial \bar{\psi}} \left(\bar{g}_r \frac{\bar{\rho}}{\rho} \right)$$

A linear dependence of $\bar{\rho}$ on \bar{T} is written as

$$\bar{\rho} = \rho + \frac{\partial \bar{\rho}}{\partial \bar{T}} (\bar{T} - T_i)$$

or,

$$\frac{\bar{\rho}}{\rho} = 1 - \beta (\bar{T} - T_i) \quad (\text{A.1})$$

where $\beta = -\frac{1}{\rho} \frac{\partial \bar{\rho}}{\partial \bar{T}}$. Therefore the above buoyancy term is equal to

$$g \sin \bar{\psi} \left(\bar{r} \frac{\partial}{\partial \bar{r}} \left(\frac{\bar{\rho}}{\rho} \right) + \frac{\bar{\rho}}{\rho} \right) - \frac{\bar{\rho}}{\rho} \frac{\partial}{\partial \bar{\psi}} (-g \cos \bar{\psi}) + g \cos \bar{\psi} \frac{\partial}{\partial \bar{\psi}} \left(\frac{\bar{\rho}}{\rho} \right)$$

After using equation A.1 and adding to it the above term, the vorticity transport equation becomes,

$$\frac{\partial \bar{\omega}}{\partial \bar{t}} + \frac{1}{\bar{r}^2 \sin \bar{\psi}} \frac{\partial(\bar{f}, \bar{\omega})}{\partial(\bar{r}, \bar{\psi})} = \nu \nabla_{\bar{\omega}}^2 \bar{\omega} - \beta g \left[\sin \bar{\psi} \bar{r} \frac{\partial \bar{T}}{\partial \bar{r}} + \cos \bar{\psi} \frac{\partial \bar{T}}{\partial \bar{\psi}} \right] \quad (\text{A.2})$$

The non-dimensionalization of equations 2.18, 2.19 and 2.20 is a transformation that maps $\bar{r} = 0$ to $R = 0$ and $\bar{r} = \bar{R}$ to $R = 1$.

$$\begin{aligned} r &= \frac{\bar{r}}{R_{\text{rep}}} & \psi &= \bar{\psi} & t &= \frac{\bar{t} \alpha_v}{R_{\text{rep}}^2} \\ f &= \frac{\bar{f}}{\alpha_v R_{\text{rep}}} & \omega &= \frac{\bar{\omega} R_{\text{rep}}}{\alpha_v} & T &= \frac{\bar{T} - T_{\text{sat}}}{T_s - T_{\text{sat}}} \end{aligned} \quad (\text{A.3})$$

Substitution of the above definitions in equations 2.18, 2.19 and 2.20 results in

$$\omega = \nabla_f^2 f \quad (\text{A.4})$$

$$\frac{\partial \omega}{\partial t} + \frac{1}{r^2 \sin \psi} \frac{\partial(f, \omega)}{\partial(r, \psi)} = \nabla_{\omega}^2 \omega - Ra Pr \left[\sin \psi r \frac{\partial T}{\partial r} + \cos \psi \frac{\partial T}{\partial \psi} \right] \quad (\text{A.5})$$

$$\frac{\partial T}{\partial t} - \frac{1}{r^2 \sin \psi} \frac{\partial f}{\partial \psi} \frac{\partial T}{\partial r} + \frac{1}{r^2 \sin \psi} \frac{\partial f}{\partial r} \frac{\partial T}{\partial \psi} = \nabla^2 T \quad (\text{A.6})$$

where,

$$\nabla_f^2 = \left(\frac{\partial^2}{\partial r^2} - \frac{\cot \psi}{r^2} \frac{\partial}{\partial \psi} + \frac{1}{r^2} \frac{\partial^2}{\partial \psi^2} \right) \div \sin \psi.$$

$$\nabla_{\omega}^2 \omega = \frac{\partial^2 \omega}{\partial r^2} - \frac{1}{r^2} \frac{\omega}{\sin^2 \psi} + \frac{\cot \psi}{r^2} \frac{\partial \omega}{\partial \psi} + \frac{1}{r^2} \frac{\partial^2 \omega}{\partial \psi^2}.$$

$$\frac{\partial(f, \omega)}{\partial(r, \psi)} = \frac{\partial f}{\partial r} \left(\frac{\partial \omega}{\partial \psi} - \omega \cot \psi \right) - \frac{\partial f}{\partial \psi} \left(\frac{\partial \omega}{\partial r} - \frac{2\omega}{r} \right)$$

The non-dimensional parameter that arises in the above formulation is the Rayleigh number,

$$Ra = \frac{\beta g R_{\text{rep}}^3 (T_h - T_i)}{\nu \alpha \nu}$$

A.2 Boundary Conditions

Since the vapor close to the bubble surface must be at saturated state,

$$\bar{T} = T_{\text{sat}} \quad \text{at} \quad \bar{r} = \bar{R}$$

The other boundary conditions are:

$$\bar{T} = T_h \quad \text{at} \quad \bar{\psi} = \frac{\pi}{2} \quad \frac{\partial \bar{T}}{\partial \bar{\psi}} = 0 \quad \text{at} \quad \bar{\psi} = 0$$

In non-dimensional form, the above boundary conditions are

$$T = 0 \quad \text{at} \quad r = R$$

$$T = 1 \quad \text{at} \quad \psi = \frac{\pi}{2} \quad \frac{\partial T}{\partial \psi} = 0 \quad \text{at} \quad \psi = 0$$

$$T = 1 \quad \text{at } r = 0$$

The streamfunction is set to zero at all the boundaries since the domain contains a fixed quantity of mass. A no-slip boundary condition is assumed at the heated surface and at the bubble surface (due to the presence of surfactants). The non-dimensional vorticity boundary conditions are

$$\omega = \frac{1}{r^2} \frac{\partial^2 f}{\partial \psi^2} \quad \text{at } \psi = \pi/2$$

$$\omega = \frac{\partial^2 f}{\partial r^2} \quad \text{at } r = R$$

$$\omega = 0 \quad \text{at } r = 0 \quad \text{and at } \psi = 0$$

The same computational procedure as in Section 2.5 with 33x33 node points has been used for the computation.

A.3 Results

If R_{rep} (the representative value of bubble radius) and $T_h - T_i$ are selected to be 0.5 mm and 20 °C respectively, then Ra is equal to 0.14. However, the flow field at this Ra was found to be very small and hence a Ra two orders of magnitude higher than this was tried.

The steady state solution was found by using equations A.4, A.5, and A.6 with a 'pseudo' time increment; i.e. the transient terms were retained and a solution invariant in time was taken to be the steady state solution. The steady state temperature, streamfunction, and vorticity fields are shown in figures A.1 through A.3.

The maximum value of streamfunction in the bubble was found to be 0.9×10^{-5} . This corresponds to a total flowfield of approximately $10^{-17} \frac{\text{m}^3}{\text{sec}}$. The maximum

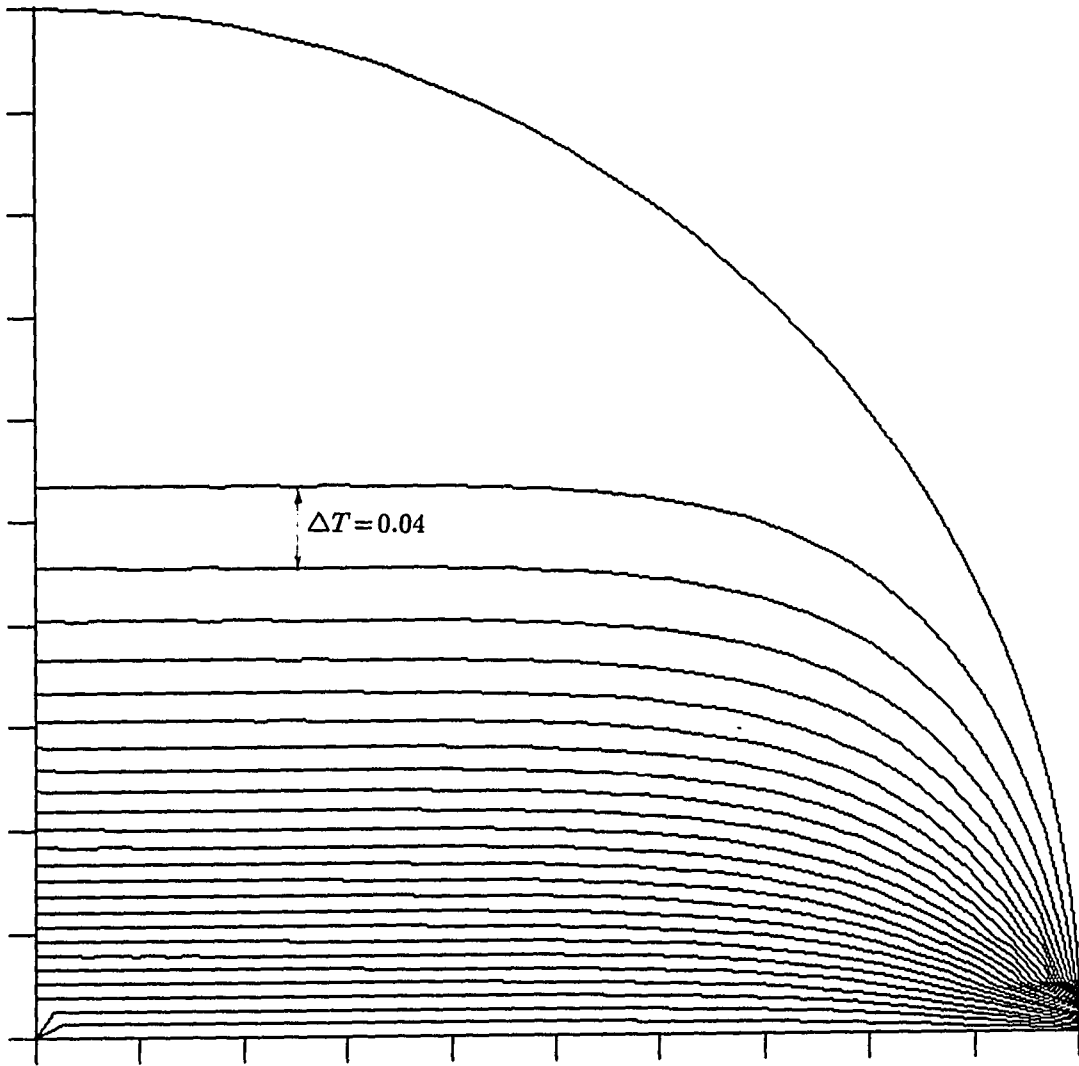


Figure A.1: Steady state solution of the problem of natural convection inside a bubble (temperature)

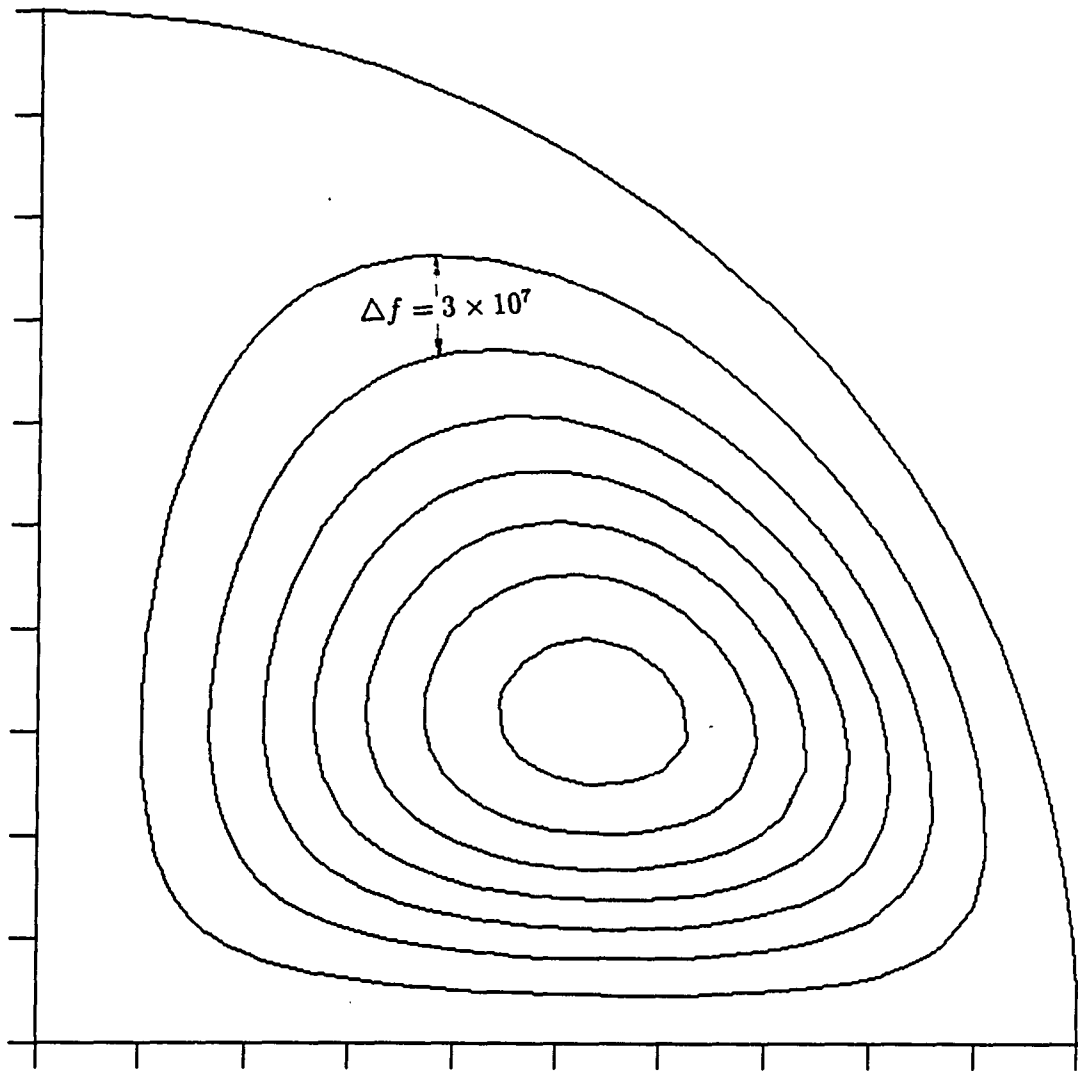


Figure A.2: Steady state solution of the problem of natural convection inside a bubble (streamfunction)

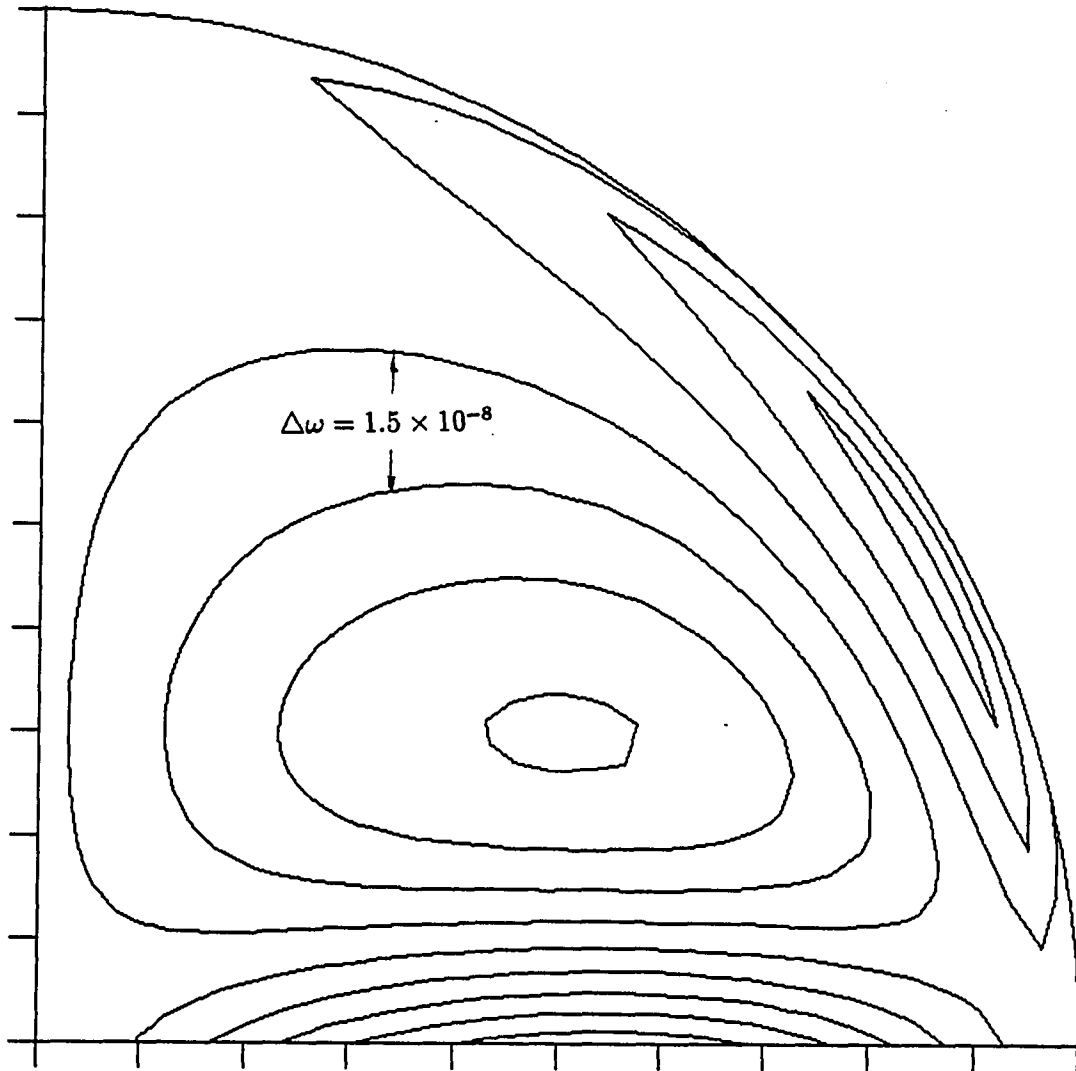


Figure A.3: Steady state solution of the problem of natural convection inside a bubble (vorticity)

velocity was 10^{-8} m/sec, which is at least 8 orders of magnitude smaller than the rate of growth of radius. The dynamic pressure due to the velocity ($P = \rho v \frac{u^2}{2}$) was of the order 10^{-17} Pa, which is extremely small. The temperature distribution is completely governed by conduction as opposed to convection.

It was found that the time required for the steady state solution is much larger than the bubble lifetime, and hence the same equations (A.4 A.5 and A.6) were solved until a life time of a typical bubble 5×10^{-3} sec. The *transient* solution for the temperature, streamfunction and vorticity at this time are shown in figures A.4 through A.6. The velocities were found to be smaller than those in the steady state solution described above, hence too small to be considered for dynamic effects.

All of the bubble is at a saturation temperature except for a very small region near the heated surface. This fact is a result of very small thermal diffusivity of vapor and a comparatively short bubble life time. The results thus indicate that natural convection effects inside the bubble are indeed negligible. For these reasons the assumption of constant vapor properties at the beginning of Chapter 2 is justified.

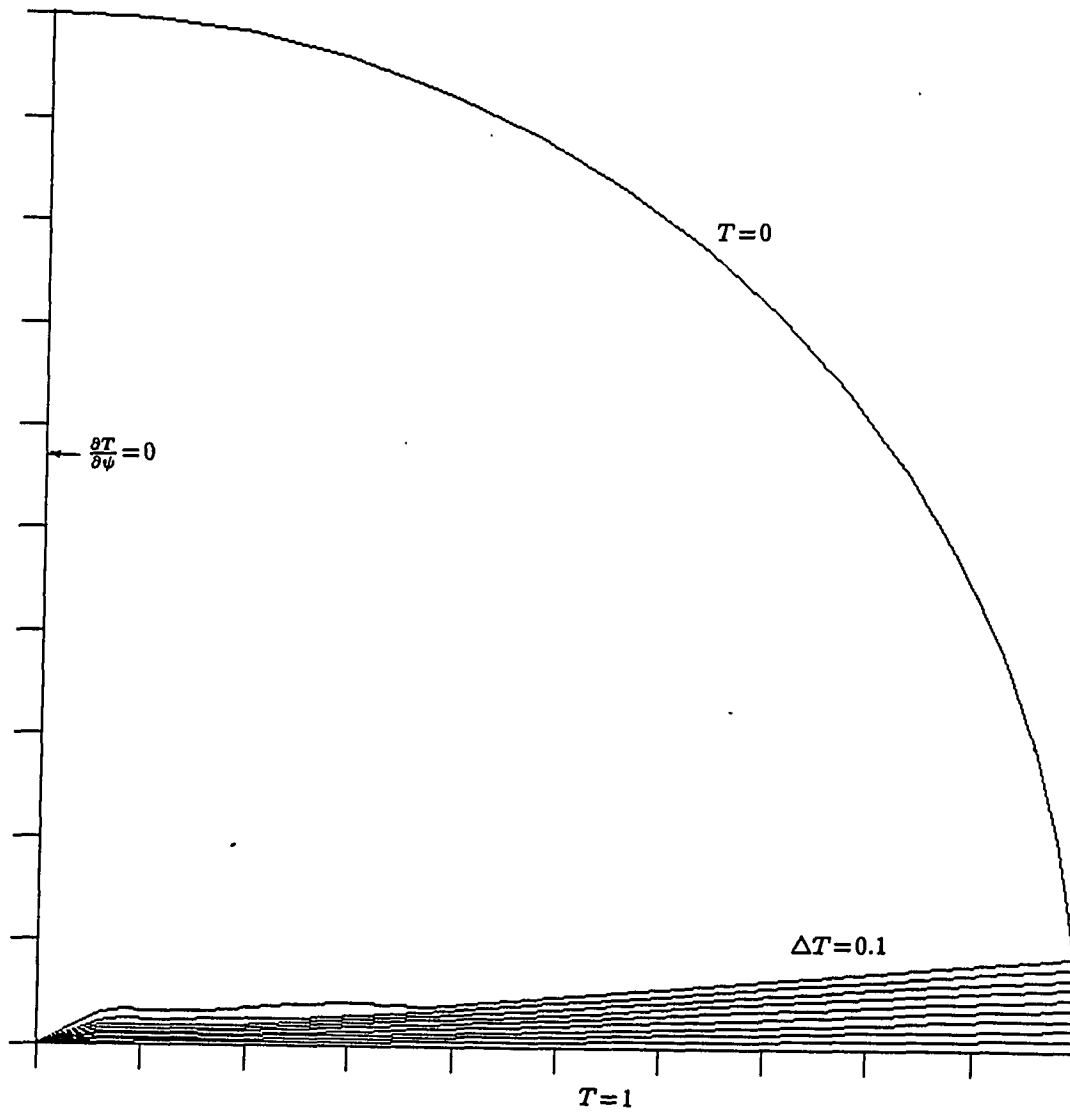


Figure A.4: The transient solution of the problem of natural convection inside the bubble at $\bar{t} = 3 \times 10^{-3}$ sec (Temperature)

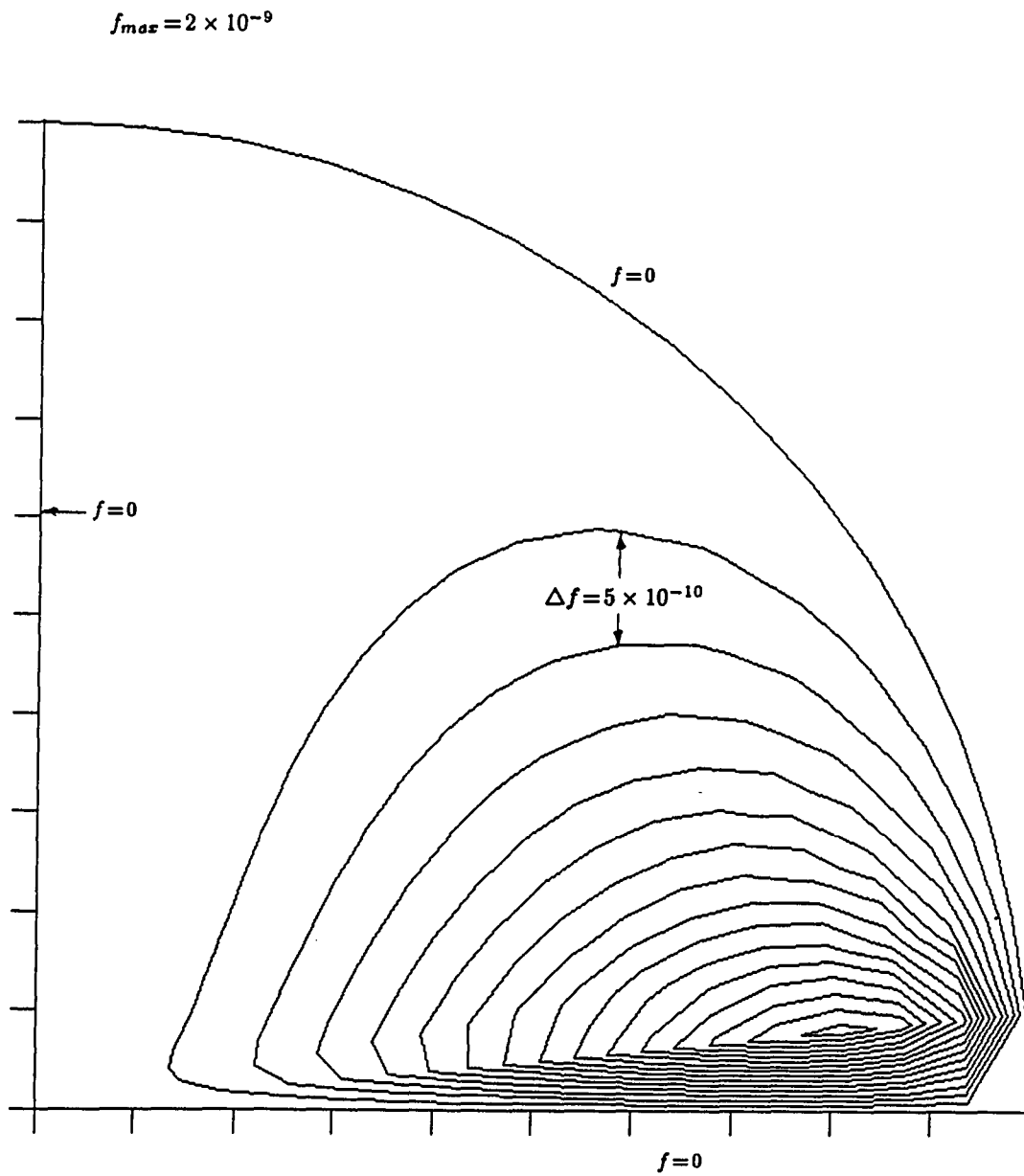


Figure A.5: The transient solution of the problem of natural convection inside the bubble at $\bar{t} = 3 \times 10^{-3}$ sec (Streamfunction)

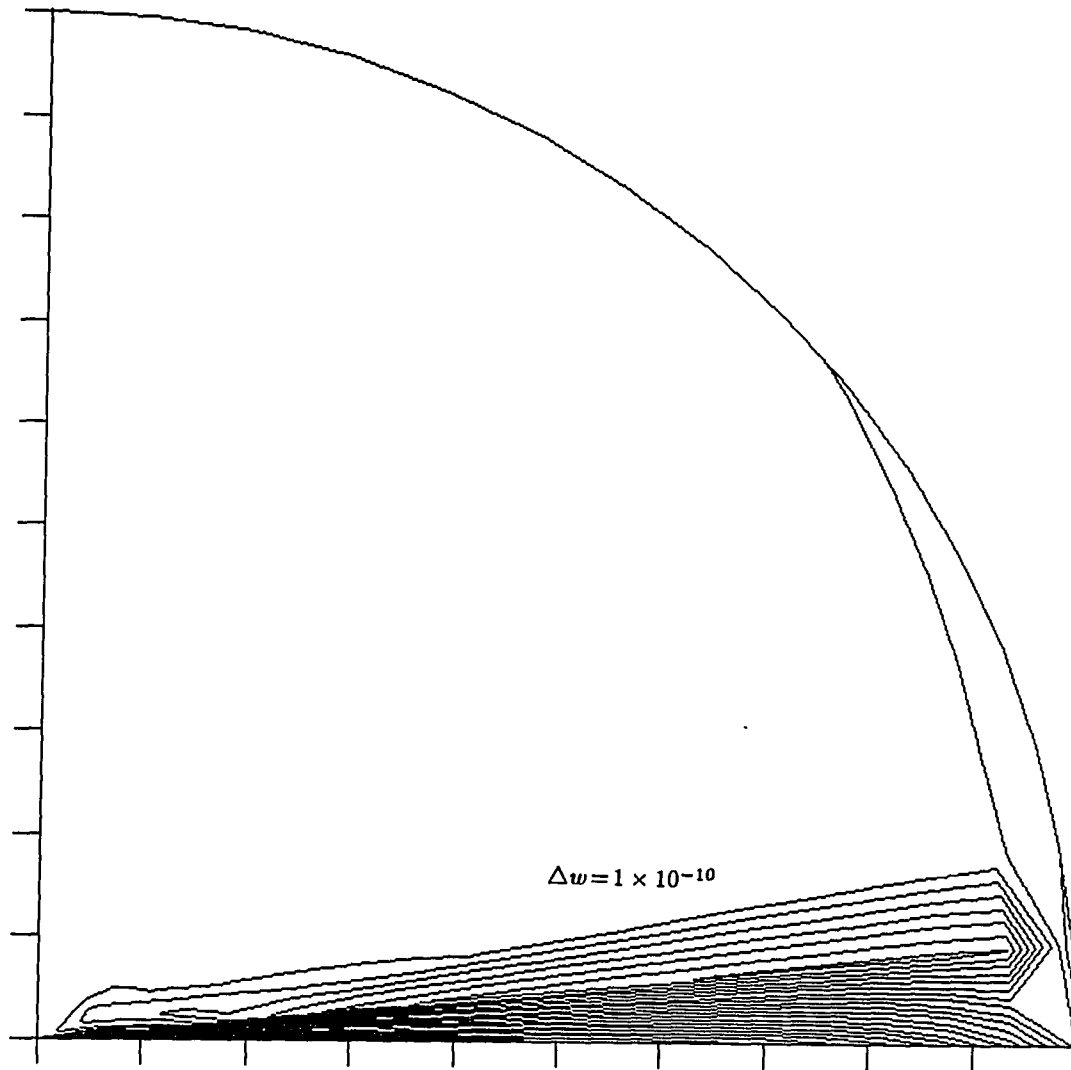


Figure A.6: The transient solution of the problem of natural convection inside the bubble at $\bar{t} = 3 \times 10^{-3}$ sec (Vorticity)

**APPENDIX B. GOVERNING EQUATIONS FOR RELATING
QUANTITIES ON EITHER SIDE OF THE VAPOR-FLUID
INTERFACE**

B.1 Vapor Velocity

Consider an expanding hemispherical control volume similar to that described in Section 2.2.1.1 such that no mass flows through its cap portion, and whose radius (\bar{R}_{cv}) is equal to the radius of bubble (Figure B.1) at the instant of consideration. Note that rate of growth of \bar{R}_{cv} and R will be different since the mass flux through the cap portion of the control volume is zero while there will be some mass flux through the bubble surface. The control volume may contain a mixture of vapor and non-condensable gas denoted by a subscript g . Reynold's transport theorem is applied to this control volume:

$$0 = \frac{\partial}{\partial t} \int_{\mathcal{V}} \rho_g d\mathcal{V} + \int_{\mathcal{A}_{\text{micro}}} \rho \vec{V} \cdot d\vec{A}$$

where \mathcal{V} , \mathcal{A}_{cap} and $\mathcal{A}_{\text{micro}}$ represent volume, surface area of the cap portion and surface area of the microlayer respectively. The last term represents the rate of mass flow from the microlayer $-\dot{m}_m$, thus,

$$0 = \frac{2}{3} \pi \bar{R}_{cv}^3 \dot{\bar{p}}_g + \bar{p}_g 2\pi \bar{R}_{cv}^2 \dot{\bar{R}}_{cv} - \dot{m}_m$$

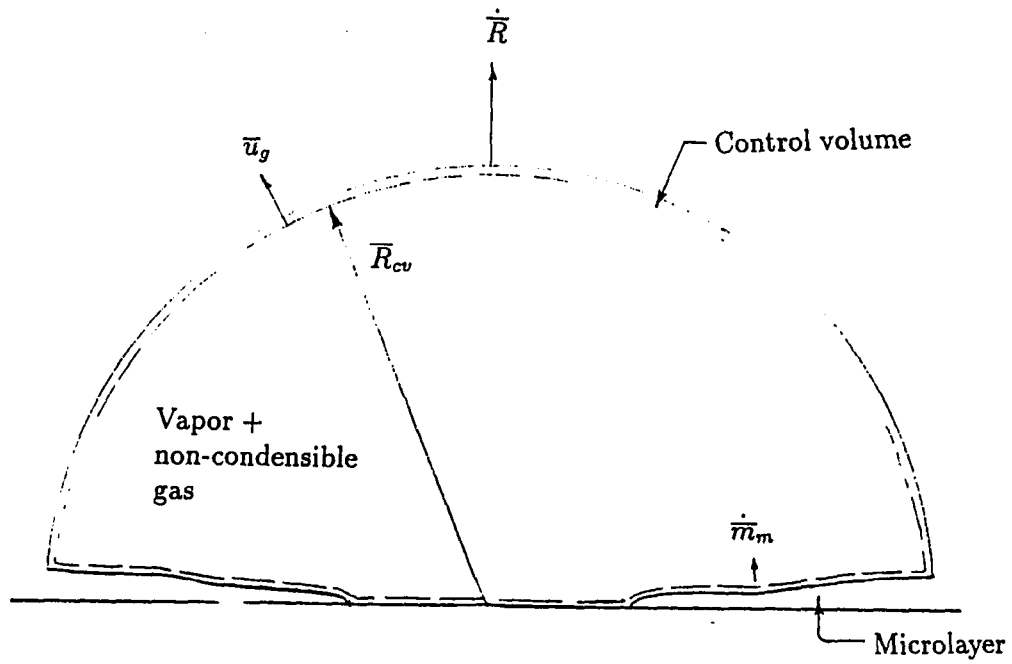


Figure B.1: An expanding control volume with no efflux of mass through the cap portion

where $\dot{\bar{m}}_m$ represents the rate of mass flow to the control volume from the microlayer. Since there is no efflux of mass from the cap portion of the control volume, \bar{u}_g at the bubble surface is equal to $\dot{\bar{R}}_{cv}$. Therefore,

$$\bar{u}_g = -\frac{\bar{R}\dot{\bar{\rho}}_g}{3\bar{\rho}_g} + \frac{\dot{\bar{m}}_m}{2\pi\bar{R}^2\bar{\rho}_g} \quad (\text{B.1})$$

\bar{u}_g is the absolute velocity of gas inside the bubble at the bubble surface. It is the effect of the addition of mass from the microlayer ($\dot{\bar{m}}_m$) and the change of density of gas inside the bubble.

B.2 Mass Balance Across the Interface

Consider again the infinitesimally thin control volume containing a portion of the bubble surface as in Figure 2.3. Application of Reynold's transport theorem of mass balance to this control volume yields

$$0 = \frac{\partial}{\partial t} \int_{\mathcal{V}} \rho v d\mathcal{V} + \int_{\mathcal{A}} \rho \vec{V} \cdot d\vec{\mathcal{A}} \quad (\text{B.2})$$

Therefore,

$$\rho (\hat{u}_{lo} - \dot{\bar{R}}) = \rho_g (\bar{u}_g - \dot{\bar{R}})$$

Substitution of \bar{u}_g from Eq. B.1 and subsequent rearrangement yields

$$\frac{\dot{\bar{m}}_m}{\bar{\rho}_g} + \frac{\rho 2\pi \bar{R}^2 (\dot{\bar{R}} - \hat{u}_{lo})}{\bar{\rho}_g} - \frac{2}{3}\pi R^3 \frac{\dot{\bar{\rho}}_g}{\bar{\rho}_g} = 2\pi \bar{R}^2 \dot{\bar{R}} \quad (\text{B.3})$$

The first and second terms in the above equation represent volume added to the bubble due to microlayer evaporation and due to evaporation at the cap, respectively. The third term accounts for to the rate of change of bubble volume due to the change

of the density of the gas. The right hand side is the resultant increase in volume of the bubble. The above equation is re-written as

$$\dot{\bar{m}}_t = \bar{\rho}_g 2\pi \bar{R}^2 \dot{\bar{R}} + \frac{2}{3}\pi \bar{R}^3 \dot{\bar{\rho}}_v \quad (\text{B.4})$$

where $\dot{\bar{m}}_t = \dot{\bar{m}}_c + \dot{\bar{m}}_m$ and $\dot{\bar{m}}_c = \rho 2\pi \bar{R}^2 (\dot{\bar{R}} - \hat{u}_{l0})$.

B.3 Momentum Balance

Eq. 2.6 applies to the cap portion of this case even when non-condensable gas is present with the vapor inside the bubble. The equation is rearranged as

$$\bar{P}_B - \hat{P}_{l0} = \frac{2\sigma}{\bar{R}} - \frac{1}{\bar{\rho}_g} \left(\frac{\dot{\bar{m}}_c}{2\pi \bar{R}^2} \right)^2 \quad (\text{B.5})$$

The left hand side of this equation stands for the pressure difference across the bubble interface, the first term on the right hand side represents the pressure due to curvature of the surface while the last term represents the inertial pressure of the vapor entering the bubble. The second term on the right hand side of Eq. B.5 represents inertial pressure which was found to be 4 to 6 orders of magnitude smaller than the first term on the right hand side in the second generation model. In the third generation model, $\dot{\bar{m}}_c$ is smaller than that in the second generation model for a given \bar{R} and the term may be neglected giving,

$$\bar{P}_B - \hat{P}_{l0} = \frac{2\sigma}{\bar{R}}. \quad (\text{B.6})$$

B.4 Energy Balance

The Reynold's transport theorem for energy is applied to an infinitesimal control volume (Figure B.2).

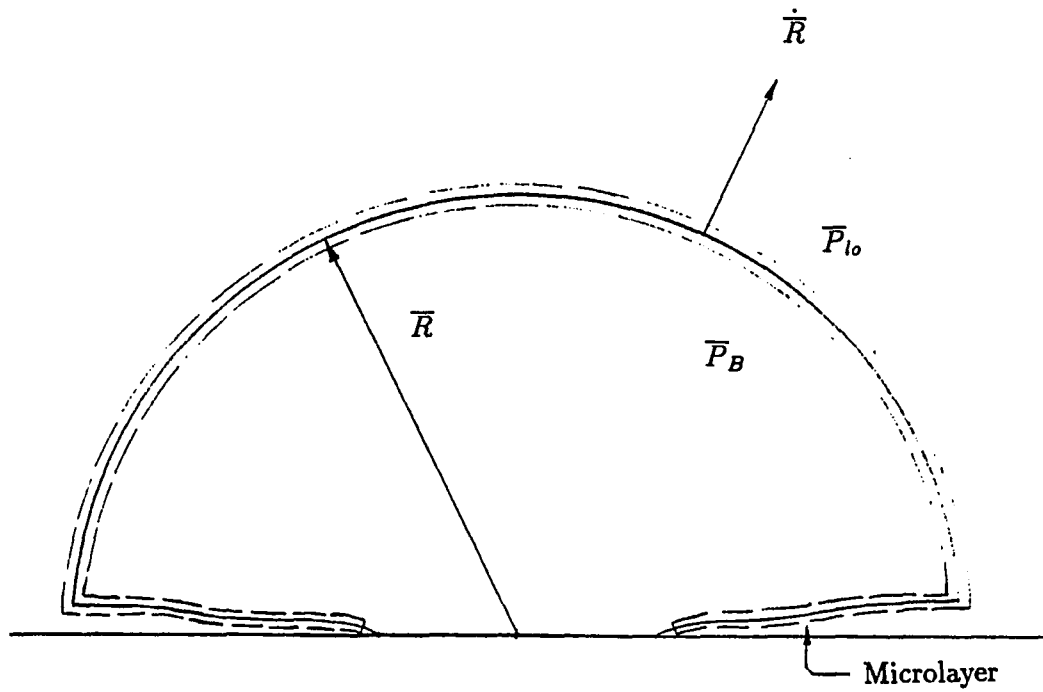


Figure B.2: An infinitesimally thin control volume containing the liquid-vapor interface

$$\dot{Q} - \dot{W} = \frac{\partial}{\partial t} \int_{\mathcal{V}} \left(u' + \frac{1}{2} |\vec{V}_1|^2 + pe_s \right) d\mathcal{V} + \int_{\mathcal{A}} \left(h + \frac{1}{2} |\vec{V}_1|^2 + pe_g \right) (\rho \vec{V}_2 \cdot d\vec{\mathcal{A}}) \quad (\text{B.7})$$

The notation in this equation is explained in Section 2.7. Due to the infinitesimal size of the control volume, the u' and $\frac{1}{2} |\vec{V}_1|^2$ terms in the volume integration are reduced to zero. Since \bar{u}_{l0}^2 was found to be approximately 6 orders of magnitude lower than h_{fg} , the second term in the area integration is neglected. And, since there is no influx or efflux of potential energy through the control surface, the third term in the area integration is also neglected. The resulting transport equation is

$$\dot{Q} - \dot{W} = \frac{\partial}{\partial t} \int_{\mathcal{V}} pe_s d\mathcal{V} + \int_{\mathcal{A}} h (\rho \vec{V}_2 \cdot d\vec{\mathcal{A}}) \quad (\text{B.8})$$

Each of the terms in the above equation are

$$\begin{aligned} \dot{W} &= (\bar{P}_{l0} - \bar{P}_B) 2\pi \bar{R}^2 \dot{\bar{R}} \\ \dot{Q} &= \dot{Q}_c + \dot{Q}_m = k \left\{ \int_{\mathcal{A}_{\text{cap}}} \frac{\partial \bar{T}}{\partial \bar{r}} d\mathcal{A} - \int_{\mathcal{A}_{\text{micro}}} \frac{\partial \bar{T}}{\partial \bar{z}} d\mathcal{A} \right\} \\ \frac{\partial}{\partial t} \int_{\mathcal{V}} pe_s d\mathcal{V} &= 4\pi \sigma \bar{R} \dot{\bar{R}} \\ \int_{\mathcal{A}} h (\rho \vec{V}_2 \cdot d\vec{\mathcal{A}}) &= -(\dot{m}_c + \dot{m}_m) h_{fg} = \dot{m}_t h_{fg} \end{aligned}$$

Hence Eq. B.8 becomes

$$\dot{Q}_c + \dot{Q}_m = \left(\bar{P}_{l0} - \bar{P}_B + \frac{2\sigma}{\bar{R}} \right) 2\pi \bar{R}^2 \dot{\bar{R}} + \dot{m}_t h_{fg} \quad (\text{B.9})$$

The left hand side of this equation represents the heat conducted to the evaporating surface of cap and microlayer, the first term on the right hand side represents work done in expanding the bubble surface and on the surrounding liquid, and the last term stands for the heat of evaporation. Using Eq. B.6, Eq. B.9 is rewritten as

$$\bar{q}_c + \bar{q}_m = \dot{m}_t h_{fg}. \quad (\text{B.10})$$

where \bar{q} denotes energy per unit time (\dot{Q}).

APPENDIX C. THE FLOW FIELD INSIDE THE BUBBLE WITH MICROLAYER

It has been pointed out in the literature review that various researchers [4] [60] [7] have hypothesized substantial flow of mass through the bubble especially in the case of subcooled boiling. The present study indicates that for subcooled boiling, there is net condensation at the cap portion. For the case of saturated boiling, condensation at the cap is negligible. During subcooled boiling at low Jakob numbers a substantial amount of mass is seen to evaporate from the microlayer and the lower part of the cap and condense at the top of the cap, causing a *net* mass flow through the bubble.

The purpose of the simulation of the flowfield was to visualize the flow field and also to get an estimate of order of magnitude of velocities of vapor in the bubble. The later would allow the verification of the assumption of uniform vapor properties. The values of \dot{V}_m , \dot{V}_c , and \dot{R} during asymptotic phase, found from the results of the third generation model were used as an input to this algorithm. Note that these quantities themselves exhibited similarity. Since the problem of bubble growth has exhibited similarity for large values of time, the solution in this section represents the flowfield in the bubble during the asymptotic phase.

An effort was made to solve the complete set of Navier-Stokes equations 2.18, 2.19 and 2.20. However, at the tail of the microlayer, the vorticity assumes two different

values depending on the direction the tail point is approached (along the dry surface, or along the vertical direction). For this reason, the formulation is singular at the tail point. In order to simplify the procedure, an inviscid calculation was performed. The boundary conditions for vorticity for the tried viscous calculation are also given in the subsequent sections. Later in this section, the vapor velocities have been found to be of the order $\frac{\dot{R}}{R}$, and based on the bubble diameter, the Reynolds number was of the order 1 to 250 for the range of cases studied. This indicates that the flowfield is considerably viscous and assumption of inviscid flow is a serious limitation.

The vapor-fluid interface in this model has been assumed to be at saturated state and hence the non-dimensional temperatures of the cap and the microlayer surface must be zero. Since from the result of the third generation model, the dry region was found to occupy only 2 to 20% of the base area, the temperature equation (2.20) was not included in the algorithm for the flow-field.

Equations 2.18, 2.19 and 2.20 are the governing equation of the flowfield. The non-dimensionalization of these equations is a transformation that maps $\bar{r} = 0$ to $\bar{R} = 0$ and $\bar{r} = \bar{R}$ to $\bar{R} = 1$. The definitions of transformation are the same as in equations A.3. Thus equations 2.18, 2.19 and 2.20 are non-dimensionalized as

$$\omega = \nabla_f^2 f \quad (\text{C.1})$$

$$\frac{\partial \omega}{\partial t} + \frac{1}{r^2 \sin \psi} \frac{\partial(f, \omega)}{\partial(r, \psi)} = \nabla_{\omega}^2 \omega \quad (\text{C.2})$$

where,

$$\nabla_f^2 = \left(\frac{\partial^2}{\partial r^2} - \frac{\cot \psi}{r^2} \frac{\partial}{\partial \psi} + \frac{1}{r^2} \frac{\partial^2}{\partial \psi^2} \right) \div \sin \psi.$$

$$\nabla_{\omega}^2 \omega = \frac{\partial^2 \omega}{\partial r^2} - \frac{1}{r^2} \frac{\omega}{\sin^2 \psi} + \frac{\cot \psi}{r^2} \frac{\partial \omega}{\partial \psi} + \frac{1}{r^2} \frac{\partial^2 \omega}{\partial \psi^2}.$$

$$\frac{\partial(f, \omega)}{\partial(r, \psi)} = \frac{\partial f}{\partial r} \left(\frac{\partial \omega}{\partial \psi} - \omega \cot \psi \right) - \frac{\partial f}{\partial \psi} \left(\frac{\partial \omega}{\partial r} - \frac{2\omega}{r} \right)$$

C.1 Boundary Conditions

From the definition of streamfunction Eq. 2.16,

$$\frac{\partial \bar{f}}{\partial \bar{\psi}} = \frac{1}{2\pi} \frac{\partial \dot{\bar{V}}_{v,c}}{\partial \bar{\psi}} \quad (\text{C.3})$$

where $\dot{\bar{V}}_{v,c}(\bar{\psi})$ is the volume flow rate of vapor at the bubble cap with respect to a frame of reference at the heated surface. The subscript v has been placed to distinguish the volume flow rate of vapor from that of volume flow rate of liquid at the surface of phase change. Due to the growth of the bubble, $\dot{\bar{V}}_{v,c}(\bar{\psi})$ is given by the difference between the evaporation rate and the rate of volume swept by the growing bubble, thus, from Eq. C.3,

$$\frac{\partial \bar{f}}{\partial \bar{\psi}} = \frac{1}{2\pi} \left[\frac{1}{\epsilon} \frac{\partial \dot{\bar{V}}_c}{\partial \bar{\psi}} - \dot{\bar{R}} \bar{R}^2 \sin \bar{\psi} \right] \quad (\text{C.4})$$

where $\bar{V}_c(\bar{\psi})$ denotes volume of the *liquid* that has been evaporated. ϵ is the ratio of density of vapor to the density of liquid. Non-dimensionalizing Eq. C.4

$$\frac{\partial f}{\partial \psi} = \frac{1}{2\pi} \left[\frac{1}{\epsilon} \frac{\partial \dot{V}_c}{\partial \psi} - \dot{R} R^2 \sin \psi \right] \quad (\text{C.5})$$

Similarly, for the microlayer portion

$$\frac{\partial \bar{f}}{\partial \bar{r}} = \frac{1}{2\pi} \frac{\partial \dot{\bar{V}}_{v,m}}{\partial \bar{r}} \quad (\text{C.6})$$

where $\dot{\bar{V}}_{v,m}(\bar{r})$ is the vapor volume flow rate at the microlayer. Hence,

$$\frac{\partial \bar{f}}{\partial \bar{r}} = \frac{1}{2\pi \epsilon} \frac{\partial \dot{\bar{V}}}{\partial \bar{r}} \quad (\text{C.7})$$

Non-dimensionalizing Eq. C.7,

$$\frac{\partial f}{\partial r} = \frac{1}{2\pi \epsilon} \frac{\partial \dot{V}}{\partial r} \quad (\text{C.8})$$

C.2 Finite Differencing

The vorticity boundary conditions are:

$$\begin{aligned}\omega_{i,NS} &= \frac{2(f_{i,NS-1} - f_{i,NS})}{R^2 \Delta\psi^2}, & 0 < r < 1, \psi = \frac{\pi}{2} \\ \omega_{i,1} &= 0 & 0 < r < 1, \psi = 0 \\ \omega_{1,j} &= 0 & r = 0, 0 < \psi < \frac{\pi}{2} \\ \omega_{NR,j} &= \left[\frac{2(f_{NR-1,j} - f_{NR,j})}{R^2 \Delta r^2} - \frac{\cot \psi}{R^2} \frac{f_{NR,j+1} - f_{NR,j-1}}{2 \Delta\psi} \right. \\ &\quad \left. + \frac{f_{NR,j+1} - 2f_{nr,j} + f_{NR,j-1}}{R^2 \Delta\psi^2} \right] \div \sin \psi & r = 1, 0 < \psi < \frac{\pi}{2}\end{aligned}$$

Note the viscous flow calculation failed due to the singularity discussed above, and hence the vorticity calculation was abandoned (inviscid flow).

Eq. C.5 is finite differenced as

$$\frac{(f_{j+1} - f_j)}{\Delta\psi} = \frac{1}{2\pi} \left[\frac{1}{\epsilon} \frac{\Delta\dot{V}_c}{\Delta\psi} - \dot{R} R^2 \sin \psi \right] \quad (\text{C.9})$$

Therefore,

$$f_{j+1} = \left[\frac{1}{\epsilon} \frac{\Delta\dot{V}_c}{\Delta\psi} - \dot{R} R^2 \sin \psi \right] \frac{\Delta\psi}{2\pi} + f_j \quad (\text{C.10})$$

The value of $f(0)$, which is the streamfunction at the symmetry line has been assigned an arbitrary value equal to zero.

Eq. C.8 is finite differenced as

$$\frac{(f_{i+1} - f_i)}{\Delta r} = \frac{1}{2\pi \epsilon} \left[\frac{\Delta\dot{V}_m}{\Delta r} \right] \quad (\text{C.11})$$

Therefore,

$$f_{i+1} = f_i + \frac{\Delta\dot{V}_m}{2\pi \epsilon} \quad (\text{C.12})$$

The value of f at $r = 0$ is zero since the line of symmetry passes through the point.

C.3 Results

A uniform grid of 47 radial nodes and 33 angular nodes has been used for computation of the flow field. Figure C.1 depicts the streamfunction at selected Jakob and subcooling numbers. Figure C.2 shows the velocity field. Note from Table 3.2 and Table 3.3, that at saturated boiling, the condensation at the bubble cap is negligible. During subcooled boiling, for the cases studied, the condensation at the cap is of the same order of magnitude as the evaporation.

The streamlines that meet the bubble cap in saturated boiling at most of the top of the cap are not due to condensation but are due to bubble growth itself. The place where the bubble cap profile is locally parallel to a streamline, the amount of volume evaporated is just balanced by the volume swept due to the growth of the bubble. Below this point evaporation rate exceeds the later quantity and above this point the reverse is true. It has been mentioned in Section 3.11 that the local rate of volume evaporated per unit radius ($\frac{\partial \dot{V}_m(r)}{\partial r}$) from the microlayer was a constant function of radius (except at the tail where it was large).

It is of interest to note that the streamlines conjectured by Plesset and Prosperetti [59] and by Plesset and Prosperetti [60] are similar to those found the present study except for the fact that the above authors have ignored the presence of the dry part at the bubble base and have also ignored the high rate of evaporation at the tail part of the microlayer. The velocity of the vapor was found by differentiation of streamfunction (Eq. 2.16), which was of the order $0.1 \frac{\text{m}}{\text{sec}}$ for the cases studied. The dynamic pressure ($P = \rho_v \frac{V^2}{2}$) is of the order 10^{-3} Pa and is extremely minute to be of any consequence. Further, since only 2 to 20 % of the base area was dry for the cases studied, and the vapor-liquid interface (at the microlayer and at the cap) was

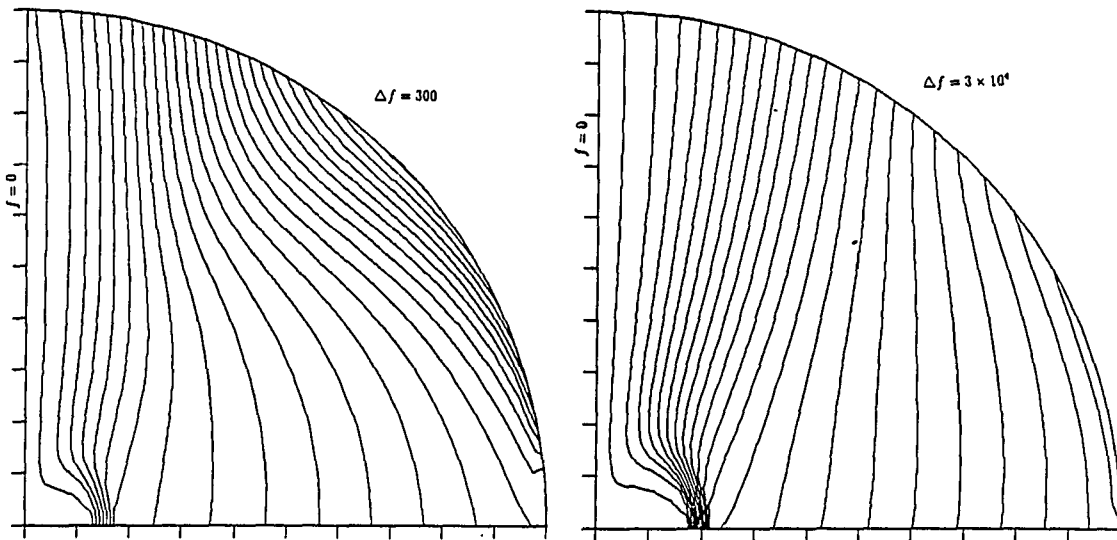
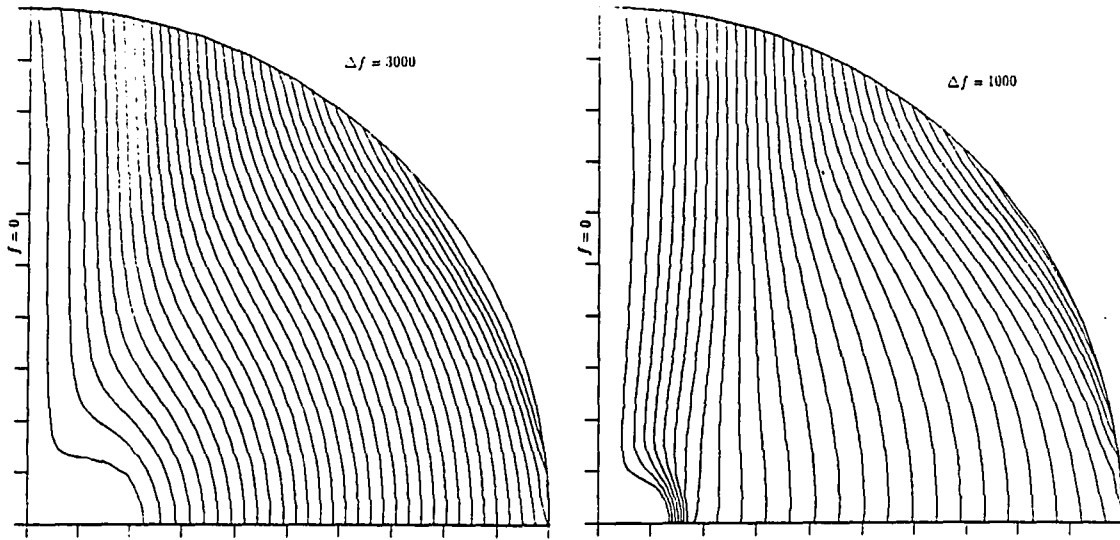
(c) $Ja=20, Sb=1$ (d) $Ja=20, Sb=0$

Figure C.1: The flow-field inside a bubble with microlayer

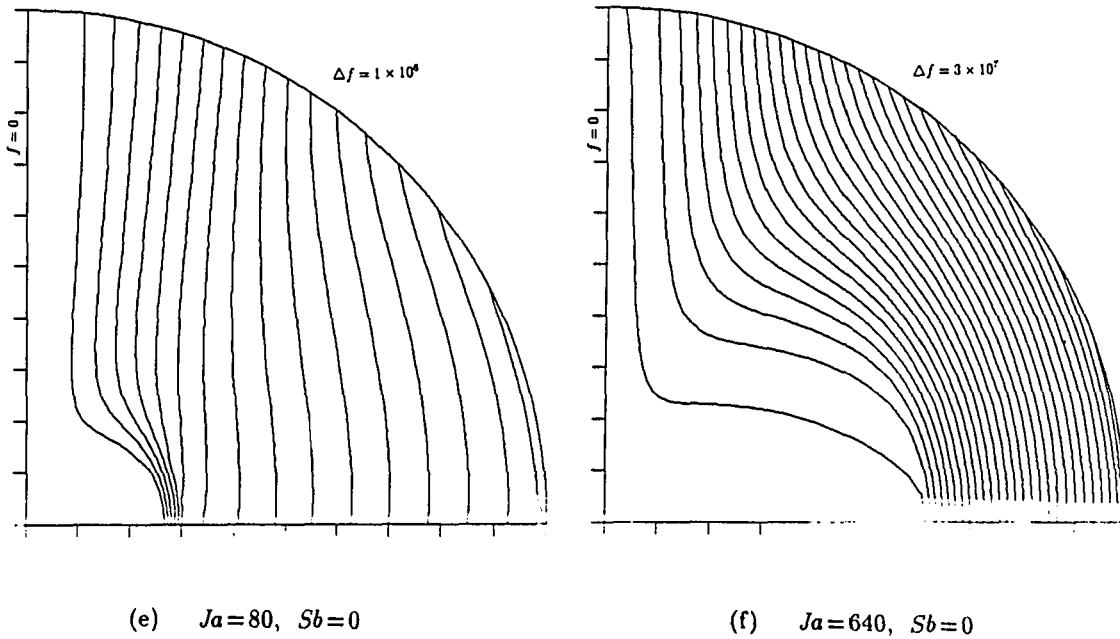
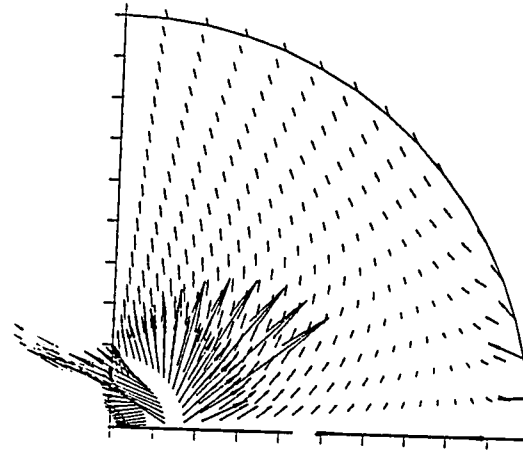
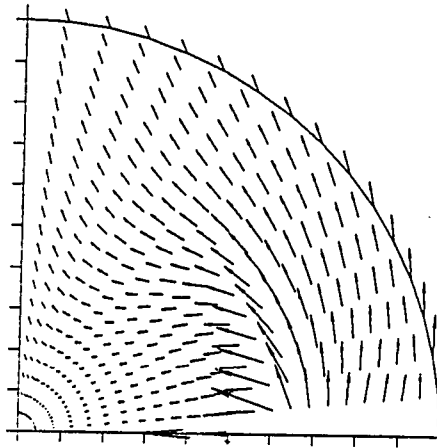


Figure C.1 (Continued)

assumed to be at a saturated state, temperature gradients in the interior must be negligible. This discussion indicates that the pressure, density, and the temperature inside the bubble must be uniform. This justifies the assumption of uniformity of vapor properties, which was made at the beginning of the third generation model. Plesset and Prosperetti [59] have analytically proved that the vapor properties must be uniform even if the temperature of the boundary was not uniform. By keeping a probe inside a bubble, Beer et al. [73] have also observed uniform vapor properties. In their computational models Joosten et al. [38], Guy and Ledwidge [65], and Lee and Nydahl have assumed uniform properties. The present study supports these facts.



(a) $Ja=20$ $Sb=0.05$



(b) $Ja=640$ $Sb=0$

Figure C.2: The velocity field inside a bubble with microlayer